Volume 138
2011

EDITORS
F. Kremer
W. Richtering

Progress in Colloid and Polymer Science

Trends in Colloid and Interface Science XXIV

VOLUME EDITORS
V. Starov
K. Procházka

Springer

Progress in Colloid and Polymer Science
Volume 138

Progress in Colloid and Polymer Science

Recently published and Forthcoming Volume

Trends in Colloid and Interface Science XXIV
Volume Editors: Victor Starov, Karel Procházka
Vol. 138, 2011

Trends in Colloid and Interface Science XXIII
Volume Editor: Seyda Bucak
Vol. 137, 2010

Gels: Structures, Properties, and Functions
Volume Editors: Masayuki Tokita, Katsuyoshi Nishinari
Vol. 136, 2009

Colloids for Nano- and Biotechnology
Volume Editors: Hórvölgyi, Z.D., Kiss, É.
Vol. 135, 2008

Surface and Interfacial Forces From Fnndamentals to Applications
Volume Editors: Auernhammer, G.K., Butt, H.-J , Vollmer, D.
Vol. 134, 2008

Smart Colloidal Materials
Volume Editor: Richtering, W.
Vol. 133, 2006

Characterization of Polymer Surfaces and Thin Films
Volume Editors: Grundke, K., Stanun, M., Adler, H.-J.
Vol. 132, 2006

Analytical Ultracentrifugation VIII
Volume Editors: Wandrey, C., Cölfen, H.
Vol. 131, 2006

Scattering Methods and the Properties ofPolymer Materials
Volume Editors: Stribeck, N., Smarsly, B.
Vol. 130, 2005

Mesophases, Polymers, and Particles
Volume Editors: Lagaly, G., Richtering, W.
Vol. 129, 2004

Surface and Colloid Science
Volume Editor: Galembeck, F.
Vol. 128, 2004

Analytical Ultracentrifugation VII
Volume Editors: Lechner, M.D., Börger, L.
Vol. 127, 2004

Trends in Colloid and Interface Science XVII
Volume Editors: Cabuil, V., Levitz, P., Treiner, C.
Vol. 126, 2004

From Colloids to Nanotechnology
Volume Editors: Zrinyi, M., Horvolgyi, Z.D.
Vol. 125, 2004

Aqueous Polymer Dispersions
Volume Editor: Tauer, K.
Vol. 124, 2004

Trends in Colloid and Interface Science XVI
Volume Editors: Miguel, M., Burrows, H.D.
Vol. 123, 2004

Aqueous Polymer – Cosolute Systems
Volume Editor: Anghel, D.F.
Vol. 122, 2002

Molecular Organisation on Interfaces
Volume Editor: Lagaly, G.
Vol. 121, 2002

Victor Starov · Karel Procházka
Editors

Trends in Colloid and Interface Science XXIV

Springer

Editors
Victor Starov
Loughborough University
Chemical Engineering
Leicestershire
UK
v.m.starov@lboro.ac.uk

Karel Procházka
Charles University in Praha
Faculty of Science
Department of Physical and
Macromolecular Chemistry
Hlavova 8
12843 Praha
Czech Republic
prochaz@natur.cuni.cz

ISSN 0340-255X e-ISSN 1437-8027
ISBN 978-3-642-19037-7 e-ISBN 978-3-642-19038-4
DOI 10.1007/978-3-642-19038-4
Springer Heidelberg Dordrecht London New York

Library of Congress Control Number: 2011929344

Cover design: eStudio Calamar S.L.

Printed on acid-free paper

Springer is part of Springer Science+Business Media (www.springer.com)

Preface

Dear readers, the current volume of Progress in Colloid and Polymer Science publish a collection of papers presented (both orals and posters) at the 24th Meeting of the European Colloid and Interface Society (ECIS) held in Prague 5–10 September, 2010. ECIS has the long scientific traditions and ECIS is a respected and recognized scientific society. ECIS' annual meetings have always been amply attended by participants both from academia and industry. The meetings provide an opportunity to exchange ideas, communicate and discuss the most recent scientific results of ECIS members and attendees with a broad audience of experienced colloid scientists, polymer chemists and physicists, physical and organic chemists, chemical engineers, etc. Besides the scientific program, the ECIS general assembly always takes place, where general questions are discussed, organization problems solved and the ECIS Board elected. The official ECIS policy is oriented towards the promotion of the scientific career of young postdocs and especially of PhD students who are invited to attend the meetings at a reduce price with a high chance of getting an oral presentation.

The Prague meeting was very successful from both the scientific and social points of view. A record number of ca. 600 participants (more than 250 PhD students) not only from Europe but from quite distant parts of the world like USA, Canada, Japan, Australia and New Zeeland, etc. met in Prague. The scientific program included several 40 min plenary lectures, Rhodia Prize lecture, Overbeek Medal Lecture, 20 min regular oral presentations and three very busy poster sessions. A total number of almost 100 oral presentations and 600 posters were presented. In Prague, similarly to several previous meetings, one parallel oral session and one poster session was devoted to the studies done in the framework of the COST D 43 action, which is scientifically tightly connected with ECIS activities.

The current volume includes 35 contributions from both leading scientists as well as young scientists. Those contributions cover a broad spectrum of topics that belong to the world trends in colloid, surface and polymer chemistry and in nanomaterial research. Individual chapters correspond to the sessions at the 24th ECIS meeting:

1. Self-assembling, stimuli-responsive and Hierarchically Organized Systems.
2. Colloid, Polymer and Polyelectrolyte Solutions; Concentrated Systems and Gels.
3. Thin Films, Interfaces and Surfaces, Wetting Phenomena.
4. Novel-Nano-to Mesostructured Functional Materials.
5. Biologically Important and Bioinspired Systems; Pharmaceutical and Medical Applications.

We hope that a reading of the presented contributions will give both an overview of the recent activities of the ECIS members and provide new knowledge and an inspiration

required for reader's own work in the multidisciplinary colloid, interface, polymer an nanomaterial science.

At the end of this short introduction, we would also like to invite you to participate at the next 25th ECIS meeting to be held in Berlin the first week in September, 2011.

Karel Procházka, Victor Starov (editors)

Contents

Novel Nano-to-Mesostructured Functional Materials

Biologically Important and Bioinspired Systems; Pharmaceutical and Medical Applications

Progr Colloid Polym Sci (2011) 138:1–6
DOI: 10.1007/978-3-642-19038-4_1

Swelling of a Sponge Lipid Phase via Incorporation of a Nonionic Amphiphile: SANS and SAXS Studies

Angelina Angelova[1,2], Borislav Angelov[3,4], Rada Mutafchieva[5], Vasil M. Garamus[3], Sylviane Lesieur[1,2], Sérgio S. Funari[5], Regine Willumeit[3], and Patrick Couvreur[1,2]

Abstract Small-angle X-ray scattering (SAXS) is employed to establish the structure of a self-assembled lipid/water system formed in excess aqueous phase by pharmaceutical-grade glycerol monooleate (GMO). A nonionic guest component (octyl glucoside) is incorporated with the purpose to study the swelling of the structure under full hydration. Small-angle neutron scattering (SANS) is used for characterization of the micellar properties of the octyl glucoside amphiphile and glycerol monooleate. The obtained SAXS and SANS patterns indicate a sponge-type supramolecular organization of the investigated lipid material. Their analysis allows determination of the average cell-cell distances in the bicontinuous bilayer sponge that are essential for the encapsulation of biomolecules and drugs. In the presence of the guest octyl glucoside (OG) the average size of the sponge cells is increased by about 14%. This would be an advantageous feature for the application of sponge-type liquid crystalline carriers as protein drug delivery vehicles, nanostructured bioreactors, and peptide-encapsulating fluid nanomaterials.

Keywords lipid-water phases • liquid crystals • swelling • sponge phase • small-angle X-ray scattering • SANS • micelles • glycerol monooleate • octyl glucoside

A. Angelova (✉)
[1]CNRS UMR8612 Physico-chimie-Pharmacotechnie-Biopharmacie, Châtenay-Malabry, F-92296 France
[2]Univ Paris Sud, Châtenay-Malabry, F-92296 France
e-mail: Angelina.Angelova@u-psud.fr
[3]Institute of Materials Research, GKSS Research Center, Geesthacht, D-21502 Germany
[4]Department of Chemistry and iNANO, Aarhus University, 8000 Århus, Denmark
[5]Institute of Biophysics, Bulgarian Academy of Sciences, BG-1113 Sofia, Bulgaria
[6]HASYLAB c/o DESY, Notkestrasse 85, Hamburg, D-22603 Germany

Introduction

Monoglyceride lipid-water phase diagrams have received considerable interest owing to the broad applications of their liquid-crystalline (LC) phases [1-10]. Depending on the hydration level and temperature [11-15], the purified powder of the lipid glycerol monooleate (GMO) gives rise to a complex phase diagram eminent by periodic mesophases of gyroid (*Ia3d*) and double diamond (*Pn3m*) cubic symmetries as well as an inverted hexagonal (H_{II}) phase. The lipid cubic phases present structural advantages as nanostructured delivery carriers of therapeutic and nutraceutic molecules and as templates for membrane protein crystallization [16-26]. These highly-ordered periodic 3D structures are characterized by a constant interfacial monolayer curvature of the constituent lipid bilayer and by a bicontinuous architecture of aqueous nanochannels. An important feature of the bicontinuous cubic phases is that they stably exist in excess aqueous environment.

The inclusion of additives into glycerol monooleate cubic phases may strongly affect their hydration, interfacial curvature, and structural phase behavior [4-10,23-29]. It is well known that under limited water conditions, the progressive reduction of the water content of the glycerol monooleate inverted cubic phase causes a phase transformation from a *Pn3m* cubic mesophase to a more curved *Ia3d* inverted cubic structure [12,14]. Adding of neutral or charged lipids or detergents to the GMO inverted cubic structure could flatten the curved lipid bilayer membranes [27,28]. As a consequence, the aqueous nanochannels diameter increases when the bilayer curvature decreases.

More recently, it has been emphasized that inhomogeneous distribution or phase separation in fluid multicomponent lipid membranes could cause structural transformations from lamellar to intermediate nonlamellar phases or to bicontinuous bilayer phases of nonuniform interfacial curvature [30]. An example of a lipid mesophase with nonperiodic organization is the sponge (L_3) phase [31,32]. The sponge (L_3) mesophase appears to be an isotropic fluid devoid of

a long-range order. Its inner organization may be represented as a completely 'melted' cubic phase involving less curved lipid bilayers. The continuous network of two aqueous subvolumes is separated in space by a random bilayer lipid membrane. Particular to the L_3 phase is the universal scaling law [31]. The topology of the sponge should remain unchanged when the system is diluted with water. As a result, the characteristic sponge cell distance must increase linearly as a function of the reciprocal lipid bilayer volume fraction.

Sponge phases in general constitute narrow regions in the lipid phase diagrams. It has been reported [33-36] that sponge phases of glycerol monooleate could be generated upon solvent (e.g. polyethylene glycol, propylene glycol, ethanol, 2-methyl-2,4-pentanediol, dimethyl sulfoxide, pentaerythritol propoxylate, N-methylpyrrolidinone, butanediol, butanol or jeffamine) addition to the binary GMO/water system.

A question which remains open regards the hydration level of the sponge L_3 phase, which controls its capacity for encapsulation of biomolecules. Some studies [34,36] have suggested that the L_3 phase would display at least three times larger aqueous channel compartments as compared to those in the corresponding bicontinuous cubic phase of the same lipid. There is a lack of sufficient structural data in the ultra small-angle X-ray scattering region in order to verify this conclusion with diverse lipid/water systems. Such results are essentially needed in order to establish the conditions of stability of the sponge lipid phases permitting the formulation of spongosome dispersions [29] and their comparison with the nanoparticles resulting from the fragmentation of other functionalized lipid mesophases (spherical and non-spherical vesicles, cubosomes, hexosomes, spherical and non-spherical reversed micelles, etc).

The present work focuses on the investigation of the hydration of the LC phase formed in excess aqueous medium by pharmaceutical-grade glycerol monooleate that is suitable for drug delivery applications. This mesophase-forming material is in fact a mixture of three components: the main component is glycerol monooleate or monoolein (MO) and it is accompanied by traces of oleic acid (OA) and diglycerol monooleate (DGMO). Space filling models of the ingredients are presented in Scheme 1. The sizes of the aqueous nanocompartments, present in the lipid supramolecular structure, are expected to be modified by incorporation of the nonionic guest molecule octyl glucoside (OG). This kind of a nonionic agent, acting as an interfacial curvature modulator, has shown a profound effect on the aqueous nanochannels hydration in the inverted cubic phase of pure glycerol monooleate [8,19,28].

Here the structural features of the amphiphiles, self-assembled in buffer, are investigated by means of SAXS and SANS in order to find out whether the swelling of the LC phase in excess water would be favored by the addition of

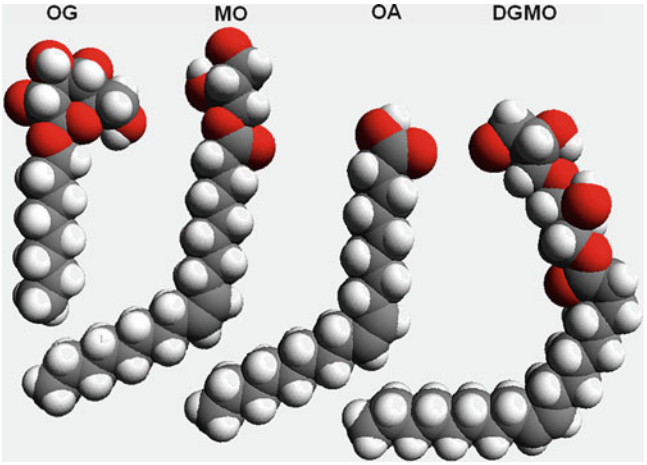

Scheme 1 Space filling molecular models of octyl glucoside (OG), glycerol monooleate (or monoolein MO), oleic acid (OA), and diglycerol monooleate (DGMO)

OG. The formation of a continuous lipid mesophase was established under full hydration of the GMO product. Its structure is disordered, unlike the periodic phases formed by the hydrated powder of pure glycerol monooleate [12].

Experimental

Pharmaceutical-grade monoglyceride [C18:1, *cis-9* glycerol monooleate] (GMO) for drug delivery applications was obtained from the *NOF Corporation* (Japanese Pharmaceutical Excipient, >99% oleic acid, ultra-purity *NOFABLE GO-991*). The NOF's glycerol monooleate (denoted here as GMO) is an isotropic liquid product at room temperature. It was analyzed by electrospray mass spectrometry (ESI-MS, Esquire-LC, Bruker) in positive and negative ion modes. The obtained ESI-MS and NMR spectra revealed that the product GMO appears to be a mixture of glycerol monooleate or monoolein (MO) (M_W 356.54), oleic acid (OA) (M_W 282.46) and diglycerol monooleate (DGMO) (M_W 430.62). The three compounds have the same hydrophobic chain (C18:1c9) but different polar headgroups. However, the supplier did not provide the exact proportions of the satellite compounds (OA and DGMO) in the pharmaceutical grade glycerol monooleate preparation (*NOFABLE GO-991*). The detergent n-octyl beta-*D*-glucopyranoside (OG) (M_W 292.4, *CMC* 20 mM, purity > 99.5%, Sigma-Aldrich Co.) was used as received. Solutions of OG for SANS measurements were prepared by dissolving the detergent either in pure D_2O (Merck Co., Darmstadt, Germany) or in phosphate buffer (NaH_2PO_4/Na_2HPO_4 (1:1 mol/mol) pH 7, p.a. grade, Merck) prepared with D_2O. The sample preparation for SAXS measurements included hydration of fluid glycerol monooleate

material in a phosphate buffer prepared with MilliQ water. Full hydration of the lipid GMO was achieved under excess aqueous phase conditions (30 wt% lipid and 70 wt% buffer solution). The self-assembled GMO/OG mixture was prepared by dispersing GMO in excess aqueous phase containing OG in the phosphate buffer. The mixing of the amphiphiles yielded a lipid-to-detergent molar ratio of 90/10 in the sample. The hydration and dispersion of the lipid in the OG solution was performed at ambient temperature (21 °C). Eight cycles of vortexing (for 1 min) and incubation (for 5 min) at room temperature were applied.

The SAXS experiments were performed at the beamline A2 of the DORIS III storage ring at the Synchrotron radiation facility HASYLAB/DESY (Hamburg, Germany). The samples were filled in glass mark tubes of 1 mm diameter. The X-ray beam wavelength, λ, was 1.5 Å. The scattered intensity was recorded using a one-dimensional (1D) detector, which area was divided into 1024 pixels. The 1D SAXS data were calibrated by a rat-tail tendon (RTT) standard.

Small-angle neutron scattering (SANS) experiments were performed with the SANS1 instrument at the FRG1 research reactor (GKSS Research Center, Geesthacht, Germany) [17]. The neutron beam wavelength was 8.1 Å with a wavelength resolution of 10% (*fwhm*). A range of scattering vectors $0.005 < q < 0.24$ Å^{-1} was obtained using four sample-to-detector distances (0.7-9.7 m). The samples were filled in quartz cells (Hellma, Germany) before measurement. The raw SANS spectra were corrected for backgrounds from solvent, sample cell and other sources by conventional procedures. The two-dimensional scattering spectra were azimuthally averaged, converted to an absolute scale, and corrected for detector efficiency via dividing by the incoherent scattering spectrum of pure D_2O water.

The GNOM program [38] was used for treatment of the experimental small-angle scattering (SANS and SAXS) data. It reads one-dimensional scattering curves and calculates the distance distribution function *p(r)*. The least-squires fitting was done by an implementation of Levenberg–Marquardt algorithm [19].

Results and Discussions

Scattering from a Pure OG/Buffer System

SANS measurements were performed at room temperature (25 °C) in order to determine the sizes of the micellar self-assembled aggregates of octyl glucoside. The SANS curves of the OG micellar solutions, obtained at OG concentrations 0.038 M and 0.061 M (which are above the *CMC* value of OG), are shown in Figure 1. To fit the small angles scattering intensity, I, we used the Dozier star polymer model [39]:

$$I = I_0 \exp\left(-\frac{q^2 R_g^2}{3}\right) + \frac{4\pi\alpha}{q\xi}\Gamma(\mu)\frac{\sin(\mu \arctan(q\xi))}{(1+q^2\xi^2)^{\mu/2}}, \quad (1)$$

where I_0 is the scattering intensity at wavevector $q = 0$, α is a normalization factor, $\xi = 2R_g/f$ is the correlation length inside the micelle, f is related to the number of molecules in the micelle, $\mu = 1/\nu - 1$, and $\nu = 0.5$ is the Flory exponent. The Euler gamma function is denoted by $\Gamma(\mu)$.

The micellar OG systems were considered to be monodispersed ones. The employed simplified model (1) allowed calculating the gyration radii of OG micelles, respectively, of 1.37 nm (at surfactant concentration 0.038M) and of 1.70 nm (at 0.061M OG concentration). The results are in close agreement with previously reported values [40]. It is anticipated that when the concentration of the amphiphile OG increases, the shape of the OG micelles will become a more elongated one and may evolve to a cylindrical shape. Because of the relatively low surfactant concentrations,

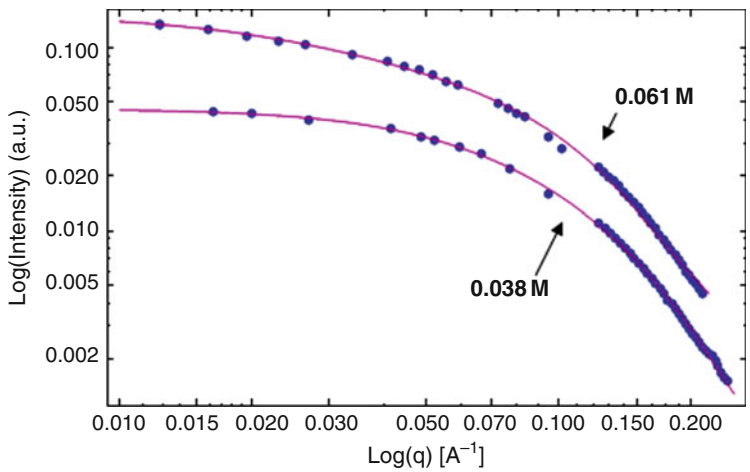

Figure 1 Experimental SANS data (dots) and model fits (solid lines) for octyl glucoside (OG) micellar solutions with concentrations 0.038 M and 0.061 M

studied in this work, the obtained OG micelles appear to be spherical rather than ellipsoidal.

When OG is added to the bicontinuous bilayer GMO supramolecular assembly, this amphiphile is expected to incorporate into the lipid membrane [19]. According to previous reports [8], the bilayer thickness of the mixed GMO/OG membrane is in the range 3.2-3.5 nm. Therefore, a half of this bilayer thickness will sterically fit to the radius of gyration of the OG micelle (1.6-1.7 nm). From a steric point of view, the ability of the glycerol monooleate bilayer to accommodate OG molecules is evidenced by the fact that it exceeds the length of the OG amphiphile (Scheme 1).

Scattering from a GMO/Buffer System

While the powder lipid glycerol monooleate forms, in a pure state, a stable bicontinuous inverted cubic phase at full hydration and in a wide temperature range [13], the investigated pharmaceutical-grade GMO material is found to self-assemble into another type of a bicontinuous lipid structure that also exist in excess water medium. Typical SANS and SAXS curves of the pharmaceutical-grade GMO (*NOF Corp.*) are presented in Figure 2 and 3a (dots) respectivelly. Multiple diffraction peaks, characteristic of cubic lattice domains, were not detected under the investigated temperature and hydration conditions. The observed single peak was attributed to a sponge (L_3) phase after model fitting of the scattering intensities. The bicontinuous L_3 phase of GMO is stable in excess buffer. On visible inspection it exhibits a phase segregation boundary between the hydrated lipid domain and the excess water environment.

The SANS and SAXS pattern in Figure 2 and 3a were fitted with a bilayer sponge cell-cell correlation function (solid line). The scattering, $I(q)$, was calculated according to the equation:

$$I(q) = \frac{c}{\xi^{-2} + (q - q_c)^2}, \tag{2}$$

where the SAS peak position is denoted by q_c. The correlation length is ξ, while the constant c describes the intensity normalization. The peak maximum was found to be centered at $q_c = 0.176 \pm 0.001$ Å^{-1} for SAXS and $q_c = 0.177 \pm 0.003$ Å^{-1} for SANS. Due to the low wavelength resolution of cold neutrons, the determination of SANS peak position was less precise as compared to SAXS peak position. The corresponding sponge cell-cell distance was determined as $L = 1/s = 0.2\ \pi/q_c = 3.55$ nm. This value is just slightly higher than the glycerol monooleate bilayer thickness, which is equal to 3.2 nm in the diamond *Pn3m* inverted cubic phase. The relatively short distance between the bilayers indicates a low hydration level of the sponge phase, formed by the pharmaceutical-grade GMO under excess water conditions, as compared to the *Pn3m* cubic phase of the purified powdered lipid. It is essential to note that if the background from the X-ray capillaries was not correctly subtracted from the SAXS curve (Fig. 3a), the scattering fit could be calculated by a microemulsion model instead by the sponge model. This could yield a misleading interpretation of the obtained structural data.

Scattering from a GMO/OG/Buffer System

Upon addition of 10 mol% OG to the GMO/water assembly, the SAXS peak position jumps to a higher value $q_c = 0.155$ Å^{-1} (Figure 3b). Such a shift of the peak position maximum corresponds to an increased average size of the sponge cells, $L = 4.03$ nm, and a larger mean diameter of the continuous water channels. The sponge cell dimension (equal to 4.03 nm), corresponding to the sum of the bilayer thickness

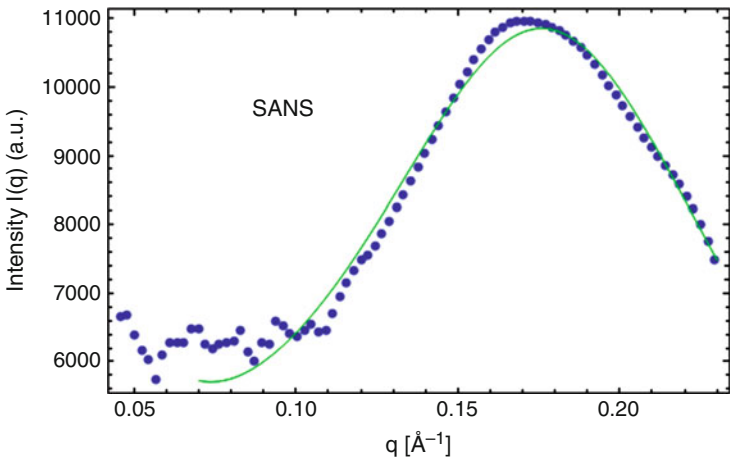

Figure 2 SANS data (dots) recorded at 25 °C with pharmaceutical-grade glycerol monooleate (GMO) hydrated in excess phosphate buffer (30 wt% lipid, 70 wt% aqueous phase). The solid line represents the model fitting to Eq.(2)

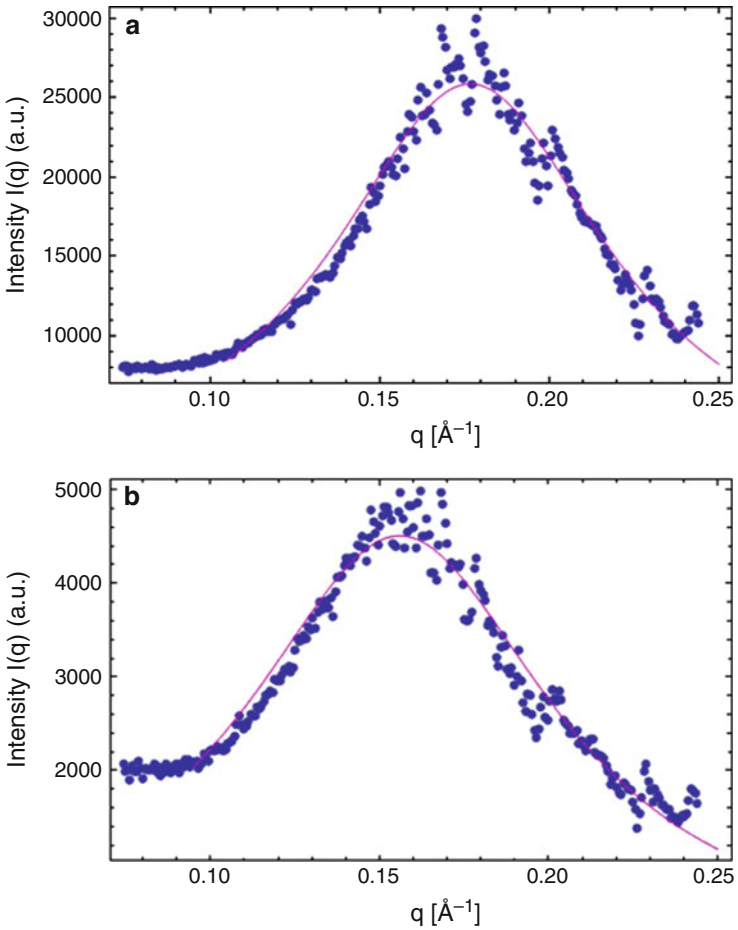

Figure 3 SAXS data (dots) recorded at 21 °C with (**a**) pharmaceutical-grade glycerol monooleate (GMO) hydrated in excess phosphate buffer (30 wt% lipid, 70 wt% aqueous phase); and (**b**) GMO/OG (90/10 mol/mol) self-assembled mixture. The solid line represents the model fitting to Eq.(2)

and the water channel, indicates that the water content of the L_3 phase is increased in the presence of OG. The enhanced sponge-structure hydration is driven by the incorporation of the OG molecules in the GMO bilayers and results from the OG-induced change in the lipid monolayer curvature. A model of the 3D organization of the sponge L_3 phase is presented in Figure 4.

Scattering from an excess of OG micellar phase was not detected in the SAXS patterns of the GMO/OG/buffer system (Figure 3b). This confirms that, at this composition of the sample, the amphiphile OG is incorporated from the micellar solution phase into the lipid membrane. The resulting increase in the mean water channel size appears to be smaller in the case of the pharmaceutical-grade-GMO/OG mixture as compared to the pure-GMO/OG system studied previously [8,19]. The shift in q_c from 0.176 Å^{-1} to 0.155 Å^{-1} (Figure 3) implies a bilayer sponge swelling of about 14% (i.e. from $L = 3.55$ nm to $L = 4.03$ nm). At variance, the OG-induced enlargement of the aqueous nanochannels in the double diamond (*Pn3m*) inverted cubic phase of purified glycerol monooleate has been nearly 50% [8].

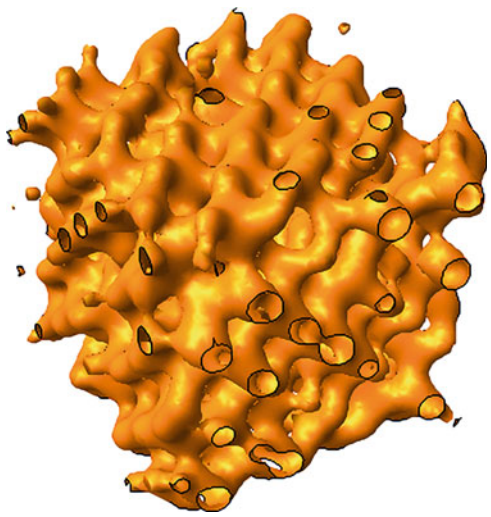

Figure 4 Sponge phase organization with a nonperiodic lipid bilayer

Conclusion

The obtained structural results revealed that the pharmaceutical-grade GMO self-assembled architecture is of a sponge type and devoid of long-range order in excess aqueous phase at ambient temperature. Further investigations of the GMO product should involve SAXS experiments as a function of the water content (e.g. aqueous phase content 60 wt%, 50 wt %, 40 wt%, 30 wt%, 20 wt%, . . .) and a comparison with the fluid organization of the anhydrous lipid material GMO. Such a study may establish the maximum swelling capacity of the sponge GMO lipid phase as well as to verify whether its swelling obeys a scaling law upon the increase of the water content.

Acknowledgment This paper is dedicated to the memory of Dr. Michel OLLIVON, a Research Director at CNRS. The research project has been supported by the European Commission under the 6th Framework Programme through the Key Action: Strengthening the European Research Area, Research Infrastructures. Contract n°: RII3-CT-2003-505925 (EU user's access programme NMI3).

References

1. Lynch ML, Spicer P.T. (Eds.) (2005) Bicontinuous Liquid Crystals: Surfactant Science Series, Vol.127, Taylor & Francis, Boca Raton.
2. Seddon JM, Templer RH (1995) in Handbook of Biological Physics (R. Lipowsky and E. Sackmann Eds.), Vol. 1, pp. 97–153, Elsevier Science, London, UK.
3. Dong Y-D, Dong AW, Larson I, Rappolt M, Amenitsch H, Hanley T, Boyd BJ (2008) Langmuir 24: 6998-7003.
4. Yaghmur A, de Campo L, Sagalowicz L, Leser ME, Glatter O (2006) Langmuir 22: 9919-9927.
5. Yaghmur A, de Campo L, Sagalowicz L, Leser ME, Glatter O (2005) Langmuir 21: 569-577.
6. Bryskhe K, Schillen K, Olsson U, Yaghmur A, Glatter O (2005) Langmuir 21: 8597-8600.
7. Angelova A, Ollivon M, Campitelli A, Bourgaux C (2003) Langmuir 19: 6928-6935.
8. Angelov B, Angelova A, Ollivon M, Bourgaux C, Campitelli A (2003) J. Am. Chem. Soc. 125: 7188-7189.
9. Angelova A, Angelov B, Papahadjopoulos-Sternberg B, Ollivon M, Bourgaux C (2005) J. Drug Delivery Sci. Technol. 15 : 108-112.
10. Borné J, Nylander T, Khan A (2002) J. Phys. Chem. B 106: 10492-10500.
11. Lindblom, G., Larsson, K., Johansson, L., Fontell, K., and Forsén, S. (1979) J. Am. Chem. Soc. 101: 5465-5470.
12. Hyde ST, Anderson S, Ericsson B, Larsson K (1984) Z. Kristallogr. 168: 213-219.
13. Czeslik C, Winter R, Rapp G, Bartels K (1995), Biophys. J. 68: 1423-1429.
14. Qui H, Caffrey M (2000) Biomaterials 21: 223-234.
15. Clogston J, Rathman J, Tomasko D, Walker H, Caffrey M (2000) Chem Phys Lipids, 107:191-220.
16. Angelova A, Angelov B, Papahadjopoulos-Sternberg B, Ollivon M, Bourgaux C (2005) Langmuir 21: 4138-4143.
17. Angelov B, Angelova A, Papahadjopoulos-Sternberg B, Lesieur S, Sadoc J-F, Ollivon M, Couvreur P (2006) J. Am. Chem. Soc. 128: 5813-5817.
18. Angelova A, Angelov B, Papahadjopoulos-Sternberg B, Bourgaux C, Couvreur P (2005) J. Phys. Chem. B 109: 3089-3093.
19. Angelov B, Angelova A, Garamus VM, Le Bas G, Lesieur S, Ollivon M, Funari S, Willumeit R, Couvreur (2007) J. Am. Chem. Soc. 129: 13474-13479.
20. Angelova A, Angelov B, Lesieur S, Mutafchieva R, Ollivon M, Bourgaux C, Willumeit R, Couvreur P (2008) J Drug Delivery Sci Technol 18: 41-45.
21. Barauskas J, Johnsson M, Joabsson F, Tiberg F (2005) Langmuir 21: 2569-2577.
22. Leser ME, Sagalowicz L, Michel M, Watzke H (2006) Adv. Colloid Interface Sci. 123-126: 125-136.
23. Cherezov V, Clogston J, Papiz MZ, Caffrey M (2006), J. Mol. Biol. 357: 1605-1618.
24. Rosenblatt KM, Douroumis D, Bunjes H (2007) J Pharm Sci. 96: 1564-1675.
25. Lee KWY, Nguyen T, Hanley T, Boyd BJ (2009) Int J Pharm. 365: 190–199.
26. Chang C, Bodmeier R (1997) J Pharm Sci. 86:747-752.
27. Engblom J, Miezis Y, Nylander T, Razumas V, Larsson K (2000) Prog. Coll. Pol. Sci. 116: 9–15.
28. Persson, G., Edlund, H., and Lindblom, G. (2003) Eur. J. Biochem. 270: 56-65.
29. Barauskas J, Misiunas A, Gunnarsson T, Tiberg F, Johnsson M (2006) Langmuir 22: 6328-6334.
30. Angelov B, Angelova A, Vainio U, Garamus VM, Lesieur S, Willumeit R, Couvreur P (2009) Langmuir 25: 3734-3742.
31. Porte G (1992) J. Phys. Condens. Matter 4: 8649-8670.
32. Lei N, Safinya CR, Roux D, Liang KS (1997) Phys. Rev. E 56: 608–613.
33. Engström S, Alfons K, Rasmusson M, Ljusberg-Wahren H (1998) Prog. Coll. Pol. Sci. 108: 93–98.
34. Ridell A, Ekelund K, Evertsson H, Engström S (2003) Colloids Surfaces A 228: 17–23.
35. Imberg A, Evertsson H, Stilbs P, Kriechbaum M, Engström S (2003) J. Phys. Chem. B 107: 2311–2318.
36. Evertsson H, Stilbs P, Lindblom G, Engström S (2002) Colloids Surfaces B 26: 21–29.
37. Gomati R, Bouguerra N, Gharbi A (2001) Physica B 299: 101–107.
38. Svergun DI (1992) J. Appl. Cryst. 25: 495-503.
39. Dozier DW, Huang JS, Fetters LJ (1991) Macromolecules 24: 2810-2814.
40. Giordano R, Maisano G, Teixeira J (1997) J. Appl Cryst. 30: 761-764.

Progr Colloid Polym Sci (2011) 138:7–16
DOI: 10.1007/978-3-642-19038-4_2

pH Induced Desaggregation Of Highly Hydrophilic Amphiphilic Diblock Copolymers

Elise Lejeune, Christophe Chassenieux, and Olivier Colombani

Abstract P(nBA$_{20\%}$-*stat*-AA$_{80\%}$)$_{100}$-*b*-PAA$_{95}$, an amphiphilic diblock copolymer consisting of a pure hydrophilic poly(acrylic acid) (PAA) block and a weakly hydrophobic statistical copolymer of *n*-butyl acrylate (*n*BA) and acrylic acid (AA) was prepared by ATRP. Kinetic studies revealed that the polymerization was well controlled, leading to a perfectly defined diblock copolymer both in terms of chemical composition and block lengths. This polymer was characterized in aqueous solution by means of light and neutron scattering experiments. In spite of its weak hydrophobic nature, P(nBA$_{20\%}$-*stat*-AA$_{80\%}$)$_{100}$-*b*-PAA$_{95}$ self-assembles in aqueous solution provided the ionization degree of the AA units is kept as low as α = 0-10%. Moreover, the relatively large aggregates (N_{agg} = 100, R_h = 18nm) formed at α = 0% molecularly dissolve at $\alpha > 20\%$. This pH sensitivity is in strong contrast with the behavior of the more hydrophobic PnBA$_{90}$-*b*-PAA$_{100}$ which forms frozen aggregates insensitive to external stimuli in aqueous solution.

Keywords Amphiphilic block copolymer • pH-sensitive • ATRP • poly(n-butyl acrylate) • poly(acrylic acid)

Introduction

Amphiphilic block copolymers consist of at least two antagonistic blocks connected together by a covalent bond. In a selective solvent for one of the blocks, they self-assemble in order to expose the solvophilic blocks to the solvent and protect the solvophobic ones[1-3], leading to various morphologies. From this point of view, they resemble somehow molecular surfactants, their low molar mass counterparts. However, whereas the self-assembly of the latter is thermodynamically controlled, the organization of amphiphilic block copolymers in selective solvents is the result of both thermodynamic and kinetic contributions[4-9]. This is especially true in aqueous medium where most amphiphilic block copolymers form out-of-equilibrium structures, so-called frozen aggregates, unable to exchange unimers[3-5, 10]. It follows that the structure of these frozen aggregates strongly depends on the way they were prepared, and requires most of the time complex dispersion processes involving the use of a non selective co-solvent which must be eliminated latter on[2, 11]. Moreover, frozen aggregates of amphiphilic block copolymers are hardly able to reorganize upon changes of external conditions even if the hydrophilic block is sensitive to stimuli such as the pH or the ionic strength[4, 9, 12].

It must be realized that a low glass transition temperature (T_g) of the hydrophobic block is not sufficient to allow aggregates of amphiphilic block copolymers to be dynamic, that is able to exchange unimers between each other[4, 5, 8, 9, 12, 13]. This is worth mentioning as polymers bearing a soft hydrophobic blocks are often claimed to be dynamic without proper experimental evidences. Actually, the key parameters to take into account to obtain dynamic aggregates are the length of the hydrophobic block[4, 7, 14, 15] as well as the interfacial tension between the hydrophobic block and the solvent[4, 12, 15-17]: both have to be low enough to allow unimer exchange. Indeed, exchange of unimers requires the hydrophobic block to go through the hydrophilic corona of the aggregates as well as through the aqueous medium, a task made easier if the hydrophobic block is not too much incompatible with the solvent. Following these guidelines, we decided to reduce the incompatibility between the hydrophobic block and the solvent by distributing hydrophilic units in the hydrophobic block of a poly(*n*-butyl acrylate)-*block*-poly(acrylic acid) block copolymer (P*n*BA-*b*-PAA). It has been shown that pure P*n*BA-*b*-PAA[9, 18] forms frozen spherical aggregates unable to reorganize upon pH changes in spite of the low T_g

C. Chassenieux (✉) and O. Colombani (✉)
LUNAM Université, Laboratoire Polymères, Colloïdes et Interfaces, UMR CNRS 6120 - Université du Maine, av. O. Messiaen, 72000 Le Mans, France
e-mail: christophe.chassenieux@univ-lemans.fr; olivier.colombani@univ-lemans.fr

(T_g = −55°C) of the P*n*BA hydrophobic block and the polyacidic character of PAA [5, 9, 12, 18]. On the contrary, P(nBA$_{50\%}$-*stat*-AA$_{50\%}$)$_{99}$-*b*-PAA$_{98}$ (the subscripts correspond to the degree of polymerization of each block), whose hydrophobic character has been moderated by incorporating 50%mol of acrylic acid units in the hydrophobic block, forms pH sensitive spherical aggregates[19]: their aggregation number depends strongly on the ionization degree α of the acrylic acid units. Importantly, the change of the aggregation number of the aggregates with α has been shown to be reversible, at least for α values equal to 10, 50 or 90%, which hints at a dynamic behavior.

These first results show that incorporating hydrophilic units in the hydrophobic block of amphiphilic block copolymers is a promising way to tune their dynamics of self-assembly. This strategy is moreover more versatile than other ones based on the use of additives such as surfactants [20, 21] or non selective cosolvents[4, 17, 20, 22] because it relies on the chemistry of the polymer itself and may be applied to any block copolymer whose hydrophilic and hydrophobic units can be copolymerized together. However, while incorporating more and more hydrophilic units in the hydrophobic block decreases its incompatibility with the solvent and apparently favors further unimer exchange between aggregates, too many hydrophilic units may lead to non associating polymers. This was indeed nicely shown by Bendejacq et al. who studied, both in the melt state[23] and in aqueous solution[24], non symmetrical P(S-*stat*-AA)$_{20}$-*b*-PAA$_{200}$ block copolymers consisting of a rather long PAA hydrophilic block (DP = 200) connected to a short statistical "hydrophobic" copolymer of styrene (S) and acrylic acid (AA) (DP = 20). In the melt state, the P(S-*stat*-AA) block forms spherical nano-objects within a matrix constituted by the PAA blocks as long as the AA ratio in the "hydrophobic" block is not higher than 24%mol. When dispersed in aqueous medium in the absence of added salt and with an overall ionization degree of the AA units equal to 50% (including both the AA units in the PAA hydrophilic block and those in the P(S-*stat*-AA) moderately hydrophobic block), these highly hydrophobic polymers form frozen spherical aggregates whose characteristics are reminiscent of the way the polymer was structured in the melt. If the AA ratio in the hydrophobic block is increased to 52%mol, the polymer no more phase segregates in the melt state because the incompatibility of the two blocks becomes too weak. In aqueous solution (α = 50%, no added salt), self-assembly however still occurs and spherical objects whose structure depends on the polymer concentration are formed. Finally, with 74%mol of AA units in the hydrophobic block, the polymer neither self-assembles in the melt state, nor in solution (at α = 50% without added salt).

The results obtained by Bendejacq et al. on P(S-*stat*-AA)-*b*-PAA tend to confirm that for very high AA contents, the block copolymers lack the required hydrophobic character to self-assemble in aqueous medium. However, the authors focused on ionization degrees of the AA units equal to 50% for these polymers. They did not study the evolution of the aggregation number with the ionization degree of the AA units for polymers containing as much as 74%mol AA, although they did for other systems[25]. Moreover, P(S$_{26\%}$-*stat*-AA$_{74\%}$)$_{20}$-*b*-PAA$_{200}$ consists of an extremely short "hydrophobic" block which corresponds to only 5 styrene units per chain. In order to investigate the influence of the AA ratio on the self-assembly of P*n*BA/PAA-based polymers in aqueous medium and somehow find a limit to the AA content which should be incorporated into the "hydrophobic" block, a polymer containing as much as 80%mol of AA in the hydrophobic block but a rather long "hydrophobic" block was targeted: P(nBA$_{20\%}$-*stat*-AA$_{80\%}$)$_{100}$-*b*-PAA$_{95}$. Its synthesis was achieved by ATRP resulting in a very good control over the length and composition of each block. Then, its self-assembling properties in aqueous solution were studied by means of static and dynamic light scattering (SLS and DLS) and small angle neutron scattering (SANS), focusing on the influence of the ionization degree of the AA units.

Material and Methods

Synthesis

Reagents

n-Butyl acrylate (*n*BA, Acros, 99%) and *tert*-butyl acrylate (*t*BA, Acros, 98%) were stirred overnight on hydroquinone (Prolabo) and calcium hydride (Acros, 93%) and then distilled under vacuum. Copper Bromide (CuBr, Acros, 98%) was stirred overnight in glacial acetic acid (CH_3COOH, Aldrich, 99.7%), filtered, and rinsed successively by acetic acid, ethanol, and ether to remove traces of $CuBr_2$. N,N,N',N',N"-Pentamethyldiethylenetriamine (PMDETA, Acros, 99%), methyl-2-bromopropionate (MBP, Aldrich, 99%), acetone (Aldrich, 99.5%), copper II bromide ($CuBr_2$, Acros, 99%), *n*-decane (Acros, 99%), SiO_2 (63–200 µm, Fluka, chromatography grade), methanol (Aldrich, 99%), THF (Aldrich, 99%), trifluoroacetic acid (CF_3COOH, Acros, 99%), and dichloromethane (Aldrich, 99.5%) were used as received.

Synthesis of P(nBA$_{20\%}$-stat-tBA$_{80\%}$)$_{100}$-Br by ATRP

Cu(I)Br (0.084g, 5.86×10^{-4} mol) was introduced in a 100 mL round bottom flask and degassed with argon for 30min. PMDETA (0.140g, 8.08×10^{-4} mol), MBP (0.264g,

$1.58x10^{-3}$ mol), *n*-decane (4.010g), acetone (13.336g), *n*BA (8.377g, 0.065mol) and *t*BA (32.193g, 0.251mol) were introduced in a second round bottom flask and degassed by three freeze/pump/thaw/flood with argon cycles. A few drops of this solution were taken as sample t_0. The rest of the solution was then transferred with a canula under argon into the first flask containing degassed Cu(I)Br and the reaction mixture was dipped in an oil bath at 60°C. Throughout the reaction, samples were withdrawn using an argon-degassed syringe in order to follow the kinetics of the polymerization. Conversion was determined by gas chromatography using decane as internal standard following an already published procedure[19, 26]. The samples were further characterized by SEC, leading to polystyrene-equivalent M_n and PDI, after removal of the copper complex by flash chromatography on a small SiO_2 column. The reaction was finally terminated at 50% conversion by cooling the flask to 0°C (ice-water) and opening it to air. Purification was performed as reported elsewhere[19], yielding a viscous yellowish polymer. (10.5g, 67% yield).

M_n (theoretical, determined from the conversion) = 13 000 g/mol

M_n(PS-equivalent, SEC-THF) = 13 300 g/mol; PDI (PS-equivalent, SEC-THF) = 1.1.

The experimental *n*BA molar content was determined by ^{1}H NMR (200 MHz, $CDCl_3$), using the integrations of the signals at δ = 4.15 ppm (2H P*n*BA, -O-CH_2-) and δ = 0.5-2.7 ppm (10H P*n*BA + 12H P*t*BA). It was compared to the theoretical content determined from the conversion of each monomer: x_{nBA} (theoretical) = 20%, x_{nBA} (^{1}H NMR) = 20%.

Synthesis of P(nBA$_{20\%}$-stat-tBA$_{80\%}$)$_{100}$-b-PtBA$_{95}$ by ATRP

The diblock was prepared following the same procedure as for the first block with the following conditions: [*t*BA]:[macroinitiator]:[CuBr]:[PMDETA] = 190:1:0.48:0.50, were P(*n*BA$_{20\%}$-*stat*-*t*BA$_{80\%}$)$_{100}$-Br was used as macroinitiator. Moreover, 5%mol of $CuBr_2$ was added relative to CuBr in order to allow a good control from the beginning of the reaction. The reaction was stopped at 50% conversion, yielding 5.9g (63% yield) of a yellowish polymer.

M_n(theoretical) = 25 000 g/mol; M_n (PS-eq., SEC-THF) = 25 700 g/mol, PDI = 1.1.

x_{nBA} (theoretical) = 10%, x_{nBA} (^{1}H NMR) = 12%.

Acidolysis of the Precursor to P(nBA$_{20\%}$-stat-AA$_{80\%}$)$_{100}$-b-PAA$_{95}$

Acidolysis of P(*n*BA$_{20\%}$-*stat*-*t*BA$_{80\%}$)$_{100}$-*b*-P*t*BA$_{95}$ into P(*n*BA$_{20\%}$-*stat*-AA$_{80\%}$)$_{100}$-*b*-PAA$_{95}$ was performed as already published using trifluoroacetic acid[19]. The polymer was ultimately recovered after freeze drying from an aqueous solution. ^{13}C NMR revealed that the reaction was quantitative: no signal was observed at δ = 80.7 ppm, corresponding to the $C(CH_3)_3$ of *t*BA units[18]. Moreover, the reaction was already proven to be selective, i.e. does not affect the *n*BA units[18].

Characterization in Solution

Reagents

The aqueous solutions were prepared using Millipore water (deionized water, resistance > 18MΩ), sodium chloride (extra pure, LaboneLine), hydrochloric acid (HCl 1M, Lab on Line) and sodium hydroxide (NaOH 1M). NaOH 1M was prepared using Titrisol concentrated solutions and back titrated with HCl 1M before use.

Static and Dynamic Light Scattering (SLS and DLS)

Refractive Index Increment dn/dc

The specific refractive index increment (dn/dc) of the polymer, required to extract the molecular weight of the scatterers from the static light scattering data, was determined at 20°C with a Spectra System P100 (Wyatt) differential refractometer and remains almost constant while varying the ionization degree of the AA units: dn/dc = 0.15 +/− 0.01 mL/g.

Preparation and Measurement of the Solutions

P(*n*BA$_{20\%}$-*stat*-AA$_{80\%}$)$_{100}$-*b*-PAA$_{95}$, obtained at an ionization degree α close to 0% after freeze-drying in water, spontaneously dissolves in pure water. Aqueous copolymer solutions were prepared by, first, dissolving the polymer in pure water at 5g/L with an appropriate quantity of NaOH to control α. The values of α indicated in the text correspond to overall ionization degrees of the AA units. Potentiometric titration experiments indeed indicate that both the AA units within the PAA_{95} hydrophilic block and those within the P(*n*BA$_{20\%}$-*stat*-AA$_{80\%}$)$_{100}$ block are accessible to NaOH[27]. Moreover, the expected content of AA units, based on the chemical structure of P(*n*BA$_{20\%}$-*stat*-AA$_{80\%}$)$_{100}$-*b*-PAA$_{95}$ agrees within experimental error with the value determined by titration[27]. The amount of NaOH required to reach the targeted α value was thus calculated based on the chemical structure of the polymer. It must be highlighted that the acidity of the AA units in both blocks may be different,

resulting in a sequential ionization of the AA units in the PAA block first, followed by the ionization of the AA units in the more hydrophobic block as was shown by Bendejacq et al. for P(S_{53}-*stat*-AA_{39})-*b*-PAA_{133}[25].

After at least one night, the polymer was correctly dispersed no matter α and the NaCl concentration was adjusted to 0.1 M using NaCl 5M. These solutions were analyzed by SLS and DLS without filtration. Measurements were performed at angles of observation ranging from 30° up to 150° with an ALV CGS3 set-up operating at λ_0 = 632nm and at 20°C. Calibration was achieved with filtered toluene.

Treatment of the SLS and DLS Data

The intensity auto-correlation functions $g_2(t)$ obtained from DLS were analysed in terms of a continuous distribution of relaxation times (A(τ)):

$$g_1(t) = \int_0^\infty \tau A(\tau) \exp(-t/\tau) d \log \tau \qquad (1)$$

Where $g_1(t)$ is the normalised electric field auto-correlation function related to $g_2(t)$ via the so-called Siegert relation [28]. The REPES routine was used to obtain A(τ), without assuming a specific shape [29]. In most of our experiments, two modes of relaxation are derived from the distributions of the relaxation times. For both of them, the average relaxation times are q^2-dependent and are used to calculate apparent diffusion coefficients at a given concentration : $D_{app} = (q^2.\tau)^{-1}$, where q is the scattering vector defined as $q=(4\pi n/\lambda)\sin(\theta/2)$ with n the refractive index of the solvent and θ the scattering angle. The apparent hydrodynamic radius $R_{h,app}$ can then be calculated using the Stokes-Einstein equation (equation 2).

$$R_{h,app} = \frac{kT}{6.\pi.\eta.D_{app}} \qquad (2)$$

with η the viscosity of the solvent, k Boltzmann's constant and T the absolute temperature.

Both modes of relaxation contribute to the scattered intensity measured by SLS, hence to the total Rayleigh ratio R_θ. The Rayleigh ratio $R_{\theta,fast}$ for the faster mode of relaxation has been derived according to equation 3 (see also refs [30] and [31]).

$$R_{\theta,fast}(q) = A_{fast} R_\theta = A_{fast} \frac{(I_\theta - I_{\theta-solvent})}{I_{\theta-toluene}} R_{\theta-toluene} \qquad (3)$$

where I_θ, $I_{\theta\text{-solvent}}$ and $I_{\theta\text{-toluene}}$ correspond respectively to the scattered intensity measured at a scattering angle θ by, the solution, the solvent and toluene. $R_{\theta-toluene}$ is the Rayleigh ratio of toluene. A_{fast} is the relative amplitude of the fast mode extracted from the DLS data as explained above.

The apparent molecular weight $M_{w\text{-app}}$ (that is the value extrapolated to zero angle but measured at a finite concentration of 5g/L) for the fast mode of relaxation was then determined classically [32] assuming that the concentration of polymer involved in the fast mode of relaxation is equal to the total polymer concentration, that is assuming that the weight concentration of polymer involved in the slow mode can be neglected (see text).

Treatment Used for Figure 6

$\tau A(\tau)$ is the relative scattered intensity of scatterers with relaxation time between log(τ) and log(τ)+d(log(τ)), which relates to their concentration c(M) and their molecular weight M according to: $\tau A(\tau) \propto M^2 c(M)$. The distribution of relaxation times can then be transformed in weight averages after division by M if one assumes for the scatterers a scaling law between their R_h and their molecular weight : $R_h \sim M^\nu$. We have chosen a value of 0.5 for ν to obtain the distribution of relaxation times represented on figure 6b.

Small-Angle Neutron Scattering (SANS)

Polymer solutions were prepared without added salt at 50g/L, using D_2O (100%, 99.97%D, Eurisotop) and NaOD (40% w/w in D_2O, 99.5%D, Eurisotop). Measurements were performed on PACE spectrometer (isotropic scattering) at Laboratoire Léon Brillouin (LLB) CEA (Saclay, France). The scattered intensity has been measured over a wide range of scattering vectors q, between 0.003Å^{-1} and 0.3Å^{-1}, using three configurations (D = 1.2m, λ = 6Å; D = 4.7m, λ = 6Å; D = 4.7m, λ = 12 Å, with Δλ/λ=10%) where D and λ are the sample-to-detector distance and the neutron wavelength, respectively. The scattered intensity was corrected for empty cell scattering and incoherent background and set on an absolute scale according to standard procedures[33, 34]. All samples were measured in 2mm quartz cells at room temperature. H_2O serving as calibration standard was measured in a 1mm cell. All of our intensities have been measured in absolute units (cm^{-1}). Data were treated according to ref [34] with the software PASINET. The adjustments were done using the SASFIT software with a model of hard spheres. The form Factor is given by equation 4.

$$I_{sphere}(q,R) = K^2(q,R,\Delta\eta) \qquad (4)$$

R is the radius of the sphere, $\Delta\eta$ is the scattering length density difference between particle and matrix and K is given by :

$$K(q,R,\Delta\eta) = \frac{4}{3}\pi R^3 \Delta\eta 3 \frac{\sin(qR) - qR\cos(qR)}{(qR)^3}$$

The forward scattering for q = 0 is given by :

$$\lim_{q=0} I_{sphere}(q,R) = \left(\frac{4}{3}\pi R^3 \Delta\eta\right)^2$$

Results and Discussion

Synthesis of P(n$BA_{20\%}$*-stat-*$AA_{80\%}$*)*$_{100}$*-b-*PAA_{95}

A P($n$$BA_{20\%}$-*stat*-$AA_{80\%}$)$_{100}$-*b*-$PAA_{95}$ was prepared in three steps following a procedure already described for the preparation of pure P*n*BA-*b*-PAA diblock copolymers[18] or of P($n$$BA_{50\%}$-*stat*-$AA_{50\%}$)$_{99}$-*b*-$PAA_{98}$[19] (Figure 1). In a first step, a P($n$$BA_{20\%}$-*stat*-*t*$BA_{80\%}$)$_{100}$-Br block was prepared by ATRP copolymerization of *n*BA and *t*BA in acetone at 60°C using CuBr/N,N,N',N',N"-Pentamethyldiethylenetriamine (PMDETA) as catalytic complex and methyl-2-bromopropionate (MBP) as initiator. The polymerization of this first block was well controlled. Indeed, $\ln([M]_0/[M])$ evolved linearly with $t^{2/3}$ (Figure 2a), a signature of the persistent radical effect[35], which may be attributed to the fact that no $CuBr_2$ was added in the reaction mixture at the beginning of the reaction. Furthermore, the number-average molecular weight M_n grows linearly with conversion, whereas the polydispersity index (PDI) decreases down to values as low as 1.1 (Figure 2b). Kinetic data (Figure 2a) moreover reveal that *n*BA and *t*BA copolymerize exactly at the same rate, resulting in a statistical first block. The same was observed for the polymerization of P($n$$BA_{50\%}$-*stat*-*t*$BA_{50\%}$)$_{99}$-Br although the monomer feed ratio was different[19]. The fact that statistical copolymers are obtained with two very different initial monomer ratios indicates that the reactivity ratios are very close to unity for the copolymerization of *n*BA with *t*BA. Indeed, other values for the reactivity ratios would induce a statistical copolymerization only at the azeotropic composition, that is for a single monomer composition. As already mentioned[19],

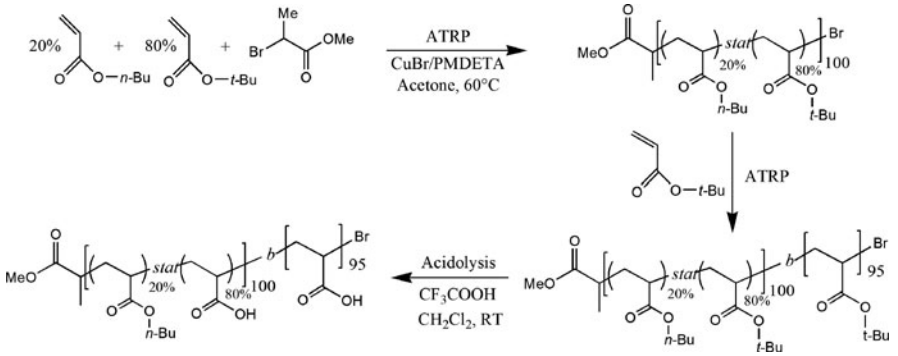

Figure 1 Three steps involved in the synthesis of P($n$$BA_{20\%}$-*stat*-$AA_{80\%}$)$_{100}$-*b*-$PAA_{95}$. From top left to bottom left: ATRP polymerization of a P($n$$BA_{20\%}$-*stat*-*t*$BA_{80\%}$)$_{100}$-Br first block; ATRP of the second block yielding P($n$$BA_{20\%}$-*stat*-*t*$BA_{80\%}$)$_{100}$-*b*-P*t*$BA_{95}$; selective and quantitative acidolysis of the *t*BA units of P($n$$BA_{20\%}$-*stat*-*t*$BA_{80\%}$)$_{100}$-*b*-P*t*$BA_{95}$ into P($n$$BA_{20\%}$-*stat*-$AA_{80\%}$)$_{100}$-*b*-$PAA_{95}$

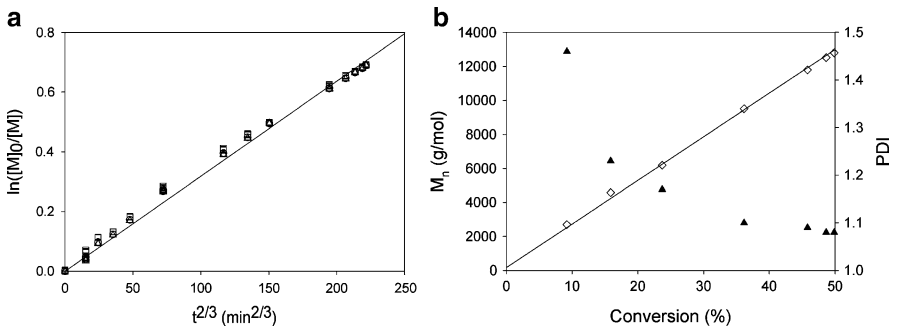

Figure 2 Kinetics of the polymerization of the P($n$$BA_{20\%}$-*stat*-*t*$BA_{80\%}$)$_{100}$-Br first block. (**a**) Semilogarithmic plot of the *n*BA (□), *t*BA (Δ) and global (○) conversions followed by gas chromatography using *n*-decane as internal standard and fitted linearly (–), vs $t^{2/3}$. (**b**) M_n (◊) and PDI (▲), determined by SEC with polystyrene standards, vs conversion. The straight line corresponds to the theoretical molecular weight calculated from the initial monomer to initiator ratio and the conversion

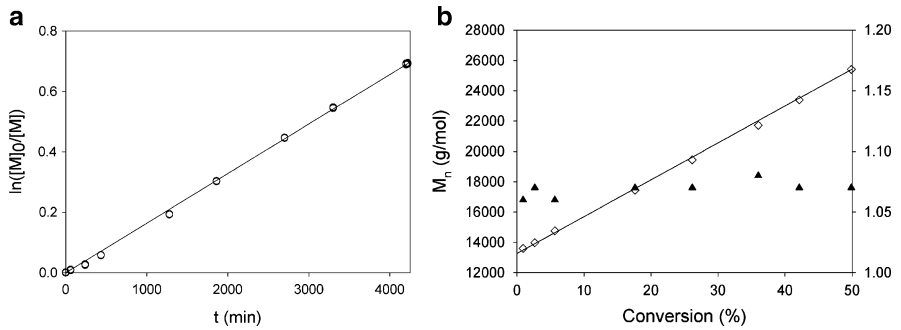

Figure 3 Kinetics of the polymerization of the second block of P(nBA$_{20\%}$-*stat*-tBA$_{80\%}$)$_{100}$-*b*-PtBA$_{95}$. (**a**) First-order plot of the monomer conversion (○) followed by gas chromatography unsing *n*-decane as internal standard and fitted linearly (–). (**b**) M_n (◊) and PDI (▲), determined by SEC with polystyrene standards, vs conversion. The straight line corresponds to the theoretical molecular weight calculated from the initial monomer to initiator ratio and the conversion

this result is not surprising given the structural similarity of the two monomers, but the distribution of monomer units in the moderately hydrophobic block will have a strong impact on the self-assembling behavior of the polymer in aqueous medium[30].

The polymerization was stopped at 50% conversion in order to minimize transfer and termination reactions and the P(nBA$_{20\%}$-*stat*-tBA$_{80\%}$)$_{100}$-Br first block was then purified and used as macroiniator to polymerize *t*BA alone, yielding the diblock P(nBA$_{20\%}$-*stat*-tBA$_{80\%}$)$_{100}$-*b*-PtBA$_{95}$. Kinetic data also reveal a controlled polymerization for the second block: both $\ln([M]_0/[M]) = f(t)$ and $M_n = f(\text{conversion})$ evolve linearly, whereas the PDI is kept very low throughout the polymerization (Figure 3). Moreover, P(nBA$_{20\%}$-*stat*-tBA$_{80\%}$)$_{100}$-*b*-PtBA$_{95}$ does not contain significant traces of residual P(nBA$_{20\%}$-*stat*-tBA$_{80\%}$)$_{100}$-Br (Figure 4), hinting at a macroinitiator efficiency close to 100%. The *t*BA units were finally selectively and quantitatively acidolysed into acrylic acid (AA) ones as already reported[18, 19], leading to P(nBA$_{20\%}$-*stat*-AA$_{80\%}$)$_{100}$-*b*-PAA$_{95}$. On the whole, narrowly distributed polymers whose composition was confirmed by ^{1}H NMR (see "Material and methods") were prepared by ATRP.

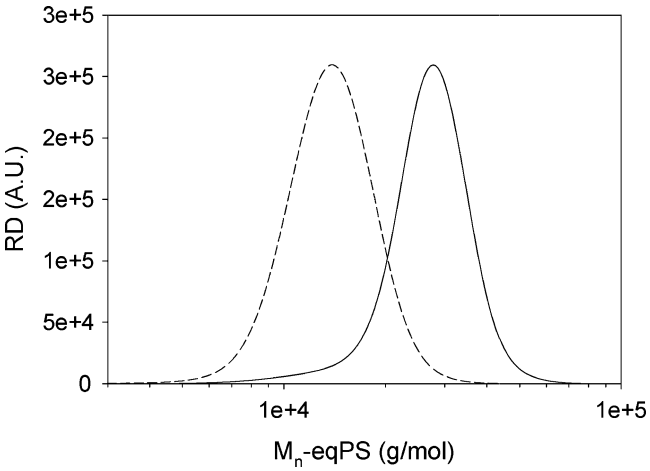

Figure 4 Size exclusion chromatograms of the first block P(nBA$_{20\%}$-*stat*-tBA$_{80\%}$)$_{100}$-Br (--) and of the diblock copolymer P(nBA$_{20\%}$-*stat*-tBA$_{80\%}$)$_{100}$-*b*-PtBA$_{95}$ (–). The molecular weights are calculated using calibration with polystyrene standards

Characterization in Aqueous Solution

The characteristics of the self-assemblies based on P(nBA$_{20\%}$-*stat*-AA$_{80\%}$)$_{100}$-*b*-PAA$_{95}$ dispersed in aqueous solution were then measured by means of static and dynamic light scattering (SLS and DLS) and small angle neutron scattering (SANS) as a function of the ionization degree α of the AA units in the polymer. The value of α was adjusted by adding the proper amount of NaOH (see "Material and Methods"). For $\alpha \geq 20\%$ and in the presence of 0.1M NaCl, DLS indicates the presence of two populations of scatterers (Figure 5b-f). The fast mode of relaxation corresponds to an apparent hydrodynamic radius $R_h \sim 2$nm for all α values $\geq$ 20%, which is compatible with free polymer chains (unimers). It would be tempting to assign the slow mode, corresponding to $R_h \sim 50$nm, to micelles in equilibrium with the unimers. However, their size could not be accounted for considering the chemical structure of P(nBA$_{20\%}$-*stat*-AA$_{80\%}$)$_{100}$-*b*-PAA$_{95}$: the contour length of a fully extended PAA$_{95}$ chain is only 24nm. Moreover, it must be realized that light scattering is sensitive to z-average sizes that is to large particles. Thus, although the slow mode is overwhelming in terms of scattered light intensity (Figure 6a), it corresponds to large aggregates whose weight fraction is negligible compared to that of the fast mode (Figure 6b). Finally, polyelectrolytes[30, 36] were already observed to form ill-defined aggregates responsible for a slow mode such as the one observed here. As a conclusion,

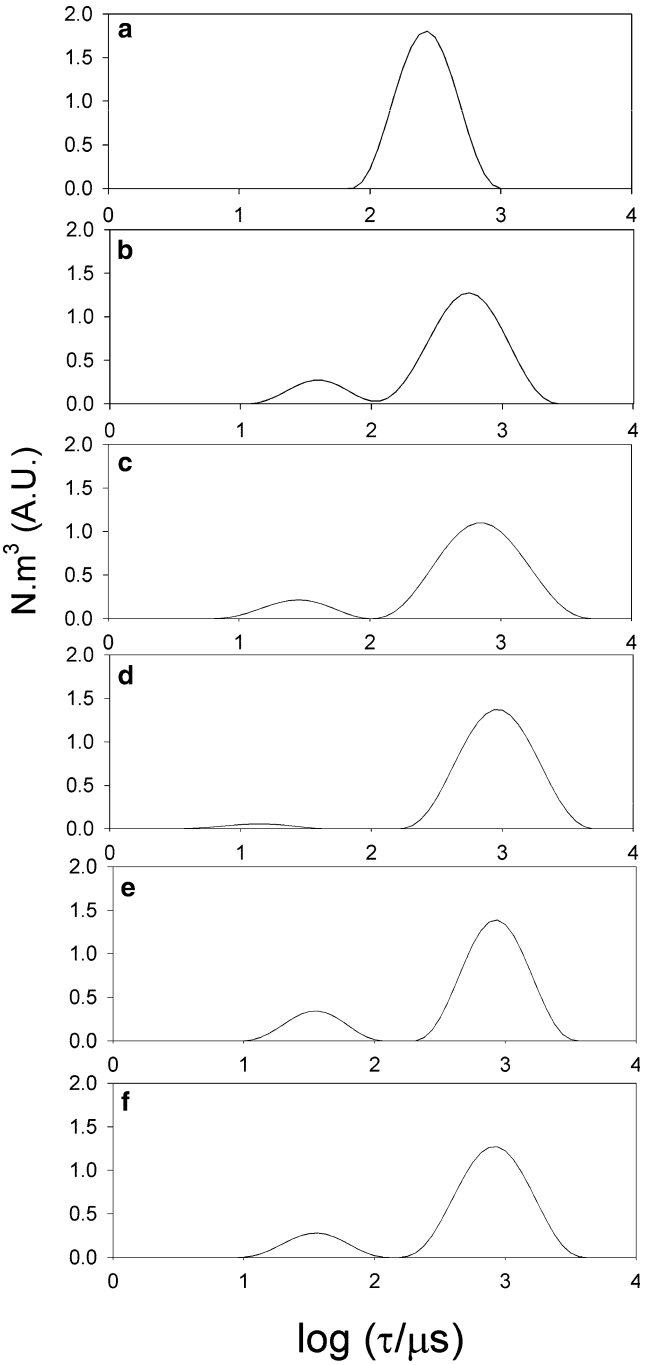

Figure 5 Intensity-weighted distributions of relaxation times in DLS at scattering angle θ = 90° for P(nBA$_{20\%}$-*stat*-AA$_{80\%}$)$_{100}$-*b*-PAA$_{95}$ in aqueous solution at 5g/L, 0.1M NaCl and for an overall ionization degree α of the AA units of (**a**) 0%, (**b**) 20%, (**c**) 50%, (**d**) 70%, (**e**) 90% and (**f**) 100%

the slow mode does not correspond to micelles in equilibrium with unimers, but to spurious aggregates whose weight fraction can be neglected although their contribution in light scattering (Figure 5b-f) and SANS (Figure 7) is dominant because of their size. The rest of the paper thus focuses on the fast mode only.

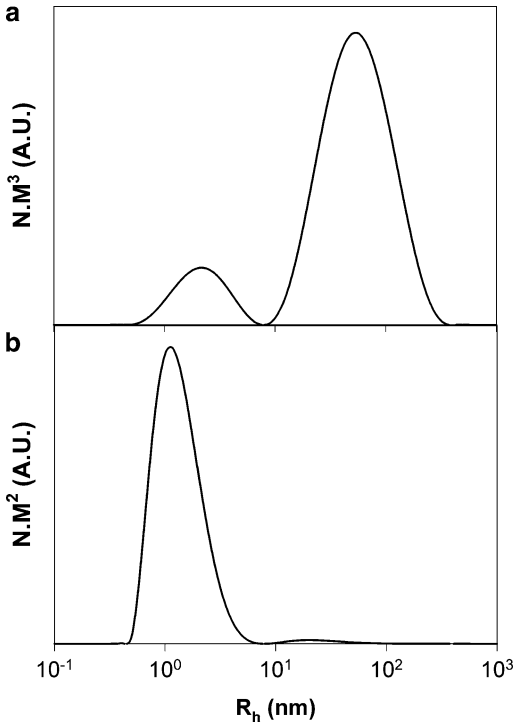

Figure 6 (**a**) z-average and (**b**) weight average distributions of hydrodynamic radii obtained from DLS measurements at scattering angle θ = 90° for P(nBA$_{20\%}$-*stat*-AA$_{80\%}$)$_{100}$-*b*-PAA$_{95}$ prepared at 5g/L, 0.1M NaCl and 50% ionization degree of the AA units

The treatment of the SLS data is complicated by the presence of the spurious aggregates because the total scattered intensity is the sum of the contributions of both the fast and the slow mode observed by DLS. However, DLS indicates to which amount each mode contributes to the total scattered intensity, thus allowing the determination of the mean intensity scattered by the sole fast mode of relaxation (see "Material and methods" as well as refs [30, 31]). Moreover, the polymer concentration corresponding to the fast mode was approximated as the overall polymer concentration since the weight proportion of spurious aggregates is negligible. Results of this treatment are collected in table 1 and confirm that the fast mode corresponds to unimers as proposed given the R_h of the objects. A small discrepancy exists between the molecular weight determined by LS and the nominal molecular weight of unimers, but both values are in fair agreement.

SANS data are also greatly affected by the spurious aggregation which causes a strong upturn of the scattered intensity at low scattering vector (Figure 7) as was already observed for the more hydrophobic P(nBA$_{50\%}$-*stat*-AA$_{50\%}$)$_{99}$-*b*-PAA$_{98}$[19]. It would thus not be reasonable to try to extract the characteristics of the small scatterers responsible for the scattering at high q values. However, data obtained at α = 50% or 90% of ionisation of the AA units agree roughly with the form factor of hard spheres having a radius R ~ 1nm, which is in qualitative agreement with the

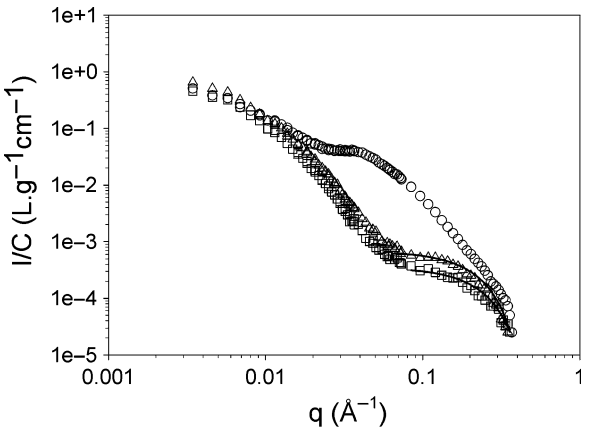

Figure 7 Small-angle neutron scattering curves for the P(nBA$_{20\%}$-*stat*-AA$_{80\%}$)$_{100}$-*b*-PAA$_{95}$ diblock copolymer prepared at 50g/L without added salt and at 10% ionization (○), 50% ionization (Δ) and 90% ionization (□). The lines for α = 50 and 90% ionization (–) correspond to adjustments using a form factor of polydisperse spheres

Table 1 SLS and DLS Results for P(nBA$_{20\%}$-*stat*-AA$_{80\%}$)$_{100}$-*b*-PAA$_{95}$ Dispersed in Aqueous Solution at 5g/L and 0.1M NaCl at Various Ionization Degrees (α)

α	$M_{w\text{-app, SLS}}$ (10^4 g/mol)[a]	$N_{agg\text{-app, SLS}}$[a]	$D_{app, DLS}$ (10^{-11} m^2/s)[a]	$R_{h\text{-app, DLS}}$ (fast) (nm)[a]	$R_{h\text{-app, DLS}}$ (slow) (nm)[b]
0%	160	96	1.22	17.6	
20%	1.69	1	7.73	2.8	33
50%	0.98	0.5	0.18	1.8	43
70%	1.33	0.7	8.25	2.6	63
90%	1.16	0.6	9.00	2.4	52
100%	1.19	0.6	1.01	2.1	46

Data were extracted from DLS and SLS and correspond either to (a) the fast mode or to (b) the slow mode (see text)

$M_{w\text{-app}}$ corresponds to the apparent weight-average molecular weight of the scatterers. $M_{w\text{-app}}$ was divided by the molecular weight of the unimers (calculated from the chemical structure and PDI = 1.1 of the polymer and taking into account the ionization degree α of the AA units) to yield the aggregation number $N_{agg\text{-app}}$. Apparent diffusion coefficients D_{app} were determined by DLS and yielded the apparent hydrodynamic radius $R_{h\text{-app}}$ using the Stocke-Einstein equation

DLS data. As a conclusion, P(nBA$_{20\%}$-*stat*-AA$_{80\%}$)$_{100}$-*b*-PAA$_{95}$ remains in the form of collapsed unimers as soon as the acrylic acid units are 20% ionized.

On the contrary, P(nBA$_{20\%}$-*stat*-AA$_{80\%}$)$_{100}$-*b*-PAA$_{95}$ self-assembles into aggregates for ionization degrees α < 20%. Indeed, DLS no more reveals two populations of scatterers at α = 0%, but only one corresponding to a weight average molecular weight of 16.10^5 g/mol, that is an aggregation number of 100, and an R_h of 18nm no more compatible with the presence of unimers (Figure 5a). Moreover, when α decreases from 50% to 10%, SANS curves are shifted to lower q values, while the "plateau" (observed in the intermediate q-range where the contribution of the spurious aggregates to the scattered intensity can be neglected) goes upward. This indicates respectively that the scatterers become larger and that they have a higher molecular weight as α decreases. More quantitatively, the "plateau" is about 2 orders of magnitude higher at α = 10% than at α = 50%. As unimers are observed for α = 50% according to LS data, it can be deduced that the aggregation number is close to 100 at α = 10%.

Because of the presence of the spurious aggregates, it is not advisable to try to extract the shape of the aggregates by fitting the SANS data at α = 10% with proper form factors. However, both P(nBA$_{50\%}$-*stat*-AA$_{50\%}$)$_{99}$-*b*-PAA$_{98}$[19] and PnBA$_{90}$-*b*-PAA$_{100}$[9] form spherical aggregates in similar conditions. Moreover, the R_h of 18nm determined for P(nBA$_{20\%}$-*stat*-AA$_{80\%}$)$_{100}$-*b*-PAA$_{95}$ at α = 0% and 0.1M NaCl is compatible with the formation of spherical aggregates composed of a "hydrophobic" P(nBA$_{20\%}$-*stat*-AA$_{80\%}$)$_{100}$ core and a rather stretched hydrophilic PAA$_{95}$ corona. P(nBA$_{20\%}$-*stat*-AA$_{80\%}$)$_{100}$-*b*-PAA$_{95}$ might thus also form spherical aggregates at α = 0%, but the experimental results are not sufficient to confirm this hypothesis without doubt yet.

Conclusion

Following a procedure already reported for the preparation of P(nBA$_{50\%}$-*stat*-AA$_{50\%}$)$_{99}$-*b*-PAA$_{98}$[19], the weakly hydrophobic P(nBA$_{20\%}$-*stat*-AA$_{80\%}$)$_{100}$-*b*-PAA$_{95}$ was prepared in a well controlled manner by ATRP polymerization. Kinetic studies indicate that the "hydrophobic" P(nBA$_{20\%}$-*stat*-AA$_{80\%}$)$_{100}$-Br block is purely statistical. Characterization of the self-assembly of the diblock in aqueous medium as a function of the ionization degree α of the AA units is affected by the presence of large (R_h ~ 50nm) spurious aggregates in the solution. However, their amount is very low in terms of weight concentration although their size makes them contribute strongly to the overall scattered intensity in light or neutron scattering experiments. Their contribution could be eliminated by treating the data with particular care and the true characteristics of the sample could be evaluated. It was concluded that, in spite of its weak hydrophobic character, P(nBA$_{20\%}$-*stat*-AA$_{80\%}$)$_{100}$-*b*-PAA$_{95}$ self-assembles into spherical aggregates whose aggregation number reaches about 100 for low α values (0-10%). As soon as 20% of ionization, the aggregates dissolve into unimers, showing that the polymer is not strongly hydrophobic but at least pH sensitive, which was the targeted property (Figure 8).

Keeping a constant length for the "hydrophobic" and hydrophilic blocks, we have thus shown that it is possible to tune the self-assembling properties of amphiphilic block copolymers based on PnBA and PAA by incorporating increasing amounts of hydrophilic AA units in the "hydrophobic" block. Indeed, PnBA$_{90}$-*b*-PAA$_{100}$, a diblock consisting of a purely hydrophobic PnBA block forms frozen aggregates insensitive to pH changes[9]. Then, P(nBA$_{50\%}$-*stat*-AA$_{50\%}$)$_{99}$-*b*-PAA$_{98}$,

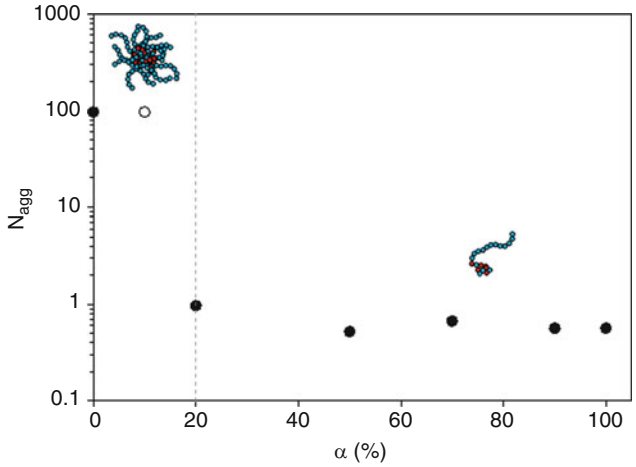

Figure 8 Influence of the ionization degree (α) on the aggregation number (N_{agg}) of the aggregates formed by the P(nBA$_{20\%}$-*stat*-AA$_{80\%}$)$_{100}$-*b*-PAA$_{95}$ diblock copolymer. Results were obtained by light scattering experiments at 5g/L and 0.1M NaCl (●); or by SANS at 50 g/L in the absence of added salt (○)

whose first block's hydrophobic character is moderated by the incorporation of 50%mol AA units, becomes pH sensitive in the whole pH range and is still present as aggregates for α = 50%[19]. Finally, the self-assembly of P(nBA$_{20\%}$-*stat*-AA$_{80\%}$)$_{100}$-*b*-PAA$_{95}$ must be regarded as an on/off aggregation triggered by pH changes, in comparison with the self-assembly of P(nBA$_{50\%}$-*stat*-AA$_{50\%}$)$_{99}$-*b*-PAA$_{98}$ which was more gradual.

The present paper shows that even though P(nBA$_{20\%}$-*stat*-AA$_{80\%}$)$_{100}$-*b*-PAA$_{95}$ contains a very low content of nBA units, it is still able to self-assemble at low α values (α < 20%). We believe the driving force for the self-assembly of these polymers to be attractive hydrophobic interactions between the nBA units of the P(nBA-*stat*-AA) block. Increasing the value of α leads to the ionization of more and more AA units, whose electrostatic repulsive interactions compensate the attractive interactions between the nBA hydrophobic units, ultimately resulting in the molecular dispersion of the polymer chains. The higher the nBA content, the stronger the attractive hydrophobic interactions and the higher α should be to disrupt the aggregates. Indeed, P(nBA$_{20\%}$-*stat*-AA$_{80\%}$)$_{100}$-*b*-PAA$_{95}$ aggregates are disrupted as soon as α = 20%, whereas P(nBA$_{50\%}$-*stat*-AA$_{50\%}$)$_{99}$-*b*-PAA$_{98}$ is still aggregated at α = 50%[19]. It must be added that at very low α values, hydrogen bonds between protonated AA units and nBA ones may add up to hydrophobic interactions and promote even further the aggregation of the polymer chains.

Acknowledgement Neutron scattering experiments were performed at Laboratoire Léon Brillouin (CEA Saclay, France) and Jacques Jestin is thanked for his help during the experiments. This work has been funded by the french government and the Agence Nationale de la Recherche in the framework ANR-09-BLAN-0174-01.

References

1. J. Rodriguez-Hernandez, F. Chécot, Y. Gnanou and S. Lecommandoux (2005) Prog. Polym. Sci. 30: 691–724; J.-F. Gohy (2005) Adv. Polym. Sci. 190: 65–136; P. Alexandridis and B. Lindman (2000) Amphiphilic Block Copolymers. Elsevier, Amsterdam - Lausanne - New York - Oxford - Shannon - Singapore - Tokyo; K. Holmberg, B. Jönsson, B. Kronberg and B. Lindman (2004) Surfactants And Polymers in Aqueous Solution. Chichester (England)
2. I. W. Hamley (2005) Block Copolymers in Solution. San Francisco
3. G. Riess (2003) Prog. Polym. Sci. 28: 1107-1170
4. T. Nicolai, O. Colombani and C. Chassenieux (2010) Soft Matter 6: 3111-3118
5. B. K. Johnson and R. K. Prud'homme (2003) Phys. Rev. Lett. 91: 118301
6. S. Cerritelli, A. Fontana, D. Velluto, M. Adrian, J. Dubochet, P. D. Maria and J. A. Hubbell (2005) Macromolecules 38: 7845-7851; S. Cerritelli, C. P. O'Neil, D. Velluto, A. Fontana, M. Adrian, J. Dubochet and J. A. Hubbell (2009) Langmuir 25: 11328–11335; L. Meli and T. P. Lodge (2009) Macromolecules 42: 580-583; L. Meli, J. M. Santiago and T. P. Lodge (2010) Macromolecules 43: 2018–2027; R. C. Hayward and D. J. Pochan (2010) Macromolecules 43: 3577–3584; D. D. Bendejacq, M. Joanicot and V. Ponsinet (2005) Eur. Phys. J. E 17: 83-92
7. I. A. Nyrkova and A. N. Semenov (2005) Macromol. Theory Simul. 14: 569–585
8. P. D. Petrov, M. Drechsler and A. H. E. Müller (2009) J. Phys. Chem. B 113: 4218-4225
9. O. Colombani, M. Burkhardt, M. Drechsler, M. Ruppel, M. Schumacher, M. Gradzielski, R. Schweins and A. H. E. Müller (2007) Macromolecules 40: 4351-4362
10. K. Letchford and H. Burt (2007) Eur. J. Pharm. Biopharm. 65: 259–269
11. M. Moffitt, K. Khougaz and A. Eisenberg (1996) Acc. Chem. Res. 29: 95-102
12. M. Jacquin, P. Muller, R. Talingting-Pabalan, H. Cottet, J.-F. Berret, T. Futterer and O. Théodoly (2007) J. Colloid Interface Sci. 316: 897-911
13. H. Schuch, J. Klingler, P. Rossmanith, T. Frechen, M. Gerst, J. Feldthusen and A. H. E. Müller (2000) Macromolecules 33:
14. I. A. Nyrkova and A. N. Semenov (2005) Faraday Discussion 128: 113–127; I. A. Nyrkova and A. N. Semenov (2005) Eur. Phys. J. E 17: 327-337; T. Rager, W. H. Meyer and G. Wegner (1999) Macromol. Chem. Phys. 200: 1672–1680; R. S. Underhill, J. Ding, V. I. Birss and G. Liu (1997) Macromolecules 30: 8298-8303; R. Zana, C. Marques and A. Johner (2006) Adv. Coll. Inter. Sci. 123–126: 345–351; J. Zhang, J. Xu and S. Liu (2008) J. Phys. Chem. B 112: 11284–11291; C. Burguière, C. Chassenieux and B. Charleux (2003) Polymer 44: 509-518; S. Piogé, L. Fontaine, C. Gaillard, E. Nicol and S. Pascual (2009) Macromolecules 42: 4262–4272
15. T. Nose and K. Iyama (2000) Comp. Theo. Polym. Sci. 10: 249-257; T. Haliloglu, I. Bahar, B. Erman and W. L. Mattice (1996) Macromolecules 29: 4764-4771; A. Halperin and S. Alexander (1989) Macromolecules 22: 2403-2412
16. Y.-Y. W. Won, H. T. Davis and F. S. Bates (2003) Macromolecules 36: 953-955; S. Abbas, Z. Li, H. Hassan and T. P. Lodge (2007) Macromolecules 40: 4048-4052; E. E. Dormidontova (1999) Macromolecules 32: 7630-7644; O. Théodoly, M. Jacquin, P. Muller and a. S. Chhun (2009) Langmuir 25: 781-793
17. R. Lund, L. Willner, D. Richter and E. E. Dormidontova (2006) Macromolecules 39: 4566-4575; R. Lund, L. Willner, M. Monkenbusch, P. Panine, T. Narayanan, J. Colmenero and D. Richter (2009) Phys. Rev. Lett. 102: 188301; R. Lund, L. Willner, J.

Stellbrink, A. Radulescu and D. Richter (2004) Physica B 350: e909-e912
18. O. Colombani, M. Ruppel, M. Schumacher, D. Pergushov, F. Schubert and A. H. E. Müller (2007) Macromolecules 40: 4338-4350
19. E. Lejeune, M. Drechsler, J. Jestin, A. H. E. Müller, C. Chassenieux and O. Colombani (2010) Macromolecules 43: 2667-2671
20. J. van Stam, S. Creutz, F. C. De Schryver and R. Jérôme (2000) Macromolecules 33: 6388-6395
21. M. Jacquin, P. Muller, H. Cottet, R. Crooks and O. Théodoly (2007) Langmuir 23: 9939-9948
22. R. Lund, L. Willner, J. Stellbrink and D. Richter (2006) Physica B 385-386: 735-737; R. Lund, L. Willner, J. Stellbrink, P. Lindner and D. Richter (2006) Phys. Rev. Lett. 96: 068302
23. D. D. Bendejacq, V. Ponsinet, M. Joanicot, A. Vacher and M. Airiau (2003) Macromolecules 36: 7289-7295
24. D. D. Bendejacq, V. Ponsinet and M. Joanicot (2005) Langmuir 21: 1712-1718
25. D. D. Bendejacq and V. Ponsinet (2008) J. Phys. Chem. B 112: 7996-8009
26. O. Colombani, P. Castignolles, O. Langelier and E. Martwong (2011) J. Chem. Educ. 88:116-121 (the DOI is 10.1021/ed100404r if required)
27. E. Lejeune, C. Chassenieux and O. Colombani (To be published)
28. B. Berne and R. Pecora (1976) Dynamic Light Scattering. Wiley, New York
29. P. Stepanek (1993), Dynamic Light Scattering: 177-241. Oxford University Press, Oxford
30. C. Lefay, B. Charleux, M. Save, C. Chassenieux, O. Guerret and S. Magnet (2006) Polymer 47: 1935-1945
31. C. Chassenieux, T. Nicolai and D. Durand (1997) Macromolecules 30: 4952-4958
32. Huglin (1972) Light Scattering from Polymer Solutions. Academic press, London, New York
33. P. Lindner and T. Zemb (2002) Neutrons, X-rays and Light Scattering Methods Applied to Soft Condensed Matter. Elsevier, North-Holland, Boston
34. A. Brûlet, D. Lairez, A. Lapp and J.-P. Cotton (2007) J. Appl. Cryst. 40: 165–177
35. H. Fischer (2001) Chem. Rev. 101: 3581-3610
36. M. Sedlak (1999) Langmuir 15: 4045-4051; M. Sedlak (2002) J. Chem. Phys. 116: 5236-5245; M. Sedlak (2002) J. Chem. Phys. 116: 5256-5262; M. Sedlak (2005) J. Chem. Phys. 122: 151102; B. D. Ermi and E. J. Amis (1997) Macromolecules 30: 6937-6942

Progr Colloid Polym Sci (2011) 138:17–20
DOI: 10.1007/978-3-642-19038-4_3

The Interaction Parameter in Binary Surfactant Mixtures of a Chelating Surfactant and a Foaming Agent

Ida Högberg, Fredrik Andersson, Erik Hedenström, Magnus Norgren, and Håkan Edlund

Abstract The micellisation in binary mixed surfactant systems of a chelating surfactant and a foaming agent has been studied by surface tension measurements in order to calculate the interaction parameter (β). 2-dodecyldiethylenetriamine pentaacetic acid, 4-C_{12}-DTPA, is an amphoteric chelating surfactant applicable for removing disturbing metal ions from industrial processes, or for heavy metal decontamination of soil or leachate. 4-C_{12}-DTPA contains multiple donor atoms and forms very stable coordination complexes with metal ions. The metal complexes can easily be recovered from water by flotation, if the foaming is enhanced by a foaming agent with strong interactions to the chelating surfactant. Two foaming agents were examined, one cationic and one anionic. As expected, strong interactions were found between the negatively charged 4-C_{12}-DTPA and the cationic dodecyltrimethylammonium chloride, DTAC. The influence of metal ion chelation, as well as pH, on the interaction parameter was also investigated.

Keywords β parameter • electrostatic interaction • mixed micellisation • chelating surfactant • amphoteric surfactant

Introduction

Chelating agents are utilized to coordinate soluble metal ions in a variety of industrial applications. By chelation, the metal ions are prevented from interfering with the process, and chelating agents are often essential for optimal process conditions. Nevertheless, the vast release of chelating agents to the natural aquatic environment has been criticised due to the resistance of the chelating agents to biodegradation.[1, 2] Chelating agents increase the mobility of heavy metals in the natural environment, and thereby increase the risk of heavy metal exposure to living materials.[3] In the light of these environmental aspects, a chelating surfactant, 2-dodecyldiethylenetriamine pentaacetic acid, 4-C_{12}-DTPA, was synthesised. The head group of 4-C_{12}-DTPA was designed with multiple donor atoms, whereby coordination complexes with metal ions can be formed. The metal ion complexes can be recovered from aqueous solutions by flotation, thereby preventing the release of chelating agents and metal ions to the recipient. The highly concentrated metal ion complexes are collected in the foam, and can be further treated to take care of the metal ions and regenerate the chelating surfactant. Chelating surfactant can be used for metal ion recovery from industrial process water, such as white water from a paper mill, as well as for decontamination of polluted soil or leachate. However, 4-C_{12}-DTPA has rather low foam stability due to its large head group, and a foaming agent may be required to enhance the recovery of metal ions. To produce stable foam containing 4-C_{12}-DTPA, there need to be strong interactions between the chelating surfactant and the foaming agent. For this purpose, β parameters, describing the net interaction between two surfactants,[4-6] were determined for binary mixtures of 4-C_{12}-DTPA and foaming agents. 4-C_{12}-DTPA is an amphoteric surfactant, *i.e.* one that can be either cationic, zwitterionic or anionic depending on the pH, and measurements were therefore made at two different pH levels. The pH was chosen to mimic the pH span between white water from a paper mill (pH 5), and leachate from a waste disposal plant (pH 8).

Materials and Methods

Materials

The synthesis and analyses of 2-dodecyldiethylenetriamine pentaacetic acid (4-C_{12}-DTPA) are given in the Electronic Supplementary Material. Dodecyltrimethylammonium

I. Högberg (✉)
Department of Natural Sciences, Engineering and Mathematics, Fibre Science and Communication Network (FSCN), Mid Sweden University, SE-851 70 Sundsvall, Sweden
e-mail: Ida.hogberg@miun.se

chloride, DTAC, and sodium dodecyl sulphate, SDS, (≥99% purity, Sigma Aldrich) and $MnCl_2 \cdot 4H_2O$ (puriss, Riedel-de Haën) were used as received.

Methods

A Krüss K6 tensiometer with a platinum du Noüy ring was used during the surface tension measurements, and the experiments were performed at a temperature of 20 °C. Concentrated surfactant solutions were prepared, and the pH was adjusted with sodium hydroxide or hydrochloric acid. The samples were prepared by dilution with Milli-Q water, buffered to the appropriate pH. The sample volumes were approximately 13 ml and the surface area of the samples were ca 15.5 cm^2. The surface tension was measured directly after pouring the liquid into the sample vessel. The surface tension value for each sample was multiplied by the appropriate correction factor, according to Harkins and Jordan.[7] The cmc was found at the break point in the surface tension versus concentration plot.

Results and Discussion

The structure of the chelating surfactant 4-C_{12}-DTPA is shown in Figure 1. The multiple donor atoms, *i.e.* from the five carboxyl units and the three tertiary amine groups, can coordinate divalent metal ions. At the same time, these groups make the surfactant amphoteric. The amine groups can become positively charged upon protonation, while the carboxyl groups can get negatively charged due to dissociation, and the net charge of 4-C_{12}-DTPA is therefore depending on the pH of the system. At very low pH 4-C_{12}-DTPA is cationic, while it is anionic at high pH. However, over a relatively wide pH interval, the chelating surfactant is zwitterionic, but with varying net charge. In the pH span examined here, 4-C_{12}-DTPA is zwitterionic with a negative net charge. By mixing two surfactants, the cmc may be lowered as a consequence of the electrostatic attraction, or screened repulsion, between the surfactant head groups, and the mixture is said to exhibit synergism.[8, 9] The micellisation of 4-C_{12}-DTPA in mixture with the cationic dodecyltrimethylammonium chloride, DTAC, was investigated at pH 5.0 by surface tension measurements, and the critical micelle concentrations, cmc, of the mixtures are shown in Figure 2. For all the investigated systems, largest synergism was found around the point where the surfactants were mixed in equal proportions. The cmc's of the pure surfactants as well as the 50/50 mixtures at pH 5.0 and 8.0 are reported in Table 1.

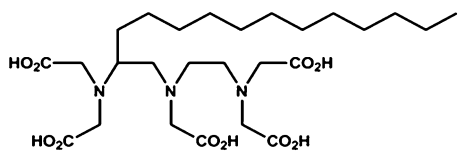

Figure 1 Chemical structure of the amphoteric chelating surfactant 2-dodecyldiethylenetriamine pentaacetic acid, 4-C_{12}-DTPA. The amine groups become protonated and the carboxyl groups dissociated at various degree depending on the pH. In the examined pH span, 4-C_{12}-DTPA is zwitterionic with a negative net charge

The shape of the curve in Figure 2 clearly shows the strong electrostatic attraction between 4-C_{12}-DTPA and DTAC. The cmc drops rapidly with the addition of DTAC to the system, and remains at the low level over a wide composition range, due to the enhanced driving force for micellization in the mixtures, compared to the pure surfactants. In order to keep the pH at 5.0 throughout the experiments, by pH adjustment with NaOH or HCl, the ionic strength was affected. The ionic strength at the cmc was highest for the pure 4-C_{12}-DTPA solution, 17 mM, but dropped

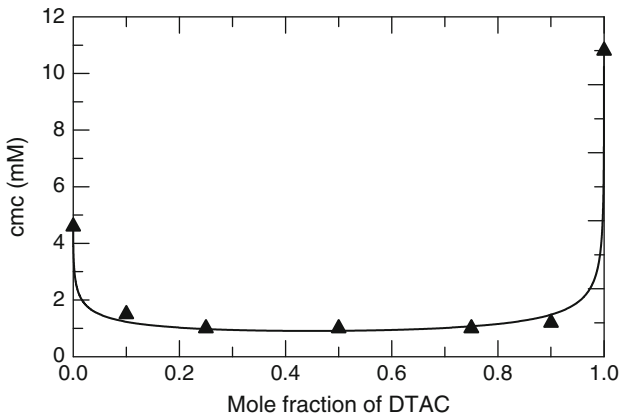

Figure 2 Cmc as a function of solution composition for the 4-C_{12}-DTPA/DTAC system at pH 5.0, symbols (▲) are experimental data, and the solid line is calculated with $\beta = -8.1$

Table 1 Critical micelle concentrations determined by surface tension measurements

Surfactant/mixture	pH	cmc (mM)
4-C_{12}-DTPA	5.0	4.6
4-C_{12}-DTPA	8.0	7.9
Mn^{II}4-C_{12}-DTPA	5.0	2.5
4-C_{12}-DTPA/DTAC 50/50	5.0	0.95
4-C_{12}-DTPA/DTAC 50/50	8.0	1.0
Mn^{II}4-C_{12}-DTPA/DTAC 50/50	5.0	0.75
DTAC	5.0	10.8
DTAC	8.0	12.5
4-C_{12}-DTPA/SDS 50/50	5.0	2.1
4-C_{12}-DTPA/SDS 50/50	8.0	3.7
SDS	5.0	7.0
SDS	8.0	7.0

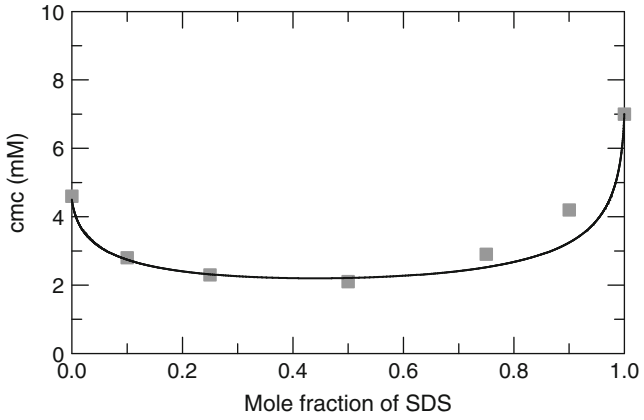

Figure 3 Cmc as a function of solution composition for the 4-C_{12}-DTPA/SDS system at pH 5.0, symbols (■) are experimental data, and the solid line is calculated with β = −3.6

immediately to 5 mM at the lowest mixing ratio with DTAC, and further to 0.01 mM in the pure DTAC solution. The ionic strength was in the same order of magnitude for all the investigated systems, only slightly higher for the 4-C_{12}-DTPA solution at pH 8.

Furthermore, the interactions of the chelating surfactant with the anionic sodium dodecyl sulphate, SDS, were examined. SDS interacts favorably with the local positive charge of 4-C_{12}-DTPA, and synergism was observed also in the 4-C_{12}-DTPA/SDS system, as can be seen in Figure 3 where the cmc is plotted versus solution composition for the 4-C_{12}-DTPA/SDS system at pH 5.0.

From the experimentally determined cmc's of the binary surfactant mixtures, as well as the cmc's of the individual surfactants, the β parameter was calculated.[4] The β parameter reflects the net interaction between two surfactants, and the stronger the attraction, the more negative is the β parameter. Here, surfactants with the same hydrophobic chain length have been studied, so the effects refer to the interactions between the head groups.[10] First, using the fact that $\Sigma x_i^{\mathrm{m}} = 1$, the mole fraction of surfactant i in the micelle, x_i^{m}, was calculated by iteration

$$F = \left(x_1^m\right)^2 \ln(x_1\ cmc) - \left(x_1^m\right)^2 \ln\left(x_1^m\ cmc_1\right) - \left(x_2^m\right)^2 \ln(x_2\ cmc) + \left(x_2^m\right)^2 \ln\left(x_2^m\ cmc_2\right) = 0 \quad (1)$$

where x_i refers to the mole fraction of component i in the solution. The β parameter was then calculated

$$\beta = \frac{1}{\left(x_1^m\right)^2} \ln\left(\frac{x_2 cmc}{x_2^m cmc_2}\right) \quad (2)$$

Table 2 Determined β parameters

Binary mixture	pH	β
4-C_{12}-DTPA/DTAC	5.0	−8.1
4-C_{12}-DTPA/DTAC	8.0	−9.2
Mn^{II}4-C_{12}-DTPA/DTAC	5.0	−7.6
4-C_{12}-DTPA/SDS	5.0	−3.6
4-C_{12}-DTPA/SDS	8.0	−2.9

From the β parameter, the cmc's for the binary mixtures were determined

$$cmc = x_1^m f_1^m cmc_1 + x_2^m f_2^m cmc_2 \quad (3)$$

$$\ln f_i^m = \left(x_i^m\right)^2 \beta \quad (4)$$

where f_i^{m} is the activity coefficient of surfactant i in the micelle.

As expected, the β parameter was more negative for the 4-C_{12}-DTPA/DTAC mixture compared to the 4-C_{12}-DTPA/SDS mixture, due to the strong mutual electrostatic attraction between the oppositely charged surfactant head groups, see Table 2.

The net charge of the 4-C_{12}-DTPA head group is increasingly negative with increasing pH, due to higher degree of carboxyl group dissociation. The cmc of the pure 4-C_{12}-DTPA was higher at the higher pH (8.0) because of the stronger electrostatic repulsions between the head groups, see Table 1. As a result, the interaction with the cationic DTAC was stronger at pH 8.0, and the β parameter was found more negative (Table 2). The interactions between 4-C_{12}-DTPA and SDS, on the other hand, were reduced by the increased pH. The more negatively charged 4-C_{12}-DTPA at the higher pH is less attracted to the anionic SDS.

Manganese was added to the 4-C_{12}-DTPA/DTAC system in equal molar amount as 4-C_{12}-DTPA, to allow 1:1 coordination between Mn^{II} ions and chelating surfactants. The interactions between 4-C_{12}-DTPA and DTAC were reduced by the chelation of manganese, see Table 2. Due to the very high binding constant, the coordinated metal ions can be regarded as chemically bound to the chelating surfactants, rather than acting as normal counterions that are exchanged regularly. The net negative charge of the Mn^{II}4-C_{12}-DTPA complex is therefore lower than for the free 4-C_{12}-DTPA, and the attraction to the cationic DTAC is consequently less, which is reflected in the less negative β parameter.

The micellar composition plotted as a function of the total solution composition is shown in Figure 4. Increasingly negative β parameters, originating from stronger electrostatic attraction, result in micellar composition tending to 50:50 mixing over the major part of the solution composition.[5] As compared to the 4-C_{12}-DTPA/SDS mixture, it is evident

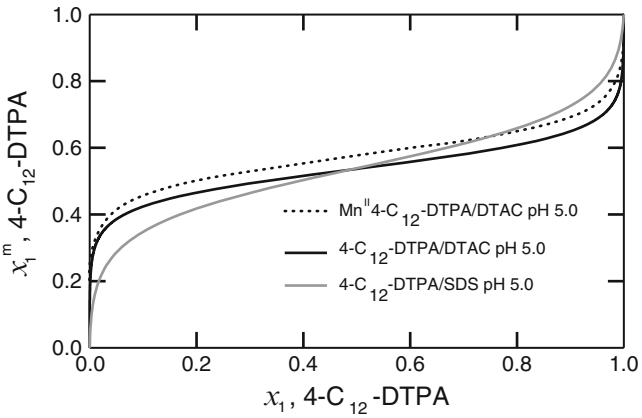

Figure 4 4-C_{12}-DTPA mole fraction in micelles, x_1^m, as a function of 4-C_{12}-DTPA mole fraction in solution, x_1, for the different surfactant systems at pH 5.0

from the more flat curves of the 4-C_{12}-DTPA/DTAC systems that the surfactants are mixed in more similar portions in the micelles, due to stronger interactions between oppositely charged surfactants. The curves over Mn^{II}4-C_{12}-DTPA/DTAC and 4-C_{12}-DTPA/DTAC also reflects the influence of the cmc values. The consistently lower cmc's in the mixtures containing Mn^{II} ions shifts the curve upwards, *i.e.* to larger mole fraction of surfactants in micelles.

Conclusions

The interactions with the amphoteric chelating surfactant 4-C_{12}-DTPA were stronger for the cationic foaming agent DTAC than for the anionic SDS, due to the net negative charge of 4-C_{12}-DTPA in the pH interval examined here (5 and 8). Large negative β parameter was found for the 4-C_{12}-DTPA/DTAC system at both the investigated pH values, even though more negative at pH 8. It is therefore reasonable to assume that the interactions would remain strong over the whole pH range from 5 to 8, which is convenient from a technical point of view since most of the industrial applications lie within this pH range. When used as a chelating agent, in any application, 4-C_{12}-DTPA would coordinate a metal ion. The result from the study with Mn^{II} ions shows that the interactions between 4-C_{12}-DTPA and DTAC are reduced, but still strong, by the chelation of metal ions.

Acknowledgement This work was financed by the European Union European Regional Development Fund and the County Administrative Board of Västernorrland. The authors thank Leif Olsson for assistance with MatLab calculations.

References

1. Knepper TP (2003) Trac-Trends in Analytical Chemistry 22:708-724 DOI 10.1016/s0165-9936(03)01008-2
2. Bucheli-Witschel M, Egli T (2001) Fems Microbiology Reviews 25:69-106
3. Gupta SK, Vollmer MK, Krebs R (1996) Sci. Total Environ. 178:11-20
4. Holland PM, Rubingh DN (1992) Mixed Surfactant Systems. American Chemical Society, Washington, DC
5. Holmberg K, Jönsson B, Kronberg B, Lindman B (2003) Surfactants and Polymers in Aqueous Solution. John Wiley & Sons Ltd., Chichester
6. Goloub TP, Pugh RJ, Zhmud BV (2000) J. Colloid Interface Sci. 229:72-81 DOI 10.1006/jcis.2000.6954
7. Harkins WD, Jordan HF (1930) J. Am. Chem. Soc. 52:1751-1772
8. Rosen MJ (1991) Langmuir 7:885-888
9. Li F, Li GZ, Chen JB (1998) Colloids and Surfaces a-Physicochemical and Engineering Aspects 145:167-174
10. Bakshi MS, Kaur I, Sood R, Singh J, Singh K, Sachar S, Singh KJ, Kaur G (2004) J. Colloid Interface Sci. 271:227-231 DOI 10.1016/j.jcis.2003.10.019

Progr Colloid Polym Sci (2011) 138:21–26
DOI: 10.1007/978-3-642-19038-4_4

Magnetorheological Elastomer Composites

Marian Zaborski and Marcin Masłowski

Abstract Smart composites based on carbonyl iron powder, micro and nano size Fe_3O_4 in ethylene – propylene and acrylonitrile – butadiene rubber were manufactured and studied. Elastomer samples with various volume fractions of magnetic particles were tested. To improve dispersion of applied fillers in polymer matrix, ionic liquids were added during the process of composites preparation. To align particles in elastomer, cross-linking process took place in magnetic field.

Keywords elastomer composites • magnetic properties • magnetorheological properties • magnetoactive fillers • ionic liquids

Introduction

Magnetorhological elastomers (MREs) are smart materials whose rheological properties can be changed by applying external magnetic field [1]. They are solid analogs of magnetorheological fluids (MRFs). MRE and MRF consist of micro or nanometer sized particles of iron compounds dispersed in elastomer matrix [2-4] As in the case of MR fluids, magnetoactive particles try to arrange themselves in the direction of applied magnetic field [5-7]. Spherical carbonyl iron (CIP) microparticles are commonly used [8]. The size of magnetically polarizable particles has a great influence on the stress generated in magnetorheological materials. It is well known from literature [9] that aggregation of magnetic particles results in local anisotropy and dispersion irregularity that drastically diminishes magnetical and magnetorheological effect of materials. Therefore, it is evident that the best magnethoreological effect can be achieved by improving dispersion stability. Ferromagnetic composites with an elastomer matrix are characterized by unique properties which are not characteristic of bulk magnetic materials. These properties, among others, are a high susceptibility to elastic strains in the magnetic field and the dependence of magnetic permeability on stress [10]. An interesting and useful property of the described composites is a change of their elasticity coefficients and other material parameters in a sufficiently high magnetic field [11]. Due to their properties, ferromagnetic composites with an elastomer matrix have already found many applications, for example in sensors, converters and controlled vibration dampers [12].

M. Masłowski (✉)
Institute of Polymer & Dye Technology, Technical University of Lodz, Stefanowskiego 12/16, 90-924 Lodz, Poland
e-mail: marcin.maslowski01@gmail.com

Materials

Acrylonitrile-butadiene rubber (NBR) – Europrene N3960 (Lanxess), acrylonitrile unit content: 28 %, ethylene-propylene rubber (EPM) Dutral CO 054 (Montedison Ferrara), propylene unit content: 40 %. Crosslinking agents: dicumyl peroxide DCP (Aldrich), triallyl-1,3,5-triazine-2,4,6(1H,3H,5H) TAC (Aldrich), zinc oxide ZnO (Huta Będzin), mercaptobenzothiazole MBT (Pneumax MBT) and sulphur S_8 (Z.P.S. Siarkopol). Fillers: micro- and nano- sized magnetite (Fe_3O_4) (Aldrich), carbonyl iron powder CIP (BASF). Ionic liquids: 1-ethyl-3-methylimidazolium diethylphosphate EMIMDEP, 1-butyl-3-methylimidazolium hexafluorophosphate $BMIMPF_6$, 1-hexyl-3-methylimidazolium chloride HMIMCl, 1-butyl-3-methylimidazolium trifluoromethanesulfonate BMIM Otf, 1-butyl-3-methylimidazolium tetrafluoroborate $BMIMBF_4$, trihexyltetradecylphosphonium chloride HPCl, 1-butyl-3-methylimidazolium chloride BMIMCl (all from Alrdich).

Composition of typical elastomer mixture: rubber - 100 phr, DCP - 2 phr, TAC – 0.5 phr, ZnO - 5 phr, MBT - 2 phr, S - 2 phr, filler 20-100 phr.

Methods

Elastomer mixtures, based on EPM or NBR filled with micro- and nano- sized iron oxides and carbonyl iron powder were prepared by the common manufacturing procedures for rubber. Magnetoactive particles were mixed with the rubber together with vulcanization system using two – roll mills at 30 °C. Injection and stirring of ionic liquids into the elastomer composites were performed in Brabender measuring mixer N50 (temp. 50 °C, speed range 40 min^{-1}, time of the process 10 min.)Then the mixtures were vulcanized at 160 °C, at 15 MPa pressure for 30 min. The vulcanizates were produced in two different ways: under the influence of magnetic field – to align magnetic particles in elastomer matrix and without the presence of magnetic field.

The mechanical properties were examined by static materials testing machine Zwick, according to ISO 37 standards. Magnetic properties of the samples were measured with vibrating sample magnetometer VSM LakeShore 7410, in the range of the field 960 kA/m. Magnetorheological properties were studied with the application of Ares Rheometer (plate-plate system, plate diameter, 20 mm; gap 2 mm; magnetic field range, 0-300 mT). Cross-linking density of vulcanizates was calculated based on rapid solvent-swelling measurements (in toluene and in toluene with ammonium vaporous) from the Flory-Rehner Equation. Microstructure observations were carried out using scanning electron microscope (SEM).

Results and Discussion

Magnetorheological Properties

Magnetorheological properties of the MREs composites were investigated by Ares Rheometer for three different systems (Fig. 1, Fig. 2, Fig. 3), which refer to the same elastomer matrix (NBR) but various fillers: micrometric Fe_3O_4 and CIP and nanometric Fe_3O_4. In all cases two types of composites were prepared: under and without the presence of external magnetic field. Dependence of the elastic (storage) modulus (G'), loss modulus (G") and loss tangent (tanδ) of

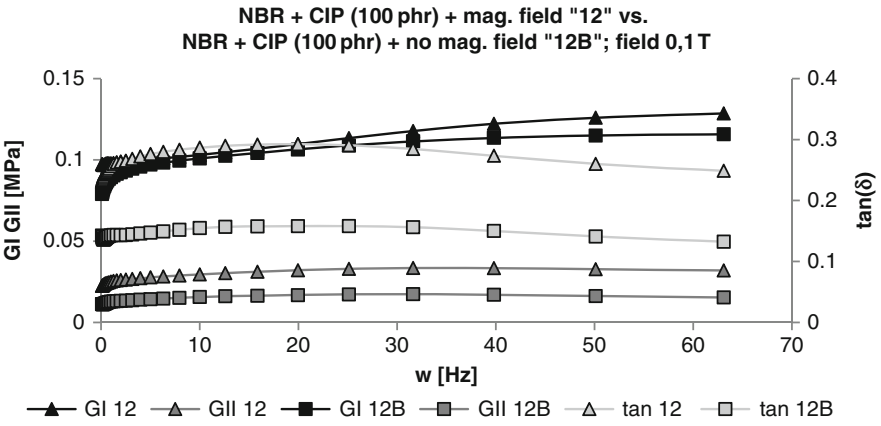

Fig. 1 Dependence of elastic (storage) modulus (G' = GI), loss modulus (G" = GII) and loss tangent (tanδ) of MRE samples containing CIP (prepared in and without the presence of magnetic field) on strain frequency

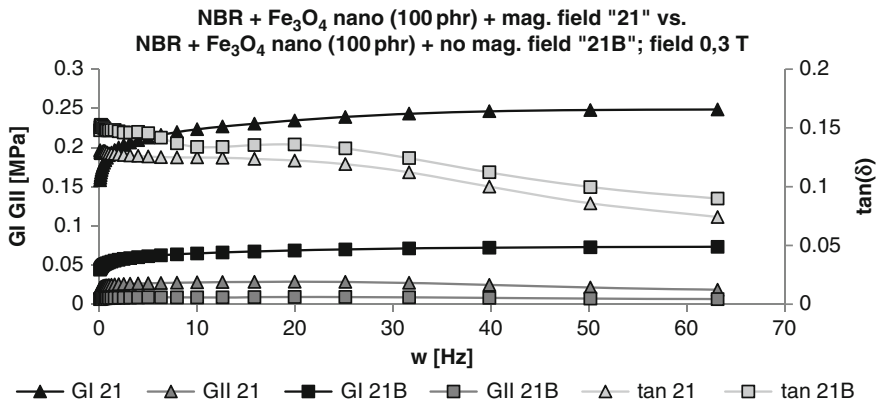

Fig. 2 Dependence of elastic (storage) modulus (G' = GI), loss modulus (G" = GII) and loss tangent (tanδ) of MRE samples containing nano Fe_3O_4 (prepared in and without the presence of magnetic field) on strain frequency

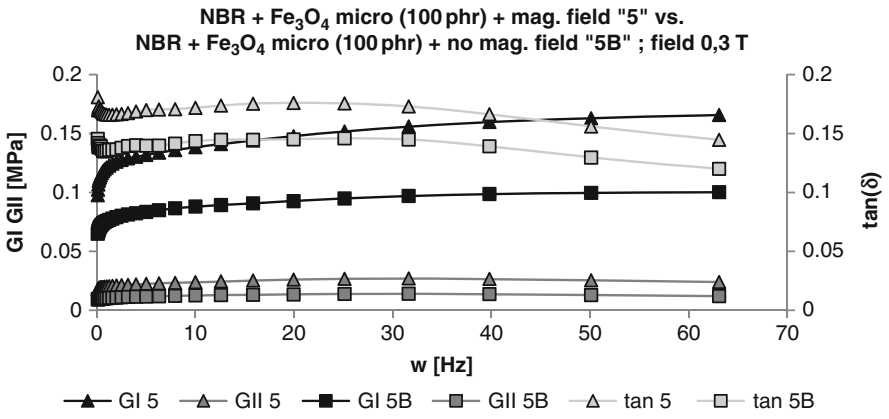

Fig. 3 Dependence of elastic (storage) modulus (G' = GI), loss modulus (G" = GII) and loss tangent (tanδ) of MRE samples containing micro Fe_3O_4 (prepared in or without the presence of magnetic field) on strain frequency

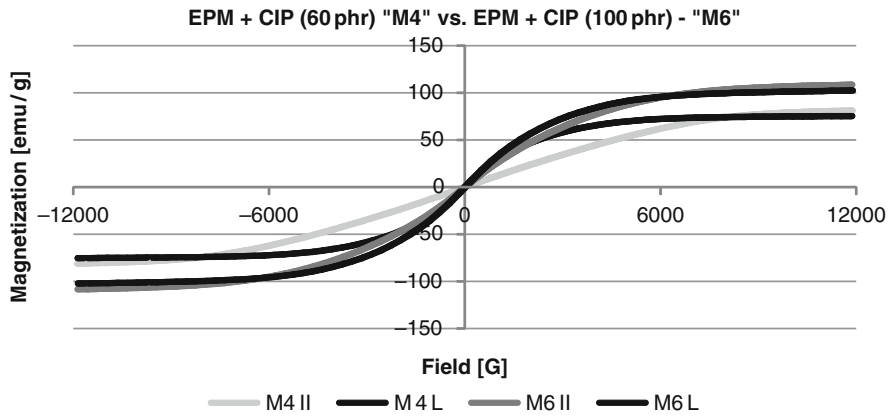

Fig. 4 Magnetic properties – hysteresis curves of MRE samples cured under magnetic field of 1,2T applied parallel (II) and perpendicular (L) to the sample

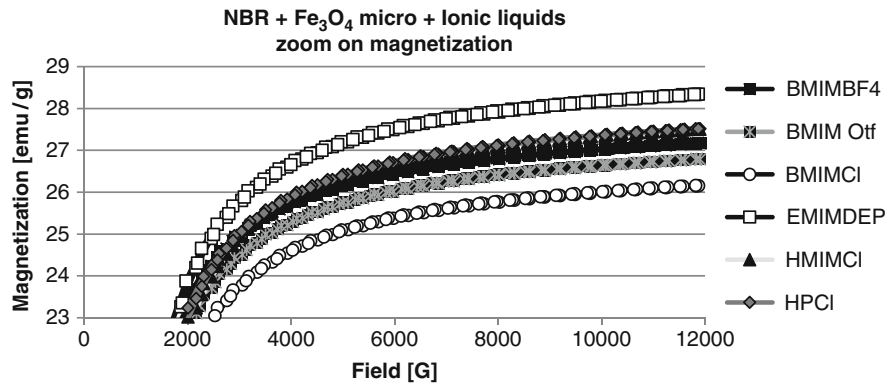

Fig. 5 Magnetic properties – hysteresis curves of MRE samples cured under magnetic field of 1.2T applied parallel (II) and perpendicular (L) to the sample

MRE samples on the strain frequency is presented. In Figs. 1 through 3. The elastic modulus increases with the strain frequency, no matter of the vulcanization type. In all cases a significant increase in elastic modulus (G'), loss modulus (G") and loss tangent (tanδ) occurs for the samples prepared in magnetic field in comparison to those vulcanized without magnetic field. Higher initial values of storage modulus for composites containing nanometer-sized Fe_3O_4 (Fig. 2) than micrometer-sized Fe_3O_4 or CIP (Fig. 1, Fig. 3) show its appropriate alignment in the elastomer matrix and larger magnetic susceptibility.

Magnetic Properties

Significant differences between hysteresis curves recorded for EPM vulcanizates containing different amounts of

Table 1 Cross-link density (ν_e), mechanical (Tensile strength - T.S, Elongation at break - E.B) and magnetic properties () of NBR vulcanizates containing carbonyl iron powder and ionic liquids as dispersing agents

CIP [phr]	Ionic liquid	ν_e*10^{-5} [mol/cm^3]	T.S. [MPa]	E.B. [%]	Coercivity (Hci) [G]	Magnetization (Ms) [emu/g]	Retentivity (Mr) [emu/g]
0	**-**	5.37+/−3%	2.43+/−5%	537+/−5%	23.83+/−1%	78.67+/−1%	0.31+/−1%
60	**EMIMDEP**	6.11+/−3%	2.31+/−5%	384+/−5%	23.07+/−1%	70.16+/−1%	0.54+/−1%
60	**BMIMPF$_6$**	5.98+/−3%	2.33+/−5%	393+/−5%	22.76+/−1%	70.76+/−1%	0.58+/−1%
60	**HMIMCl**	6.93+/−3%	3.14+/−5%	333+/−5%	23.23+/−1%	69.86+/−1%	0.46+/−1%
60	**BMIM Otf**	6.00+/−3%	3.20+/−5%	455+/−5%	22.92+/−1%	70.18+/−1%	0.51+/−1%
60	**BMIMBF$_4$**	6.15+/−3%	3.47+/−5%	434+/−5%	22.51+/−1%	70.16+/−1%	0.53+/−1%
60	**HPCl**	6.48+/−3%	3.08+/−5%	321+/−5%	22.60+/−1%	76.64+/−1%	0.41+/−1%
60	**BMIMCl**	6.90+/−3%	2.86+/−5%	326+/−5%	22.47+/−1%	70.28+/−1%	0.47+/−1%

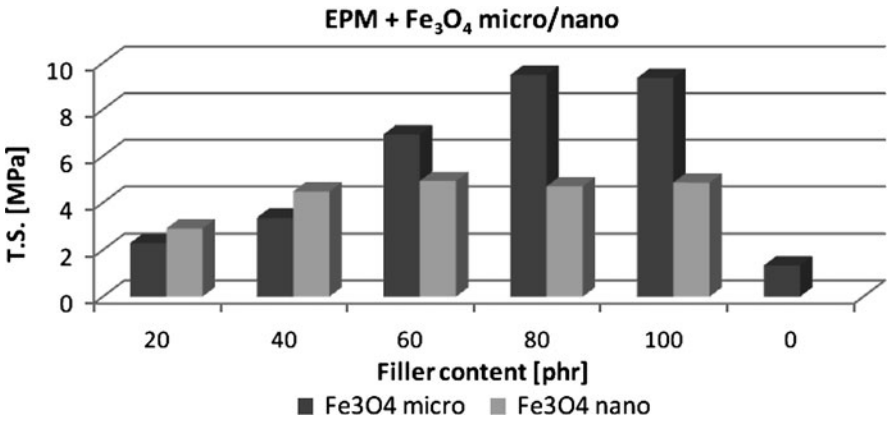

Fig. 6 Mechanical properties (Tensile strength - T.S.) of EPM vulcanizates containing micro and nano sized Fe_3O_4

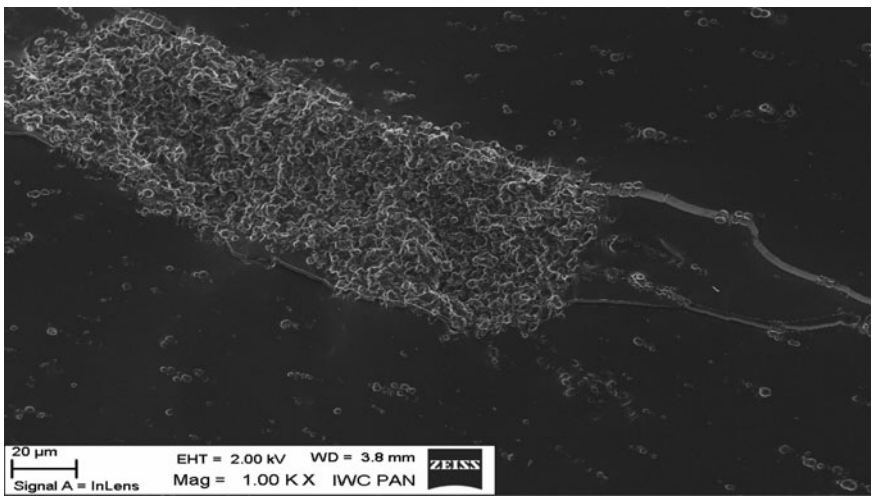

Fig. 7 SEM image of NBR vulcanizate filled with 60 phr CIP

carbonyl iron powder can be seen in Fig. 4. This is certainly due to the influence of applied external magnetic field: parallel or perpendicular to the sample long axis (corresponding to the magnetic field direction during vulcanization). Moreover, hysteresis curves observations indicates that for M4 sample a visibly anisotropic network of particles is formed.

Additionaly, to improve the dispersion of applied filler properties, ionic liquids were added during preparation (Fig 5). No matter what kind of IL was admixed, all composites demostrate magnetic properties. The highest values of magnetization characterize the vulcanizates containing EMIMDEP and HPCl.

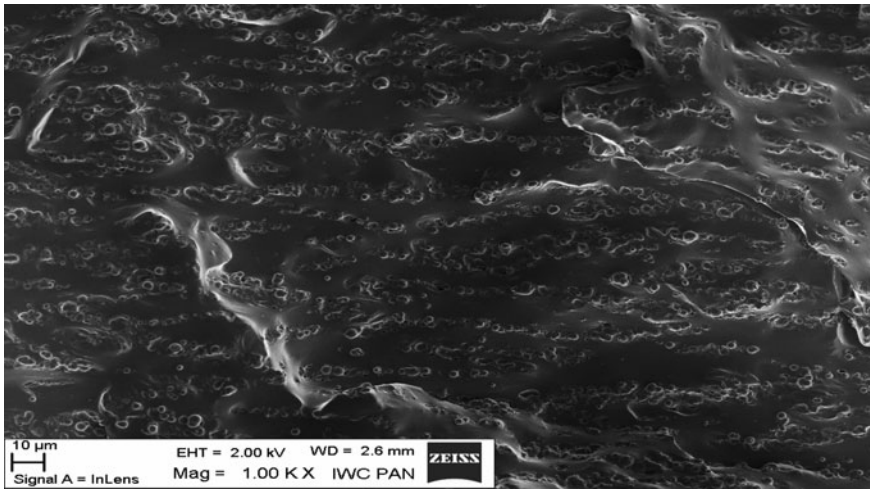

Fig. 8 SEM image of NBR vulcanizate filled with 60 phr CIP and HPCl

Mechanical Properties

As shown in Tab. 1 (samples were measured perpendicular to the aligning field – long axis), all applied ionic liquids influence the cross-linking density of composites and, hence, the tensile strength (T.S.) and elongation at break (E.B). This is surely due to better dispersion of carbonyl iron particles in NBR matrix (Fig. 7, 8). Application of ILs to MRE composites, improves their mechanical properties.

The comparison of mechanical properties of EPM vulcanizates filled with micrometer and nanometer sized Fe_3O_4 shows the effect of fillers size and its influence on vulcanizates tensile strength (Fig. 6). The results suggest, that the optimal content of micro sized Fe_3O_4 is 80 phr and 60 phr for nano sized Fe_3O_4.

Conclusions

MRE composites were prepared according to the commonly used methods. It was found that micro- and nano- sized iron oxides and carbonyl iron powder were active fillers improving mechanical properties of elastomers. Additionally, they also changed their magnetic properties and reinforced magnetorheological effect of composites. Dispersion of nano- and micro- sized Fe_3O_4 or CIP in the elastomer matrix can be improved by using ionic liquids as dispersing agents.

References

[1] Munoz BC, Jolly MR, (2001) Performance of Plastics. Carl Haser Verlag, Munich
[2] Jolly MR, Carlson JD, Munoz BC, (1996) Smart Mater Struct 5: 607
[3] Wang Y, Hu Y, Gong X, et al. (2007) J Appl Polym Sci 103: 3143
[4] Wang Y, Hu Y, Deng H, et al. (2006) Polym Eng Sci 264: 154
[5] Zhou GY, (2003) Smart Mater Struct 12:139
[6] Farshad M, Benine A, (2004) Polym Test 23:347
[7] Jolly MR, Carlson JD, Munoz BC, Bullions TA, (1996) J Intel Mater Syst Struct 7:613
[8] Kordonski WI, Gorodkin SR, Novikova ZA, 6th International Conference on Electo-Rheological Fluids, Magneto-Rheological Suspensions and their Applications, World Scientific, Yonezawa, Japan 1997.
[9] Lokander M, Stenberg B, (2003) Polym Test 22: 677
[10] Jin S, Tiefel TH, Wolfe R, et al. (1992) Science 225:446.
[11] Kordonski WI, Shulman ZP, et al. (1990) J Mag Mag Mater 85:114
[12] Zal'tsgendler EA, Kolomentsev AV, et al. (1985) Mag Hydr 4:105

Progr Colloid Polym Sci (2011) 138:27–32
DOI: 10.1007/978-3-642-19038-4_5

Salt-Induced Behavior of Internally Self-Assembled Nanodrops: Understanding Stabilization by Charged Colloids

François Muller[1], Anniina Salonen[2], Martin Dulle[3], and Otto Glatter[3]

Abstract We explored the structural effects induced by the addition of salt on lipid-based liquid crystalline drops stabilized in aqueous media by charged sphere-like colloids. This allows us to distinguish two different stabilization regimes. In one case, the internal liquid crystalline phase has the ability to reorganize upon the coalescence of the drops and in the other not. This in turn depends mainly on the contact angle and the internal phase viscosity.

Keywords charged colloids • lipid-based crystalline phases • stabilized domains • salt

Introduction

From the late 90's, when Larsson and co-workers produced the first dispersions in water of lipid-based liquid crystalline phases [1], these systems have been seen as of particular interest for many potential applications from cosmetics to the food industry [2]. Because of the low viscosity of the dispersions, their high interfacial area, including both hydrophilic and hydrophobic regions, these dispersed particles are highly relevant as further carriers of active molecules [3]. During the last decade, the fundamental understanding of these systems has been extended by exploring ways to control the particles' internal structure, with changing temperature or with additives without the destabilization of the particles [4], and by theoretically studying the unusual sequence of mesophases observed [5].

To date, most of the experimental work has been carried out using organic macromolecules that include surfactants, polymers, and proteins as stabilizers. It was only very recently that the principle of Ramsden-Pickering emulsions [6] was applied in order to disperse and stabilize liquid crystalline phases [7]. An important feature of using colloids instead of organic macromolecules as stabilizers is the arrest of Ostwald ripening, due to the irreversible adsorption of colloids at the interface which leads to an increase of the dispersion stability, and the possibility of functionalising the drops through exploitation of the colloids at the interface. In addition, with dispersions of liquid crystalline phases, the internal phase can be also exploited. This therefore should open new possibilities and potentialities for many application purposes. As first approaches, the cases of negatively charged disk-like [7],[8] and sphere-like [9] colloids with similar radii (of around 12-13 nm) were investigated as stabilizers of two commonly used lipids: monoglyceride and phytantriol. These studies were carried out as a function of the nature of the internal phase, the temperature, and the stabilizer concentration in salt-free solutions. The results indicated a complex link between the colloidal geometry, the nature of the lipid, and the stiffness of the internal phase. It can be nevertheless expected that the effective interactions between colloids (adsorbed or not) play an important role. Hence, understanding the structural effects induced at different length scales by tuning these interactions should help to explain the stabilization process and to control the system's structural properties. This is the aim of this contribution.

Herein, we focus on the case of the negatively charged sphere-like colloids as stabilizers. Different lipid-based internal phases, different lipids, and sphere-like colloid concentrations have been investigated as the interactions between the colloids are tuned by addition of monovalent salt, once the dispersions have been prepared in pure water solvent. Light scattering technique is used to investigate the salt-induced effects on the stabilized drops' sizes. The local changes are explored using small-angle x-ray scattering.

F. Muller (✉)
[1]Laboratoire Léon Brillouin, CEA Saclay, 91191 Gif sur yvette Cedex, France
e-mail: francoi.muller@cea.fr
[2]Laboratoire de Physique des Solides, Université Paris Sud, CNRS UMR 8502, 91405 Orsay Cedex, France
[3]Physical Chemistry, University of Graz, Heinrichstrasse 28, AT-8010 Graz, Austria

Experimental Section

Dimodan U/J (DU) was supplied by Danisco A/S (Braband, Denmark). It contained 96% distilled monoglycerides, of which 62% were linoleate and 25% oleate. Phytantriol (PT, purity > 95%) was purchased from DSM Nutritional Products Ltd. (Basel, Switzerland). Tetradecane (TC), a linear alkane chain of composition C14H30, was purchased from Sigma Chemical Co. (St. Louis, MO). The colloidal silica spheres had an average diameter of 25 nm (TM, Ludox TM-50, DuPont). The particles are negatively charged with a specific surface area of 140 m^2/g and are stabilized with sodium counterions. Samples with DU:TC and PT:TC ratios of 50:50, 70:30, 100:0 were prepared in excess water. The preparation was carried out by weighing the DU:TC (PT:TC, respectively) mixture, the stabilizer (Ludox TM), and the water into vials. The raw mixture was ultrasonicated (SY-Lab GmbH, Pukersdorf, Austria), without external cooling, for 20 min at 30% of the maximum power in pulse mode (0.5 s on and 1.5 s off), and the samples were then sealed and left to equilibrate at room temperature. The weight fraction of the DU:TC (PT:TC, respectively) mixture was kept constant at 5 wt%, and that of the stabilizer varied from 0.50 wt% to 5 wt%. Sodium chloride was then added to the dispersions in order to obtain added salt concentrations ranging from 0 mM to 10 mM. The samples were measured 1 day after addition of salt. All other data shown are also from fresh samples (i.e., taken less than 2 days after preparation), before significant hydrolysis of monoglyceride chains leading to possible phase transitions [7]. This chemical process does not affect the physical stabilization of the drops [7] and phytantriol chains are not affect by it.

The DLS instrument used was the same laboratory-built setup as in reference [9]. The measurements were carried out at a scattering angle of $\theta = 90°$, and the temperature was fixed at 25 $°C$. All prepared samples were turbid, but as previously reported they are kinetically stable at least on intermediate time scales. As a consequence, all samples were diluted using doubly distilled water (pure or of the corresponding brine) at least 10000 times. The data were collected in repeated measurements of 10×30 s. The intensities of the pseudo-cross-correlation functions were averaged. The average diffusion coefficient D was obtained from these functions by means of second-order cumulant analysis allowing determination of the hydrodynamic radii, R_H, through the well-known Stokes-Einstein relation and the width of the size distribution, noted W. The SAXS equipment consisted of a slit-geometry camera with high flux and low background (SAXSess, Anton-Paar, Austria). The operating mode is similar to the one described in the reference [9]. The temperature of the capillary was fixed at 25 $°C$, and a thermal equilibration time of 30 min was used prior to each SAXS measurement. The measuring times were 3×5 min for all dispersions allowing for the proper subtraction of cosmic rays that were registered when using a CCD camera. The scattering of the water solvent, $I_w(q)$, was measured for equivalent times and further subtracted from $I(q)$, thus giving the scattering intensity from the dispersions. We are aware that the data were smeared with the beam profile (slit profile).

Results and Discussion

The results obtained by DLS on samples composed of DU:TC and PT:TC at 50:50 ratio (L_2 inverse micellar phase) stabilized by TM concentrations ranging from 0.5 wt% to 5 wt% are summarized in Table 1. A first important remark is on the visual aspect of the emulsions, which are white emulsions with no coalescence or phase separation within weeks [7],[9]; hence, a good stabilization has been obtained. Although, the widths of the distributions, W, reflect that the quality of the stabilization is better in the case of DU than for PT, similarities on the behavior between both lipids can be distinguished. At a given TM concentration, the hydrodynamic radius, R_H, has been found to increase with the added salt concentration. This shows that the L_2 internally self-assembled

Table 1 Sample compositions and results obtained by DLS for L_2 internal phase

Composition	C_{TM} (wt%)	S (mM)	Dilution	$< R_H >$ (nm)	W (%)
DU:TC 50:50	0.5	0	10000	100.6	28.5
DU:TC 50:50	1	0	10000	112.4	24.9
DU:TC 50:50	2	0	10000	96.1	30.7
DU:TC 50:50	2	0	20000	97.3	34.2
DU:TC 50:50	5	0	10000	90.5	37.5
DU:TC 50:50	5	0	20000	88.4	41.4
PT:TC 50:50	0.5	0	10000	139.5	40.2
PT:TC 50:50	1	0	10000	285.9	45.6
PT:TC 50:50	2	0	10000	202.8	54.6
PT:TC 50:50	5	0	20000	239.6	57.6
DU:TC 50:50	0.5	1	10000	129.7	27.4
DU:TC 50:50	1	1	10000	120.3	27.0
DU:TC 50:50	2	1	10000	98.7	27.3
DU:TC 50:50	5	1	10000	91.2	36.5
PT:TC 50:50	0.5	1	10000	365.8	56.4
PT:TC 50:50	1	1	10000	336.0	54.6
PT:TC 50:50	2	1	10000	297.0	60.4
PT:TC 50:50	5	1	10000	230.0	100
DU:TC 50:50	0.5	10	10000	294.8	41.8
DU:TC 50:50	1	10	10000	254.7	38.6
DU:TC 50:50	2	10	10000	136.6	31.6
DU:TC 50:50	5	10	10000	92.4	41.7
PT:TC 50:50	0.5	10	10000	345.6	48.6
PT:TC 50:50	1	10	10000	313.8	49.5
PT:TC 50:50	2	10	10000	325.0	44.6
PT:TC 50:50	5	10	10000	261.4	55.4

drops (based on both lipids) are able to coalesce to some extent when the electrostatic interactions between the charged stabilizers are screened. From this behavior, it appears fundamental to explore the changes at the local scale, in particular, the behavior of the TM colloids during such a rearrangement and SAXS is the perfectly adapted tool for it. In the Q-range available with the SAXSess apparatus, we know that the signal is composed of three uncorrelated signals [9]: at high Q-values the signal is dominated by the liquid crystalline phase signal, while at intermediate and lower Q-values the signal is given by the TM scattering and the Porod law of the drops. Due to the size of the drops, the last contribution can be considered invariant with the size of the drops and salinity. The intensities corresponding to the scattering from TM depend on their apparent volume fraction, $\phi_{TM}^{app} = \phi_{TM}^{ads} + \phi_{TM}^{free}$. Below $C_{TM} \approx 1.5wt\%$, we have demonstrated that all the particles are found at the interface, while above there is a fraction free in bulk [9]. The SAXS data on the PT:TC (50:50) with 0.5 and $2wt$ % in brine are displayed in Figure 1. Remarkably, there is no change in the scattering curves for the two concentrations. This first indicates that the drop coalescence under the addition of salt has no effect on the internal phase. Interestingly, the data also demonstrate that whatever the TM concentration regime (all TM at interfaces or some also in bulk), ϕ_{TM}^{app} does not change during the process of coalescence. This thus means that no TM are removed from the interfaces or additionally included during the coalescence process. Following this, the number of TM per drop, N_P, varies with the addition of salt as:

$$N_P \approx A \times [n_D(S)]^{-1} \approx B \times [R_D(S)]^3 \qquad (1)$$

with $n_D(S)$ and $R_D(S)$ the number of drops and the drops' radius, respectively, at the added salt concentration S, and A, B are dimensionless system constants. Whereas, this shows that N_P strongly increases with S, this does not necessarily imply a full coverage of the drops. Indeed, χ, the TM coverage per drop, is:

$$\chi \approx \frac{N_P}{4}\left(\frac{R_{TM}}{R_D(S)}\right)^2 \approx C \times R_D(S) \qquad (2)$$

This translates as a slight increase of χ with S. In fact, the results indicate that $\chi(0)$ is low in any case. Indeed, in the hypothesis of a compact TM armor on the drops (maximum $\chi(0)$), the drop's coalescence with the added salt should lead to a loss of TM at the interfaces since the surface to cover is smaller; this is not the case. This also explains that no additional structural peaks can be observed in the scattering curves when S increases (Figure 1): $\chi(0)$ was small and $\chi(S)$ is still far from corresponding to a dense layer. Of course we worked at a fixed added salt concentration for all TM concentrations. Therefore the added salt could be insufficient to screen the charges in particular for high TM concentrations. This study will be done separately.

However, the effect of added salt at a given TM concentration could depend on the internal phase, as the reorganization after coalescence can depend on the internal phase viscosity. We thus investigated other liquid crystalline phases starting by the $Fd3m$ inverse micellar cubic phase found in the DU:TC (70:30) system, a phase that is not observed for the PT-based system. Interestingly, when increasing the TM stabilizer concentration, the size of $Fd3m$ drops also varies as for the L_2 phase (Table 2). The addition of salt also results in an increase in the size of the drops, but the increase is more pronounced even with just 1 mM of added salt (Table 2) and the samples are completely destabilized at 10 mM. However, the SAXS investigation confirms that the behavior of TM during the coalescence process

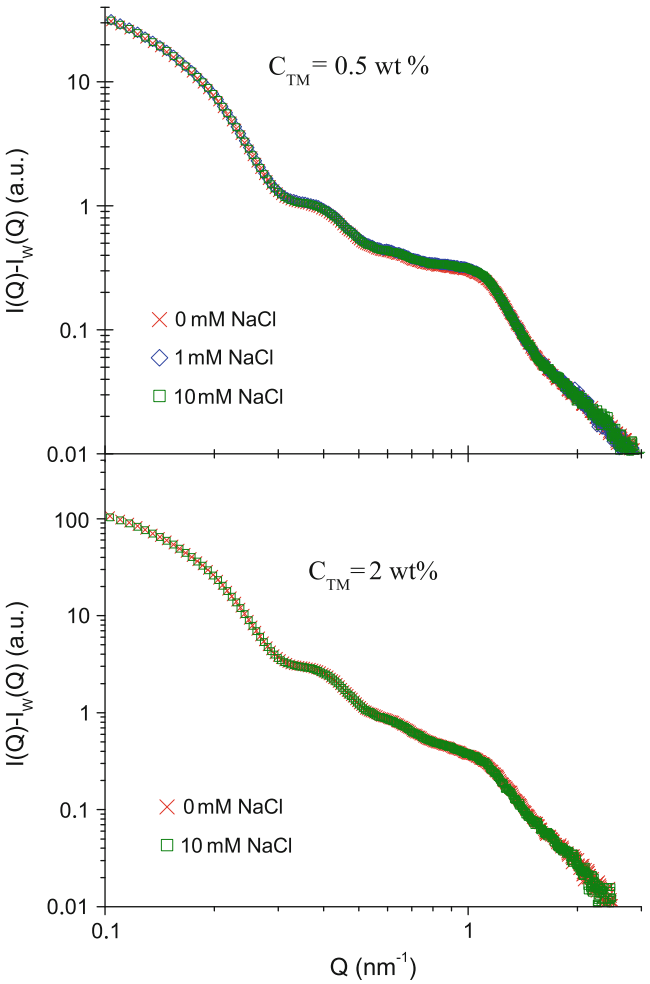

Fig. 1 X-ray scattering curves for PT:TC 50:50 drops stabilized by: $0.5wt\%$ TM with 0 mM, 1 mM, and 10 mM added NaCl (up panel); 2 wt& TM with 0 mM and 10 mM added NaCl (bottom panel). The symbols are displayed in both panels

Table 2 Sample compositions and results obtained by DLS for *Fd3m* and *Pn3m* internal phases

Composition	C_{TM} (wt%)	S (mM)	Dilution	$< R_H >$ (nm)	W (%)
DU:TC 70:30	0.5	0	10000	98.4	35
DU:TC 70:30	1	0	10000	189.5	46
DU:TC 70:30	2	0	10000	98	36.2
DU:TC 70:30	5	0	10000	94	40
DU:TC 70:30	0.5	1	10000	244.2	41.7
PT:TC 100:0	0.5	0	10000	140.0	58.3
PT:TC 100:0	1	0	10000	142.3	54.2

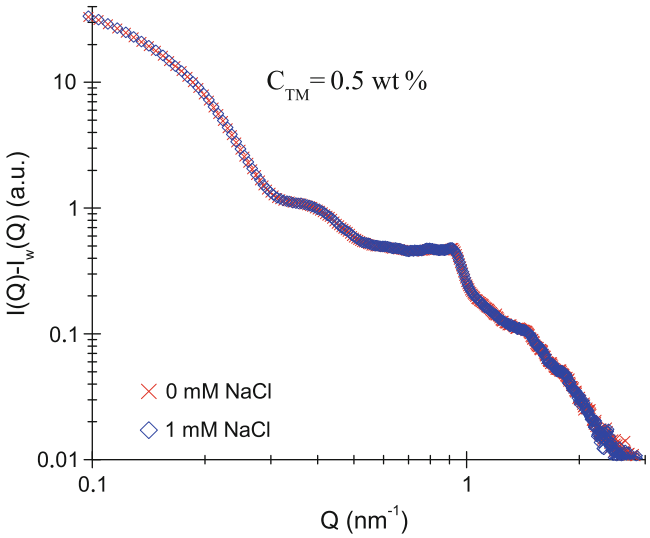

Fig. 2 X-ray scattering curves for DU:TC 70:30 drops stabilized by 0.5*wt%* TM with 0 mM and 1 mM added NaCl. The symbols are displayed in the Figure

is similar to the L_2 phase (Figure 2), since ϕ_{TM}^{app} does not change. These results indicate that the equilibrium obtained, which originates from the balance between Coulombic repulsion due to the TM, the contact angle and the viscosity of the bulk phase, is more unstable. A small charge screening induces a stronger drop coalescence leading to a faster destabilization of the domains than in the L_2-based systems. For *Pn3m* double diamond cubic phase (100:0), any rearrangement of the drops would be very slow and probably would not have time to occur during the time-scale of the experiment due to their high viscosity. An indication of such behavior is shown in Table 2, where the size of the PT-based cubosomes does not change with changing TM concentration. This implies that the contact angle is very small, and the TM stabilization process is thus more related to absorption onto solid surfaces than on fluid interfaces. This suggests that the adsorption is now reversible because TM are less tightly bound. This in turn would imply that even small amounts of added salt should destabilize the drops, which indeed is experimentally the case for both phases. The colloids are removed from the interfaces due to the screening of the electrostatic interactions. Interestingly, we remind that it is not possible to obtain a DU:TC *Pn3m* phase with the TM in contrast to a PT:TC *Pn3m* phase. This means that there are also lipid-specific interactions between TM and the lipid head, which are dominant because of the low contact angle of TM with the surface. Further experiments are in progress to confirm this stabilization process.

Conclusions

We reported on the salt-induced behavior of internally self-assembled nanodrops stabilized in water by charged sphere-like colloids. Two fundamental regimes of stabilization have been evidenced. For liquid crystalline phases with low viscosity, the adsorption of the stabilizers is irreversible and the stabilization process corresponds to the adsorption of colloids at an oil/water interface with a balance between Coulombic repulsion, the contact angle and the viscosity of the bulk phase. For liquid crystalline phases with high viscosity, the stabilization process is related to the adsorption of colloids to solid surfaces. The adsorption of the stabilizers is reversible and the specific interactions between the colloids and the lipid becomes central. Further experiments should be done to confirm such results by means of SANS with contrast matching conditions. The effects of salt would surely be different using another geometry for the colloidal stabilizers, and would help to answer further questions on the interactions between colloids and lipids, and the stabilization of liquid crystalline phases.

References

1. Larsson K.J., Colloidal dispersions of ordered lipid-water phases, Journal of Dispersion Science and Technology, 20, 27-34 (1999)
2. Mezzenga R., Schurtenberger P., Burbridge A., Michel M., Understanding foods as soft materials, Nature Materials, 4, 729-740 (2005)
3. Chang C.M., Bodmeier R.J., Effect of dissolution media and additives on the drug release from cubic phase delivery systems, Journal of Controlled Release, 46, 215-222 (1997)
4. Yaghmur A., Glatter O., Characterization and potential applications of nanostructured aqueous dispersions, Advances in Colloid and Interface Science, 147-48, 333-342 (2009)
5. Lee W.B., Mezzenga R., Fredrickson G.H., Anomalous phase sequences in lyotropic liquid crystals, Physical Review Letters, 99, 187801 (2007)
6. (a) Ramsden W., Proceedings of the Royal Society (London) B 72, 156-164 (1903); (b) Pickering S.U., Emulsions, Journal of the Chemical Society 91, 2001-2021 (1907).
7. Salonen A., Muller F., Glatter O., Dispersions of internally liquid crystalline systems stabilized by charged disklike particles as pickering emulsions: Basic properties and time-resolved behavior, Langmuir, 24, 5306-5314 (2008)

8. (a) Muller F., Salonen A., Glatter O., Phase behavior of Phytantriol/water bicontinuous cubic Pn3m cubosomes stabilized by Laponite disc-like particles, Journal of Colloid and Interface Science, 342, 392-398 (2010) (b) Muller F., Salonen A., Glatter O., Monoglyceride-based cubosomes stabilized by Laponite: Separating the effects of stabilizer, pH and temperature, Colloids and Surfaces A, 358, 50-56 (2010)
9. Salonen A., Muller F., Glatter O., Internally self-assembled submicrometer emulsions stabilized by spherical nanocolloids: finding the free nanoparticles in the aqueous continuous phase, Langmuir, 26, 7981-7987 (2010)

Progr Colloid Polym Sci (2011) 138:33–38
DOI: 10.1007/978-3-642-19038-4_6

Distribution of Tert-Butylhydroquinone in a Corn Oil/$C_{12}E_6$/Water Based Emulsion. Application of the Pseudophase Kinetic Model

María-José Pastoriza-Gallego[1], Verónica Sánchez-Paz[2], Laurence S. Romsted[3], and Carlos Bravo-Díaz[2]

Abstract We have determined the distribution of the antioxidant tert-butylhydroquinone, TBHQ, between the oil and interfacial regions of an emulsion composed of stripped corn oil, acidic water and hexaethyleneglycol monododecyl ether, $C_{12}E_6$, by employing a kinetic method based on the reaction between the hydrophobic 16-hexadecylbenzenediazonium ions, 16-ArN_2^+, and TBHQ. The kinetic data are interpreted under the light of the pseudophase kinetic model and provide estimates of the partition constant, and hence the distribution, of TBHQ between the oil and the interfacial region of the emulsion. Our results show that more than 80% of TBHQ is located in the interfacial region even at low emulsifier volume fractions, and the fraction of TBHQ in that region increases upon increasing [$C_{12}E_6$].

Introduction

A large number of food products consist of a lipid phase dispersed in an aqueous medium and therefore can be described as oil-in-water (o/w) emulsions[1-5]. Emulsions form the basis for many kinds of traditional foods, e.g., milk, cream, beverages, dressings, dips, sauces, batters and deserts[1, 5, 6]. They are increasingly being used in nutritional beverages designed to deliver nutrients to infants, elderly, athletes, or the sick and this increase corresponds to a huge demand for easy-to-use tasty products with a long shelf-life that also fit nutritional recommendations such as decrease the total fat content and increase amounts of omega-3 fatty acids[1, 7, 8].

However, before reaching the consumer, food emulsions undergo a variety of processes including chemical reactions such as denaturation, polymerization of protein, interface aging and lipid oxidation[2, 9]. The latter has an appreciable influence on the technological, sensory and nutritional qualities of the products[3, 9, 10].

Lipid peroxidation first targets unsaturated lipids and can take place under a range of environmental conditions, provided oxygen is present[11]. It induces many side effects generally considered to be detrimental to product quality, giving rise to undesirable off-flavors and potentially toxic compounds directly derived from fatty acid degradation[9, 12-15]. All these observations prompt renewed interest in a better understanding of lipid oxidation in emulsified systems to optimize our ability to prolong their shelf life as much as possible and enhance their quality by employing, for instance, natural antioxidant instead of synthetic ones[9, 15, 16].

Establishing reliable criteria for selecting the most efficient antioxidant, AO, for a particular application is a major unsolved problem in food emulsions and dispersions[5-7] and one of general importance in nutrition and health. Recent reviews[5,10,11] point to multiple factors that affect activities of antioxidants including: the properties and reactions of the antioxidant and the polyunsaturated lipids being oxidized; the locations or distributions of the antioxidant within emulsified food; the effect of other components on antioxidant activity; and the relevance of the model system to real food. Frankel and Meyer's summarized the antioxidant distribution problem highlighthing the crucial role of the antioxidant distribution into emulsifier-rich interfacial layers in heterophasic food emulsions[9, 17].

Component partitioning between two immiscible phases is traditionally characterized by partition constants using a variety of experimental methods[18, 19]. The Hansch octanol-water partition constant, P_W^O, is probably the most widely accepted physicochemical property used to characterize the polarity of compounds[20, 21] and it is also a widely used

M.-J. Pastoriza-Gallego (✉)
[1]Universidad de Vigo, Facultad de Ciencias del Mar, Dpto. Física-Aplicada, 36310 Vigo, Spain
C. Bravo-Díaz (✉)
[2]Universidad de Vigo, Facultad de Química, Dpto. Química Física, 36310 Vigo, Spain
e-mail: cbravo@uvigo.es
[3]Chemistry Dpt., Rutgers, The State University of New Jersey, New Brunswick, NJ 08903 USA

descriptor for quantitative structure-activity relationships, QSAR, studies in biphasic systems. The partition constant, P_W^O, is defined by a unitless concentration ratio of the AO or other component in each phase, equation 1, where V_O, V_W and n_O, n_W are the volumes of each phase and the moles of AO present in the oil (O) and water (W) phases, respectively.

$$P_W^O = \frac{n_O/V_O}{n_W/V_W} = \frac{(AO_O)}{(AO_W)} \quad (1)$$

Determining the partition constants of AOs and their chemical reactivities in surfactant based emulsions is more complex because the emulsifier creates a new region in solution, the interfacial region at the interface of the oil and water regions and both AOs and other reactive components distribute between and react with each other in all three regions[5, 22, 23]. In general, two partition constants are needed to describe the distribution of an AO or other components in an emulsion composed of oil, interfacial and water regions, Scheme 1, one between the oil-interfacial regions, P_O^I, and the other between the aqueous-interfacial regions, P_W^I[24-27].

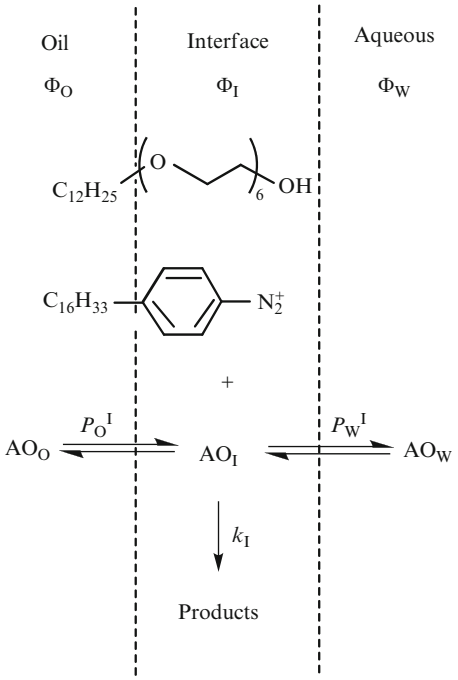

Scheme 1 Basic two-dimensional plot showing the interfacial region of an emulsion based on the pseudophase model illustrating the partitioning of an antioxidant, AO, between the oil, O, interfacial, I, and aqueous, W, regions. Φ indicates the volume fraction of a region, P is the partition constant, and k_I is the rate constant for reaction between 16-ArN_2^+ (see scheme 2 for 16-ArN_2^+ structure) and the AO in the interfacial region

The interfacial region cannot be physically separated from the other two regions, which means that traditional methods for determining component partition constants in a true two-phase system cannot be used and hence P_O^I and P_W^I can not be measured independently by isolating and analyzing the concentration of an AO in each region. Thus, determining AO or other component distributions in emulsions requires determining partition constants within the emulsion itself.

During the last years we have developed a kinetic method for determining values of P_O^I and P_W^I of AOs in emulsions [25-28] based on the reaction of a hydrophobic arenediazonium ion, 4-hexadecylbenzenediazonium, 16-ArN_2^+, with an antioxidant, Scheme 1. The theoretical interpretation of the experimental results is grounded on the pseudophase model[9, 15, 17, 29-31], and provides both P_O^I and P_W^I and also the second order interfacial rate constant, k_I. Once the partition constants are known, determining the antioxidant distribution is straightforward. Here, we have applied our kinetic methodology to determining the distribution of tert-butylhydroquinone in a corn oil based emulsion prepared by employing hexaethylene glycol monododecyl ether, $C_{12}E_6$, as emulsifier.

Experimental

Materials. Tert-butylhydroquinone (Sigma), hexaethyleneglycol monododecyl ether $C_{12}E_6$ (Fluka, 98%) and stripped corn oil (Acros Organics) were of the highest purity available and used as received. Hydrochloric acid, HCl, was from Riedel de Haën (37%) and its concentration was determined by potentiometric titration. All solutions were prepared with Milli-Q grade water. 16-ArN_2BF_4 was prepared in high yield and purity from commercial 4-hexadecylaniline (Aldrich, 97%) by diazotization following a published method[32, 33].

Emulsion preparation. Emulsions of 1:1 and 1:4 corn oil to water volume ratios were prepared as indicated elsewhere [25, 26, 28] by mixing together the appropriate amounts of aqueous 3 mM HCl and corn oil (total volume = 10 mL) and a weighed amount of $C_{12}E_6$. The volume fraction of surfactant, Φ_I, was varied from 0.005 to 0.03. A single aqueous stock solution of 3 mM HCl (pH = 2.5) was prepared by diluting concentrated reagent grade HCl.

Determining Observed Rate Constants, k_{obs}, in Emulsified Systems. The concentration of unreacted 16-ArN_2^+ is determined by adding an aliquot of an emulsion containing 16-ArN_2^+ and TBHQ to an ethanolic solution of the coupling agent *N*-(1-naphthyl)ethylenediamine, NED, Scheme 2. The

final mixture is homogeneous and optically transparent permitting direct spectrometric measurement of the azo dye absorbance.

Figure 1A shows the spectrum of the azo dye product. Two main absorption bands are observed at 436 nm and 572 nm. We used the band centered at $\lambda = 572$ nm because of its higher extinction coefficient and because the calibration curves of absorbance of the azo dye *vs* [16-ArN_2^+] are linear and independent of the surfactant volume fraction employed to prepare the emulsion, Figure 1B. Other components in the final mixture are colorless and do not interfere. Experimental conditions were optimized so that the coupling reaction is much faster than that of 16-ArN_2^+ with TBHQ. By monitoring azo dye formation spectrophotometrically at $\lambda = 572$ nm, we estimated values of $t_{1/2} < 10$ s for the coupling reaction when employing [NED] > 0.01 M.

In a typical experiment, a freshly prepared emulsion (10 mL) is placed in a continuously stirred, water-jacketed cell (T = 25 °C). An aliquot (80 μL) of a 0.37 M stock solution of TBHQ is added to the emulsion and the mixture is thermostated for at least 15 min. Independently, 25 numbered and stoppered test tubes are placed in a thermostated bath (T = 25 °C), 2.5 mL of a 0.01 M ethanolic solution of NED are added to each test tube and temperature equilibrated for at least 20 min.

The reaction between TBHQ and 16-ArN_2^+ is initiated by adding an aliquot (20 μL) of a 0.17 M stock 16-ArN_2^+ solution in acetonitrile to the emulsion. Aliquots (200 μL) of the reaction mixture are removed at specific time intervals and added immediately to test tubes to initiate azo dye formation between NED and unreacted 16-ArN_2^+. Final concentrations of NED were at least 10 times higher than those of 16-ArN_2^+ to ensure that all 16-ArN_2^+ is consumed. Under such conditions, 16-ArN_2^+ reacts with NED much more rapidly than with TBHQ (see above) and the azo dye absorbance is proportional to the concentration of unreacted 16-ArN_2^+. Figure 2 shows a representative example of the variation of azo dye absorbance with time and the ln plot used to calculate k_{obs}. Duplicate or triplicate experiments gave k_{obs} values within 9%.

The time scale for corn oil oxidation at room temperature and in the absence of pro-oxidant substances is in the order of days[34, 35], hence much larger than that for the reaction between ArN_2^+ and TBHQ, Figure 1. Consequently, oil peroxidation should not be competitive under our experimental conditions and thus we can safely consider the

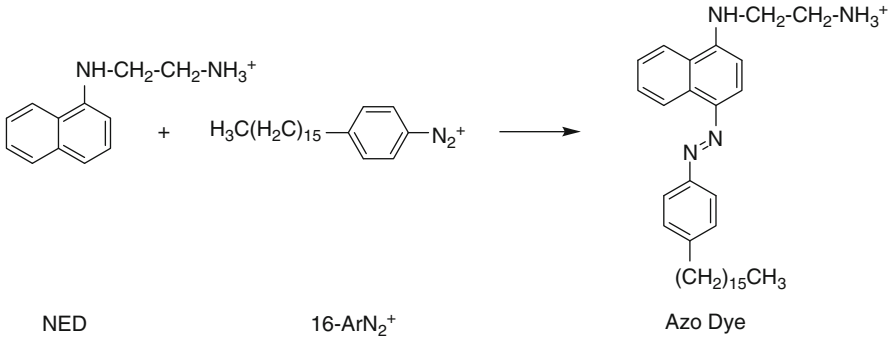

Scheme 2 Derivatization reaction of 16-ArN_2^+ with NED to give a stable azo dye

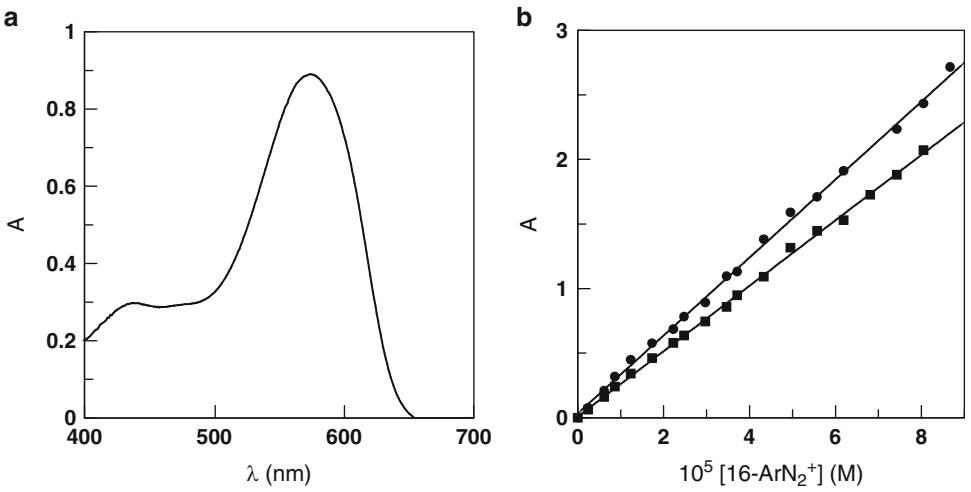

Fig. 1 (**a**) Absorption spectrum of the azo dye product from reaction of 16-ArN_2^+ with NED, Scheme 2, formed in a ethanolic solution. [16-ArN_2^+] = 3.3×10^{-4} M, T = 25 °C. (**b**) Plot of azo dye absorbance, A, versus [16-ArN_2^+] at two surfactant concentrations. 16-ArN_2^+ was dissolved in a continuously stirred 1:1 corn oil/$C_{12}E_6$/water ([HCl] = 3.2 mM) in the absence of TBHQ, and aliquots (200 μL) of the emulsion were added to 2.5 mL of a 0.01 M ethanolic solution of NED. T = 25 °C

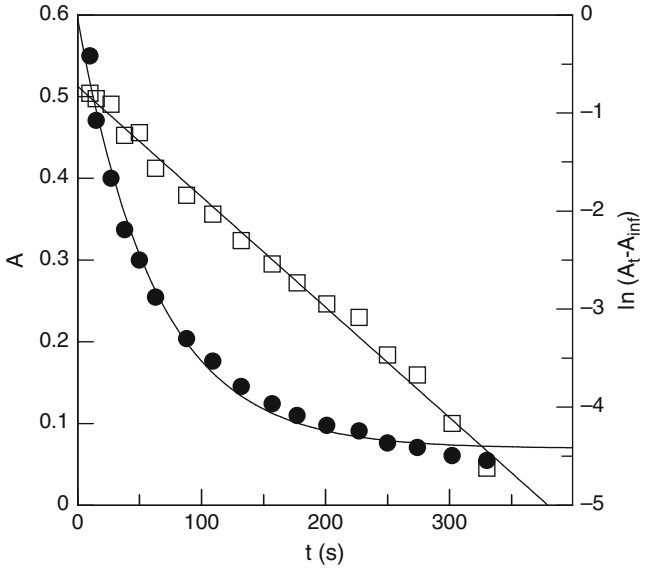

Fig. 2 Example of the determination of k_{obs} by employing the derivatization method for the reaction of 16-ArN_2^+ with TBHQ in a 1: 1 corn oil/$C_{12}E_6$/water ([HCl] = 3.2 mM) showing the variation of the absorbance of the azo dye with time and the corresponding ln plot. [16-ArN_2^+] = 3.3x10^{-4} M, [TBHQ] = 4.0x10^{-3} M, T = 25 °C

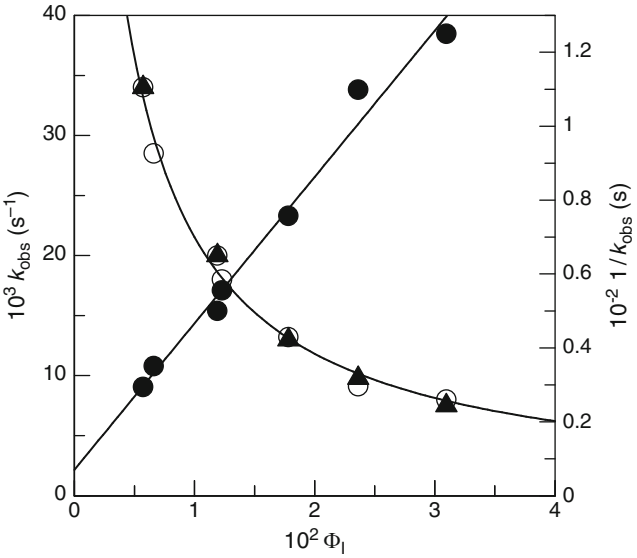

Fig. 3 Variation of k_{obs} with the volume fraction Φ_I in emulsions of 1:1 (○) and 1:4 (▲) emulsions determined by the derivatization method and the variation of 1/ k_{obs} with Φ_I according to equation 4 (data points for the 1:1 and 1:4 emulsions are displayed all together)

amount of TBHQ in the system equal to its stoichiometric concentration and it remains practically constant throughout the course of the reaction between ArN_2^+ and TBHQ.

Results and Discussion

Figure 3 shows the variation of k_{obs} with the $C_{12}E_6$ volume fraction Φ_I in emulsions of 1:1 and 1:4 oil to water ratios, illustrating that the k_{obs} values are basically independent of the oil to water ratio employed to prepare the emulsion. Its values decrease asymptotically by a factor of ~3 with increasing Φ_I at constant [TBHQ] and Φ_O /Φ_W ratio.

For a bimolecular reaction in an emulsion, Scheme 1, the observed rate is the sum of the rates in each region of the macroemulsion[36-38]. Because 16-ArN_2BF_4 is, itself, a water- and oil-insoluble ionic surfactant, we assume that it is located only in the interfacial region of the emulsions with negligible concentrations in the oil and water regions. [26, 28] Hence, k_{obs} values depend only on the rate constant and concentrations of 16-ArN_2^+ and the AO in the interfacial region:

$$k_{obs}[16-ArN_2{}^+{}_T] = k_2[16-ArN_2{}^+{}_T][TBHQ_T] = k_I(16-ArN_2{}^+{}_I)(TBHQ_I)\Phi_I \quad (2)$$

where k_2 and k_I are, respectively, the observed second-order rate constant and the second-order rate constant in the interfacial region; square brackets, [ ], denote the concentration in moles per liter of total emulsion volume; parentheses, (), indicate concentration in moles per liter of the volume of a particular region; subscript T stands for the stoichiometric or total concentration; the subscript I indicates the interfacial region, respectively; and Φ_I is the volume fraction of the interfacial region, defined as $\Phi_I = V_I/(V_I + V_O + V_W)$, which is assumed to be equal to the surfactant volume fraction[26-27].

Reactions are run under pseudo first order conditions, i.e., $[TBHQ_T] >> [16\text{-}ArN_2{}^+{}_T]$, and because 16-$ArN_2^+$ is insoluble both in water and oil because of has hexadecyl tail (C_{16}) and a cationic headgroup,[39], the reaction between 16-ArN_2^+ and the antioxidant takes place exclusively in the interfacial region of emulsions, Scheme 1.

For antioxidants such as TBHQ, which is basically insoluble in water as demonstrated by auxiliary experiments (not shown) and because the solubility of hydroquinone in water is very low[40], a simplification can be made by considering that its concentration in the aqueous region of the emulsion is effectively zero, i.e., TBHQ is only distributed between the water and the interfacial regions, Scheme 1, and the rate expression for k_{obs} given by equation 3 can be obtained. Further details on the derivatization of equation 3 are given elsewhere[26-27].

$$k_{obs} = \frac{k_I[TBHQ_T]P_O^I}{\Phi_O + P_O^I\Phi_I} \quad (3)$$

where Φ_O is the oil volume fraction (defined in a similar way as the interfacial volume fraction) and $P_O{}^I$ = $(TBHQ_I)$/

($TBHQ_O$) is the partition constant between the interfacial and oil regions. Equation 3 predicts that: (a) k_{obs} decreases with increasing Φ_I because k_I is a constant and $[AO_T]$ and Φ_O are constant in any one kinetics experiment; and (b) addition of surfactant increases Φ_I, which increases the value of the denominator and reduces the value of k_{obs}. Equation 4 is the reciprocal form of equation 3, and shows that plots of $1/k_{obs}$ versus Φ_I should be linear as illustrated in Figure 3 with positive intercepts from where the values for k_I and P_O^I can be obtained from the slope and intercept, respectively.

$$\frac{1}{k_{obs}} = \frac{\Phi_O}{k_I[AO_T]P_O^I} + \frac{1}{k_I[AO_T]}\Phi_I \tag{4}$$

Once the partition constant is obtained, the percentage of TBHQ in the oil ($TBHQ_O$), and interfacial (TOC_I) regions of the emulsion can be calculated bearing in mind that the percentages of TBHQ in the interfacial and oil regions are given by equations 5 and 6, respectively.

$$\%TBHQ_I = \frac{100[TBHQ_I]}{[TBHQ_T]} \tag{5}$$

$$\%TBHQ_O = \frac{100[TBHQ_O]}{[TBHQ_T]} \tag{6}$$

Bearing in mind that $[TBHQ_I] = (TBHQ_I)\Phi_I$, $[TBHQ_O] = (TBHQ_O)\Phi_O$, and that $[TBHQ_T] = (TBHQ_I)\Phi_I + (TBHQ_O)\Phi_O$, then the percentage of TBHQ in each region is given by equations 7 and 8.

$$\%TBHQ_I = \frac{100\Phi_I P_O^I}{\Phi_I P_O^I + \Phi_O} \tag{7}$$

$$\%TBHQ_O = \frac{100\Phi_O}{\Phi_I P_O^I + \Phi_O} \tag{8}$$

The variation of the percentage of TBHQ in each region with the surfactant volume fraction Φ_I is illustrated in Figure 4.

$TBHQ_I$ increases from about 80% (emulsion 1:1) to ~95% over the surfactant volume fraction range used for $C_{12}E_6$. Added surfactant increases the interfacial to oil volume ratio and a progressively larger fraction of TBHQ dissolves in the interfacial region, showing that antioxidant distribution depends strongly on the emulsifier concentration. This is in keeping with literature results indicating that one of the main variables controlling the antioxidant distribution is the surfactant volume fraction.[28] Moreover, this strong association with the interfacial region is consistent with results of other water insoluble antioxidants such as tocopherol. It may be worth noting that the interfacial region of the emulsion is a mixed solvent composed of water, polyoxyethylene groups and hydrocarbon in which polar organic molecules are more soluble than they are in the oil.

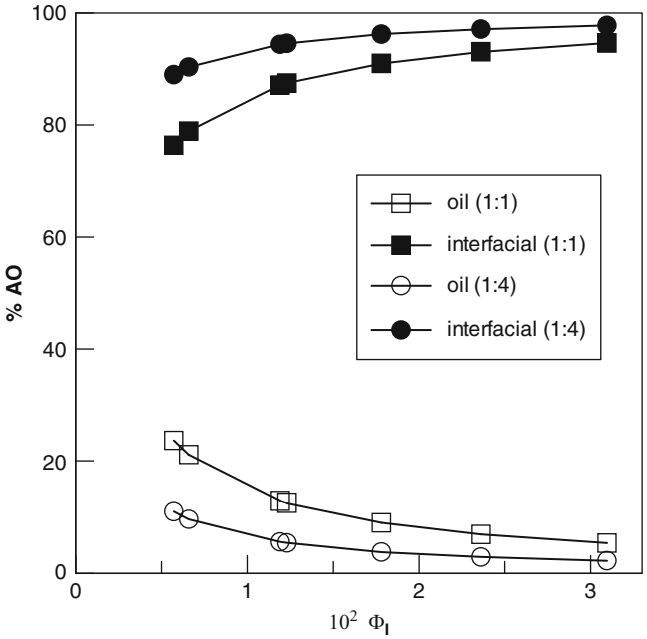

Fig. 4 Distribution of TBHQ in 1:1 and 1:4 corn oil/$C_{12}E_6$/water emulsions as a function of the surfactant volume fraction Φ_I

Finally, the rate constant for reaction in the interfacial region, k_I, between 16-ArN_2^+ and TBHQ, Scheme 1, can be determined by using equation 4 and the estimated P_O^I value, $k_I = 0.063\ M^{-1}\ s^{-1}$. No similar values have been reported up to date for this antioxidant and emulsion, hence no reliable comparisons of the k_I values can be made. Determining k_I values should help to lay the basis for a scale of antioxidant activity that is independent of the antioxidant distribution in the emulsion.

Final Remarks

The determination of distributions of antioxidants in emulsified foods is an unsolved problem in food science and its knowledge is crucial to evaluate their efficiencies at inhibiting peroxidation of unsaturated fats and oils[9].

AOs and, in general, polar solutes distribute between the oil, interfacial and water regions of the emulsion [9, 41, 42], but little is known about the fraction of AO in each region. A number of attempts have been made to measure AO distributions in emulsions, primarily by separating the phases and analyzing the AO concentration in each phase. The distribution of AOs between two inmiscible phases, e.g., oil and water, $P_W^O = [AO_{oil}] / [AO_{water}]$, depends on the chemical structure of the antioxidant and, to a first approximation, on its polarity. However, determining P_W^O does not provide information on the fraction of an AO in the interfacial

region, or surfactant layer, Scheme 1, because this layer cannot be physically isolated and analyzed separately from the oil and water phases.

The work reported here illustrates the application of the new approach we have developed for estimating AO distributions in opaque, well-mixed, fluid macroemulsions to determining the distribution of one of the most employed antioxidants, TBHQ, in a food-grade emulsion. The interpretation of the experimental results is grounded on the pseudophase model for thermodynamically stable microemulsions and is, in principle, applicable to any polar or nonpolar organic solute that reacts with a probe molecule located in the interfacial region of an emulsion.

The results obtained show that we can separate the contributions of substrate concentration and its intrinsic reactivity in the interfacial region to k_{obs} and estimate the distribution of the antioxidants between the different regions of the macroemulsion. The results show that, even at the lowest emulsifier concentrations employed, a large proportion of TBHQ is located in the interfacial region of the macroemulsions, and its percentage increases on increasing the emulsifier concentration.

Given that most of antioxidants bear –OH groups in their chemical structures, the distribution of antioxidants is expected to depend on a number of parameters including its chemical structure, HLB, the acidity of the solution, temperature, etc. The effects of these and other parameters such as oil polarity, emulsifier HLB, etc. on antioxidant distributions are being investigated and will be part of future communications.

Acknowledgement Financial support from the following institutions is acknowledged: Ministerio de Educación y Ciencia (CTQ2006-13969-BQU), Xunta de Galicia (PGDIT06PXIB314249PR), FEDER and Universidad de Vigo. V. S-P thanks M.E.C. for a FPU grant.

References

[1] D. J. McClements, Food Emulsions, CRC Press, Boca Raton, USA, Vol. 2005.
[2] D. L. Madhavi, N. R. Deshpande, and D. K. Salunkhe, Food Antioxidants, Technological, Toxicological and Health Perspectives, Marcel Dekker, NY, Vol. 1996.
[3] E. Dickinson and D. McClements, Advances in Food Colloids, Vol. Chapman y Hall, London, 1996.
[4] Withehurst, Emulsifiers in Food Technology, Blackwell Publishing, UK., Vol. 2004.
[5] S. E. Friberg and K. Larsson, Food Emulsions, Vol. Marcel Dekker, NY, 1997.
[6] O. R. Fennema, Food Chemistry, 4rd ed. CRC Press;, Vol. 2007.
[7] D. H. Watson, Food Chemical Safety, CRC Press, Cambridge (Woodhead), UK, Vol. 2002.
[8] M. Juárez, A. Olano, and F. Morais, Alimentos Funcionales, FECYT, Madrid, Spain, Vol. 2005.
[9] E. N. Frankel, Lipid Oxidation, Vol. The Oily Press, PJ Barnes & Associates, Bridgwater, England, 2005.
[10] C. Jacobsen, Fett/Lipid, 101,(1999), 484
[11] C. Genot, A. Meynier, and A. Riaublanc, Lipid Oxidation in Emulsions, in "Lipid Oxidation Pathways", Afaf Kalman-Eldin, Ed. AOC Press, USA, Vol. 1999.
[12] A. J. St. Angelo, Crit. Rev. Food Sci. Nutr., 36,(1996), 175
[13] K. Yagi, Chem. Phys. Lipid, 45,(1987), 337
[14] G. O. Adegoke, M. Kumar, M. Vijay, A. G. Krishna, M. C. Vadaraj, K. Sambaiah, and B. R. Lokesh, J. food Sci. Technol., 35,(1998), 283
[15] E. N. Frankel, Food Chem., 57,(1996), 51-55
[16] S. M. Barlow, Toxicological Aspects of antioxidants used as Food Additives, in "Food Antioxidants", Hudson, B.J. F., Ed., Vol. Elsevier, London, 1990.
[17] E. N. Frankel and A. S. Meyer, J. Sci. Food Agric., 80,(2000), 1925-1941
[18] N. C. Santos, M. Prieto, and M. A. R. B. Castanho, Biochi. Biophys. Acta, 1612,(2003), 123-135
[19] A. Berthod and S. Carda-Bosch, J. Chromatog. A, 1037,(2004), 3-14
[20] A. Leo, C. Hansch, and D. Elkins, Chem. Rev., 71,(1971), 525-616
[21] G. Klopman and H. Zhu, Mini-Reviews in Medicinal Chemistry, 5,(2005), 127-133
[22] P. Binks, Modern Aspects of Emulsion Science, The Royal Society of Chemistry, 1998, Vol.
[23] J. Sjöblom, Encyclopedic Handbook of Emulsion Technology, Vol. Marcel Dekker, NY, 2001.
[24] L. S. Romsted and J. Zhang, J. Agric. Food. Chem., 50,(2002), 3328-3336
[25] K. Gunaseelan, L. S. Romsted, E. González-Romero, and C. Bravo-Díaz, Langmuir, 20,(2004), 3047-3055
[26] K. Gunaseelan, L. S. Romsted, M. J. Pastoriza-Gallego, E. González-Romero, and C. Bravo-Díaz, Adv. Colloid. Interf. Sci., 123-126, (2006), 303-311
[27] V. Sánchez-Paz, M. J. Pastoriza-Gallego, S. Losada-Barreiro, C. Bravo-Diaz, K. Gunaseelan, and L. S. Romsted, J. Colloid. Interface Sci., 320,(2008), 1-8
[28] M. J. Pastoriza-Gallego, V. Sánchez-Paz, S. Losada-Barreiro, C. Bravo-Diaz, K. Gunaseelan, and L. S. Romsted, Langmuir, 25, (2009), 2646-2653
[29] E. N. Frankel, J. Oleo Sci., 50,(2001), 387-391
[30] E. N. Frankel, S. W. Huang, J. Kanner, and J. B. German, J. Agric. Food Chem., 42,(1994), 1054-1059
[31] E. N. Frankel, Lipid Oxidation, Vol. Dundee, The Oily Press, 1998.
[32] M. P. Doyle, Bryker, W.J., J. Org. Chem., 44,(1979), 1572-1574
[33] M. C. Garcia-Meijide, C. Bravo-Diaz, and L. S. Romsted, Int. J. Chem. Kinet., 30,(1998), 31-39
[34] M. Hu, D. J. McClements, and E. A. Decker, J. Agric. Food Chem., 51,(2003), 1696
[35] H. Nakazumi, I. Szele, and H. Zollinger, Tetrahedron Letters, (1981), 3053
[36] R. da Rocha Pereira, D. Zanette, and F. Nome, J. Phys. Chem., 94, (1990), 356-361
[37] L. Garcia-Rio, J. R. Leis, and J. A. Moreira, J. Am. Chem. Soc., 122,(2000), 10325-10334
[38] M. A. Lopez-Quintela, C. Tojo, M. C. Blanco, L. Garcia Rio, and J. R. Leis, Curr. Opinion Colloid Interface Sci., 9,(2004), 264-278
[39] L. S. Romsted, 'Interfacial Compositions of Surfactant Assemblies by Chemical Trapping with Arenediazonium Ions: Method and Applications', in "Reactions and Synthethis in Surfactant Systems", (Ed.: J. Texter), Marcel Dekker, NY, USA, Vol. 2001.
[40] X. Li, Q. Yin, W. Chen, and J. Wang, J. Chem. Eng. Data, 51, (2006), 127
[41] K. Schwarz, E. N. Frankel, and G. J.B., Fett/Lipid, 98,(1996), 115-121
[42] K. Schwarz, S. W. Huang, J. B. German, B. Tiersch, J. Hartmann, and E. N. Frankel, J. Agric. Food. Chem., 48,(2000), 4874-4882

Progr Colloid Polym Sci (2011) 138:39–44
DOI: 10.1007/978-3-642-19038-4_7

Kinetic Studies of Gold Nanoparticles Formation in the Batch and in the Flow Microreactor System

M. Luty-Blocho, K. Pacławski, W. Jaworski, B. Streszewski, and K. Fitzner

Abstract In this study, synthesis of gold nanoparticles (Au NP's) in the batch and flow reacting systems was carried out either in the presence or in the absence of PVA (polyvinyl alcohol) used as stabilizing agent. As the reductant of gold (III) chloride complex ions, the ascorbic acid was used. To determine the rate equation of the reduction process, the kinetic measurments based on spectrophotometry UV-Vis and DLS were carried out. Consequently, the rate equations of gold(III) complex ions reduction and Au NP's formation were determined. To synthesize gold nanoparticles in the flow microreactor system the cartridge with T–type geometry of microchannels was used. Next, to calculate the parameters of the flow which enable precipitation of the gold clusters, obtained kinetic equations were applied. This type of microreactor, as well as different reagents flow rates, gave us the chance to inject Au NP's stabilizer (PVA) at the proper instant of time. It was found that applied method is promising one for the preparation of gold nanoparticles with well defined shape (spheres) and with narrow size distribution (98 % of the Au NP's with diameter ranged from 1 to 3 nm). Morphology of obtained Au NP's was characterized using DLS and TEM.

Keywords Gold nanoparticles • Chemical kinetics • Microreactor system • Stabilization

Introduction

One of the methods used for gold nanoparticles (Au NP's) synthesis is the reduction in solution [1,2]. In this method, formation of Au NP's consists of several steps. In the first step, the redox reaction of gold ions with reducing agent leads to the gold nuclei formation, which further growth results in Au NP's formation. Next, obtained nanoparticles agglomerate to a larger scale, due to the presence of Van der Waals forces [3,4]. To prevent from agglomeration process, the addition of stabilizer, e.g. PVA, into reaction mixture can be applied [5]. However, the injection of stabilizer must be done in the proper instant of time before coagulation step is achieved. It requires the knowledge of the rate of Au particles formation which must be determined experimentally. Then, knowing the kinetics of such a process it can be possible to inject the stabilizer in the proper moment.

In this work we would like to present our results on the synthesis of Au NP's in the flow microreactor system using the reduction of chloride gold(III) ions with ascorbic acid (H_2Asc). This microsystem, with the connecting T-type channels, gives the chance for stabilizer's (PVA) injection at different stages of the reaction, characterized by time τ. Before this kind of synthesis is accomplished, kinetic studies of chloride gold(III) ions reduction and gold colloid formation were carried out. Time τ was calculated from the rate equation of chloride gold(III) reduction as well as from kinetic of gold colloid formation determined in the batch reactor system. To adjust τ, different flow rates of reagents in microreactor system were applied. Obtained results (size and size distribution of Au NP's) as well as empirically determined rate equations are given in the next chapters.

Experimental

Materials

As Au NP's precursor and reducing agent, 0.15 mM $HAuCl_4$ (p.a., POCh, Poland) aqueous solution (pH = 1, adjusted with HCl) and L-ascorbic acid (H_2Asc) (p.a., Sigma Aldrich, Germany) were used, respectively. As a stabilizing agent,

M. Luty-Blocho (✉)
AGH University of Science and Technology, Faculty of Non-Ferrous Metals, Laboratory of Physical Chemistry and Electrochemistry, 30 Mickiewicza Ave., 30-059, Cracow, Poland
e-mail: mlb@agh.edu.pl

1% aqueous solution of polyvinyl alcohol (PVA) (p.a., Sigma Aldrich, Germany) with M_w = 67000 g/mol was used.

Methods

Kinetic measurements were performed using UV-Vis spectrophometry (Shimadzu U-2501PC, Japan), stopped-flow technique (SX-20 apparatus from Applied Photophysics, UK) working in the range of wavelength 190-900 nm and Dynamic Light Scattering equipment (ALV GmbH, Germany) with the HeNe laser source (632.8 nm). Synthesis of Au NP's was carried out using microreactor system (Syrris, UK), PTFE tube with 0.5 mm diameter. The experimental setup for Au NP's synthesis is shown in the Fig. 1.

Using different flow rates of reagents (precursor and reducing agent), different time of PVA injection into the system was adjusted. All kinetic equations were determined using TcCurve software. Morphology of obtained Au NP's was analyzed using UV-Vis spectrophotometry, DLS apparatus and TEM microscope (JOEL JEM-2010ARP, Philips). Conditions of synthesis are gathered in Table 1.

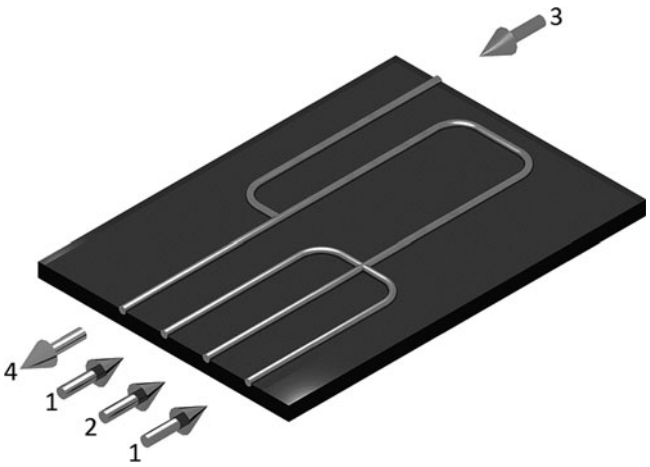

Fig. 1 The scheme of microreactor used for Au NP's synthesis: 1 – input of reducing agent (H_2Asc), 2 – input of Au NP's precursor ($HAuCl_4$), 3 – input of stabilizer (PVA), 4 – output of Au NP's. Diameter of microchannels - 100 μm

Table 1 Experimental conditions under which Au NP's were synthesized:

Initial precursor concentration $C_{0,[AuCl4]^-}$, mM	Molar ratio of reactants $C_{0,[AuCl4]^-} : C_{H2Asc}$	Flow rate, mL/min	Temperature, °C
0.15	1:20 1:50 1:100	0.25, 0.5 1.0, 2.0	25

Results and Discussion

Kinetic Studies in Homogenous System

In order to determine the kinetic equation of gold(III) ions reduction, spectrophotometric studies were carried out. From registered changes in absorption bands of chloride gold(III) complex ions ($[AuCl_4]^-$), which took place after addition of H_2Asc into the system (disappearing of absorbtion peak at 314 nm wavelength), the kinetic curves were obtained for different reductant concentration and temperature. It can be suggested that reaction of the first step of gold(III) reduction is:

$$[AuCl_4]^- + H_2Asc \xrightarrow{k_1} [AuCl_2]^- + H_2Asc(oxidized) \quad (1)$$

where k_1 is the second-order rate constant.

Since the large excess of H_2Asc was applied (at least 20-fold), the concentration of H_2Asc can be considered as a constant during the course of the reaction. Therefore, the differential rate equation for reaction (1) can be described as pseudo-first order equation:

$$\frac{dC_{[AuCl_4]^-}}{dt} = -k_{obs}C_{[AuCl_4]^-} \quad (2)$$

where k_{obs} is observed rate constant and $C_{0,[AuCl_4]^-}$ is initial concentration of precursor.

Taking into account isolation conditions in the studied system, k_{obs} is equal to:

$$k_{obs} = k_1 C_{H_2Asc} \quad (3)$$

Fitting the solution of kinetic equation (2) to the obtained kinetic curves, linear dependence of $\ln(C_{[AuCl_4]^-})$ vs. time is obtained, which suggests the first-order reaction with respect to the gold(III) ions. Derived concentration dependence vs. time is:

$$C_{[AuCl_4]^-}(t) = C_{0,[AuCl_4]^-} \exp(-k_{obs}t) \quad (4)$$

For experimental confirmation of equation (3), the influence of reducing agent concentration on the rate of chloride gold (III) complex ions reduction was measured. Obtained results are shown in Fig. 2.

The straight-line dependence, with the intercept at (0,0) point, strongly suggests the bimolecular mechanism of the studied reaction. From the slope of this dependence the value of the second-order rate constant ($k_1 = 8.583 \times 10^3$ $M^{-1}s^{-1}$) was obtained.

Finally, from Arrhenius Equation and Eyring Equation plots (Fig. 3), activation parameters, e.g. energy (E_A), enthalpy (ΔH^*) and entropy (ΔS^*) of activation, were calculated. Values of these parameters are gathered in Table 2:

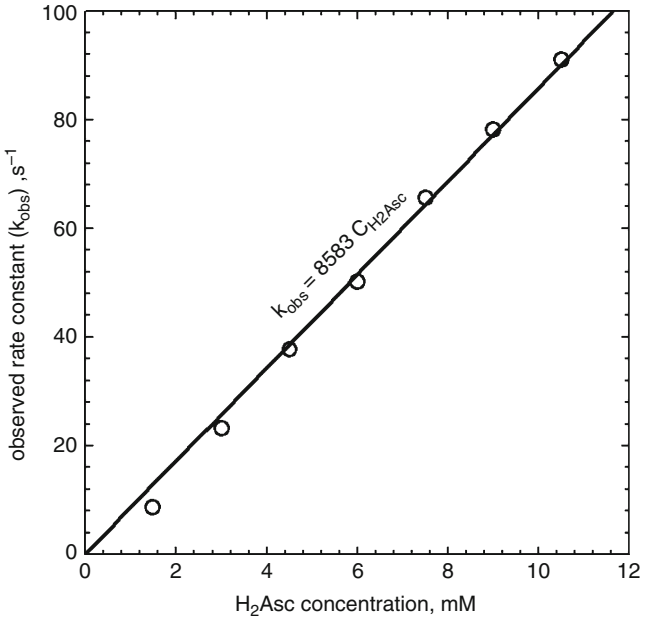

Fig. 2 Observed rate constant (k_{obs}) for chloride gold(III) complex ions reduction reaction as a function of reductant (H_2Asc) concentration. Conditions: $C_{0,[AuCl4]^-}$ = 0.15 mM, temp. = 25°C

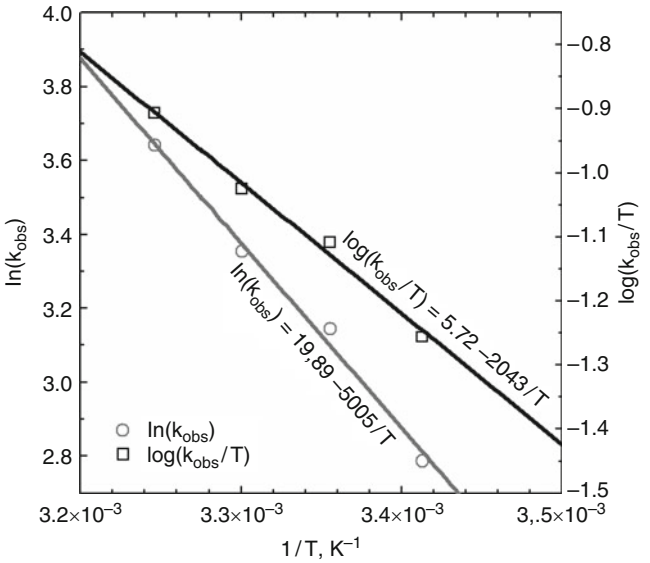

Fig. 3 Arrhenius ($\ln(k_{obs})$ vs. $1/T$) and Eyring ($\log(k_{obs}/T)$ vs. $1/T$) relationships for the reaction of chloride gold(III) complex ions with ascorbic acid (H_2Asc). Conditions: $C_{0,[AuCl4]^-}$ = 0.15 mM, $C_{0,H2Asc}$ = 3 mM

Combining Arrhenius equation with Eq. (4), the final form of the rate equation as a function of temperature (T) can be given as:

$$C_{[AuCl_4]^-} = C_{0,[AuCl_4]^-} \exp\left[4.34 \times 10^8 \exp\left(-\frac{5005}{T}\right)t\right] \quad (5)$$

Table 2 Parameters in Arrhenius and Eyring equations determined for reaction of chloride gold(III) complex ions with ascorbic acid in aqueous solution

Arrhenius parameters		Eyring parameters	
A, s^{-1}	E_A, kJ/mol	ΔH^*, kJ/mol	ΔS^*, J/(K·mol)
4.34×10^8	41.62	16.99	-89.26

Kinetics of Au NP's Formation in the Batch Reactor

Intermediate products of gold(III) ions reduction are the gold (I) ions. Their presence in the studied system was demonstrated by the discoloration of the sample. In the last stage of reaction, the reduction of gold(I) to metallic form occurs. Consequently, formation of pink colloid was observed. The presence of plasmon absorption bands with maximum at ca. 550 nm (Fig. 4a) enabled us to measure the kinetics of gold particles formation. Examples of kinetic curves registered spectrophotometrically are shown in Fig. 4b. Sigmoidal shape of these curves suggests that gold particles formation has autocatalytic character, and the process of gold(I) ions reduction can be described as:

$$[AuCl_2]^- + H_2Asc \xrightarrow{k_2} Au + products \quad (6)$$

$$[AuCl_2]^- + H_2Asc + Au \xrightarrow{k_3} 2Au + products \quad (7)$$

According to the Watzky-Finke model [6], the reactions (6) and (7) correspond to slow continuous nucleation, and fast autocatalytic growth of Au NP's surface, respectively. Using this model, integral kinetic equation of Au NP's formation for isolation conditions (excess of reductant) can be derived:

$$C_{Au} = \frac{\frac{k_2}{k_3}\left[\exp\left[(k_2 + k_3 C_{0,[AuCl_2]^-})t\right] - 1\right]}{1 + \frac{k_2}{k_3 C_{0,[AuCl_2]^-}}\exp\left[(k_2 + k_3 C_{0,[AuCl_2]^-})t\right]} \quad (8)$$

The calculated values of k_2 and k_3 for the studied systems are collected in Table 3. It can be noted that obtained values of k_2 and k_3 rate constants increased with reductant concentration.

The changes in Au NP's hydrodynamic radius (R_H) during the process of nucleation and growth were also recorded using DLS method. Obtained results for different H_2Asc concentration are shown in Fig 5. It can be observed that with the increase of reductant concentration, Au NP's exhibit higher hydrodynamic radius. The rate of these changes is in good agreement with registered evolution of plasmon absorption band. This fact strongly suggests that both techniques applied to determine the rate equation of Au NP's formation registered the same process, i.e., nucleation and growth of gold particles.

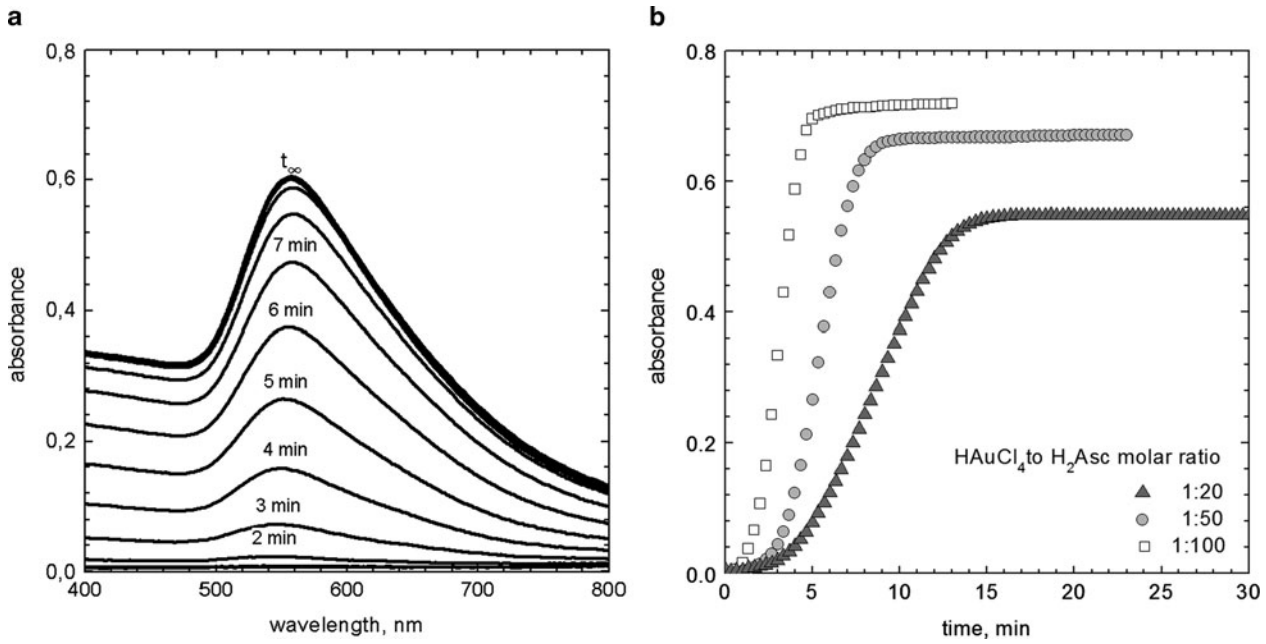

Fig. 4 Time evolution of plasmon absorption band (every 1 min.) during Au NP's formation after reduction of Au(III) complex ions with 50-fold excess of H_2Asc (a). Kinetic curves of Au NP's formation, for different reductant concentration obtained in the batch reactor (b). Conditions: $C_{0,[AuCl4]^-}$= 0.15 mM, temp.= 25°C

Table 3 Values of the rate constants for nucleation and growth of Au particles in aqueous solution during the redox reaction between chloride gold(III) complex ions and ascorbic acid. Temperature 25°C

Molar ratio of reactants $C_{0,[AuCl4]^-}$: C_{H2Asc}	k_2, s^{-1}	$k_3/2$, $M^{-1}\ s^{-1}$
1:20	6.26×10^{-5}	35.47
1:50	4.27×10^{-5}	60.89
1:100	1.08×10^{-4}	100.3

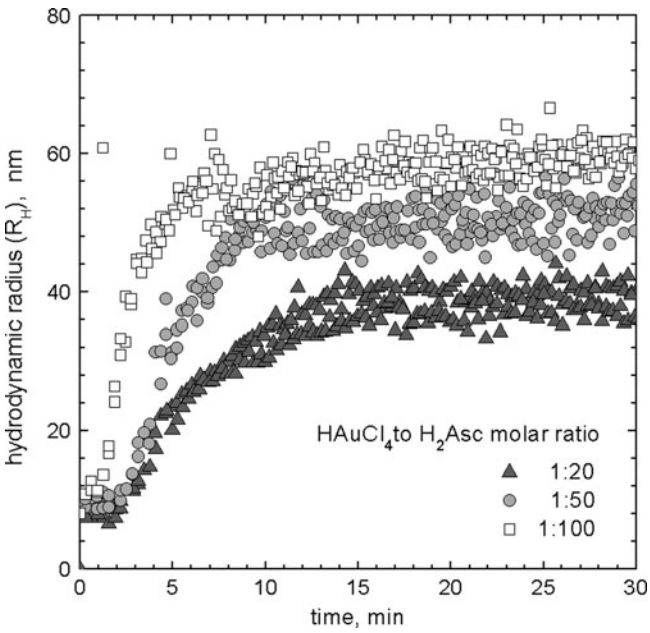

Fig. 5 Kinetic curves of Au NP's formation obtained from DLS studies. Conditions: $C_{0,[AuCl4]^-}$=0.15 mM, temp.= 25^0C

Synthesis of Au NP's in the Flow Microreactor System

Using different flow rates of reactants in microreactor system, the gold colloids were fabricated and stabilized with PVA addition. Next, obtained Au NP's were characterized using UV-Vis spectrophotometry, DLS and TEM. Obtained results are shown in Fig. 6.

It can be observed that for higher flow rate of the reactants (shorter time τ) position of the maximum of plasmon absorption band ($\lambda_{max,Au}$) was shifted to shorter wavelengths, e.g. for the flow rate ranged from 0.50 to 2.00 mL/min, $\lambda_{max,Au}$ was changed from 558 to 538 nm. These results indicate that Au particles become smaller. It is also evident from TEM images (Fig. 6c) that increase of the flow rate of reactants, results in smaller Au particles formation. For example, for the flow rate 2.0 mL/min, the diameter of 98% Au NP's was ranged from 1 to 3 nm.

Summary

1. In the studied system, reduction of gold(III) chloride complex ions in the batch reactor is faster than reduction of gold(I) ions. Under these conditions the Watzky-Finke model was found to be useful to describe kinetic equation of Au NP's formation.
2. The rate equation of the reduction reaction of chloride gold (III) complex ions using ascorbic acid was determined as

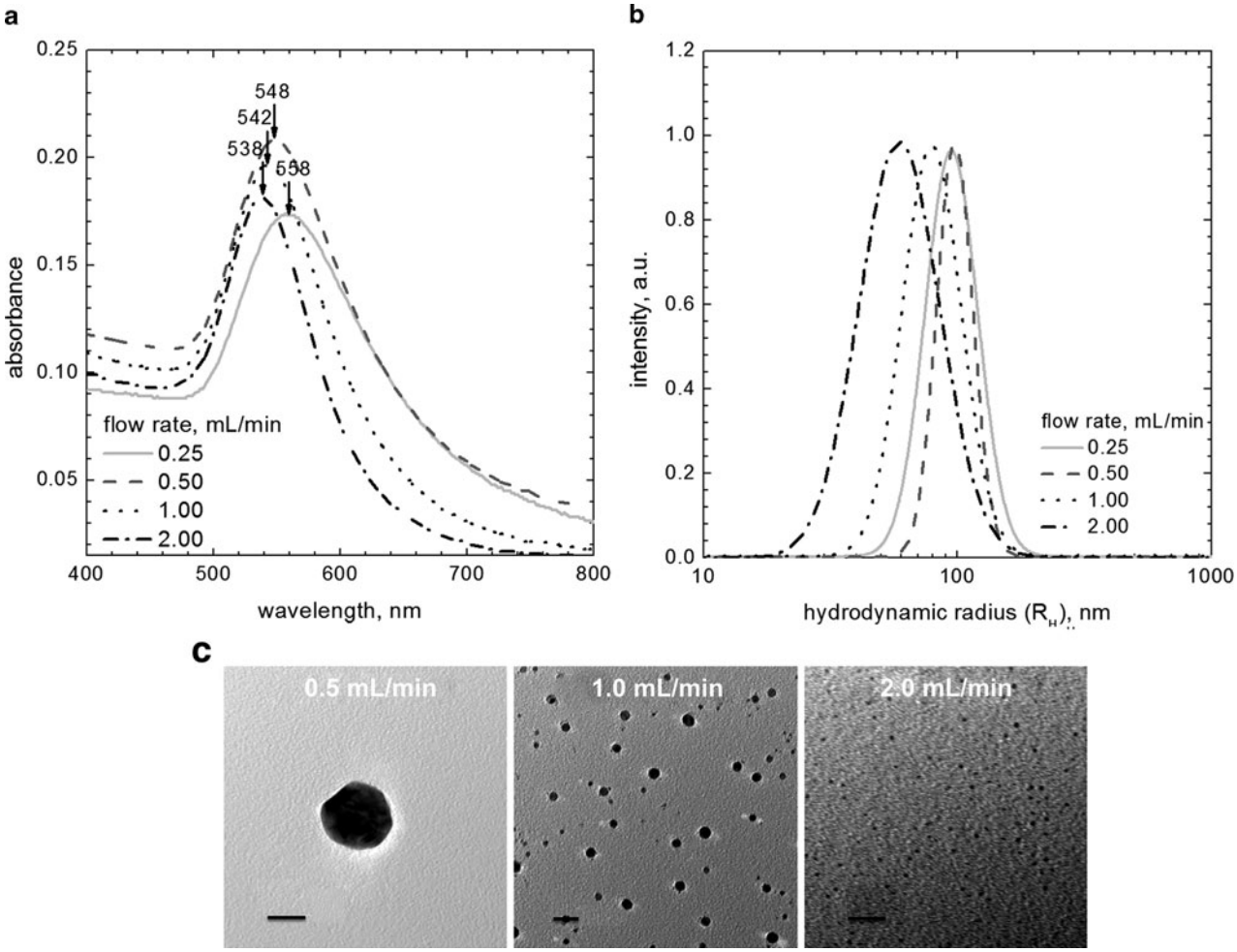

Fig. 6 Plasmon absorption bands (a), hydrodynamic radius distribution (b) and TEM images (c) of Au NP's obtained at different flow rates of reactants. Conditions: $C_{0,[AuCl4]^-}$ = 0.15 mM, C_{H2Asc} = 7.5 mM, temperature 25°C, scale bar in TEM images 20 nm

a function of temperature (Eq. 5). The reaction is first-order with respect to $[AuCl_4]^-$ ions. The values of the rate constant (k_{obs}) for different temperatures and reductant concentrations are given in the text. This equation was next applied to adjust reagents flow rate during synthesis of Au NP's in microreactor system.

3. From the kinetic studies in heterogeneous system, the rate equation of Au NP's formation was also determined. The rate constants k_2 and k_3 are given in the text (Table 3). Since the reduction reaction of chloride gold(I) complex ions is strongly accelerated in the microreactor system, this rate equation can be used to adjust the time of stabilizer's injection into the batch reactor only.
4. To synthesize gold nanoparticles in the flow microreactor system, the cartridge with T–type geometry of microchannels connection can be used. This type of micromixer as well as different rates of reagents flow, give the chance for injection of stabilizing agent (PVA) in the proper instant of reaction time. It was found that this method is promising one for the preparation of the Au NP's with well defined shape and narrow size distribution. Obtained sizes of Au NP's varied from 1 to 35 nm.

Acknowledgements This work was supported by the European Regional Development Fund under the Innovative Economy Operational Programme (Grant No. 01.01.02-00-015/09-00).

References

1. Zhou QF, Bao JC, Xu Z (2002) J Mater Chem 12: 384
2. Mandal S, Selvakannan P, Phadtare S, Pasricha R, Sastry M (2002) P Indian AS-Chem Sci 114: 5513
3. Overbeek JThG (1966) Faraday Discuss 42: 7
4. Derjaguin BV (1966) Faraday Discuss 42: 317
5. Khannaa PK, Gokhalea R, Subbaraoa VVVS, Vishwanatha AK, Dasa BK, Satyanarayanab CVV (2005) Mater Chem Phys 92: 229
6. Watzky MA, Finke RG (1997) J Am Chem Soc 118: 10382

Progr Colloid Polym Sci (2011) 138:45–48
DOI: 10.1007/978-3-642-19038-4_8

Influence of the Counterions on the Behaviour of Polyelectrolytes

Ute Böhme, Brigitte Hänel, and Ulrich Scheler

Abstract The influence of the counterions on the hydrodynamic size and the effective charge of poly(styrene sulfonate) has been investigated applying a combination of pulsed-field gradient (PFG) NMR and electrophoresis NMR. From the diffusion coefficient, determined by PFG NMR the hydrodynamic radius as a measure of the size is inferred. Electrophresis NMR yields the electrophoretic mobility and thus the effective charge of the macromolecule. An increased ionic strength of the solution results in a more coiled conformation of the polyelectrolyte, an effect which is more pronounced for bivalent ions. If the dielectric constant of the solution is lowered, the effective charge is reduced as well. The effect on the overall conformation strongly depends on the kind of the counterion. While a small effect is observed for the acid form, the most drastic effect is found for sodium as a counterion.

Keywords Polyelectrolytes • counterions • PFG NMR • electrophoresis NMR

Introduction

The conformation of polylectrolytes strongly depends on their effective charge. The effective charge usually is significantly lower than the nominal charge because of condensation of counterions [1]. The effect of counterion condensation has been derived from basic arguments of the thermal energy of the counterions in the solution experiencing the electric field of the macromolecule and the gain of entropy, when they escape the macromolecule. The affinity of bivalent counterions is much stronger than that of monovalent counterions [2]. Recent developments in the theoretical description of the interaction between polyelectrolytes and counterions can be found in [3, 4]. The influence of the interaction of the charges along the polymer chain on the overall conformation of the polyelectrolyte and the collapse of the chain in a poor solvent has been described in [5]. Although the size and the valence of the counterion have a strong impact on the interaction of the counterions with the macromolecule additional effects arising from specific interactions, solvent-polyelectrolyte and solvent-counterion interactions have to be considered [6, 7, 8, 9].

The hydrodynamic size of macromolecules in solution has been determined by pulsed-field gradient (PFG) NMR [10, 11]. From the dependence of a characteristic length on molecular weight scaling exponents have been derived [12, 13]. The combination of diffusion and electrophoresis NMR has been proven to be a suitable method for the determination of the effective charge of macromolecules in solution [14, 15, 16, 17]. Recently new experimental developments for electrophoresis NMR have been reported by Stilbs and coworkers [18]. The application of an electric field in a solution generates a force on charged moieties, so that these are accelerated until the force from the electric field is balanced by the velocity-dependent hydrodynamic friction. Assuming this force balance the effective number of charges is calculated without any model [19, 20]. This approach has recently been applied to study the influence of molecular weight [21], ionic strength and the dielectric constant of the solution [22] on counterion condensation and the effective charge of polyelectrolytes.

In the present contribution the effect of different salts and of the variation of counterions on the effective charge of poly(styrene sulfonate) (PSS) has been investigated. The interaction between the charges along the polymer chain leads to a more extended conformation of the polyelectrolytes compared to the uncharged polymer. Thus as the effective charge would be reduced upon the increase of the ionic strength or the decrease of the dielectric constant of the solution a more coiled conformation resulting in a reduced hydrodynamic size would be expected.

U. Scheler (✉)
Leibniz-Institut für Polymerforschung Dresden e.V., Hohe Str. 6, 01069 Dresden, Germany
e-mail: scheler@ipfdd.de

Experimental

The sodium salt of poly(styrene sulfonate) with a narrow molecular weight distribution (PSS77, GPC standard grade, M_w ~77 kg/mol) has been obtained from Fluka. The powder was evacuated to remove any residual water content. The lithium salt of poly(styrene sulfonate) (30% wt in H_2O, M_w ~75 kg/mol) and poly(styrene sulfonic acid) (18% wt in H_2O, M_w ~75 kg/mol) have been purchased from Aldrich. Both samples have been concentrated in a rotary evaporator and subsequently dried under vacuum. For all experiments a concentration of 5 mmol/l (monomer) in deuterated solvents (D_2O, CD_3OD and their mixtures) has been used.

The diffusion experiments have been performed on a Bruker Avance 500 NMR spectrometer operating at a Larmor frequency of 500 MHz for protons using a DIFF 30 probehead generating a maximum gradient strength of 12 T/m. The gradient pulse duration δ and diffusion time Δ have been adjusted between 0.7 to 1.5 ms for δ and 10 to 15 ms for Δ respectively. The narrow distribution of the molecular weight distribution permits the determination of the diffusion coefficients by a linear fit to the Stejskal-Tanner equation [23].

Electrophoresis NMR experiments have been performed on a Bruker Avance 300 NMR spectrometer operating at a Larmor frequency of 300 MHz for protons employing an in-house-built electrophoresis probehead [2], utilizing a Bruker micro2.5 imaging gradient system generating magnetic field gradient strength of up to 1 T/m and custom-built DC amplifier generating up to +/-1000 V. The electrophoretic mobility is determined free of any model from the two-dimensional electrophoresis NMR spectrum [19]. Data processing has been performed in matNMR [24] and in-house written scripts. The result is a two-dimensional electrophoresis NMR spectrum correlating chemical shift with the electrophoretic mobility. The determination of the electrophoretic mobility does not assume any number of components.

The hydrodynamic radius of the polyelectrolytes as a measure of the size of the polymer has been determined from the diffusion coefficient D by the Stokes-Einstein equation,

$$D = \frac{k_B T}{f} = \frac{k_B T}{6\pi\eta R_h} \tag{1}$$

where η is the solvent viscosity, $f=6\pi\eta R_h$ is the friction coefficient of a compact sphere in the solvent.

The viscosities of deuterated water, methanol and their mixtures have been derived from [25, 26].

The effective charge z of the polyelectrolyte is determined from the diffusion coefficient D and the electrophoretic mobility μ according to eq. (2) following [20].

$$z = \frac{\mu \cdot k_B \cdot T}{e \cdot D} \tag{2}$$

where e is the elementary charge.

Results and Discussion

In Figure 1 the dependence of the hydrodynamic radius of PSS77 as a function of the ionic strength adjusted using three different salts is shown. The basic behaviour for all three salts is similar, there is an initial strong decrease of the hydrodynamic size, which at higher ionic strengths becomes less pronounced. The reduction in the hydrodynamic size at the initial addition of salt is much more significant on the addition of a bivalent salt, which is expected because a bivalent counterion compensates two charges of the macromolecule.

The difference found between Ca and Mg is explained by the difference in the effective ion sizes arising from larger charge density and though stronger interactions with the solvent of the smaller cation Mg^{2+}, resulting in a bigger hydration shell. Comparable size effects of cations with equalent valence but different affinity to the macromolecule are observed by [7].

PSS with different counterions has been investigated as well. In addition to the acid form the sodium salt and the

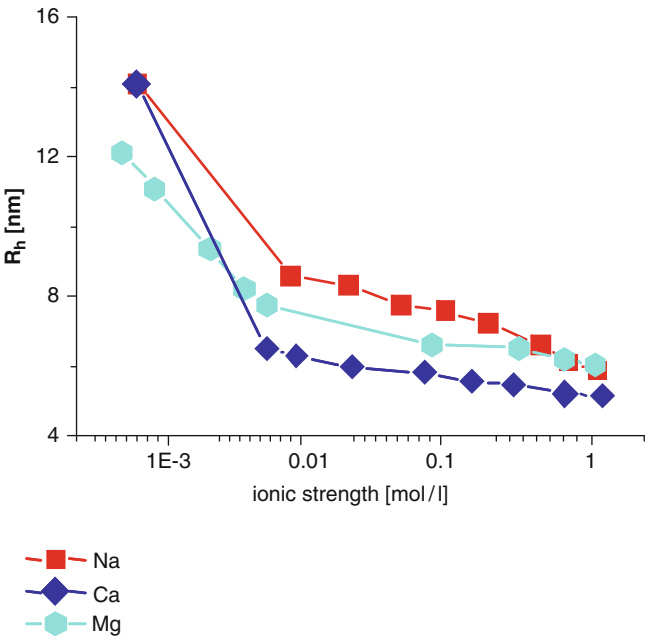

Fig. 1 Hydrodynamic radius of PSS77 as a function of the ionic strength adjusted using NaCl, $CaCl_2$ and $MgCl_2$. The differences between R_h in the salt-free solution result from different batches of PSS77

lithium salt have been investigated. There the influence of the solvent quality and dielectric constant has been studied. Figure 2 shows the relative variation of the hydrodynamic size with the variation of the solvent. The corresponding effect on the effective charge is depicted in Figure 3.

Three different PSS samples with proton, lithium and sodium as counterions have been studied. Their molecular weights are comparable, therefore the hydrodynamic size and the effective charge in salt-free aqueous solution are comparable but not exactly the same. In order to characterize the effect of different counterions in salt-free solutions under variation of the dielectric constant of the solution relative measures are depicted only. There is a strong effect of the nature of the monovalent counterions on both the conformation and the effective charge of PSS under a change of the dielectric permittivity of the solvent. The change of the

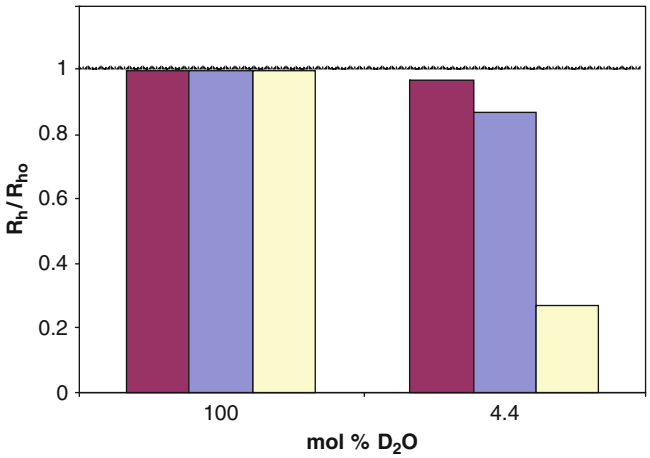

Fig. 2 Relative variation of the hydrodynamic radius of PSS with different counterions in pure D_2O and a mix of D_2O and CD_3OD

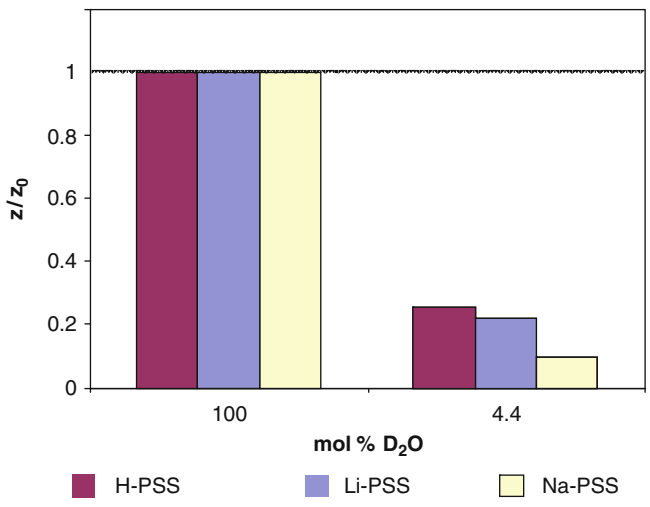

Fig. 3 Relative variation of the effective charge of PSS with different counterions in pure D_2O and a mix of D_2O and CD_3OD

hydrodynamic radius of the acid form of PSS is marginal even though there is a drop of the effective charge by a factor of four. The reduction of the effective charge for the lithium is similar and even stronger for the sodium salt of PSS. The result for the sodium salt follows what has been found earlier in a more detailed study [22, 27]. In contrast to the acid form of PSS there is clear change of the hydrodynamic size of the lithium salt and a dramatic drop of the hydrodynamic radius of the sodium salt. The decrease in size of the polyelectrolytes with increasing size of the different counterions follows the diminishing solubility of HCl, LiCl and NaCl in pure methanol [28]. The acidic form of PSS is soluble in both, D_2O and CD_3OD. Although a significant higher concentration of NaCl is soluble in pure methanol than the used polyelectrolyte concentration of 5 mmol/l, the sodium salt of PSS is insoluble. Additional to the strong decrease of the size with increasing methanol content in the mixture there is a significant line broadening in the ^1H spectrum of Na-PSS, but no change in the line shape of H-PSS has been observed, indicating different interaction between the counterion and the polymer chain depending on the counterion. Besides of the decreasing permittivity, resulting in a tightened counterion condensation and therefore in a more coiled conformation of the polyelctrolyte, the size of the counterion and counterion solute interactions are playing an important role in that behaviour.

Conclusions

The influence of counterions and of salt ions on both the overall conformation and the effective charge of polyelectrolytes has been studied using diffusion and electrophoresis NMR on the example of poly(styrene sulfonate). The effective charge of the polyelectrolyte is about one third of the nominal charge in a salt-free aqueous solution and is further reduced upon the increase of the ionic strength of the solution. The conformation of polyelectrolytes depends on the charge and the resulting repelling interaction along the polymer chain. Therefore the hydrodynamic size of the polyelectrolyte is strongly reduced, when the ionic strength of the solution increases. The effect is much more pronounced for bivalent counterions. There is an additional effect from the size of the salt ions.

In solutions free of additional salt there is a dependence of both the effective charge and the hydrodynamic size on the kind of counterion, affecting the solubility of the polyelectrolyte in mixed solvents as well. If the dielectric constant of the solvent is lowered, there is little effect on the acid form of PSS. The hydrodynamic size of the Li salt decreases slightly, while there is a dramatic decrease for the sodium salt of PSS. On the other hand the effective charge for all three

forms of PSS is significantly reduced, when the dielectric constant of the solution is reduced. The change in the conformation of the PSS cannot solely explained by the electrostatic interaction along the chain.

References

[1] Manning GS (1974) In: Sélégny E, Mandel M, Strauss UP (editors) Polyelectrolytes. D. Reidel Publishing Company, Dordrecht-Holland, p. 9 ff.
[2] Böhme U, Scheler U (2004) Macromol Symp 211:87
[3] Dobrynin AV (2008) Curr Opin Colloid Interface Sci 13:376
[4] Holm C, Joanny JF, Kremer K, Netz RR, Reineker P, Seidel C, Vilgis TA, Winkler RG (2004) Adv Polym Sci 166:67
[5] Kundagrami A, Muthukumar M (2010) Macromolecules 43:2574
[6] Schweins R, Huber K (2004) Macromol Symp 211:25
[7] Wakagawa M, Hayashi M, Kuroki S, Satoh M (2009) J Polymer Sci B 47:2132
[8] Katz AA, Leibler L (2009) Soft Matter 5:2198
[9] Loh P, Deen GR, Vollmer D, Fischer K, Schmidt M, Kundagram A, Muthukumar M (2008) Macromolecules 41:9352
[10] Callaghan PT (1991) Principles of Nuclear Magnetic Resonance Microscopy. Clarendon Press, Oxford, p. 441 ff.
[11] Kimmich R (1997) NMR Tomography, Diffusometry, Relaxometry. Springer, Berlin Heidelberg
[12] Böhme U, Scheler U (2002) Macromol Symp 184:349
[13] Sagidullin A, Fritzinger B, Scheler U, Skirda VD (2004) Polymer 45:165
[14] Grass K, Böhme U, Scheler U, Cottet H, Holm C (2008) Phys Rev Lett 100:096104
[15] Stilbs P, Furó I (2006) Curr Opin Colloid Interface Sci 11:3
[16] Böhme U, Vogel C, Meier-Haack J, Scheler U (2007) J Chem Phys B 111:8344
[17] Griffiths PC, Paul A, Hirst N (2006) Chem Soc Rev 35:134
[18] Hallberg F, Furó I, Yushmanov PV, Stilbs P (2008) J Magn Reson 192:69
[19] Scheler U (2002) In: Tripaty SK, Kumar J, Nalwa HS (editors) Handbook of Polyelectrolytes and Their Applications, vol 2. American Scientific Publishers, Stevenson Ranch, California, USA, p. 173 ff.
[20] Böhme U, Scheler U (2003) Colloids Surf A 222:35
[21] Böhme U, Scheler U (2007) Macromol Chem Phys 208:2254
[22] Böhme U, Scheler U (2010) Adv Colloid Interface Sci 158:63
[23] Stejskal EO (1965) J Chem Phys 43:3597
[24] van Beek JD (2007) J Magn Reson 187:19
[25] In: Lechner MD (ed) D' Ans Lax, Taschenbuch für Chemiker und Physiker, 4. Auflage, Band 1, Physikalisch-chemische Daten, Springer, Berlin Heidelberg New York (2001).
[26] Wensink EJW, Hoffman AC (2003) J. Chem. Phys 119:14
[27] Böhme U, Scheler U (2007) J Colloid Interface Sci 309:231
[28] Synowietz C, Schäfer K (1984) Chemiker Kalender. Springer, Berlin Heidelberg New York Tokyo, p121, p133

Progr Colloid Polym Sci (2011) 138:49–54
DOI: 10.1007/978-3-642-19038-4_9

Liposome Deformation by Imbalance of pH and Ionic Strength Across the Membrane

Osami Kuroda[1,2], Hiroshige Seto[1], Takayuki Narita[1], Michio Yamanaka[2], and Yushi Oishi[1]

Abstract The deformation of giant dioleoylphosphatidylcholine (DOPC) liposomes in solution and the properties of DOPC monolayers were investigated by florescence microscopy and surface pressure-area (π-A) isotherm measurements, respectively. These measurements were taken as functions of pH and ionic strength. When the ionic strength was changed from 0.001 to 0.6 at constant pH of 5.6, the coverage of the DOPC monolayer expanded by 10%, and the liposomes formed small protrusions. When the pH was changed from 5.6 to 3.5 at a constant ionic strength of 0.001, the monolayer coverage shrank by 10 %. During this process the external liposome morphology remained the same, but new, smaller vesicles appeared within the interior of the liposomes. Simultaneously changing the pH and the ionic strength to their final values (3.5 and 0.6, respectively), resulted in an expanded monolayer and produced long, protruded liposomes. Our results suggest that the deformation of liposomes is not only driven by osmotic pressure but also the condensed states in each monolayers composing liposome membrane.

Key words Giant liposome • Monolayer • π-A isotherm • Dioleoylphosphatidylcholine(DOPC) • pH • Ionic strength

Introduction

There has been much interest in phospholipids bilayer liposomes in recent years because of their similarity both to living cells and the vesicles found within cells [1-3]. Cells and vesicles can take on a variety of shapes, for example, red blood cells are flexible concave disks. Studies of artificial liposome deformation may thus help to uncover potential relationships between the shape and function of living cells. In addition, detailed studies of artificial liposomes may one day allow for engineered liposomes to be used for drug delivery applications [4].

Giant liposomes (GUV) are known to deform with temperature changes [5-7], by exposure to electric fields [8], and from osmotic pressure differences between the inside and outside of the liposome [9,10]. Shape deformations of GUV have been explained theoretically based on an area difference model instead of spontaneous curvature [11,12], which considers the driving force of deformations to be the membrane bending elasticity assuming the differences between the surface area of the inner and outer leaflets (phospholipids monolayers) which comprise the bilayer membrane of liposome. Since a change in leaflet surface area can be easily achieved by applying an osmotic pressure gradient across the liposome membrane, many studies have been done on these types of deformations [9-12].

Similarly, when monolayers of GUV's are prepared, the coverage of the monolayers can be controlled by adjusting the properties of the solution in contact with the monolayer, such as pH [13], ion strength, biological solute concentration [14], and temperature [15]. Thus, the application of pH and/or ionic strength differences across the liposome membrane should allow liposomes to deform their shape without the osmotic pressure difference. The difference in the surface area of the two GUV leaflets should be estimated indirectly from the coverage of the Langmuir monolayers on the aqueous subphase as function of the above solution conditions. However, to date, no study has been reported that explores the relationship between the experimental monolayer properties and the deformation of individual liposomes. In this study, we demonstrate that pH and/or ionic strength differences across the membrane of the liposome causes deformation of liposome, and these deformations will be considered by changes to the surface pressure-area (π-A) isotherms of the Langmuir monolayers.

T. Narita (✉)
[1]Department of Chemistry and Applied Chemistry, Saga University, 1 Honjo-machi, Saga-city, Saga, Japan
e-mail: naritat@cc.saga-u.ac.jp
[2]Department of Chemistry, Faculty of Sciences, Kyushu University, 6-10-1 Hakozaki, Higashi-ku, Fukuoka, Japan

π-A isothermal measurements for Langmuir monolayers provide information about the occupied area of a monolayer, as well as the compressibility modulus of such a monolayer on the air-water interface of a given aqueous solution [16]. Though Langmuir films are planar and mono-molecular films, these monolayer properties obtained by π-A isothermal measurement should be able to identify as that of a bilayered membrane in GUV because of the characteristic slow flip-flop diffusion [17], as opposed to the lateral diffusion [18] on the bilayer membrane [19]. Additionally, since the bilayer bending modulus which relates the deformation of liposome is proportional to the compressibility modulus of membrane in liposome [20-22], information from π-A isothermal measurement can be used to evaluate deformation of liposome. In this study, we estimated the properties of monolayers of these bilayered GUV liposomes from π-A isotherm measurements in the air-water interface, while the composition of the buffer solution over which they were formed was adjusted.

Experimental Section

Preparation of Giant Liposomes in Glass Capillaries [23]

1,2-Dioleoyl-sn-glycero-3-phosphocholine (DOPC) (NOF corporation) was dissolved in chloroform-filled glass vial (10 mM) with small amounts of perylene (Wako Pure Chemical Industries), as a fluorescent lipid probe. Several glass capillaries with an inner diameter of 0.34 mm and an outer diameter of 0.82mm were then placed into the solution-filled vial. The glass capillary was used to suppress the convection which sweeps away liposome from the microscope field. This DOPC solution was pre-dried by blowing dry nitrogen gas gently over the surface, and the remainder of the solution was evaporated in a desiccator in vacuum at room temperature for 1h, resulting in the formation of a lipid film on the walls of the capillaries. This lipid film was then hydrated in water for 6 h at 60°C to produce DOPC liposomes within the capillaries which contained ultra pure water (ionic strength = 0, pH = 5.6, electrical resistivity = 18.2MΩ-cm) in its inside. All reagents were of analytical grade and used without further purification.

Fluorescence Microscopic Observation

2-(N-morpholino) ethanesulfonic acid (MES) (Dojindo Laboratories.) and NaOH were used as buffer agents. Three types of solutions were prepared with specific pH's and ionic strengths. These solutions were of pH 5.6 and ionic strength 0.60 (case 1), pH 3.5 and ionic strength 0.001 (case 2), and pH 3.5 and ionic strength 0.60 (case 3), respectively. To expose the liposomes to these solutions, one end of the liposome-filled capillaries was dipped into 1 mL of the specified buffer solution and allowed to equilibrate. The glass capillary was then placed on the observation stage of fluorescence microscope (Leica DMI3000 B, Leica, Solms, Germany) and magnified images of liposomes in the capillary were captured every 10s for 2 h by a 10-bit camera (QImaging, Burnaby, BC, Canada) attached to the fluorescence microscope under a filter cube (L5, Leica, Solms, Germany) with an excitation filter of 480/40 nm. Obtained images were subjected to deconvolution using Image-Pro plus (version 7.0; Sharpstack; Media Cybernetics Inc., Silver Spring, MD). Experiments were carried out at the room temperature which was adjusted to 296 K using an air-conditioner.

Surface Pressure–Area (π–A) Isotherm Measurements

DOPC was dissolved in analytical grade chloroform (Sigma, 99%) at a concentration of 1.0×10^{-3} M. This chloroform solution of DOPC was gently applied to the surfaces of the aqueous buffer solutions with known pH and ionic strength. After standing for 30 min, π–A isotherm of each monolayer was measured under compression by two barriers at an area change rate of 3.2×10^{-3} nm^2/molecule with a microprocessor-controlled film balance system (FSD-300, USI System Co., Ltd.). The subphase temperature, T_{sp}, was adjusted to 296±0.5 K. Room temperature was adjusted to the same temperature as T_{sp} using an air-conditioner.

Results and Discussion

We will show below the results of the deformations for liposome after exchanging the outer solution various at pH and I.S, and results of π-A isotherms for DOPC monolayers on MES buffer solutions with their pH and Ionic strength. The results of the liposome deformation were discussed based on the results of π-A isotherms. First, we confirmed that no significant deformation of liposome was observed when exchanging the outer solution from ultra pure water to the MES buffer with pH 5.6 and ionic strength 0.001.

Case 1: Ionic Strength Change Effects

Figure 1(a) shows the fluorescence microscopy images of DOPC liposome after exchanging the outer solution from ultra pure water to the MES buffer with pH 5.6 and ionic

strength 0.6., as well as the schematic representation of the liposome at each time. First, liposomes condensed into a non-spherical shape at 24 min after exchange, and then showed an outward protrusion of the liposome membrane at 30 min. This deformation is due to an osmotic pressure difference across the liposome membrane because of a difference in the MES concentration through the semipermeability liposome membrane.

Figure 1(b) shows the π-A isotherms of a DOPC monolayer on a MES buffer solutions with pH 5.6 and ionic strength 0.6 (solid curve) and on a MES buffer with pH 5.6 and ionic strength 0.001 (dashed curve) at a constant temperature of 296 K. Surface pressure in both π-A isotherms gradually increased with a decrease in surface area without any appearance of a plateau region. The surface areas at a rising point of surface pressure were 1.01 nm^2 and 1.14 nm^2 for the monolayer on buffer solution with pH 5.6 and ionic strength 0.001 and pH 5.6 and ionic strength 0.6, respectively. And also, the π-A isotherm shifted to a larger area side with maintaining the slope of isotherm by exchanging the subphase to the buffer solution with higher ionic strength. The expansion of surface area by increasing ionic strength may be due to a less attractive electrostatic interaction of each phospholipid, which results from a shielding of the internal electrostatic interactions in the higher ionic strength solutions.

These results demonstrate that an increase in the ionic strength of the buffer outside the liposome will decrease the molecular density in the DOPC monolayer. The expansion in the monolayer should indicate that the outer leaflet expands more than the inner leaflet in the liposomes. Hence, it is expected that the difference of area between leaflets contributes to the outward protrusion of the membrane in liposome.

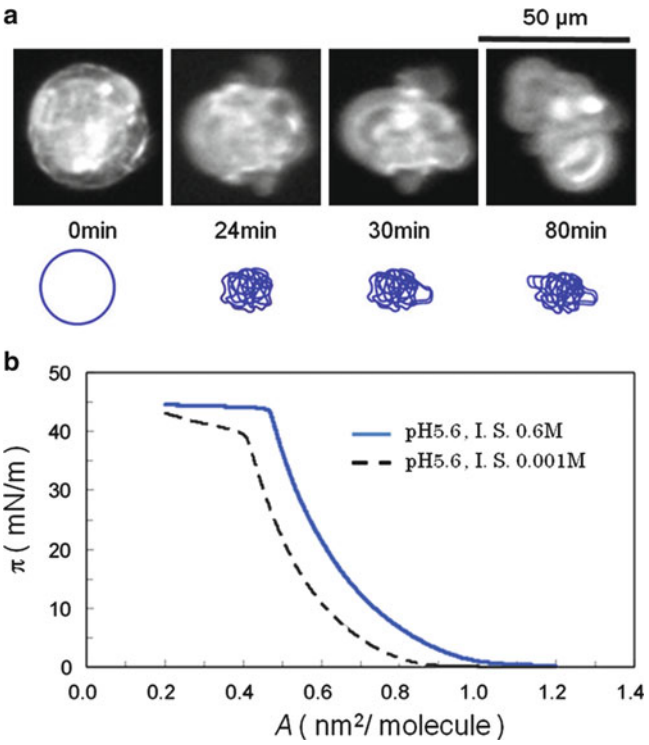

Figure 1 (a) Fluorescence microscope images of DOPC liposomes after exposure to solutions of MES buffer with pH 5.6 and ionic strength 0.6, accompanied by illustrations of the corresponding liposome deformations for each time. The times below the images display the elapsed time since the liposomes were exposed to the selected buffer. (b) π–A isotherms for DOPC monolayers over MES buffers with pH 5.6 and ionic strength 0.6 (solid curve) or with pH 5.6 and ionic stength 0.001 (dashed curve)

Case 2: pH Change Effects

Figure 2(a) shows behavior of the liposomes after exposure to the MES buffer with pH 3.5 and ionic strength 0.001. The liposomes kept their shape for 5 min into the exposure, after which time the membrane buckled and folded in on itself, resulting in small inward protrusions within the still-spherical, yet smaller liposome. These deformations at created by pH gradients across the membrane surfaces suggests that liposomes deform not only by osmotic pressure differences,

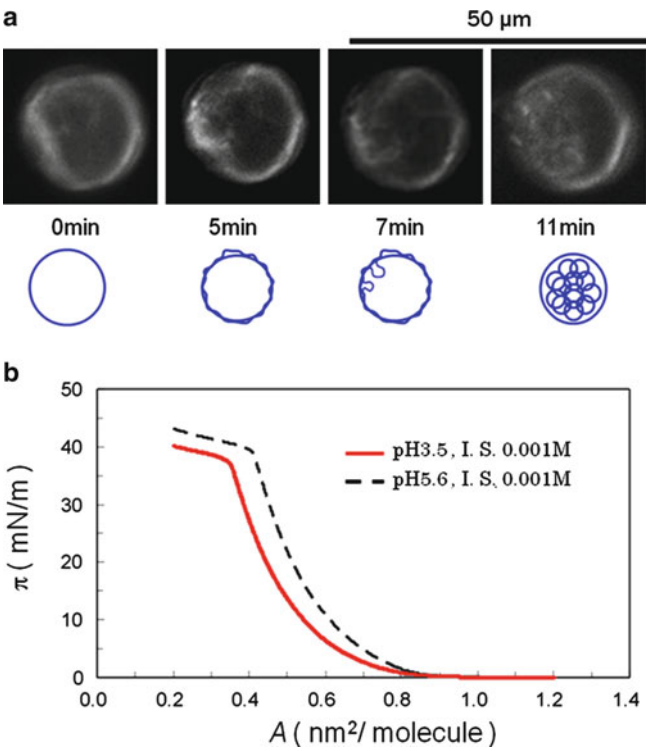

Figure 2 (a) Fluorescence microscope images of DOPC liposomes after exposure to a MES buffer with pH 3.5 and ionic strength 0.001, accompanied by illustrations of the corresponding liposome deformations for each time. (b) π–A isotherms for DOPC monolayers on MES buffers with pH 3.5 and ionic strength 0.001 (solid curve) or with pH 5.6 and ionic strength 0.001 (dashed curve)

but also by pH differences between inside and outside liposome. This is supported by the fact that the liposomes showed no significant shape deformation over 1h after they were exposed to pH 5.6, ionic strength 0.001 buffer solution.

The solid curve in Fig. 2(b) shows the π-A curve corresponding to the DOPC monolayer on the buffer solution with pH3.5 and ionic strength 0.001; the dashed curve corresponds to the π-A curve produced over the buffer solution with pH5.6, ionic strength 0.001. Since the buffer used in conjunction with this dashed curve had the almost same ionic strength and pH as the solution inside the liposomes, it can be thought of as a reference isotherm. The solid π-A isotherm in Fig. 2(b) shows a gradual rise of the surface pressure with the decreasing surface area without any appearance of transition. This slope is significantly lower than the slope of reference curve, especially in the low-surface-pressure regions of the curve. The surface area coverages for a molecule at 20mN/m [24] were 0.45 and 0.51 nm^2 at pH3.5 and pH 5.6, respectively. Therefore, one can see that the exposure to the lower pH solution causes an approximately 10% decrease in the surface area coverage of monolayer relative to the reference. This decrease in surface area coverage may be related to a reduction of the magnitude of the zeta-potential of the membranes [27]. This means that the DOPC membranes have an electric neutral point near pH 4.0, and thus, the individual DOPC molecules repel each other the least at this pH. The weakest repulsive force between each pair of DOPC molecules at around pH 4.0 would reduce the surface area coverage of the DOPC monolayer on the buffer solution at pH3.5.

By considering these π-A results, the surface area of inner leaflet in the liposome would exceed the area of inner leaflet when the external pH of the solution is smaller than the internal pH. As a result, the inner leaflet becomes pressed into the inside of liposome by the outer leaflet, creating an inward protrusion into the liposome. Notably, this deformation is observed in the absence of osmotic pressure differences across the liposome membrane wall.

Case 3: pH and Ionic Strength Change Effects

Figure 3(a) shows the deformation of DOPC liposome when the exterior of the liposomes were exposed to buffer with pH3.5 and ionic strength 0.6 (both pH and ionic strength were changed simultaneously). The liposomes aggregated immediately after the solvent exchange. After 80 min, the individual liposome membranes started to show outward protrusions. The membrane protrusions developed gradually with time and grew into much larger tumors in comparison with the protrusions created in case 1. Both in this case and in case 1, these protrustions are likely created by the osmotic

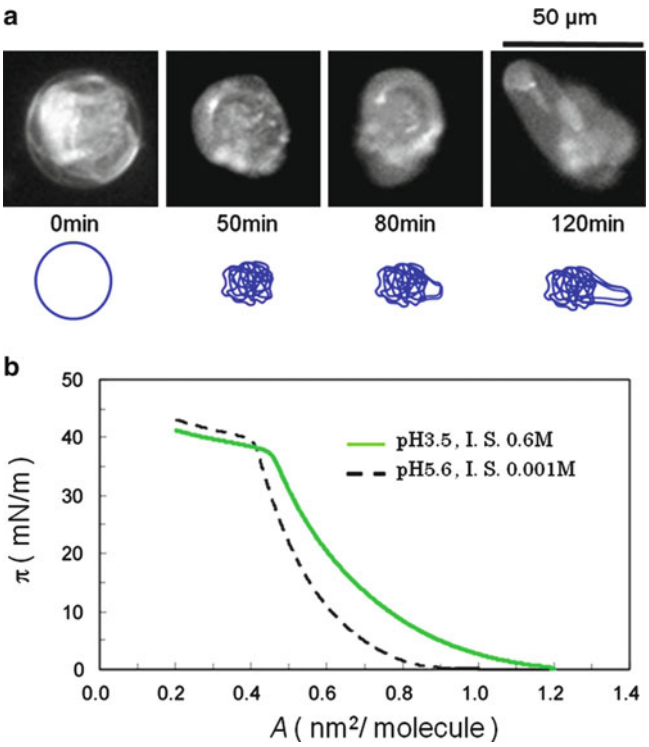

Figure 3 (a) Fluorescence microscope images of DOPC liposomes after exposure to MES buffer solutions with pH 3.5 and ionic strength 0.6, accompanied by illustrations of the corresponding liposome deformations for each time. (b) π–A isotherms for DOPC monolayers on MES buffer solutions with pH 3.5 and ionic strength 0.6 (solid curve) or with pH 5.6 and ionic strength 0.001 (dashed curve)

pressure difference across the liposome membrane walls, since the osmotic pressure difference increases the surface area of the external liposome leaflet preferentially over the internal leaflet. [9-12].

Fig 3(b) shows the π-A curve of a DOPC monolayer over a buffer solution with pH3.5 and ionic strength of 0.6. The π-A curve for this experiment slowly increases with a decrease in surface area, as was the result in case 2. However, in this experiment, the curve begins to rise to a surface area of 1.2nm^2/molecules, which is larger than that of the reference curve. This new profile can be interpreted as a summation of the ion strength effect suggested in case 1 and the pH effect in case 2. Therefore, the combination of a rise in ionic strength and a decrease in pH expanded the DOPC monolayers and also reduced their compressibility modulus to 7 mN/m [28], which is about half the value of the reference monolayers. If these monolayer properties for this third case are used to interpret the properties of each leaflet of the liposomes, it can be deduced that the outer leaflet area exceeds area of inner leaflet because the area of outer monolayer at case 3 have larger occupied area than that of inner monolayer at the reference. This excess in outer monolayer on liposome may drive the protrusion into outside of liposome. Furthermore,

since the bilayer bending modulus at liposome membrane should scale as the area-compressibility modulus times the membrane thickness squared [20-22], the softening at the outer leaflet, indicated by the reduced compressibility modulus, should further facilitate the deformation of membrane, lowering the energy necessary to produce the initial protrusions. This idea is consistent with the generation of larger protrusion in case 3 than that in case 1.

Conclusion

In this study, the deformation behaviors of giant liposomes were discussed with respect to the DOPC monolayer properties of the surface area coverage and the compressibility modulus of membrane as obtained by π-A isotherms measurements. These deformations could be predictably driven by the osmotic pressure differences that are caused by ionic strength gradients across the liposome membrane. Our results also reveal that gradients in pH across the membrane of giant liposomes can deform the liposomes by creating non-isotropic deformations of the inner and outer leaflets of the liposome. These results also demonstrate that the measurement of monolayer properties can be applied back to the discussion of individual the liposome deformations in a meaningful way.

Acknowledgment The authors want to thank Dr. Michael Ibele for pointing out mistakes and many valuable discussions of the manuscript. This work was supported by JSPS Research Fellowships for Young Scientists and by Grants-in-Aid for Scientific (No. 21750221).

References

[1] Tresset G (2009), PMC Biophysics, 2:3
[2] Moscho A, Orwar O, Chiu DT, Modi BP, Zare RN (1996) Proc Natl Acad Sci. 93:11443
[3] Simons K (2004) Annu Rev Biophys Biomol Struct 33:269
[4] Geng Y, Dalhaimer P, Cai S, Tsai R, Tewari M, Minko T., Discher DE (2007) Nat Nanotechnol 2:249
[5] Bagatolli LA, Gratton E (1999) Biophys J 77(4):2090
[6] Baumgart T, Hess ST, Webb WW (2003) Nature 425:821
[7] Yanagisawa M, Imai M, Taniguchi T (2008) Phys Rev Lett 100:148102
[8] Helfrich, W (1974) Z Naturforsch 29c:182
[9] Boroske E, Elwenspoek M, Helfrich W (1981) Biophys J 34 (1):95
[10] Mui BLS, Cullis PR, Evans EA, Madden TD (1993) Biophys J 64:443
[11] Seifert U, Berndl K, Lipowsky R (1991) Phys Rev A 44(2):1182
[12] Svetina S (2009) Chem Phys Chem 10:2769
[13] Rodríguez Niño MR, Lucero A, Rodríguez Patino JM (2008) Colloids Surf A 320:260
[14] Tagami Y, Ikigai H, Oishi Y (2006) Colloids Surf A 284:475.
[15] Seul M, Chen VS, (1993) Phys Rev Lett 70:1658.
[16] Petty MC (1996) Langmuir-Blodgett Films. Cambridge University Press, Cambridge
[17] Victor G (1991) Bioelectrochem Bioenerg 25:105.
[18] Vattulainen I, Mouritsen OG (2005) Diffusion in Membranes, Diffusion in Condensed Matter. In: Heitjans P and Kärger J (ed) Methods, Materials, Models, 2nd ed. Springer, Berlin pp 471-509
[19] Another difference of Langmuir monolayer to monolayer in bilayer GUV is that the monolayer contact with the gas phase. The interaction between the terminal end of DOPC and gas phase is weaker than that between the terminal ends of DOPC. This difference, however, should be a negligible contribution because of the tiny contact area at terminal ends of DOPC with which the gas phase contact compared to other area of DOPC.
[20] McIntosh TJ, Vidal A, Simon SA (2003) Biophys J 85:1656
[21] Evans E, Rawicz W (1990) Phys Rev Lett 64:2094
[22] Sackmann E (1994) FEBS Lett 346:3
[23] Bangham AD, Horne RW (1964) J. Mol. Biol. 8:660
[24] The surface pressure applied at liposome have been estimated about 17-25 mN/m[25, 26]
[25] Rytomaa M, Mustonen P, Kinnunen PKJ (1992) J Biolog Chem 261:22243
[26] Konttila R, Salonen I, Virtanen JA, and Kinnunen PKJ (1988) Biochem 27:7443
[27] Rinaudo M, François Q, Pépin-Donat B (2009) Macromol Symp 278:67
[28] Compressibility modulus of Langmuir monolayers can be determined from the slope of the π–A isotherms (Vollhardt D et al. (2006) Adv Colloid Interf Sci 127:83). The compressibility modulus: $E_0=\Gamma(d\Pi/d\Gamma)_T$, where $\Gamma=1/AN$, and A, N, and π are molecular area, Avogadro's number, and surface pressure, respectively.

Progr Colloid Polym Sci (2011) 138:55–60
DOI: 10.1007/978-3-642-19038-4_10

Surface Charge and Conductance in Dispersions of Titania in Nonaqueous and Mixed Solvents

M. Kosmulski[1,2], P. Dahlsten[1], P. Próchniak[2], and J.B. Rosenholm[1]

Abstract The nature and speciation of ions, and their affinities to mineral surfaces are well-known for aqueous solutions, and less well-known for mixed water-organic and nonaqueous solutions. Weak acids show strong preferential adsorption of anions on titania, and support a high negative surface charge on titania particles in organic solvents in spite of the very low degree of dissociation of these acids. The interaction between solutions of weak acids in organic solvents and titania particles results in enhanced electrical conductance with respect to the original solutions (in the absence of titania). This phenomenon is explained in terms of surface-induced electrolytic dissociation of weak acids. In mixed water-organic solvents the conductance behavior gradually shifts from water-like behavior (titania depresses the conductance) to opposite behavior (titania enhances the conductance). A quantitative model was proposed to explain the complex effect of the electrolyte and titania concentration on the conductance of the dispersion and zeta potential of the particles.

Keywords mixed solvent • conductance • zeta potential • surface charge • adsorption • surface sites

Introduction

The interaction between multiprotic acids and colloidal particles in alcoholic solutions has been extensively studied [1-3]. Addition of multiprotic acids resulted in more negative ζ potentials, and at sufficiently high acid concentration, the sign of the ζ potential was reversed from positive to negative. This phenomenon indicates uptake of anions from solution. A strong effect of acids on the ζ potential is surprising in view of low dissociation constants of multiprotic acids in nonaqueous solvents [4-6]. Namely, the acids occur chiefly in molecular form, and the concentrations of ions in their solutions are lower by several orders of magnitude than in aqueous solutions of those acids. Typically the dissociation constant of a weak acid in methanol is lower by 3 orders of magnitude than in water. The ability of very weak acids to reverse the sign of the ζ potential was explained in terms of the "surface-induced electrolytic dissociation". In alcoholic solutions of multiprotic acids, the concentration of pre-existing ions is low. Due to high affinity of the mineral surface to the anions, the interaction between electroneutral acid molecule and mineral surface leads to a surface complex involving the anion and solvated proton in solution. A mechanistic model of adsorption in such systems has been forwarded [7]. This model predicts enhanced conductance of colloidal dispersions in alcoholic solutions. Indeed, addition of mineral oxides to alcoholic solutions of multiprotic acids often results in enhanced conductance. Such a behavior is somewhat surprising, and it is opposite to "normal" behavior observed for aqueous solutions, in which addition of mineral oxides to a solution depresses the conductance.

The difference in adsorption mechanism of multiprotic acids from aqueous solutions on the one hand and from alcoholic solutions on the other is that in aqueous solution, pre-existing ions are adsorbed, and the conductance is depressed. In alcoholic solution, adsorption of neutral molecules produces ions in solution, e.g.,

$$\equiv \mathrm{Ti} + \mathrm{H_3PO_4} = \equiv \mathrm{Ti} - \mathrm{H_2PO_4^-} + \mathrm{H^+} \qquad (1)$$

This may lead to net increase in concentration of ionic species in solution, and to enhanced conductance. Certainly, there are some ions in alcoholic solution, and the surface-induced electrolytic dissociation is accompanied by uptake

M. Kosmulski (✉)
[1]Center of Excellence for Functional Materials and Graduate School of Materials Research at Laboratory of Physical Chemistry, Åbo Akademi University, Porthansgatan 3-5, 20-500, Åbo, Finland
e-mail: mkosmuls@abo.fi
[2]Lublin University of Technology, Nadbystrzycka 38, 20-618, Lublin, Poland

of pre-existing ions. Thus, the measured conductance of dispersions may be enhanced or depressed, as the result of two processes acting in opposite directions.

The equivalent conductance of proton (lyonium) is substantially higher than specific conductance of other ionic species. This property is well-known for aqueous solutions of acids, and it is also observed in alcoholic solutions [8-10]. This is why the protons in solution produced in reaction (1) or in analogous reactions with other mineral oxides and other multiprotic acids, can be easily detected by means of conductometric measurements.

The interaction between multiprotic acids and mineral oxides has been studied in dispersions in anhydrous or nearly anhydrous n-alcohols. In this study we present analogous results obtained in mixed water-ethanol and water-methanol solvents. The values of pK_a of multiprotic acids and solvent properties relevant to the present study smoothly change from the properties of water to the properties of alcohol in those solvents. The study of the interactions between multiprotic acids and colloidal particles in mixed solvents makes it possible to verify the above model, and to test the derived relationship between ζ potential and conductance on the one hand and the pK_a of multiprotic acids and solvent properties on the other.

Experimental

Reagents

Aeroxide (TiO_2) from Degussa was used as received. It is chiefly anatase (with a small admixture of rutile), the particle diameter is 30 nm, the BET specific surface area is about 50 m^2/g, and the PZC and IEP is about 6.5 [11]. Methanol (>99.8 %, <0.02 % water) was from Baker, and ethanol (94 % by mass) was from Altia, Rajamäki, Finland. Water was MilliQ. Oxalic acid dihydrate (>99.5 %) was from Fluka.

Procedures

Acoustosizer IIs (Colloidal Dynamics, Warwick, USA) with a built-in conductivity meter and thermometer was used to measure the ζ potential and conductance of solutions of phosphoric and oxalic acid solutions in mixed (water-ethanol and water-methanol) solvents and of TiO_2 dispersions (1-10 % by mass). The apparatus was kept in a fume-hood. A flow-through system and stirrer prevented sedimentation of dispersions. An external thermostat was used to keep the solutions and dispersions at 25 ± 1 °C. 4 mL of 1 M acid was added in 0.1 mL portions to 170 mL of initial solution or dispersion in 2-min-intervals. The so-called "Smoluchowski" ζ potential (obtained at one frequency, and not corrected for the inertia effect) is reported in this study.

Results and Discussion

ζ potential

A representative set of zetametric curves obtained at various solid-to-liquid ratios is presented in Fig. 1.

The ζ potential becomes more negative on addition of phosphoric acid, and at sufficiently high acid concentration the sign is reversed to negative. At even higher concentration of acid a plateau is reached, that is, further addition of acid does not affect the ζ potential. The critical concentration, at

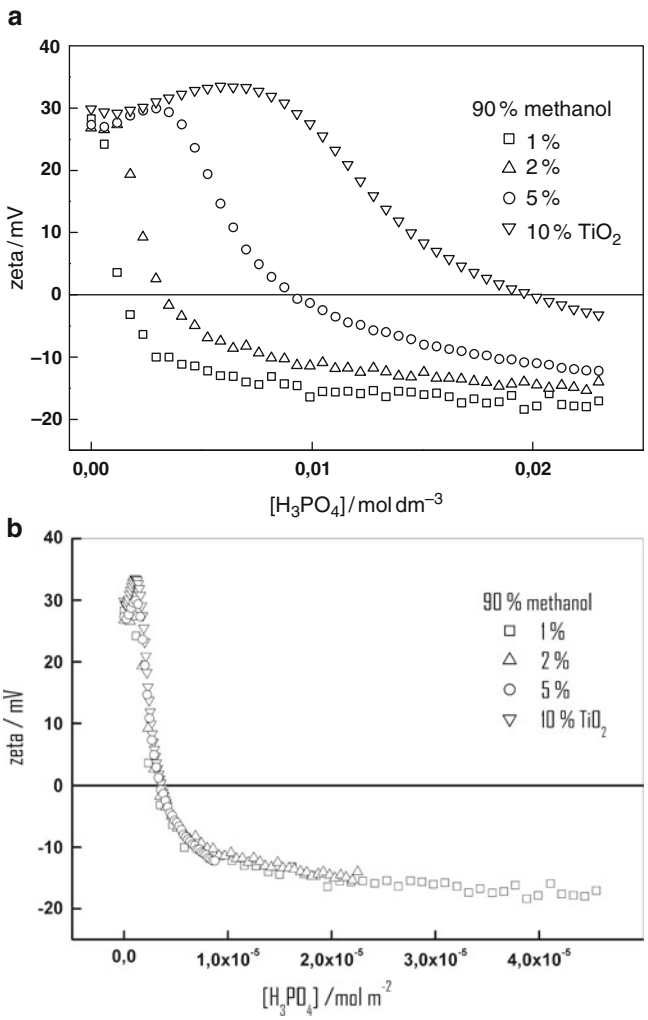

Figure 1 The ζ potential of titania in solutions of phosphoric acid in 90 % methanol plotted against a) solution concentration b) surface concentration of phosphoric acid

which the sign is reversed is roughly proportional to the titania concentration. In other words, the 4 curves shown in Fig. 1 a merge to one master curve (Fig. 1 b) when the ζ potential is plotted against the surface concentration of phosphoric acid (amount of acid divided by the surface area of titania used in the experiment). Similar sets of zetametric curves were obtained at different methanol concentrations, and in different water-ethanol mixtures, for phosphoric and oxalic acid. The behavior shown in Fig. 1 is consistent with the adsorption model described by Eq. 1. The critical concentration, at which the sign is reversed (isoelectric point, IEP) corresponds to the surface concentration of negatively charged surface complexes, which neutralizes the pre-existing positive charge of titania particles. The begin of the plateau corresponds to the saturation of surface sites, which are responsible for dissociative adsorption of phosphoric acid.

A set of zetametric curves in a series of mixed solvents of various compositions is presented in Fig. 2.

The graphs shown in Fig. 2 are analogous to the master curves presented in Fig. 1 b, but to avoid overcrowding of data points, only the data points for one solid-to liquid ratio (2 % titania in this case) are explicitly shown in Fig. 2. Similar results were obtained for other solid-to-liquid ratios (1, 5, and 10 % TiO_2), and for aqueous methanol (60-90 %). In the case of oxalic acid the IEP is rather insensitive to the solvent composition (20-94 % ethanol and 60-100 % methanol), and the IEP is at about 1.5×10^{-6} mol/m^2 $H_2C_2O_4$. The match between IEP obtained for different solvent compositions shown in Fig. 2 is a result of a fortuitous coincidence (interplay between pK_a and affinity of acid to the surface) rather than a general rule, and in principle the IEP is a function of solvent composition. Another set of zetametric curves in a series of mixed solvents of various compositions is presented in Fig. 3. To avoid overcrowding of data points, only the data points for one solid-to liquid ratio (10 % titania in this case) are explicitly shown in Fig. 3.

In the case of phosphoric acid the IEP gradually shifts to higher acid concentration as the methanol concentration increases. The IEP as the function of solvent composition are summarized in Table 1.

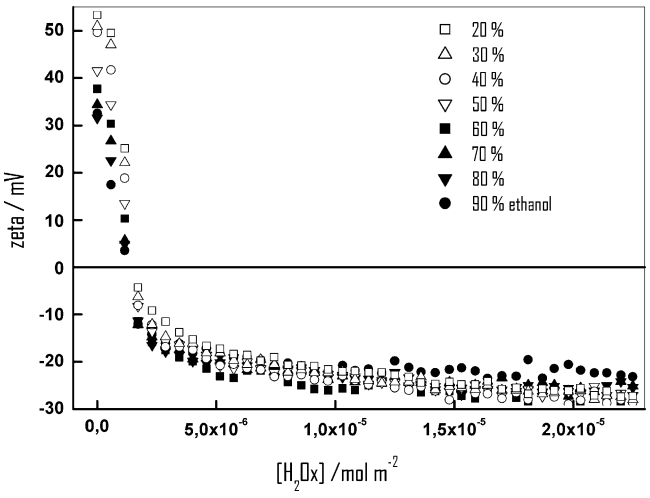

Figure 2 The ζ potential of titania in solutions of oxalic acid in 20-90 % ethanol

Conductance

The enhanced conductance of dispersions of titania with respect to the acid solution is illustrated in Fig. 4.

Figure 4 shows a similar phenomenon as that originally observed in nonaqueous or nearly nonaqueous solvents. The addition of titania enhances the conductance of a solution of phosphoric acid in alcohol-rich mixed methanol-water solvent, and at sufficiently high acid concentration, the conductometric curve of the dispersion is roughly parallel to the original conductometric curve of the solution. The distance between the parallel lines representing the dispersion on the

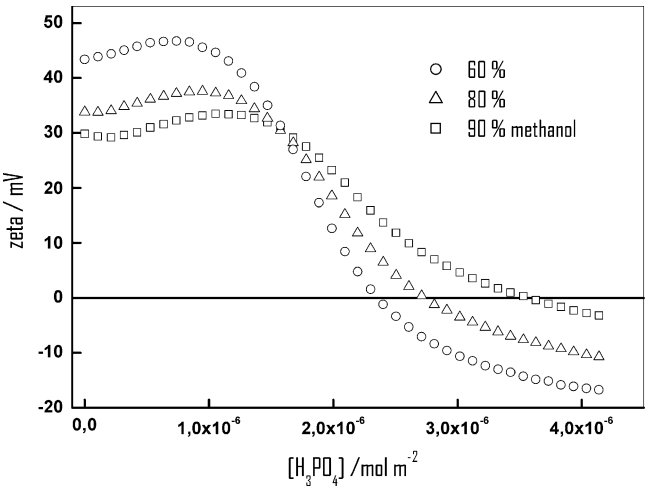

Figure 3 The ζ potential of titania in solutions of phosphoric acid in 60-90 % methanol

Table 1 The IEP of titania in solutions of phosphoric acid in mixed water-alcohols solvents

solvent	IEP (μmol/m^2)
Water [1]	2
60 % methanol	2.4
80 % methanol	2.7
90 % methanol	3.6
100 % methanol [1]	No IEP (only positive ζ)
20 % ethanol	2.2
40 % ethanol	2.2
60 % ethanol	2.3
80 % ethanol	2.4
94 % ethanol	2.8 (this study, fast titration) 4 ([1], slow titration)

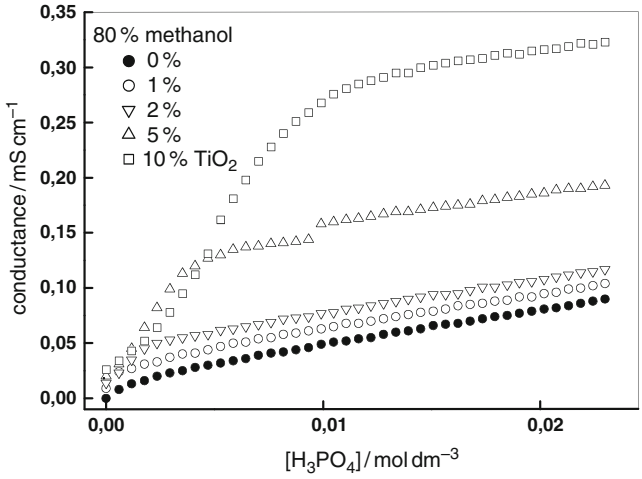

Figure 4 The conductance of dispersions of titania in solutions of phosphoric acid in 80 % methanol

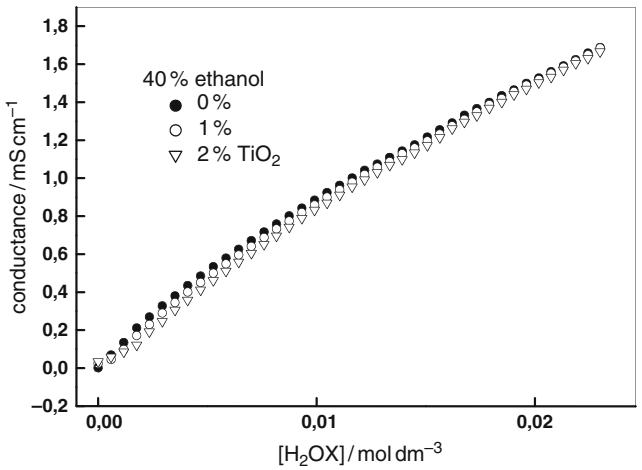

Figure 5 The conductance of dispersions of titania in solutions of oxalic acid in 40 % ethanol

one hand and solution on the other is roughly proportional to titania concentration. This distance represents the concentration of surface sites responsible for the surface reaction analogous to reaction 1. However, the enhancement of the conductance in mixed solvent is less pronounced than in pure methanol. Qualitatively similar effects were observed in solutions of oxalic and phosphoric acids in alcohol-rich mixed methanol-water and ethanol-water solvents.

In water-rich mixed solvents, the conductometric behavior of the dispersions gradually shifts to the "normal" behavior, similar to that observed in water, and illustrated in Fig. 5.

The addition of titania depresses the conductance of solutions of oxalic acid in water-rich mixed ethanol-water solvent. Qualitatively similar effects were observed in solutions of oxalic and phosphoric acids in water-rich mixed methanol-water and ethanol-water solvents. It should be emphasized, that there is no sharp transition from water-like behavior illustrated in Fig. 5 to alcohol-like behavior illustrated in Fig. 4, that is, at about 50-50, there is a broad range of solvent compositions over which the titania may enhance or depress the conductance, dependent on acid and titania concentration.

Discussion

The present model of adsorption is based upon reaction 1 (or analogous reaction for oxalic acid), and another surface reaction:

$$\equiv \mathrm{Ti} + \mathrm{H_3PO_4} = \equiv \mathrm{Ti} - \mathrm{H_3PO_4} \qquad (2)$$

(or analogous reaction for oxalic acid). Reaction 2 is responsible for the initial portion of the conductometric curves corresponding to low acid concentrations (cf. Fig. 4) in which the enhancement of the conductance is not proportional to the titania concentration. Reactions (1) and (2) occur on two different types of surface sites. The densities of the both types of surface sites and equilibrium constants of reactions (1) and (2) (and analogous reactions for oxalic acid) are the adjustable parameters of the model. Moreover, the model requires the dissociation constants of acids in the solvent of interest. The parameters can be adjusted using the conductance data of the dispersions at various solid to liquid ratios. In the particular cases of experimental curves, obtained in the present study, and in our previous studies (in anhydrous or nearly anhydrous alcohols), the sites responsible for reaction (2), and for analogous reactions (different acids and different oxides) occur at low concentrations, and show very high affinity constants. Thus they only affect the initial portion of the conductance vs. acid concentration curves, and their effect on the plateau level is rather insignificant.

It is relatively easy to adjust model parameters for a single data set [7]. However, several different sets of model parameters may reproduce the experimental results equally well. This is a real challenge to developing a consistent model covering a range of mixed solvents. In particular the densities of both types of surface sites and equilibrium constants of reactions (1) and (2) should change smoothly with the solvent composition. It should be emphasized that the site densities for certain solvent system are not relevant to another solvent system, and in general the densities of surface sites responsible for adsorption of inorganic ions decrease as the alcohol fraction in the mixed solvent increases [12]. The exact match between the site densities responsible for adsorption of oxalic and phosphoric acid is not required. These ions form multidentate surface complexes in aqueous system, and probably also in mixed solvents. Thus the surface areas occupied by the both ions can be

different. The model calculations based upon the experimental data presented above are in progress.

Acknowledgements The authors acknowledge the Academy of Finland support for the Center of Excellence for Functional Materials and for Graduate School of Materials Support. Moreover the Academy of research contract, No. 116466 is acknowledged.

References

[1] Kosmulski M, Prochniak P, Rosenholm JB (2009) J.Phys.Chem.C 113:12806
[2] Kosmulski M, Prochniak P, Rosenholm JB (2010) Langmuir 26:1904
[3] Kosmulski M, Prochniak P, Maczka E, Rosenholm JB (2010) J.Phys.Chem.C 114:17734
[4] Gumtya SK, Lahiri SC, Aditya S (2002) Z.Phys.Chem. 216: 971
[5] Bhattacharyya A, Maandal AK, Lahiri SC (1980) Electrochim. Acta 25: 559
[6] Bandyopadhyay G, Lahiri SC (2002) Z.Phys.Chem. 216: 729
[7] Kosmulski M (2010) Adsorption 16: 343
[8] De Lisi R, Goffredi M, Turco Liveri V (1976) J.Chem.Soc. Faraday Trans 1 72: 436
[9] De Lisi R, Goffredi M, Turco Liveri V (1978) J.Chem.Soc. Faraday Trans 1 74: 1096
[10] De Lisi R, Goffredi M, Turco Liveri V (1980) J.Phys.Chem. 84: 307
[11] Kosmulski M (2009) Surface Charging and Points of Zero Charge, Taylor and Francis, Boca Raton
[12] Szczypa J, Wasowska L, Kosmulski M (1988) J. Colloid Interf. Sci. 126: 592

Progr Colloid Polym Sci (2011) 138:61–66
DOI: 10.1007/978-3-642-19038-4_11

Self-Assembled Structures of Disc-Like Colloidal Particles

S. Junaid S. Qazi[1,*], Göran Karlsson[2], and Adrian R. Rennie[1]

Abstract Self-assembly is an important phenomenon that leads to formation of interesting and novel structures in colloidal dispersions. We present experimental evidence for the existence of a 'cubatic' phase in a colloidal dispersion of disc-like particles of nickel hydroxide colloidal dispersions. In this structure, disc-like particles self-assemble as domains of a few parallel discs and the orientation tends to be orthogonal in adjacent domains. This phase has been predicted previously by computer simulations. The domains are approximately equiaxial and are predicted to exist only within a limited range of aspect ratios and volume fractions. We have used the real space technique of cryo-transmission electron microscopy in our studies as this locally ordered structure could not be identified readily using scattering techniques, since the patterns are expected to be similar to those of isotropic liquid phases.

Key words Cubatic Phase • Plate-like colloids • Cryo–transmission electron microscopy

Introduction

Self-assembly is a means to form ordered structures in colloidal dispersions. Interparticle interactions, size-distribution and the thermal motion play vital roles. Ordered structures of anisotropic colloidal particles have significant importance to basic science and are of major practical interests. For example, they provide better mechanical properties as fillers in composite materials. A variety of different self-assembled structures[1,2,3,4] are reported for anisotropic particles on changing the concentration and temperature of dispersions.

Polydispersity is important for the structure of colloidal dispersions. It is difficult to synthesise highly monodisperse colloids. Computer simulations of spherical colloids have shown that polydispersity can suppress the formation of crystal phases[5,6]. Dispersions of hard spheres[7] with high polydispersity have shown fractionation into several solid phases that coexist with a fluid phase. In contrast, low polydispersity in length does not affect the phase behaviour of rod-like colloids, as nematic order does not depend strongly on length. Polydispersity above 18% was seen to suppress formation of a smectic phase of rods[8]. Polydisperse rods were seen to separate into phases with different length distributions[9]. An experimental study of goethite particles has shown that polydispersity favours the columnar phase over smectic structure that cannot accommodate particles with different lengths[10].

The present work concerns discs. Computer simulations on cut spheres, that approximate discs in shape, are reported

*On study leave from COMSATS Institute of Information Technology, Pakistan.

S.J.S. Qazi (✉)
[1]Materials Physics, Department of Physics and Astronomy, Ångström Laboratory, Uppsala University, Box 516, SE-75120, Uppsala, Sweden
e-mail: Junaid.Qazi@fysik.uu.se
[2]Department of Physical and Analytical Chemistry, Uppsala University, Box 579, 75123, Uppsala, Sweden

[1] Gabriel J-CP, Davidson P (2000) Adv. Mater. 12, 9.
[2] Brown ABD, Clarke SM, Rennie AR (1998) Langmuir 14, 3129. (1999) Langmuir, 15, 1594.
[3] Brown ABD., Ferrero C, Narayanan T, Rennie AR (1999) Eur. Phys. J. B **11**, 1999, 481.
[4] van der Kooij FM, Kassapidou K, Lekkerkerker HNW (2000) Nature 406, 868.
[5] Bolhuis PG, Kofke DA (1996) Phys. Rev. E 54, 634.
[6] Bartlett P, Warren PB (1999) Phys. Rev. Lett. 82, 1979.
[7] Fasolo M, Sollich P (2003) Phys. Rev. Lett. 91, 068301–1.
[8] Bates MA, Frenkel D (1998) J Chem. Phys. 109, 14, 6193.
[9] Speranza A, Sollich P (2003) J. Chem. Phys. 118, 11, 5213.
[10] van den Pol E, Thies-Weesie DME, Petukhov AV, Vroege GJ, Kvashnina K (2008) J. Chem. Phys. 129, 164715.

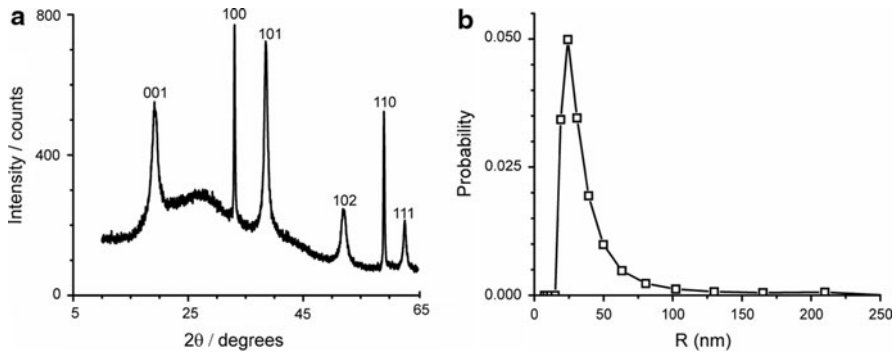

Figure 1 (a) X-ray diffraction pattern for the $Ni(OH)_2$ dispersions. Diffraction experiments used a monochromatic Cu Kα X-ray beam (wavelength 0.154056 nm). The 001 peak is markedly broader than the 100 peak indicating that the particles are thin along the direction of the 001 plane normal. (b) Distribution of hydrodynamic radius for the nickel hydroxide particles derived from dynamic light scattering data. The data in (b) were obtained at a fixed scattering angle of 90° with a He-Ne laser emitting vertically polarised light at a wavelength of 632.8 nm

in the literature[11,12]. The phase diagrams with many structures that depend on the concentration as well as the aspect ratio, L/D where L is the thickness of the disc and D is the diameter[13,14] are described. A cubatic phase was identified[11,15,16] with self-assembly in domains that consist of a few parallel discs. The orientation tends to be perpendicular in adjacent domains. Cubatic structure has been predicted for L/D = 0.2 in the density range ρ*0.5 to 0.62 where ρ* is defined as the ratio of the volume fraction of particles to that of a close packed structure. In this article, we describe the observation of cubatic order in a dispersion of disc-like nickel hydroxide particles using cryo-transmission electron microscopy (cryo-TEM).

Experimental

Uniform hexagonal disc-like particles of nickel (II) hydroxide were prepared and sterically stabilised by adsorbing a layer of sodium polyacrylate on the surface according to the procedure of Brown et al[2] who developed the original synthesis of Durand-Keklikian et al.[17]. The stabilised sample was then centrifuged and redispersed in water and centrifuged again to the required concentration. Three different concentrations 20% wt., 24% wt. and 30% wt. of nickel hydroxide dispersions were prepared for the experiments. The sample, which has shown the cubatic phase, had a concentration of 20% wt..

The disc-like nickel hydroxide particles were characterised by X-ray diffraction and dynamic light scattering to determine the dimensions, thickness of the adsorbed polymer layer and the polydispersity. The 001 peak in the X-ray diffraction pattern, shown in Figure 1a, is broader than the 100 peak. Average dimensions of the $Ni(OH)_2$ crystals in these directions can be calculated from the peak widths. Details about the methods[18] of analysis and the sample[19] used in the current study have been provided elsewhere. The nickel hydroxide core was found to be 6 nm thick and 80 nm in the diameter. Combining this with light scattering indicates that the overall particle diameter, D, was ~103 nm (including both nickel hydroxide and stabiliser), and the thickness, L, was ~23 nm. The estimated thickness of the adsorbed polymer layer was 8.5 nm. The size distribution in Figure 1b indicates the presence of some large particles up to 200 nm diameter and a polydispersity index from a cumulant fit of about 0.2. The aspect ratio defined as the overall thickness divided by the overall diameter is thus about 0.22.

Results and Discussions

A cryo-TEM image is shown in Figure 2 that indicates structures with cubatic order.

Cryo-transmission electron microscopy (cryo-TEM) is a technique that is used to study a wide variety of samples in fluid media for which the dispersed structure is important,

[11] Veerman JAC, Frenkel D (1992) Phys. Rev. A. 45, 5632.
[12] Alder BJ, Wainwright TE (1962) Phys. Rev. 127, 2, 359.
[13] Bates MA, Frenkel D (1998) Phys. Rev. E 57, 4, 4824.
[14] Bates MA, Frenkel D (2000) J. Chem. Phys. 112, 22, 10034.
[15] Frenkel, D (1991) Freezing and the Glass Transition, edited by Hansen, J. P., and Levesque, D., North-Holland, Amsterdam, p.691.
[16] Duncan PD, Dennison M, Masters AJ, Wilson MR (2009) Phys. Rev. E 79, 031702–1.
[17] Durand-Keklikian L, Haq I, Matijevic E (1994) Colloids & Surfaces A 92, 267.
[18] Qazi SJS, Rennie AR, Cockcroft JK, Vickers M (2009) J. Colloid Interf. Sci. 338, 105.
[19] Qazi SJS, Karlsson G, Rennie AR (2010) J. Colloid Interf. Sci. 348, 80.

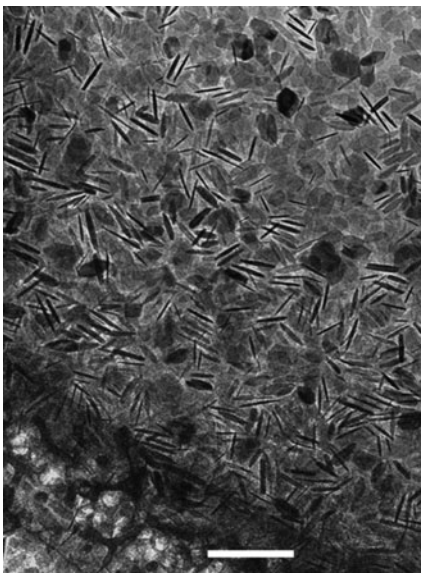

Figure 2 Cryo-TEM micrograph of particles at 20 wt% concentration showing cubatic order. Particles are present in small equiaxial domains of the size of the diameter of the particle. The sample in the thicker regions shows more order which decreases in thinner regions near the top of the micrograph. Scale bar is 200 nm

such as structured liquids[20,21] where information about texture is vital. The images were taken with a Zeiss EM 902A transmission electron microscope that was operated at 80 keV in zero loss bright field mode. Ultra fast freezing, during the sample preparation process, prevents formation of ice crystals and preserves the sample structure close to its equilibrium state. A general review of the cryo-TEM sample preparation and image recording is available elsewhere[22]. The perforated polymer film used in the sample preparation for the cryo-TEM analysis was about 300 nm thick. This gives an estimate of the sample thickness near the edges at the bottom of the image in Figure 2. In normal cases, the thickness decreases to less than 50 nm for a dilute sample at the middle of a hole in the grid. In the present case, the sample was concentrated and the sample thickness could be about 100 nm as some edge wise particle are observed close to the middle of holes in a grid (top of the image in Figure 2).

In Figure 2, more columnar stacks are observed in the thicker regions where the sample shows bulk structure of the order of few hundreds of nanometres. The very dark full hexagonal regions in the image are certainly not a single particle but could be stacks of several particles. Images from cryo-TEM are two-dimensional which make it impossible to determine how many particles lie in stacks with their large face in the plane of the sample. The stacks of discs lying edge wise out of the image are clear and they tend to be equiaxial as seen in Figure 2. In areas where the sample is thinner, the stacks are tilted and one such tilted stack is highlighted in Figure 3a. This tilt could arise from the sample preparation: flow and blotting during the preparation can distort the short columns in to tilted stacks. These regions of the sample may be too thin to allow equiaxial domains with particles of the diameter used in the present study.

Columnar stacks shown in Figures 3b,c and d illustrate some structural effects that can arise from polydispersity. Small discs (b) have more free space locally. Particles with large diameters can fit within a column (c) by tilting with respect to neighbouring particles. In some cases, (d) tilt is about 90 degrees if the gap between two particles is of the order of the diameter of a disc. The observed tilt of particles may arise from thermal motion with a sample quenched so as to reveal a range of orientations. However, on average, particles prefer to assemble in a short column of the order of the average diameter of the particle.

Analysis of several micrographs from different regions of the sample allows us to quantify the order in the structure. An average of 4.1 particles per stack in the sample is consistent with cubatic order. The length of an average column compares well with the mean diameter of particles as expected in a cubatic phase. The number of particles in a stack decreases with increasing concentration and no stacks were seen in a sample at a concentration of 30% wt. as discussed previously[19]. The average gap between the particles in a stack, determined from the cryo-TEM micrographs, is ~13 nm. This is less than twice the estimated polymer thickness(17 nm). However, if the particles are not laying exactly edge wise in the cryo-TEM images they will appear thicker and obscure the polymer regions. Both polydispersity and thermal motion of the particles are expected to have significant effects on the cubatic phase. The sample used in the current studies had a polydispersity index of 0.2 in the particle radius as discussed earlier. A cubatic phase for slightly polydisperse thin circular discs is shown schematically in Figure 4a.

Particles bigger in diameter than the column can be incorporated with tilt. If a tilted particle occurs, it may be preferentially at the end of a stack where there is more space. This might favour the cubatic structure as shown schematically in Figure 4b rather than long columns. We have observed that the particles with different dimensions separate in different columns (not shown in the micrographs in the paper). In such case, whole columns with bigger particles are tilted to obtain a column width, W, that is smaller than D, the diameter of particle in the stack. One such example is shown schematically in Figure 4b. These different structures for a polydisperse

[20] Ferreira DA, Bentley MVLB, Karlsson G, Edwards K (2006) International Journal of Pharmaceutics, 310, 203.

[21] Fan W, Snyder MA, Kumar S, Lee P, Yoo WC, McCormick AV, Penn RL, Stein A, Tsapatsis M (2008) Nature Materials 7, 984.

[22] Almgren M, Edwards K, Karlsson G (2003) Colloid Surf. A 174, 3.

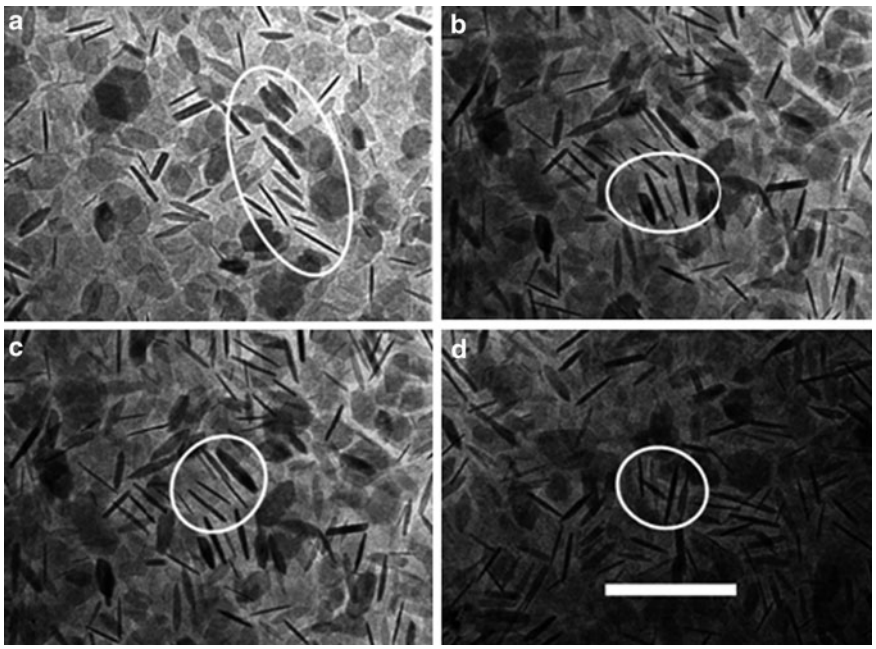

Figure 3 Illustrations of irregular packing in columns. (a) Tilt in an entire column, (b) packing of small particles within a column, (c) tilt of individual particles with respect to its neighbours in a column and (d) in some cases, smaller particle get more space between its neighbouring particles and can rotate. Scale bar is 200 nm

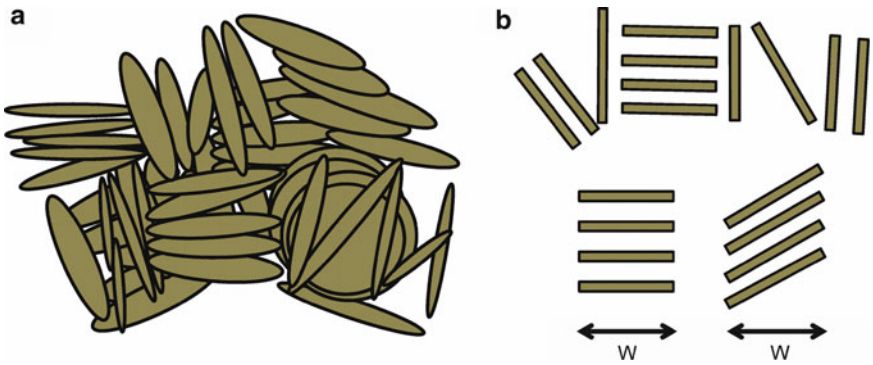

Figure 4 Diagram of cubatic phase for thin circular discs that includes particles with different diameters: (a). The domains that are locally orthogonal are shown schematically. (b). Means to pack bigger particles with tilt. If the width of the stack, W, is smaller than the diameter of the discs, D, then whole stack is tilted. Single larger or smaller particles can be inserted with tilt away from the average orientation in a stack

sample strongly alter the maximum packing density as discussed in a previous paper[19]. For perfect monodisperse hexagonal discs, the maximum packing fraction is 1. If one assumes that particles up to one standard deviation above the mean diameter will pack in columns of width defined by the mean diameter, then the maximum packing fraction for the size distribution, used in the current experiments, would be decreased to roughly 0.5. The ratio of volume fraction to maximum packing, ρ^*, would then be increased[19]. The effect on ρ^* would be even larger if we include the particles from the tail of the size distribution in Figure 1b.

It is very important to understand the effect of size shape and polydispersity on the ordered mesostructures in the design of materials with organization at nanometre length scale. This study provides a further indication of how polydispersity might alter the packing of discs and complements the observations of columnar phases[3,4]. Previous studies of dispersions of disc-like particles using X-ray and neutron scattering have not identified cubatic structure but the similarity of the scattering patterns to those of isotropic liquids would make this very difficult.

Conclusions

Locally order has been observed in cryo-TEM micrographs that resembles the computer simulations of a cubatic phase. Disc-like particles form approximately equiaxial stacks that tend to be orthogonal in adjacent domains. The structure is dominant in the thick regions. In thin regions, the sample is not thick enough to retain an equilibrium structure of several hundred nanometres and the regions may be perturbed by flow. Moderate polydispersity affects strongly on the packing of disc-like particles, it causes a large excluded volume and reduces the packing density. Incorporation of different

size particles in the observed structure indicates that the boundaries of different ordered phases with respect to concentration may be altered by a large factor. Further computer simulations would be helpful to account for the free energy of polydisperse colloids.

Acknowledgements We gratefully acknowledge a gift of Dispex N40 from Ciba Chemicals, UK that was used in the sample preparation and the help of Martin Vickers, Department of Chemistry, University College London in performing the X-ray measurements. We thank Professor Katarina Edwards, Uppsala for suggestions and advice about cryo-TEM.

Progr Colloid Polym Sci (2011) 138:67–72
DOI: 10.1007/978-3-642-19038-4_12

Multi-Bridging Polymers. Synthesis and Behaviour in Aqueous Solution

P. Malo de Molina[1], C. Herfurth[2], A. Laschewsky[2,3], and M. Gradzielski[1]

Abstract We synthesized novel hydrophobically end-capped poly(N,N-dimethylacrylamide) (PDMA) star polymers of variable functionality by the RAFT procedure. The properties of these polymers in aqueous solutions were characterised by means of DLS, SANS, and rheology measurements. It was observed that they form interconnected aggregates with a correspondingly increased viscosity. Although the static structure of these systems does not depend to a larger extent on the number of hydrophobic stickers per polymer, the dynamic properties and in particular the rheological properties vary substantially with the number of arms. An increase of non-diffusive relaxation with increasing number of arms is observed by DLS and this complex dynamic behaviour is correlated to an increase of the elastic properties of the formed aggregate networks.

Keywords end-capped • polymer network • RAFT • associative thickening

Introduction

Telechelic associative polymers have received considerable attention because of their wide range of applications as rheological modifiers of aqueous systems, either simply in water or together with other amphipiles. Up to now almost all investigations have been restricted to doubly end-capped hydrophilic polymers, i.e., bifunctional briding polymers. The most common case are hydrophobic ethoxylated urethane (HEUR) associative thickeners, which are widely used for applications and for which it has been found that the viscosity increases with a power law with increasing length of the hydrophobic sticker [1]. In particular, doubly hydrophobically end-capped polyethylene oxide (PEO) has been studied intensively with respect to its ability to form transient networks in the presence of surfactant. Such systems were for instance studied by means of small-angle neutron scattering for the case of admixing to micellar solutions [2] or microemulsions [3,4,5] and these experiments confirmed for the case of the microemulsions that the admixture of the telechelic polymer does not lead to a change of the size of the microemulsion droplets but to a substantial enhancement of the viscous properties. Due to the presence of the hydrophobic micellar or microemulsion domains this effect becomes substantially enhanced. However, already without their presence there is a tendency for formation of a transient network due to the ability to form hydrophobic network points from the hydrophobic end-caps. At a concentration of a few wt% of polymer in water then formation of viscoelastic solutions is observed [6]. From fluorescence studies a rather high polydispersity of the contained aggregates has been deduced [7] and DLS measurements have shown a multi-modal relaxation process once the concentration required for network formation is surpassed [2].

However, the topology and functionality of the bridging polymer should have a substantial effect on the structures formed and in particular on the dynamics of the networks formed by them, and thereby on their rheological behaviour. For instance the increase in functionality of the bridging polymer can be expected to introduce an additional attractive interaction into the systems. Accordingly in order to gain further insight into the relevance of the molecular architecture with respect to the properties of such bridging associative polymers we investigated polymers where we varied the number of hydrophobic stickers on one polymer molecule in a systematic fashion from 2 to 4. This was done by an appropriate synthetic strategy employing the reversible

P. Malo de Molina (✉), M. Gradzielski (✉)
[1]Stranski-Laboratorium für Physikalische und Theoretische Chemie, Institut für Chemie, Technische Universität Berlin, Strasse des 17. Juni 124, Sekr. TC7, 10623 Berlin, Germany
e-mail: paulamalodemolina@gmail.com and michael.gradzielski@tu-berlin.de
[2]Institut für Chemie, Universität Potsdam, Karl-Liebknecht-Str. 24-25, 14476 Potsdam-Golm, Germany
[3]Fraunhofer Institut für Angewandte Polymerforschung IAP, Geiselbergstr. 69, 14476 Potsdam-Golm, Germany

addition fragmentation chain transfer (RAFT) technique, which allows for a very controlled approach to such multi-armed end-capped polymers. As hydrophilic part poly(N,N-dimethyl acrylamide) was chosen, which is very well water soluble, neutral polymer. Their behaviour in aqueous solution was then studied by means of DLS, SANS, and rheology and correlated to their molecular architecture.

Experimental Section

Size Exclusion Chromatography (SEC) was performed using a mixture of 80% 0.05 M Na2SO4 in deionised water and 20% acetonitrile with a flow rate of 1 mL/min on a setup consisting of a four channel degasser SCM 400 from Spectra Physics, an isocratic pump P 1000 from Spectra Physics, a set of TSK-GEL PW columns (7.5 × 300 mm) from TOSOH Biosep (Guard, 6000, 5000, 4000, 3000), a Dawn DSP MALLS detector from Wyatt, a UV/VIS detector UV2000 from Spectra Physics and a dual detector for viscosity and refractive index η-1002 from WGE Dr. Bures. The recorded traces were analysed and processed using Astra 4.9 software from Wyatt.

Small Angle Neutron Scattering (SANS) were performed at the spectrometer PAXY at the Laboratoire Léon Brillouin (LLB, CEA-CNRS, Saclay, France) with a neutron wavelength 5 and sample-to-detector distances of 1.145 and 5.045 m. The covered range of the magnitude of the scattering vectors was from $0.07 < Q < 3.3 nm^{-1}$. The SANS data were treated according to standard procedures for absolute scaling, radial averaging, detector efficiency and background subtraction [8]. Water was used as an incoherent scatterer to calibrate the detector efficiency and the attenuated direct beam was used to determine the absolute scaling. All samples were contained in D_2O as solvent to reduce the incoherent background and increase the contrast and they were measured between 1 mm spaced Saphire windows.

Dynamic Light Scattering (DLS) were performed at 25°C using a setup consisting of an ALV7004 correlator, an ALV CGS-3 goniometer, and a He-Ne Laser with a wavelength of 632.8 nm. Cylindrical sample cells were placed in an index matching toluene vat. Autocorrelation functions were recorded under different angles between 50° and 130°.

Rheology measurements were carried out by means of a Bohlin Gemini 150 rheometer equipped with a high-frequency extension with a piezo rotary vibrator [9]. A plate-plate geometry of aluminium was used with a diameter of 40 mm. This set-up then allows for measurements up to 2000 Hz.

Results and Discussion

Polymer Synthesis and Characterization

The polymers were synthesized using reversible addition fragmentation chain transfer (RAFT) polymerization [10]. As RAFT agents a number of multifunctional trithiocarbonates designed for the R group approach were used. These RAFT agents were synthesized using a multifunctional benzyl bromide, to give an R group predetermining the number of arms the star polymer was to have. As Z groups n-dodecylthiol was employed, thereby introducing dodecyl chains as hydrophobic end linkers. The synthesis was carried out in an aqueous solution of potassium hydroxide in the presence of a phase transfer catalyst [11]. Thus, a library of RAFT agents was prepared, varying the number of arms (2, 3 and 4 arms) as well as the length of the alkyl chain. As a monomer, N,N-dimethylacrylamide (DMA) was used, which is a non-ionic hydrophilic monomer. First studies on bifunctional RAFT agents (with x=3 and 17 and y=2) had shown the usefulness of this synthetic strategy and the appropriate match of the RAFT agents with monomer DMA for achieving well controlled polymerizations [12]. Polymerizations were carried out in benzene at 90°C using 1,1′-Azobis(cyclohexane-1-carbonitrile) (V40) as initiator [13]. The use of the multifunctional RAFT agents bearing n-alkyl chains allow for the formation of amphiphilic star polymers in one step. The polymers are obtained in yields of about 90%. SEC analysis reveals polydispersities as low as 1.15 (see figure 2 a). As SEC is operated using a multi-angle laser

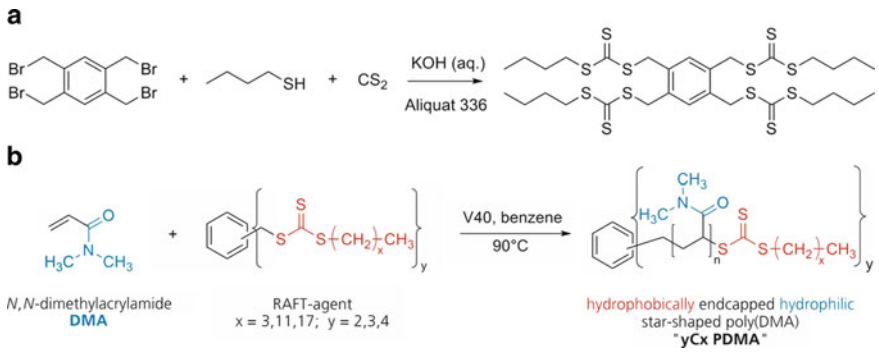

Fig. 1 Synthetic sequences employed for the preparation of the endcapped star polymers

light scattering (MALLS) detector, it is possible to obtain absolute values for the molar masses, using dn/dc = 0.161 mL/g [14]. To verify the star structure of the polymers, M_w is plotted over the elution volume (figure 2 b). As the plot shows, a 4 arm star polymer has a higher molecular weight at the same elution volume than the 3 arm star polymer, which has a higher molecular weight at the same elution volume than the linear polymer. As the elution volume is directly correlated to the hydrodynamic radius of the polymer in solution, this indicates that the star polymers feature a more compact structure than the linear polymer, which is a typical behaviour of star polymers. The finally obtained products had a M_w of 6–8 · 10^4 g/mol (table 1) with two, three, or four dodecyl chains as endgroups, correspondingly named 2C12PDMA, 3C12PDMA, and 4C12PDMA.

To verify high end group functionality, UV/vis spectra of the polymers are recorded. As the trithiocarbonate end groups show a high absorption around 309 nm, the absorption can be used to calculate the molar mass of the polymer using $M_n = \frac{\varepsilon \cdot m \cdot d}{A \cdot V}$, where ε is the absorption coefficient, m is the mass of the polymer, d is the optical path length, A is the absorption and V is the volume of the solution [12, 15, 16]. Comparing the M_n results from the UV/vis end group analysis with the M_n from MALLS-SEC, the end group functionality was calculated to be in the range of 90%.

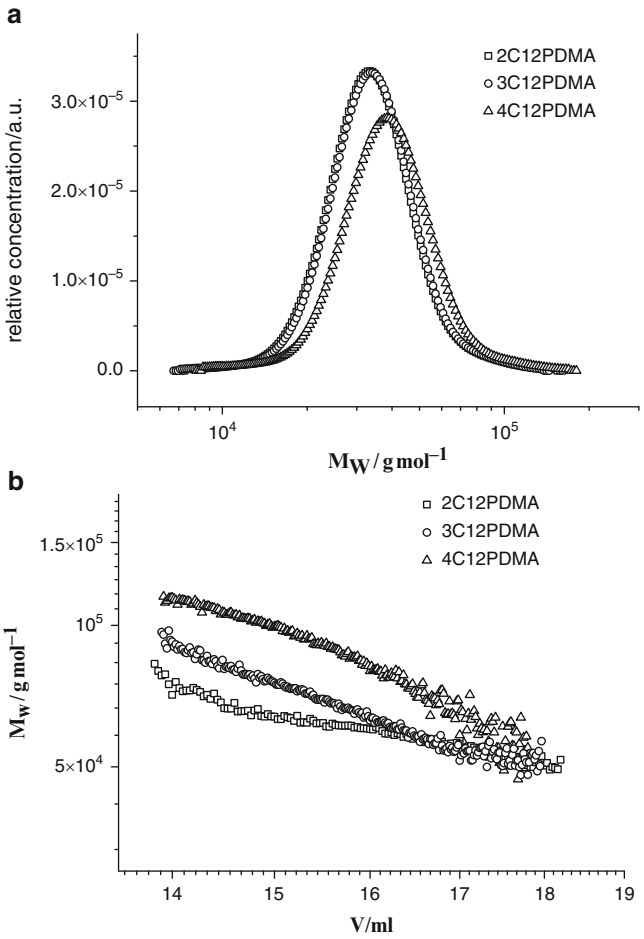

Fig. 2 (a) Size-exclusion chromatograms (SEC) for the polymers with different numbers of arms. (b) the corresponding results of the MALLS detection

Physico-Chemical Characterisation of the Associating Behaviour of the Multi-Bridging Polymers in Water

The SANS patterns (Figure 3) for 5wt% solutions of 2C12, 3C12 and 4C12 PDMA in D_2O show no significant difference. In all cases a relatively high scattering intensity is observed, which indicates the formation of aggregates, but apparently the number of arms has no impact on their structure. All curves exhibit a characteristic correlation peak around 0.27 nm^{-1} (indicating a mean spacing of aggregates

Table 1 Molecular weight of the polymers, M_W, obteined by GPC, volume fraction of the dodecyl stickers, ϕ_{HC}. [a)] Parameters calculated by the position of the peak: aggregation number (per polymer molecule), N_{agg}, aggregation number of the stickers, N_{St} and radius of the cores, R_{core}. [b)] Parameters derived from the detailed fits: radius of gyration, R_G, correlation length inside the star, ξ and hard sphere radius, R_{HS}

Polymer	M_w/ KDa	$\phi^{a)}_{HC}$ ·10^4	$N^{a)}_{agg}$	$N^{a)}_{St}$	$R^{a)}_{core}$/ nm	$R^{b)}_{G}$/ nm	$\xi^{b)}$/ nm	$R^{b)}_{HS}$/ nm
2C12PDMA	61	6.2	7.6	15	1.3	7.5	3.9	10.5
3C12PDMA	69	8.2	6.7	20	1.4	6.6	4.4	9.8
4C12PDMA	83	9.2	5.6	23	1.5	6.8	4.6	10.5

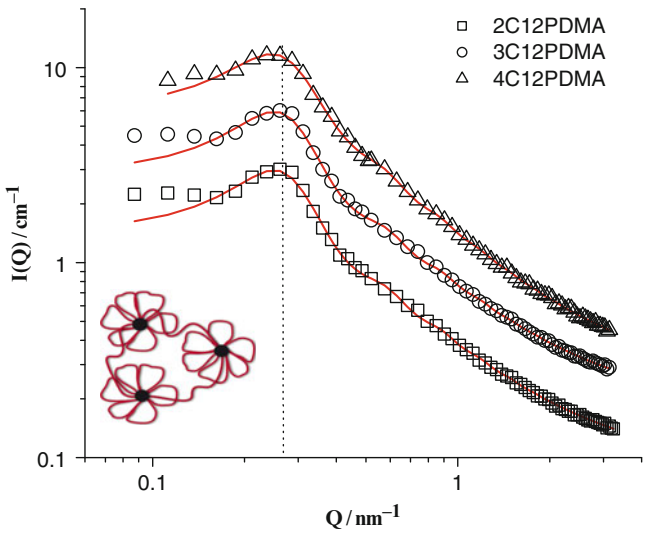

Fig. 3 SANS patterns of the aggregates of 2C12(squares), 3C12(circles) and 4C12 (triangles) PDMA at a concentration of 5 wt% in D2O at room temperature. The absolute intensity is correct for 2C12PDMA and subsequent curves are multiplied by a factor 2^n. The lines correspond to the fitted curves with a star form factor and a hard sphere structure factor

of 24 nm) and show a scattering pattern as typically observed for globular aggregates that interact repulsively. Assuming a cubic packing of the hydrophobic cores, one can obtain the number of the dodecyl chains per micelle (N_{St}) and, therefore the average number of polymer molecules associated to one micelle (N_{agg}). Considering the relatively low volume fraction of hydrophobic alkyl chains of between 0.06-0.09% (table 1) the observation of such a correlation peak in an uncharged system is rather surprising. The only explanation for its appearance is that the hydrophilic polymer chains (which have a much larger volume fraction and even more so as the PDMA will be strongly hydrated) introduce significant repulsive interaction into this system. The attractive part of the interaction due to bridging is overwhelmed by an effective repulsive interaction due to the numerous surrounding hydrophilic chains that lead to a substantial steric hindrance. It can be assumed that the scattering observed at middle q arises primarily from the hydrophobic alkyl chains that form hydrophobic cores, while the water-soluble polymer is homogeneously distributed around these cores.

Assuming that the polymers self-assemble into flower-like micelles (inset of fig 3) that interact with a spherically symmetric potential, the scattering intensity can be expressed as

$$I(Q) = nV^2 \Delta\rho^2 P(Q) S(Q) \tag{1}$$

where n is the number density of scatterers, V the volume of the scatterers, $\Delta\rho^2$ is the square of the difference between the coherent scattering length of the micellar unit and the one of the solvent, P(Q) the form factor and S(Q) the structure factor that takes into account the interactions between aggregates. In order to describe de conformational structure of the aggregates we emploied a form factor for a star proposed by Fetters et al [17]

$$nV^2 \Delta\rho^2 P_{star}(Q) = I(0) e^{-\frac{1}{3}Q^2 R_G^2} + \frac{4\pi\alpha}{Q\xi} \times \frac{sin[\mu tan^{-1}(Q\xi)]}{[1+Q^2\xi^2]^{\mu/2}} \Gamma(\mu) \tag{2}$$

with $\mu = 1/\nu - 1$ where ν is the excluded volume parameter, R_G is radius of gyration, I(0) is the forward scattering, α is the scale parameter for the fractal term, ξ is the correlation length inside the star and $\Gamma(\mu)$ is the gamma fuction of argument μ. To account for the repulsive interactions a model of hard spheres structure factor, $S(Q, R_{HS}, \phi_{HS})$ in the Percus Yevik aproximation [18, 19] was employed, where R_{HS} is the effective hard sphere radius and the volume fraction of the hard spheres (ϕ_{HS}) is given by the number density of hydrophobic cores given by

$$n = \frac{3\phi_{HS}}{4\pi R_{HS}^3} = \frac{N_{AV} C w_{St}}{M_{St} N_{St}} \tag{3}$$

where N_{AV} is the Avogadro number and Cw_{St}, M_{St}, N_{St} are the weight concentration, molecular weigth and the aggregation number of the stickers. According to eq.3 the volume fraction, ϕ_{HS}, and the hard sphere radius, R_{HS}, are directly related to each other and enter only as an additional fit parameter. One observes that R_{HS} (table 1) is always about 10nm, irrespective of the number of arms. This is reasonable as the PDMA chains attached to the hydrophobic cores are always of similar length.

This model fits our experimental data rather well (fig. 3) and accordingly seems to be one accurate description of the structural situation. Apparently the hydrophobic domains formed by the various polymers are rather similar irrespective of the number of arms.

In order to obtain further insight into the structural and dynamical properties of these multi-bridging polymers in aqueous solution DLS measurements were done. Examples (for 90°) for the obtained intensity autocorrelation functions are shown in Figure 4. One always observes a rather complex relaxation behaviour that proceeds via three clearly separated relaxation modes, as similarly observed before for the case of $C_{12}EO_{460}C_{12}$[2]. This demonstrates that one does not observe a simple diffusion process here but the complex behaviour has to be associated with the network formed by the polymers in solution.

The $g^2(t)$ data were fitted to a sum of one simple exponential and two stretched exponential functions.

$$g^2(t) - 1 = \left[a_1 \cdot e^{-t/\tau_1} + a_2 \cdot e^{(-t/\tau_2)^{\beta_1}} + a_3 \cdot e^{(-t/\tau_3)^{\beta_3}} \right]^2 \tag{4}$$

From the angular dependence of the relaxation times (see inset of fig. 4) one can conclude that the fast relaxation is

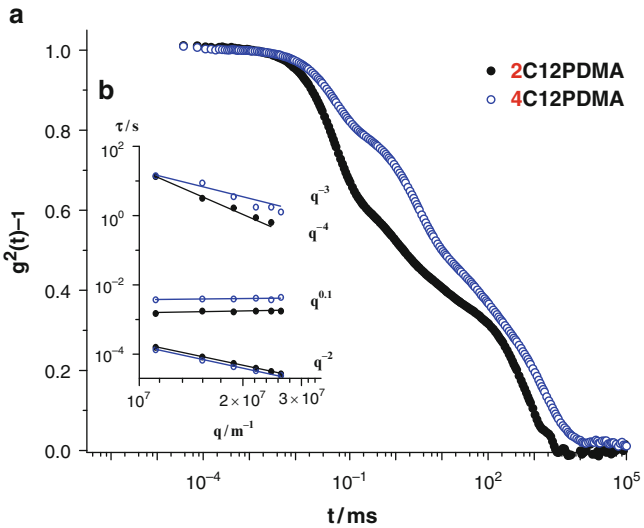

Fig. 4 Intensity correlation function −1 as a function of time for solutions of 2C12 and 4C12 PDMA 5wt% in water at a scattering angle of 90° and a temperature of 25°C. The inset shows the q dependency of the three relaxation times

purely diffusive as shown by its q^{-2} dependence. The effective diffusive coefficients are $D_{eff}(2C12) = 5.75 \cdot 10^{-11}$; $D_{eff}(4C12) = 6.44 \cdot 10^{-11} m^2 s^{-1}$ that correspond to apparent hydrodynamic radii of 3.8 and 4.2 nm respectively. This value is in rather good agreement with the size of the hydrophobic cores observed by SANS (table 1). The somewhat larger value for the hydrodynamic radius is presumably due to the slowing down of the diffusion process by the PDMA corona of these aggregates. The intermediate relaxation mode is almost not q dependent while the slow relaxation mode shows a rather strong dependency with the scattering vector, following a power law of 3–4, as it is characteristically observed for viscoelastic networks. The intermediate relaxation time is in the range observed for the rheological relaxation and appears to be related to the macroscopic relaxation process of this network. It is interesting to note that the first, diffusive mode becomes much smaller in amplitude when going from the 2-arm to the 4-arm polymer, which indicates that the movement of the particles is increasingly hindered with increasing number of arms. At the same time in particular the intermediate relaxation mode becomes more prominent, which points to an increasing elasticity of the samples (in agreement with the rheological observations).

All samples are highly viscous and were correspondingly characterised by means of rheological experiments in order to study the frequency dependent viscoelastic properties of these transient networks. The obtained values for storage modulus G' and loss modulus G'' are given in fig. 5. Both are increasing for lower frequencies but not with the power law of 2 and 1, respectively, as predicted by the Maxwell model. Accordingly these are not simple rheological systems but G' nonetheless effectively approaches a plateau value for frequencies above 100 Hz. In addition, the 2C12PDMA sample shows a deviation of the G' curve at low frequencies that might be related to a slower relaxation mechanism that becomes visible here.

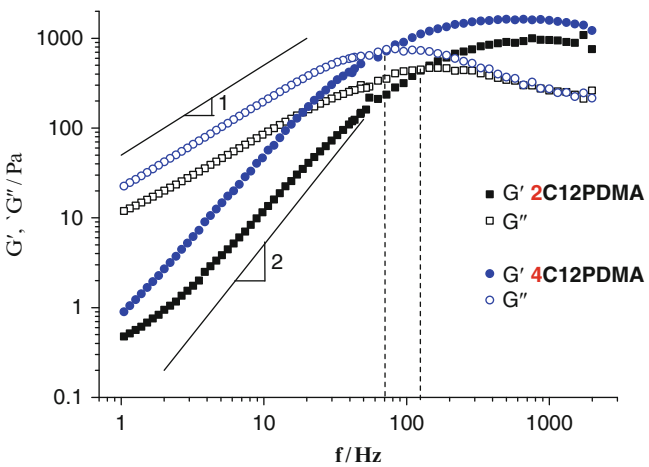

Fig. 5 Storage (G') and loss modulus (G'') as a function of the frequency (f) for solutions of 2C12PDMA and 4C12PDMA for a concentration of 5wt% in water at room temperature. The lines indicate the respective power of 1 and 2 predicted by the Maxwell model

The cross over point of G' and G'' can be taken as an effective rheological relaxation frequency from which a characteristic relaxation time can be calculated that increases from 7.9 to 15.8 ms, when going from the 2-arm to the 4-arm polymer, where this time is related to the intermediate relaxation process of DLS, that shows no angular dependence (17ms for 2C12PDMA and 34ms for 4C12PDMA) since they are in the same order of magnitude and follow exactly the same tendency. At the same time, the plateau value of the elastic modulus, G_0, increases from 800 to 1600 Pa. This shows that with increasing number of arms the relaxation process becomes slower and the elastic properties of the network increase.

According to the basic theory of networks [20] high frequency storage modulus is simply given by $G_0 = \nu K_B T$, where ν is the number density of elastically connected points. This theory can be applied to the experimental data and from the number density on can calculate the corresponding theoretical aggregation numbers that are 2 and 1 for 2C12PDMA and 4C12PDMA, respectively. This means that in the network every 2C12PDMA molecule stores $\frac{1}{2}$kT of elastic energy, while this value is 1 kT for the 4C12PDMA, i.e., the elastic energy is directly proportional to the number of arms. N_{St} would be 4 in both cases.

Conclusion

Poly(N,N-dimethylacrylamide) (PDMA) star polymers with 2, 3, and 4 arms and with dodecyl chains as hydrophobic end-caps were obtained in high yield with narrow polydispersities by means of the RAFT technique. At sufficiently high concentration they form interconnected hydrophobic domains, i.e., a transient network. SANS experiments show that these hydrophobic domains contain about 20 dodecyl chains and they interact repulsively due to the PDMA chains that separate them. While the static structure is only very little affected by the number of arms this applies not at all to the dynamic properties as observed by DLS and rheology. Here one observes in DLS a complex, trimodal relaxation process, where the slower modes become more pronounced with increasing number of arms. The fast mode corresponds to the diffusion of the hydrophobic domains while the second mode shows no q-dependence and corresponds in its values to the time deduced from the cross-over of G' and G'' in the oscillatory rheological experiments. Finally the slowest motion shows a rather pronounced q-dependence and is presumably linked to a more complex relaxation mechanism of

the whole network that could be related to deviations of the rheological curves at low frequency. Rheology shows that at a given total composition of the system the shear modulus increases with the number of arms, while at the same time the characteristic relaxation time becomes longer. This demonstrates that the number of arms of these multi-bridging associative polymers has a profound impact on the dynamic properties of the transient networks formed by them. Accordingly appropriate control of the morphology of the polymers allow to control the dynamic properties of the networks formed by them.

Acknowledgements This work has been funded via the DFG grant GR1030/9-1 and LA611/8-1. For SANS beamtime allocation we are grateful to LLB, Saclay and it was funded by the NMI3 EU program. For very valuable help with performing the SANS experiments we are thankful to Laurence Noirez (LLB, Saclay). Furthermore we thank C. Wieland (Fraunhofer IAP, PotsdamGolm) for help with SEC measurements. P.M.M. gratefully acknowledges a grant from DAAD-La Caixa

References

1. T. Annable, R. Buscall, R. Ettelaie, D. Whittlestone, Journal of Rheology **37**(4), 695 (1993)
2. E. Alami, M. Almgren, W. Brown, J. Francois, Macromolecules **29**(6), 2229 (1996)
3. M. Gradzielski, A. Rauscher, H. Hoffmann, Journal De Physique IV **3**(C1), 65 (1993)
4. M. Filali, M.J. Ouazzani, E. Michel, R. Aznar, G. Porte, J. Appell, Journal Of Physical Chemistry B **105**(43), 10528 (2001)
5. S. Maccarrone, H. Frielinghaus, J. Allgaier, D. Richter, P. Lindner, Langmuir **23**(19), 9559 (2007)
6. J.F. Berret, Y. Sereo, B.Winkelman, D. Calvet, A. Collet, M. Viguier, Journal Of Rheology **45**(2), 477 (2001)
7. R.J. English, I. Ratcliffe, R.L. Blanchard, B.J. Parsons, Macromolecules **40**(18), 6699 (2007)
8. P. Lindner, T. Zemb, *Neutron, X-ray and Light Scattering: Introduction to an Investigative Tool for Colloidal and Polymeric Systems*. (North-Holland,. Amsterdam, 1991)
9. L. Kirschenmann, W. Pechhold, Rheologica Acta **41**(4), 362 (2002)
10. G. Moad, E. Rizzardo, S.H. Thang, Australian Journal Of Chemistry **62**(11), 1402 (2009)
11. I. Degani, R. Fochi, A. Gatti, V. Regondi, Synthesis-Stuttgart (11), 894 (1986)
12. K. Skrabania, W. Li, A. Laschewsky, Macromolecular Chemistry And Physics **209**(13), 1389 (2008)
13. H. Chaffey-Millar, M.H. Stenzel, T.P. Davis, M.L. Coote, C. Barner-Kowollik, Macromolecules **39**(19), 6406 (2006)
14. A.J. Convertine, B.S. Lokitz, A.B. Lowe, C.W. Scales, L.J. Myrick, C.L. McCormick, Macromolecular Rapid Communications **26** (10), 791 (2005)
15. W. Wang, K. Troll, G. Kaune, E. Metwalli, M. Ruderer, K. Skrabania, A. Laschewsky, S.V. Roth, C.M. Papadakis, P. Muller-Buschbaum, Macromolecules **41**(9), 3209 (2008)
16. A.M. Bivigou-Koumba, E. Gornitz, A. Laschewsky, P. Muller-Buschbaum, C.M. Papadakis, Colloid And Polymer Science **288** (5), 499 (2010)
17. W.D. Dozier, J.S. Huang, L.J. Fetters, Macromolecules **24**(10), 2810 (1991)
18. J.K. Percus, G.J. Yevick, Phys. Rev. **110**(1), 1 (1958)
19. D.J. Kinning, E.L. Thomas, Macromolecules **17**(9), 1712 (1984)
20. M.S. Green, A.V. Tobolsky, The Journal of Chemical Physics **14** (2), 80 (1946).

Progr Colloid Polym Sci (2011) 138:73–80
DOI: 10.1007/978-3-642-19038-4_13

Analysis and Prediction of Cluster Formation

B.A. Di Giovanni, R.G. Holdich, and V.M. Starov

Abstract An experimental and theoretical analysis of the interaction of titanium dioxide particles during coagulation was performed, using laser light dynamic scattering (LDS) and both von Smoluchowski and reversible coagulation approaches. For cluster formation, different initial particle numbers and different shear rates were investigated and the experimental data were fitted to a mathematical model based on aggregation and disaggregation processes. The primary particle size was less than 1 micrometre, but in all cases the LDS information showed that primary clusters of 3.5 micrometres were rapidly formed, which then went on to cluster further to provide larger aggregates. Hence, the modelling approach was one of cluster-cluster aggregation and disaggregation, rather than primary particle aggregation.

Keywords Reversible coagulation • Irreversible coagulation • Titanium dioxide

Introduction

Interaction of particles is a very important topic in particle technology concerning both natural and industrial fields, and this work is part of a more comprehensive investigation in to solid-liquid separations. The behaviour of single particles and non-interacting concentrated suspensions is well understood thanks to Stokes and other fundamental theories [1]. Nevertheless, there is a problem when the particles are able to interact with each other in order to form different dynamic entities [2]. The main aim of this paper is to study how colloidal titanium dioxide interacts, starting from an experimental investigation using laser light scattering, in order to monitor the aggregation process. The relevance of cluster formation [3], a theoretical approach based on von Smoluchowski [4] and a mathematical model suitable for aggregation and disaggregation processes occurring simultaneously [5] are considered. The latter was used to model the experimental trend of the change of number of clusters with time.

R.G. Holdich (✉)
Department of Chemical Engineering, Loughborough University, Loughborough, LE11 3TU, UK
e-mail: R.G.Holdich@Lboro.ac.uk

Fundamentals

The process which considers the destabilization of the particles, through the reduction of the repulsive forces is called coagulation [6]. In particular, the addition of electrolytes (coagulants) in solid-liquid suspensions will affect the thickness of the double layer with a reduction of it [7]. By using appropriate electrolytes as well as a specific amount of them, the repulsion forces might be then reduced or completely cancelled. In the first case the mechanism referred to potential energy among two particles is called slow; rapid coagulation occurs when only attractive forces are acting in the system [8]. All the mechanism mentioned are only a part of the well-known DLVO theory [9].

Once the coagulation process starts the particles that are increasing in size might be subjected to different mechanisms of breakages: shattering, rupture and erosion [10]. The occurrences of interactions among different entities are primary-primary particles, primary particle-clusters and cluster-clusters. The structure of the reformed clusters will be weak and fragile [11]. In particular, when both aggregation and disaggregation processes occur the coagulation is called reversible. In irreversible coagulation, instead, disaggregation process is not considered [9].

Von Smoluchowski [4] was the pioneer of the study of particle interactions using a population balance in order to explain and illustrate the variation over time of the number of particles changing in size due to the

formation of aggregates. The population balance equation is given by:

$$\frac{dn_k}{dt} = \frac{1}{2}\sum_{\substack{i+j\to k\\ i=1}}^{i=k-1} k_{ij}n_i n_j - n_k \sum_{\substack{i+j\to k\\ i=1}}^{\infty} k_{1k}n_1 \qquad (1)$$

where n_i, n_j and n_k are the number of particles having size i, j and k, respectively. Two different kinetic rate constants are presented: k_{ij} which consider the formation of aggregates of size k and k_{ik} which consider the loss of aggregates of size k due to the formation of larger aggregates.

The kinetic rate constants can have different functionality depending on the types of transport mechanisms under which the particles are subjected. In details, perikinetic aggregation is the mechanism when the particles are only subjected to Brownian motion and orthokinetic aggregation is the mechanism when the particles are subjected to any kind of shear field. Sometimes, when the conditions are suitable, particles might come together following both of the mechanisms mentioned above [2, 6]. However, it is necessary to note that perikinetic aggregation is significant only for particle size less than 1 μm and subjected to a shear field less than 10 s^{-1} [2]. When perikinetic aggregation occurs, the kinetic rate constant is defined by:

$$k_{ij} = \frac{2KT}{3\mu}\frac{(x_i + x_j)^2}{x_i x_j} \qquad (2)$$

where K is the Boltzmann's constant, T is the absolute temperature, x_i and x_j are the particles radii of i and j respectively, μ is the dynamic viscosity. In case of orthokinetic aggregation instead:

$$k_{ij} = \frac{4}{3}G(x_i + x_j)^3 \qquad (3)$$

where x_i and x_j are the particles radii and G is a variable depending on the shear field [12]. Considering the case of monosize particle distribution, the kinetic rate described in equation (2) will assume a constant value. There is a strong dependence from the particles radii (cubic power) in case of orthokinetic aggregation. Equation (1) is only valid in case of irreversible coagulation since there are no considerations of aggregate breakages due to thermal or hydrodynamic stresses [13]. One of the first models which considered the breakages of aggregates is presented by Harris et al. [14] in which they introduce a size distribution function including various formations of aggregates and break-up models. An extra parameter, called fraction of collision (α), is introduced in order to count the amount of successful collisions under which larger aggregates will be formed. Serra and Casamitjana [15] discussed and predicted experimental data, using latex particles placed in couette flow system. A population balance was considered with the introduction of two parameters called "effective probability for collision" to count aggregation and "break up coefficient" for shear fragmentation. Both parameters were investigated under different shear fields and volume fraction of the particles.

A model, in which there are two different but related kinetic constants, was presented by Starov et al. [5]. The model is suitable for only reversible coagulation due to the consideration of both aggregation and disaggregation processes. Only single particles are considered joining clusters already formed and only single particles can be obtained from the disaggregation. Defining k (= 1, 2, 3, ...) as the size of the clusters, it is possible to distinguish four different steps which are two for the aggregation process and two for the disaggregation process:

Taking the four possible events in consideration and

AGGREGATION	DISAGGREGATION
1) $A_1 + A_n \rightarrow A_{n+1}$	3) $A_{n+1} \rightarrow A_1 + A_n$
2) $A_1 + A_{n-1} \rightarrow A_n$	4) $A_n \rightarrow A_1 + A_{n-1}$

introducing two rate kinetic constants, "**a**" for the aggregation process and "**b**" for the disaggregation process, the following system of equations can be written:

$$\frac{dN_1}{dt} = -aN_1N - aN_1^2 + b(N - N_1) + bN_2 \qquad (5)$$

$$\frac{dN_k}{dt} = aN_{k-1}N_1 - bN_{k+1} - bN_k - aN_kN_1 \quad \text{for } k = 2, 3, \ldots \qquad (6)$$

where:

$$N = \sum_{1}^{\infty} N_k \qquad (7)$$

is the total number of clusters. The initial conditions, defining N_0 the initial number of primary particles, are:

$$N = N_0$$
$$N_k = 0 \quad \text{for } k = 2, 3, \ldots$$

This model has been used in this paper in order to fit the experimental data regarding the kinetic of aggregation at different shear fields. A discussion about the assumptions and all the experimental and predicted results can be found later.

Material

The powder used in the experiments was commercial AEROXIDE titanium dioxide P25 (Evonik Industries AG). This powder is a mixture of the two main forms of titania: anatase (80%) and rutile (20%). The particle density and the refractive index (referred to the water) were 4.03 g/cm^3 and 1.90 respectively. Titania suspensions were prepared in deionised water, in which sodium nitrate (Fisher Scientific UK Ltd) and magnesium sulphate (Sigma-Aldrich Co.) were previously added in order to have 10^{-3} M solutions. The primary particle size measured by LDS technique was 0.1 μm (in distilled water). However, as shown in Figures 1a and 1b, P25 is formed of nano-primary particles. These nano primary particles have a regular spherical shape and a size around 21 nm. Such small particles with very high specific surface (50 ± 15 m^2/g) are highly "reactive". The stabilisation occurs with the formation of large aggregates (clusters) having different shape, different density and different porosity from the primary particles (Figure 1b). Further aggregation, among clusters, might be still be present with highly porous final structures (Figure 1a). The construction, of such large structures, arises from the specific process of preparation of P25 powder which is called AEROSIL. For this reason, 0.1 μm was identified as "primary cluster" size and interactions cluster-cluster were considered.

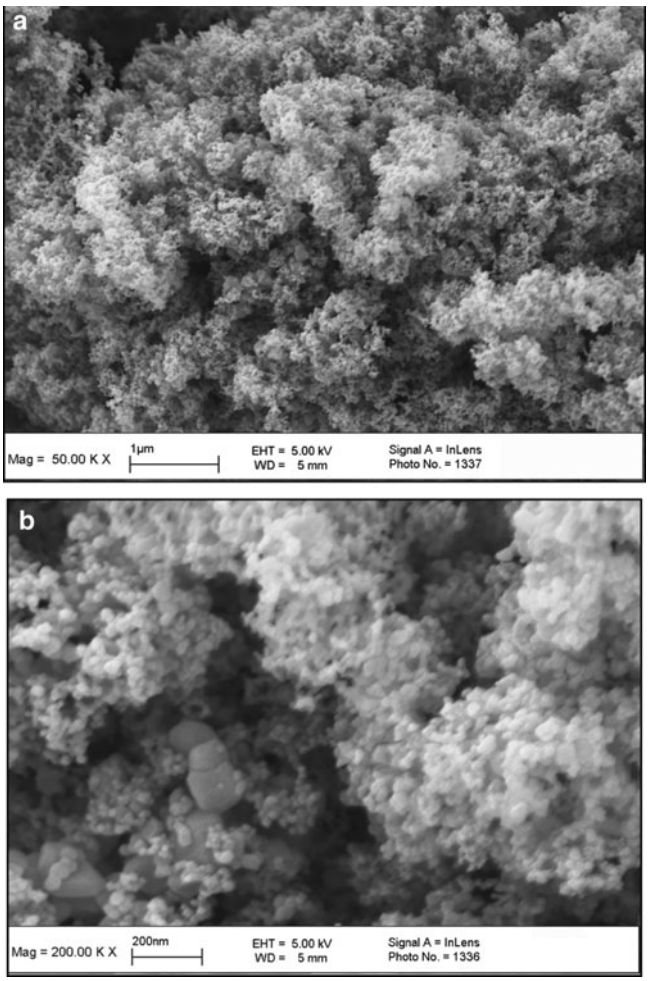

Fig. 1 (**a**) Scanning electron microscopic photograph P25-Magnification 50K X (**b**) Scanning electron microscopic photograph P25-Magnification 200K X

Experimental Procedure

A laser diffraction particle sizing instrument Horiba LA-920 was used to measure particle/cluster size by dynamic light scattering technique. The optical system includes a He-Ne laser for large particles and tungsten halogen lamp for fine particles. The instrument is equipped with a circulation system which uses a centrifugal pump and it is also provided of an ultrasonic probe. Careful cleaning of the cell was done before the start of each run in order to avoid the possible presence of material sticking to the cell walls and the possibility of influencing the results. The obscuration, which is an important parameter in laser diffraction technique [16], was always within 5% to maintain the validity of the results.

Two (corresponding to 34 mg of dry powder) or three (51mg) droplets of suspension having a concentration of 1% by volume, were added to the sample vessel which was filled with 135 mL of solution containing 10^{-3} M of $NaNO_3$ and 10^{-3} M of $MgSO_4$. Naturally, the concentration of titanium dioxide in the Horiba vessel decreased drastically from the initial 1% v/v concentration due to dilution: this point is connected with the requirement to keep the light transmission within an acceptable range. A larger amount of sample caused the obscuration level to be too high. The initial value of the built-in pump speed for all the experiments was always one. Five different shear field levels were investigated and each run was stopped when the mean diameter reached a constant value. Although, maximum sonication was always used, it was not possible to obtain the primary particle size in a short time. Only subjecting samples to a very long period time of sonication led to have the primary cluster size (dispersion of the droplets in distilled water).

Results and Discussion

A preliminary investigation was performed in order to understand which kind of coagulation occurred. In this case the sample was subjected to two different shear field levels for a period of time long enough to reach a steady state based on constant size. In all experiments, the size at the beginning

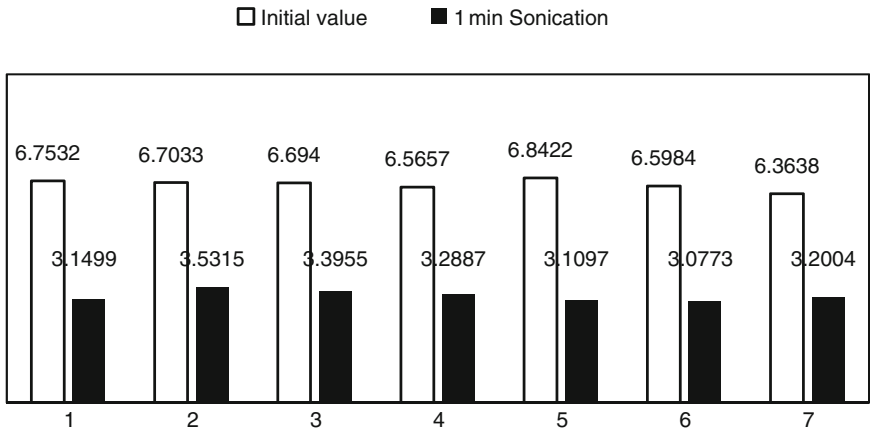

Fig. 2 Reproducibility of initial mean size and first value after sonication for 7 repeat experiments

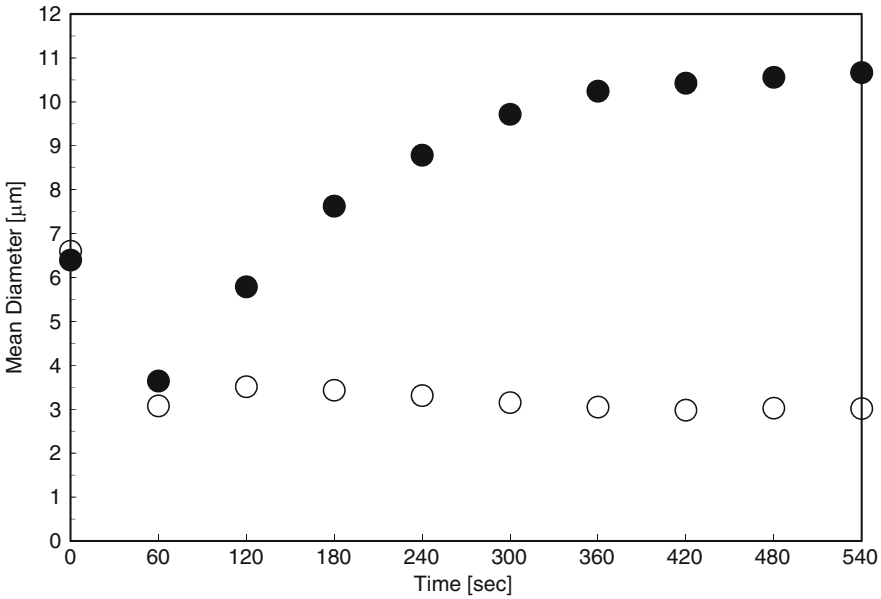

Fig. 3 Trend of the mean diameter over time for two different shear field levels: pump speed 1 (●) and pump speed off (○)

and after sonication (1 minute) was recorded at the same value of shear field value (pump speed 1). The mean diameter by volume was the variable under investigation. Multiple tests were performed as test of data reproducibility which was found to be good (see Figure 2).

It is evident that the mean value after 1 minute of ultrasonic energy is not the primary particle size, but a fairly consistent value of 3.2 micrometres was provided. A large amount of energy (20 minutes of sonication) was not even enough to achieve the primary particle size. For this reason, the following theoretical investigation considers "primary cluster size" instead of primary particle size.

In Figure 3, the time evolution of the mean diameter for two different values of pump speed is presented. In particular when the shear field level is zero, the mean diameter maintains a fair constant value, achieved after 1 minute of sonication, over all the recorded time. Different behaviour is evident when the pump speed is kept constant at a value of 1: the mean diameter increases from 3.2 micrometre up to reach a steady state correspondent to a mean diameter around 11 micrometres. So, the black circles form an increasing trend over time indicating the presence of coagulation similar to orthokinetic but possibly reversible. Furthermore, the steady value at the end of the test suggests the clear equilibrium between both aggregation and disaggregation processes. By the trend of the white circles the absence of significant perikinetic coagulation can be affirmed.

The evident presence of orthokinetic type coagulation led to have an investigation with different shear field levels. In particular, five different values of shear field levels (corresponding to five different values of pump speeds) were used, in order to understand how the shear affects the aggregation process.

As expected, looking at Figure 4, the greater the shear field level the smaller the ultimate aggregate size is due to

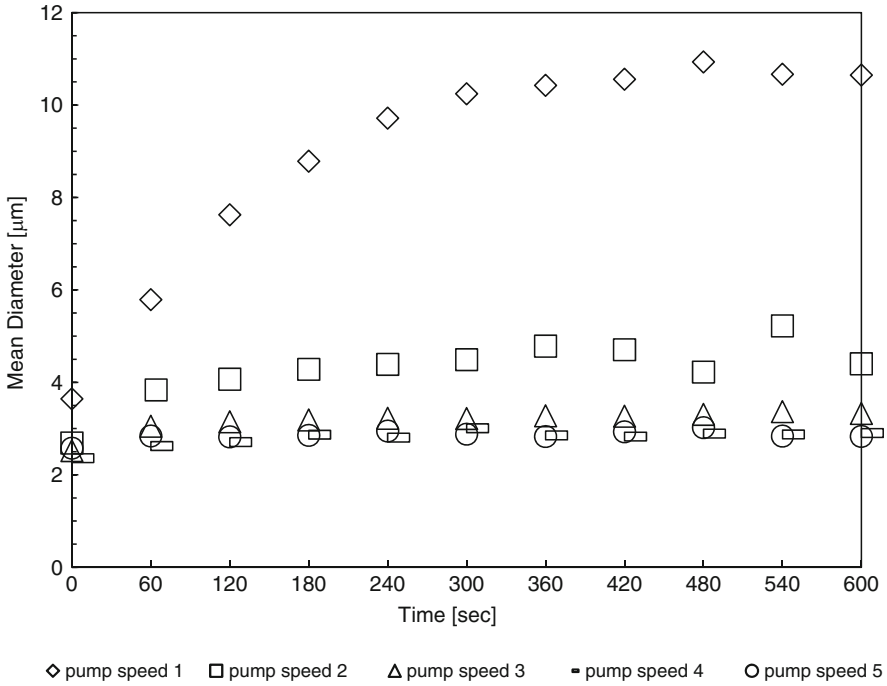

Fig. 4 Mean diameter against time for five different values of shear field levels

Table 1 Number of primary particles in clusters formed at equilibrium at different pump speeds

Solidosity:		0.7 % v/v		1 % v/v		3 % v/v	
Pump speed (-)	Equilibrium Cluster Diameter (μm)	Number primary particles in cluster (-)	Number of clusters (-)	Number primary particles in cluster (-)	Number of clusters (-)	Number primary particles in cluster (-)	Number of clusters (-)
1	10.6	1057	2*10^8	1494	1*10^8	4528	4*10^7
2	4.4	75	3*10^9	106	2*10^9	320	6*10^8
3	3.3	32	6*10^9	46	4*10^9	138	1*10^9
4	2.9	21	9*10^9	30	6*10^9	92	2*10^9
5	2.8	20	9*10^9	28	7*10^9	85	2*10^9

the continuous breakages of the larger aggregates. The equal starting value in all tests was achieved subjecting the sample at the lowest shear field available (corresponding to pump 1). Once the initial value was recorded the increment of the shear field was set.

An analysis of the initial number of "primary clusters" and final number of clusters, during aggregation process, has been done. Experimentally was found that the initial amount of "primary clusters" in the system does not affect the final size of the aggregates. Considering the initial number of the "primary clusters" within two drops and making the following assumptions:

- shape of clusters perfectly spherical
- "primary clusters" randomly placed into each cluster
- clusters with constant value of porosity
- "primary clusters" considered as primary particle

it was possible to calculate the number of clusters and the number of "primary clusters" within the clusters. Relation (8) shows how the initial number of clusters was calculated.

$$N_0 = \frac{6}{\pi}\frac{C_0}{d_0^2}(V_s + V_l) \tag{8}$$

where C_0 is the concentration by volume of the droplets, d_0 is the initial cluster diameter, V_s and V_l are the volume of the solids and of the liquid respectively (of the droplets added to the Horiba reservoir). With the appropriate modifications the number of clusters was also calculated.

As shown in Table 1, three different values of cluster solidosity were considered for the cluster characterisation. The two lower values were the initial solid concentration of the suspensions made for batch settling tests; the larger one is the final average concentration value of the sediment, resting on the base of the vessel, at the end of the sedimentation tests. Higher pump speeds (shear field levels) cause a larger amount of clusters due to the breakages of the larger ones [17]. This effect leads to smaller cluster diameter and a less number of primary clusters within each cluster.

Considering the assumptions already mentioned above a fair match of the experimental data was found with the use of the mathematical model which considers both aggregation and disaggregation processes [5]. In order to run computer simulations (COMSOL Multiphysics 3.5a), both kinetic constants for aggregation and disaggregation were combined in a single parameter called "**c**". The new parameter, defined as the ratio of the kinetic disaggregation constant rate (**b**) and the kinetic aggregation constant rate (**a**), simplified the analysis to have only a single "curve-fitting" parameter rather than two. The initial number of "primary clusters" and final numbers of clusters were also specified.

Reasonable values for the parameter **c** having a good match between the experimental and predicted results are shown in Figure 5. The plateau of each simulated curve gives the average number of clusters for each value of shear field [17].

In Figure 6 the different values of the parameter **c** versus the pump speed values (shear field levels) are plotted. As expected the value of **c** increases with increasing the shear field level.

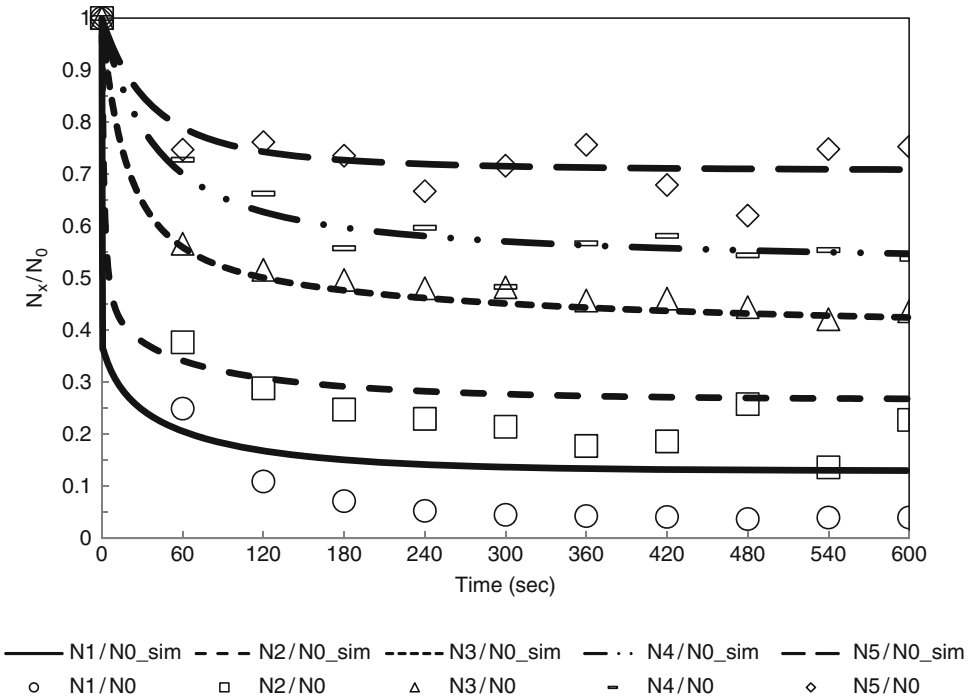

Fig. 5 Experimental and simulated time evolution of clusters

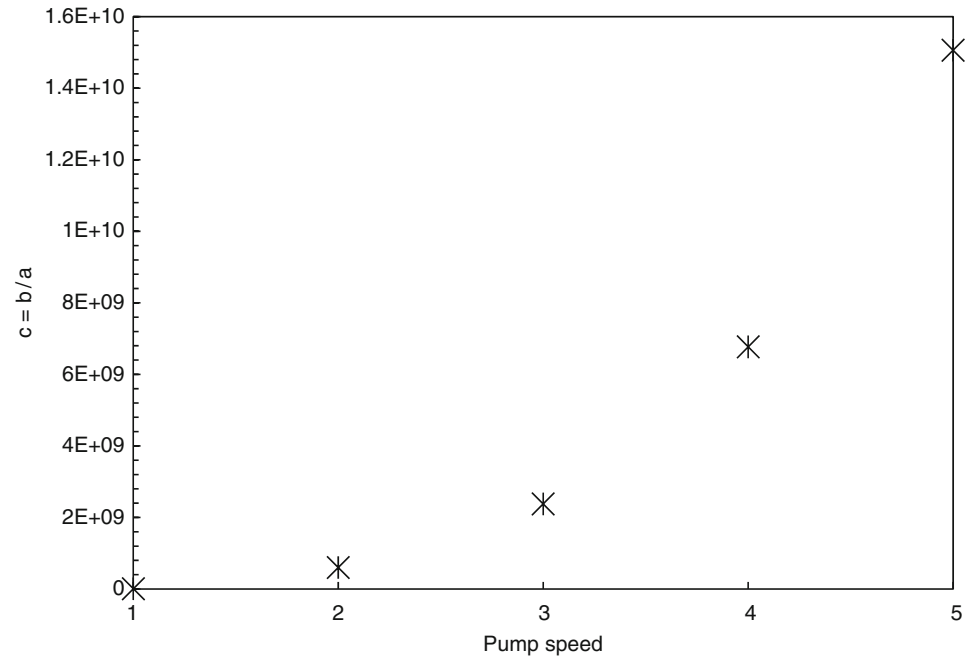

Fig. 6 Value of the parameter **c** versus pump speeds

This means that at high values of shear field level the disaggregation will exceed the aggregation and clearly the disaggregation kinetic constant rate will be higher than the one for aggregation process (referred to each value of pump speed). The data shown are in agreement with the ones obtained using different material and different techniques [15].

Conclusions

Understanding cluster formation is an important aspect in modelling sedimentation. The titanium dioxide example illustrated here has a primary particle size below what would reasonably be expected to sediment, yet appreciable sedimentation velocities are recorded after sufficient time has elapsed to enable cluster formation. Independent analysis of size analysis (using laser light scattering), under identical conditions of ionic liquid composition, demonstrated that clusters are readily formed and appreciable cluster sizes in the 10's of micrometres are possible under appropriate conditions. These tests also demonstrated that a uniform primary cluster size of between 3 and 4 micrometres was formed, after mild sonication. In the absence of shear the cluster size remained at this value and no visible sedimentation took place in the laser light scattering device. However, in the presence of very low shear fields, considerable further aggregation of the primary clusters did occur, giving significantly larger secondary clusters. Hence, the modelling approach adopted was one of considering cluster formation based on primary and secondary clusters, rather than cluster formation from primary particles. The net rate constant for the aggregation and disaggregation of the primary clusters was determined, as a function of the shear used in the laser light scattering equipment. In further work the net rate, under conditions of low shear, will be used to model the formation of clusters within the sedimentation vessel, in order to kinetically determine the rate of aggregate formation.

Acknowledgements The authors wish to acknowledge the financial support of the UK Engineering and Physical Sciences Research Council. The work was undertaken as part of the DIAMOND project into Decommissioning, Immobilisation And Management Of Nuclear wastes for Disposal.

References

1. G. J. Kynch, A theory of sedimentation, *Trans. Faraday Soc.*, 48 (1952), 166 – 176.
2. J. C. Berg, An introduction to interfaces & colloids The bridge to nanoscience, World Scientific, Singapore, 2010.
3. W. Pietsch, Agglomeration in Industry: Occurrence and Application Volume1-2, WILEY-VCH, Germany, 2005.
4. M. Von Smoluchowski, Versuch einer mathematischen Theorie der Koagulationskinetik kolloidaler Lösungen, Ztsch. Phys. Chem., 92 (1917), 129–168.
5. V. Starov, V. Zhadanov, N. M. Kovalchuk, Kinetic models of micelles formation, *Colloids and Surfaces A: Physicochem. Eng. Aspects* 354 (2010), 268 – 278.
6. A. Rushton, A. S. Ward and R. G. Holdich, Solid-Liquid Filtration and Separation Technology, VCH, Germany, 1996.
7. G. Frens and J. T. Overbeek, Repeptization and the theory of electrocratic colloids, *Journal of Colloid and Interface Science*, 38 (1972), 376 – 387.
8. N. Kovalchuk, V. Starov, P. Langston and N. Hilal, Formation of stable clusters in colloidal suspensions, *Advances in Colloid and Interface Science*, 147 – 148 (2009), 144 – 154.
9. S. Biggs, Aggregate Structures and Solid-Liquid Separation Processes, KONA, 24 (2006), 41 – 53.
10. L. Xie, C. D. Rielly and G. Őzcan-Taşkin, Break-Up of Nanoparticles Agglomerates by Hydrodynamically Limited Processes, *Journal of Dispersion Science and Technology*, 29 (2008), 573–579.
11. M. M. Clark and J. R. V. Flora, Floc restructuring in varied turbulent mixing, *Journal of Colloid and Interface Science*, 147 No 2 (1991), 407 – 421.
12. P.G. Saffman and J.S. Turner, On the collision of drops in turbulent clouds, *Journal of Fluid Mechanics* 1 (1956), 16–30.
13. J. Ke, X. Cai and Z. Lin, Reversible aggregation processes with time-dependent rate kernels, *Physics Letters A*, 331 (2004), 281–287.
14. H. S. Harris, W.J. Kaufman, R. B. Krone, Orthokinetic Flocculation in Water Purification, *J. San. Eng. Div. ASCE*, 92 (1966), 95.
15. T. Serra and X. Casamitjana, Modelling the aggregation and breakup of fractal aggregates in shear flow, *Applied Scientific Research*, 59 (1998), 255–268.
16. M. G. Rasteiro, F. A. P. Garcia, P. Ferreira, A. Blanc, C. Negro, E. Antunes, The use of LSD as a tool to evaluate flocculation mechanisms, *Chemical Engineering and Processing*, 47 (2008), 1323–1332.
17. M. Elimelech, J. Gregory, X. Jia and R. Williams, Particle deposition & aggregation: measuring, modelling and simulation, *Butterworth-Heinemann Ltd* (1995).

Progr Colloid Polym Sci (2011) 138:81–84
DOI: 10.1007/978-3-642-19038-4_14

Superhydrophobicity of Self-Assembled PFDTS Nanostructures

M.A. Raza, E.S. Kooij, A. van Silfhout, and B. Poelsema

Abstract The self-assembled formation of PFDTS features on mono- and multilayered silica sphere arrays is studied. The multiscaled roughness induced by PFDTS nanostructures on multilayer arrays gives rise to superhydrophobic behaviour. In contrast to previous work, the role of PFDTS is two-fold: it lowers the surface energy and simultaneously provides the essential roughness to achieve superhydrophobicity. The importance of water in the formation of the nanostructured surfaces is discussed.

Keywords Superhydrophobic • self-assembly • nanostructured surface

Introduction

Driven by practical application in areas such as coatings, adhesives, textiles, self-cleaning, micro- and nanofluidics [1], there is significant interest within the fundamental science community in the (de)wetting of natural as well as artificial surfaces. Superhydrophobicity, characterized by macroscopic contact angle (CA) values larger than 150° and small sliding angles, has attracted considerable attention. It is nowadays well-accepted that the wettability of (nano)structured surfaces is governed by two key factors: (i) interface chemistry and (ii) surface morphology.

The chemical nature of the substrate, combined with the liquid surface tension, defines the liquid CA on a perfectly clean, flat surface. To control the wettability of surfaces, often (hydrophobic) polymers with specific low surface tension end-groups are used. The surface tension of typical substituent end-groups decreases in the following order: CH_2(36dyn/cm) > CH_3(30dyn/cm) > CF_2(23dyn/cm) > CF_3(15dyn/cm) [2]. This sequence accounts for the fact that among the numerous molecules available, fluorinated polymers with CF_3 end-groups are widely used as dewetting/antisticking coatings. In many application involving oxide surfaces, PFDTS (1H,1H,2H,2H-perfluoro-decyltrichlorosilane) is used to modify the interaction between the substrate and the liquid deposited onto it.

It was recognized long ago that surface roughness also has a profound effect on the macroscopic wettability of (nano) structured substrates [3–11]. Naturally occurring surfaces, such as that of the Lotus leaf, exhibit self-cleaning properties owing to the hierarchical roughness with different length scales [11–13]. Several studies have focused on reproducing similar surfaces by different means, mimicking the multiple length scales [7–11]. The wetting of these surfaces has been investigated both experimentally and theoretically, revealing different mechanisms including the limiting cases described by Wenzel and Cassie-Baxter; truly superhydrophobic surfaces are only possible for surfaces on which the liquid adopts the Cassie-Baxter state [6, 8, 9, 12–14].

In the present work we show that under specific experimental conditions, the adsorption of PFDTS on silica sphere arrays leads to the self-assembled formation of nanostructures. Therewith the role of the fluoroalkylsilane polymer becomes two-fold: (i) it simultaneously reduces the surface energy and (ii) leads to an increase of the surface roughness. As far as we are aware, such a double role for PFDTS has not been observed previously.

PFDTS Films on Silica Sphere Monolayers

We investigated the effect of PFDTS treatment on monolayer and multilayer arrays of silica microspheres with varying diameters. Details pertaining to the preparation methods and experimental conditions are available elsewhere [15]. In Figure 1 the formation of a homogeneous layer on silica sphere monolayers and the formation of nanostructures on

E.S. Kooij (✉)
Solid State Physics, IMPACT Institute, University of Twente, P.O. Box 217, NL-7500AE, Enschede, The Netherlands
e-mail: e.s.kooij@utwente.nl

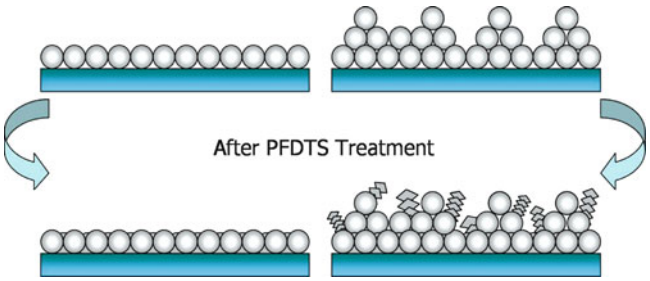

Fig. 1 Schematic representation of the adsorption of PFDTS on monolayer (left) and multilayer (right) arrays of silica spheres. The silica spheres are deposited by means of spin coating, while the PFDTS deposition is done by immersion into PFDTS-in-toluene solution

multilayer arrays is schematically shown; the latter will be discussed in the next section.

Scanning electron microscopy (SEM) images after PFDTS treatment of monolayers of silica spheres with different sizes are shown on the left side of Figure 2. It can be clearly seen that PFDTS forms a homogeneous layer on the surface of the silica spheres. Moreover, close examination of the SEM images reveals the formation of 'bridges' between neighboring microspheres. The cross-section views in the insets of Figure 2 also depict connections between the silica spheres and the substrates.

We suggest that the mechanism for the formation of the PFDTS films is a combination of hydrolysis and condensation reactions both in solution as well as at the substrate surface. The hydrolysis can be represented by

$$R_f - SiCl_3 + 3H_2O \rightarrow R_f - Si(OH)_3 + 3HCl \quad (1)$$

where $R_f = CF_3(CF_2)_7(CH_2)_2$, while the condensation reaction occurs via

$$2[R_f - Si(OH)_3] \rightarrow [R_f - Si(OH)_2 - O - Si(OH)_2 - R_f] + H_2O \quad (2)$$

Details of these reactions during chlorosilane deposition have been studied extensively by different techniques and are well-documented in literature. The formation of silane networks (Si-O-Si) was detected by FTIR [16–19], while the presence of low surface energy elements ($-CF_3$) was confirmed by XPS and verified by contact angle measurements [19–24].

The wetting behaviour of close-packed monolayers is assessed by performing static contact angle (CA) measurements using the sessile drop method as well as dynamic sliding angle (SA) measurements. Results for the static CA are shown in the insets of Figure 2, while the resulting CA and SA values are summarized in Table 1. For the PFDTS-treated monolayer arrays typical CA values between 135° and 140° are found, together with fairly large sliding angles. The CA values are considerably larger than the values observed on morphologically flat surfaces. The enlargement can be quantitatively accounted for by considering the Cassie-Baxter and Wenzel [6, 8, 9, 12–14, 25, 26] models for rough surfaces. The droplets are in a mixed state, i.e. partially wetting the hemispherical surface, partly entrapping air pockets. A detailed description was recently presented elsewhere [15].

PFDTS Nanostructures on Silica Sphere Multilayers

When the PFDTS deposition is carried out on multilayers of silica spheres, characteristic protrusions are formed as shown in Figure 2 (right). Since they only form during the coating with PFDTS the extruding nanostructures are considered to consist of polymerized PFDTS. Careful observation reveals that the nanostructures consist of an assembly of cubical elements with a typical size of 150nm. Comparing SEM images for different sizes of silica spheres, we find that the size and surface coverage of the PFDTS nanostructures increases with decreasing sphere diameter (see also Table 1).

In the formation of PFDTS nanostructures, water is a key factor. The aforementioned experiments were all performed under ambient conditions. This implies that the solvent for PFDTS solutions contains a finite amount of water. The evaporation rate of toluene is considerably larger than that of water, leading to increasing concentrations during the PFDTS treatment. We assume that during this evaporation, there is an uneven distribution of water within the multilayered arrays, which develops into "water pockets". These pockets act as nucleation sites for the polymerization leading to the PFDTS nanostructures. Due to the limited thickness and the open structure of monolayer arrays, nanostructures are absent on these surfaces. For the largest confinement within multilayer arrays consisting of the smallest spheres, the largest density of PFDTS nanofeatures is found on these arrays.

To verify the important role of water in the PFDTS self-assembly, we performed a control experiment under controlled, water-free conditions in a glove box, using a solution prepared with anhydrous solvent. Results reveal that in the absence of sufficient water, the PFDTS nanostructures are not formed.

Multilayer silica sphere arrays decorated with PFDTS nanostructures turn out to be superhydrophobic. Considerably larger CA values exceeding 160° are observed (see Table 1 and the insets in Figure 2), with small sliding angles of only a few degrees (listed in Table 1). The increase in hydrophobicity is explained by the second length scale introduced by the PFDTS nanostructures [6–11]. Liquid droplets are only in contact with the protrusions for sufficiently

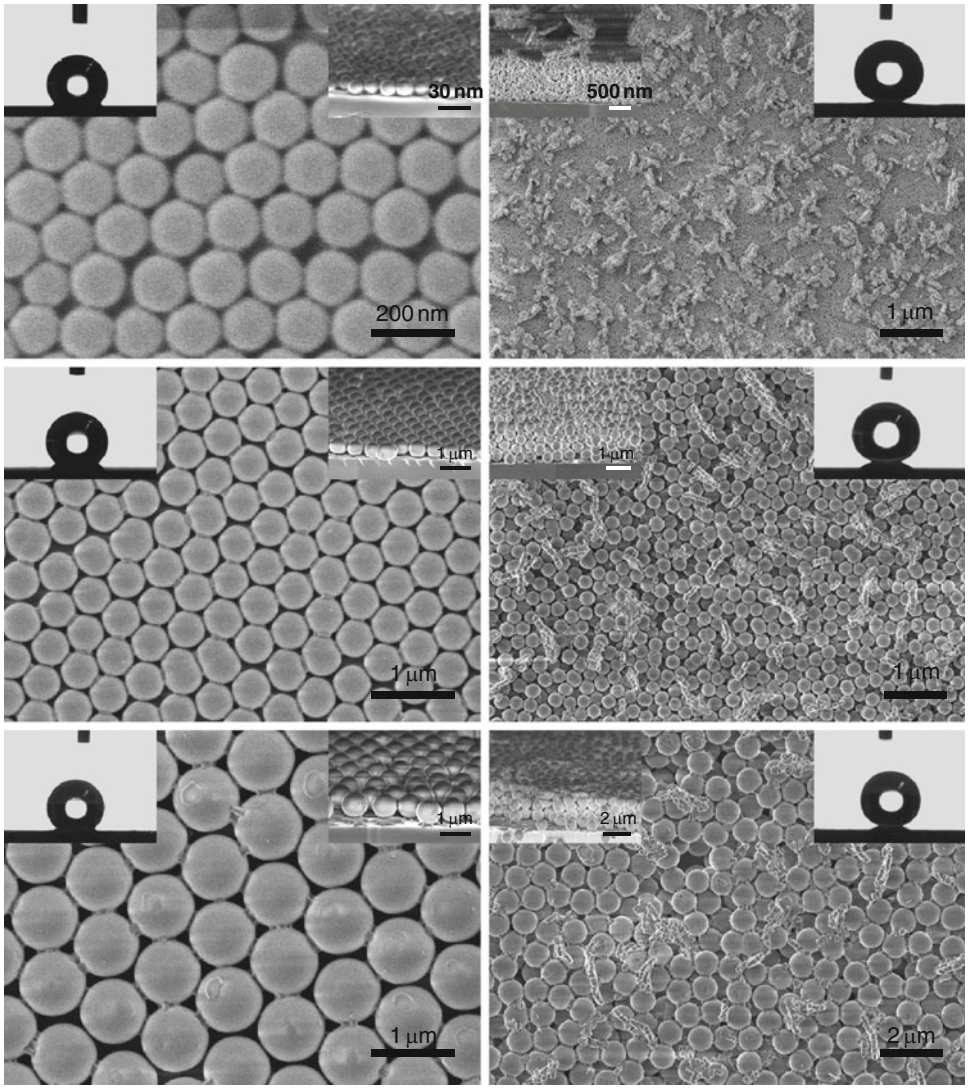

Fig. 2 Top-view SEM images of monolayer (left) en multilayer (right) silica sphere arrays after PFDTS assembly. The silica sphere diameters amount to 140 nm (top), 440 nm (middle) and 830 nm (bottom). The insets show side-view images of cleaved samples, as well as the large static contact angles (8μl droplets) revealing the (super) hydrophobicity of the superstructures

Table 1 Water contact angles (CA) and sliding angle (SA) on PFDTS-treated mono- and multilayer arrays for different silica sphere diameters. Also, the surface coverages of PFDTS nanostructures are given

SiO_2 diameter	monolayer		multilayer		nanostructure surface coverage
	CA	SA	CA	SA	
140nm	135°	60°	163°	3°	3%
440nm	138°	54°	160°	5°	0.9%
830nm	140°	50°	160°	5°	0.3%

high densities of nanostructures, i.e. in the Cassie-Baxter state, with considerable amounts of air trapped between the liquid meniscus and the substrate.

Conclusions

We have investigated the effect of PFDTS deposition on monolayer and multilayer arrays of silica spheres having different sizes. PFDTS deposition under ambient conditions onto silica sphere arrays gave rise to bridge formation between the spheres on monolayers. On multilayers, the PFDTS formed finger-like self-assembled nanostructures. The diameter of the silica spheres determined the size and density of PFDTS nanostructured protrusions. Under water-free conditions, PFDTS nanostructures were not formed, indication the importance of water presence for the formation of these structures. Surfaces decorated with the PFDTS nanostructures exhibit two length scales, determined by the nanoprotrusions and the silica spheres. Combined with the low surface energy of the PFDTS end-groups, this multi-scale roughness gives rise to superhydrophobic properties as expressed by contact angles as large as 163° and negligible sliding angles.

Acknowledgements We thank O. Bliznyuk (Univ. Twente) for helpful discussions. We gratefully acknowledge the support by MicroNed, a consortium to nurture microsystems technology in The Netherlands. One of the authors (M.A. Raza) acknowledges support from the Higher Education Commission in Pakistan.

References

1. P.G. de Gennes, F. Wyart-Brochard, D. Quéré, *Capillarity and Wetting phenomena: Droplets, Bubbles, Pearls, Waves*, Springer-Verlag, New York (2004)
2. J. Wang, C.K. Ober, Macromolecules **30**, 7560 (1997)
3. F.E. Bartell, J.W. Shepard, J. Phys. Chem. **57**, 211 (1953)
4. S. Herminghaus, Europhys. Lett. **52**, 165 (2000)
5. R.H. Dettre, R.E. Johnson, in CA, *wettability; Advances in Chemistry Series No. 43*, p. 136 American Chemical Society, Washington DC (1964)
6. A. Lafuma, D. Quéré, Nat. Mater. **2**, 457 (2003)
7. N.A. Patankar, Langmuir **20**, 8209 (2004)
8. N.J. Shirtcliffe, G. McHale, M.I. Newton, C.C. Perry, Langmuir **21**, 937 (2005)
9. E. Bormashenko, T. Stein, G. Whyman, Y. Bormashenko, R. Pogreb, Langmuir **22**, 9982 (2006)
10. P. Roach, N.J. Shirtcliffe, M.I. Newton, Soft Matter **4**, 224 (2008)
11. D. Quéré, Ann. Rev. Mater. Sci. **38**, 71 (2008)
12. A. Marmur, Soft Matter **2**, 12 (2006)
13. M. Nosonovsky, B. Bhushan, Adv. Funct. Mater. **18**, 843 (2008)
14. M. Nosonovsky, B. Bhushan, J. Phys.: Condens. Matter **20**, 225009 (2008)
15. M.A. Raza, E.S. Kooij, A. van Silfhout, B. Poelsema, Langmuir **26**, 12962 (2010)
16. S. Arifuzzaman, A.E. Ozcam, K. Efimenko, Biointerphases **4**, FA33 (2009)
17. A. Vilcnik, I. Jerman, A.S. Vuk, M. Kozelj, B. Orel, B. Tomsic, B. Simoncic, J. Kovac, Langmuir **25**, 5869 (2009)
18. D.L. Angst, G.W. Simmons, Langmuir **7**, 2236 (1991)
19. W. Xu, H. Liu, S. Lu, J. Xi, Y. Wang, Langmuir **24**, 10895 (2008)
20. B. Leng, Z. Shao, G. de With, W. Ming, Langmuir **25**, 2456 (2009)
21. H.F. Hoefnagels, D. Wu, G. de With, W. Ming, Langmuir **23**, 13158 (2007)
22. C.H. Xue, S.T. Jia, J. Zhang, L.Q. Tian, Thin Solid Films **517**, 4593 (2009)
23. Y. Li, X.J. Huang, S.H. Heo, C.C. Li, Y.K. Choi, W.P. Cai, S.O. Cho, Langmuir **23**, 2169 (2007)
24. K. Paso, R.M.L. Helberg, S. Raaen, J. Sjoblom, J. Colloid Interface Sci. **325**, 228 (2008)
25. A. Cassie, S. Baxter, Trans. Faraday Soc. **40**, 546 (1944)
26. R.N. Wenzel, Ind. Eng. Chem. **28**, 988 (1936)

Progr Colloid Polym Sci (2011) 138:85–88
DOI: 10.1007/978-3-642-19038-4_15

A Facile Colloidal Route for Superhydrophobic Films with Hierarchical Roughness

M.A. Raza, E.S. Kooij, A. van Silfhout, and B. Poelsema

Abstract We present a simple bottom-up colloidal route towards the manufacture of hierarchical substrates. Owing to the double length scale roughness, these super-structure arrays exhibit superhydrophobic wetting behaviour, characterized by large contact angles, limited hysteresis and small sliding angles. The assembly procedure of the nanocolloidal silica and gold particles is reviewed, as well as the chemical treatments required to obtain stable, reproducible substrates.

Keywords Superhydrophobic • colloidal assembly • nanoparticles

Introduction

Fabrication of (super)hydrophobic surfaces has attracted a lot of interest over the past few decades, due to their many possible technological applications [1]. It is well-known that surface roughness, i.e. the morphology, and surface chemistry are the important factors, which control their macroscopic wettability [2–7]. Hierarchical roughness on different (micro- and nano-) length scales plays a key role to achieve stable superhydrophobicity of the surfaces as depicted by biomaterials such as the Lotus leaf [2–5, 7–10]. The wetting of these surfaces has been investigated revealing different mechanisms including the limiting cases described by Wenzel and Cassie-Baxter; truly superhydrophobic surfaces (characterized by contact angles $> 150^\circ$ with sliding angles $< 10^\circ$) are only possible for surfaces on which the liquid adopts the Cassie-Baxter state. Multiple length scales in the roughness serve to reduce contact angle hysteresis, promoting the Cassie-Baxter state in which droplets are on top of the surface asperities [4, 5, 8, 9, 11–13].

Owing to an increasing demand for superhydrophic surfaces in modern technology, manufacturing of such surfaces has been a hot issue in both experimental and theoretical research over the past decade [3–5, 15]. In attempts to mimic nature, artificial (super)hydrophobic surfaces (both sticky and non-sticky [2, 12, 13]) can be created by many different routes. In this work we present a simple bottom-up colloidal route to obtain hierarchical roughness for superhydrophobic surfaces. This hierarchical structure is achieved by self-assembled arrays of particles varying from micrometers down to the low-nanometer range. The largest length scale is provided by (multi-)layers of silica spheres with a diameter of 500nm. Decoration of these spheres with gold nanoparticles (50nm) provides the second length scale. The chemistry of the structured surfaces is modified by functionalizing the silica spheres with 1H,1H,2H,2H-perfluorooctyltriethoxysilane and the gold nanoparticles with dodecanethiol.

Experimental Details

The various steps in the bottom-up assembly of hierarchical surfaces is schematically shown in Figure 1. Clean silicon substrates were cleaved from polished wafers, covered with an approximately 2nm thick native oxide layer. Subsequently, silica sphere arrays were deposited by means of spin-coating [16] (WS-400B-6NNP-lite Spin Coater, Laurell, USA). Further details are given elsewhere [17].

To enable deposition of gold nanoparticles with 50nm diameter on flat or hemispherical surfaces (left and right parts of Figure 1, respectively), the silica was functionalized with a monolayer of (3-mercaptopropyl)trimethoxysilane (MPTMS). The silane groups polymerize with the oxide groups on the surface, while the thiol end groups provide a large affinity for irreversible adsorption of the citrate-stabilized gold nanoparticles. Details on gold nanoparticle

E.S. Kooij (✉)
Solid State Physics, IMPACT Institute, University of Twente, P.O. Box 217, NL-7500AE Enschede, The Netherlands
e-mail: e.s.kooij@utwente.nl

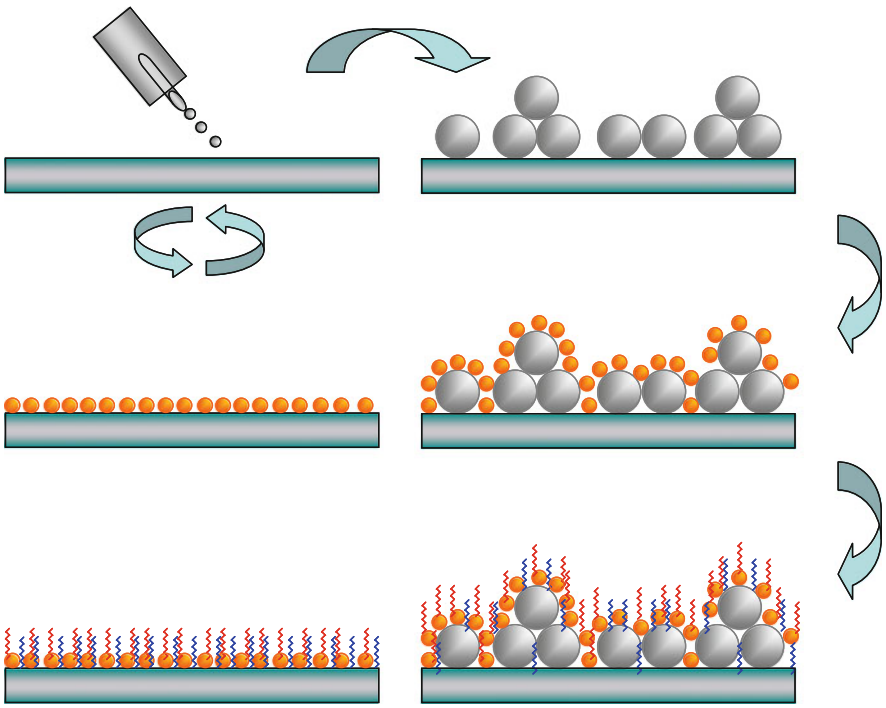

Fig. 1 Schematic representation of the manufacture of (super) hydrophobic substrates. Either flat clean silicon samples, coated with a natural oxide film, are considered (left) or samples onto which silica spheres are deposited by means of spin-coating (right). Subsequently, gold nanoparticles are deposited by MPTMS-mediated self-assembly on the silica surface. Finally, PFOTS is adsorbed onto the exposed silica areas to provide sufficient stability, while DDT is deposited onto the gold surface to lower its surface energy

synthesis and MPTMS derivatization is well-documented in literature [18, 19].

Following assembly of the colloidal particles into superstructures, the exposed silica surfaces are functionalized with 1H,1H,2H,2H-perfluoroctyltriethoxysilane (PFOTS) to ensure sufficient stability of the substrates; hydrolysation and condensation of the silane groups gives rise to 'binding' of the silica spheres to each other and to the substrate. Moreover, it lowers the surface energy of the oxide. Finally, the gold nanoparticles are hydrophobized by lowering the surface energy through adsorption of dodecanethiol (DDT). On flat gold surfaces modified with DDT, static contact angles of 98.5° are typically observed. More details pertaining to the chemical treatment will be described elsewhere [20].

The surface morphology of the structured samples was determined by scanning helium ion microscopy (HIM, ORION-Zeiss, USA). Contact angle measurements were performed using the sessile drop method on a Dataphysics OCA15+ goniometer under ambient conditions at room temperature. Advancing and receding contact angles were determined by increasing or decreasing the droplet volume while it was in contact with the surface; sliding angles were determined by tilting the sample holder. Typically, 4μl or 8μl water droplets were used; contact angle values were determined by the average of at least five independent measurements.

Morphology and Wettability of Hierarchical Colloidal Superstructures

Microscopy images of different substrates are compiled in Figure 2. Also shown are the sessile drops to assess the wettability. For flat silicon substrates, as well as silica sphere arrays without any chemical coating, very small contact angles are observed, as expected for clean silica surfaces. As shown in the middle two panels in Figure 2, after coating the flat or hemispherical surfaces with PFOTS, the morphology remains unchanged. In comparison to the untreated surfaces, there appears to be a little more contrast on the flat surface, while the sphere arrays seem to develop PFOTS-'bridges' between touching spheres.

The wettability is modified considerably. The flat surface exhibits contact angles of approximately 110°, while the more corrugated silica sphere arrays shows even larger contact angles. This can be understood qualitatively by considering the roughness induced by the silica spheres. By considering the droplets to be in a mixed state, i.e. partially wetting the spheres, partly entrapping air between them, we can quantitatively account for the larger contact angles as compared to flat surfaces [11, 17]. The silica spheres are partly in contact with the liquid, providing a larger contact area than the projected surface area. The entrapment of air between the spheres under the liquid meniscus provides the predominant contribution to the enhanced hydrophobicity.

The bottom panels in Figure 2 depict the flat surface and silica arrays after deposition of gold nanoparticles. On both the flat and curved surfaces, there is a random distribution of nanoparticles. Nevertheless, there is clearly a minimum distance separating the nanoentities, arising from the surface charge of the particles in solution [21, 22].

Results of static, advancing and receding contact angles as well as sliding angle measurements on the surfaces considered in this work are summarized in Table 1. From the absolute value of the contact angles, the contact angle hysteresis (deduced from advancing and receding CAs) and the sliding angles, it can be concluded that only in the case of hierarchical surface roughness actual superhydrophobicity is achieved.

For the nanoparticle surfaces, a similar mixed wetting state as described above is assumed [11, 17]. Only on silica sphere arrays decorated by gold nanoparticles we observe CA $>$ 150°, reduced hysteresis and SA $<$ 5°, which are characteristic for superhydrophobic substrates. Although a detailed characterization of the wetting mechanism on these hierarchical surfaces lies outside the scope of this work, we assume that the droplets on the substrates with hierarchical roughness are neither in the Wenzel nor Cassie-Baxter state. Most likely they reside in a mixed state as presented by Bormashenko et al. [5]: the droplets partially wet the smaller nanoparticles, while entrapping air between the larger silica spheres. As described in previous literature reports, this is a prerequisite for pushing out the liquid into the suspended Cassie-Baxter state, therewith considerably reducing the contact angle hysteresis and thus giving rise to superhydrophobic wetting characteristics [2, 4, 5, 7–9]. Within the time scale of our experiments, i.e. typically an hour, the superhydrophobic state is stable as indicated by the static contact angles, which remain unchanged. As such, we assume that the previously described Cassie-Baxter to Wenzel transition does not occur on the time scale of our present measurements [2, 12–14].

Table 1 Static, advancing and receding contact angles (SCA, ACA and RCA, respectively) as well as contact angle hysteresis (CAH) and sliding angles (SA) for different substrates considered in this work

	SCA	ACA	RCA	CAH	SA
substrate + PFOTS	110°	125°	93°	32°	180°
AuNPs + PFOTS + DDT	125°	140°	85°	55°	180°
silica spheres + PFOTS	140°	152°	120°	32°	180°
spheres + AuNPs + PFOTS + DDT	160°	167°	155°	12°	3°

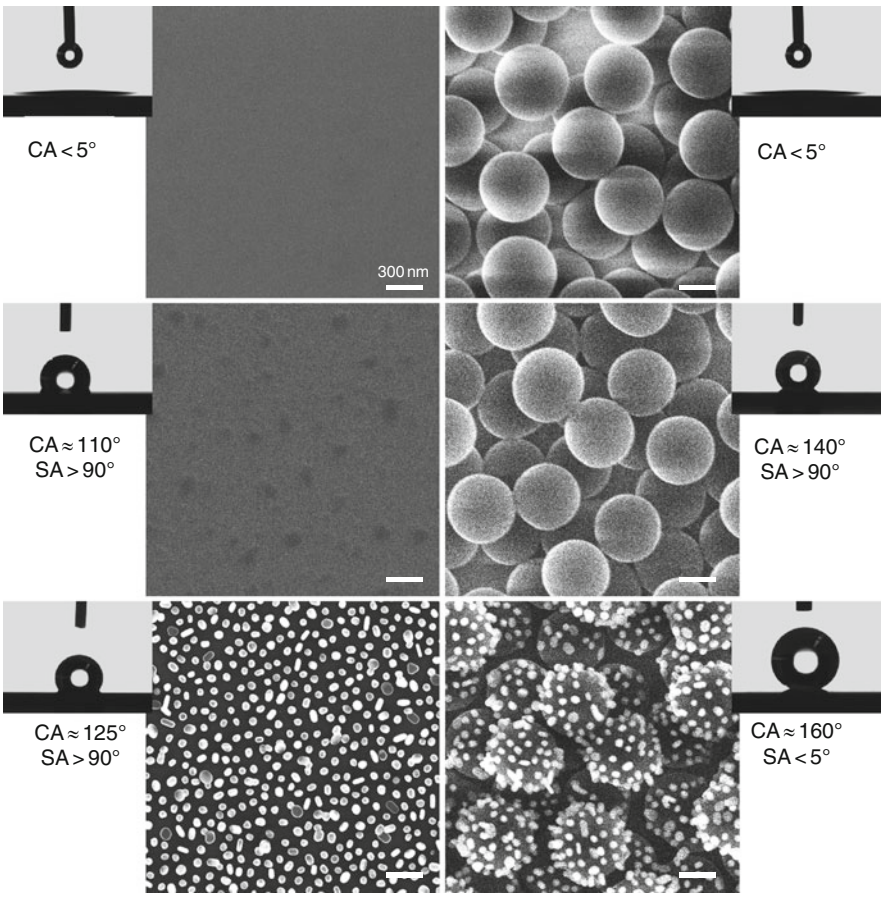

Fig. 2 Top-view microscopy images of different substrates considered in this work. (top) Flat silicon and silica sphere arrays before chemical treatment. (middle) Similar substrates after PFOTS treatment. (bottom) Images of flat silicon and silica sphere arrays decorated by gold nanoparticles. The wettability results (insets) show that superhydrophobicity is achieved on hierarchical structures as depicted by a large contact angle for identical surface chemistry

Conclusions

Summarizing, we have presented a simple bottom-up colloidal route to make substrates with hierarchical roughness that exhibit superhydrophobic behaviour. Single length scale roughness leads to sticky hydrophobic surfaces with sliding angles SA $> 90°$. Multiple length scale roughness induced by assembling spheres with diameters differing one order of magnitude give rise to non-sticky, truly superhydrophobic surfaces with sliding angles SA $< 5°$. We conclude that besides the surface chemistry, wettability can be controlled by changing the size and/or length scales of the hierarchical superstructures.

Acknowledgements We gratefully acknowledge the support by MicroNed, a consortium to nurture microsystems technology in The Netherlands. One of the authors (M.A. Raza) acknowledges support from the Higher Education Commission in Pakistan.

References

1. P.G. de Gennes, F. Wyart-Brochard, D. Quéré, *Capillarity and Wetting phenomena: Droplets, Bubbles, Pearls, Waves*, Springer-Verlag, New York (2004)
2. A. Marmur, Langmuir **19**, 8343 (2003)
3. N.A. Patankar, Langmuir **20**, 8209 (2004)
4. N.J. Shirtcliffe, G. McHale, M.I. Newton, C.C. Perry, Langmuir **21**, 937 (2005)
5. E. Bormashenko, T. Stein, G. Whyman, Y. Bormashenko, R. Pogreb, Langmuir **22**, 9982 (2006)
6. J.T. Han, S. Kim, A. Karim, Langmuir **23**, 2608 (2007)
7. M. Nosonovsky, B. Bhushan, Adv. Funct. Mater. **18**, 843 (2008)
8. L. Gao, J. McCarthy, Langmuir **22**, 2966 (2006)
9. Y. Kwon, N. Patankar, J. Coi, J. Lee, Langmuir **25**, 6129 (2009)
10. Y. Su, B. Ji, K. Zhang, H. Gao, Y. Huang, K. Hwang, Langmuir **26**, 4984 (2010)
11. A. Marmur, Langmuir **19**, 8343 (2003)
12. D. Bartolo, F. Bouamrirene, E. Verneuil, A. Buguin, P. Silberzan, S. Moulinet, Europhys. Lett. **74**, 299 (2006)
13. S. Moulinet, D. Bartolo, Eur. Phys. J. E **24**, 251 (2007)
14. P. Tsai, R.G.H. Lammertink, M. Wessling, D. Lohse, Phys. Rev. Lett. **104**, 116102 (2010)
15. Y. Li, X.J. Huang, S.H. Heo, Y.K. Choi, W.P. Cai, S.O. Cho, Langmuir **23**,2169 (2007)
16. D. Wang, H. Möhwald, Adv. Mater. **16**, 244 (2004)
17. M.A. Raza, E.S. Kooij, A. van Silfhout, B. Poelsema, Langmuir **26**, 12962 (2010)
18. K.R. Brown, D.G. Walter, M.J. Natan, Chem. Mater. **12**, 306 (2000)
19. S.H. Park, J.H. Im, J.W. Im, B.H. Chun and J.H. Kim, Microchem. J. **63**, 71 (1999)
20. M.A. Raza, E.S. Kooij, A. van Silfhout, B. Poelsema, to be published
21. E.S. Kooij, E.A.M. Brouwer, H. Wormeester, B. Poelsema, Langmuir **18**, 7677 (2002)
22. E.S. Kooij, E.A.M. Brouwer, H. Wormeester, B. Poelsema, Encyclopedia of Nanoscience and Nanotechnology, p.1515-1523 (2004)

Progr Colloid Polym Sci (2011) 138:89–94
DOI: 10.1007/978-3-642-19038-4_16

Enhanced Keratinocyte Cell Attachment to Atelocollagen Thin Films Through Air and Nitrogen Plasma Treatment

Jorge López García[1], Jiří Pacherník[2], Marián Lehocký[3], Ita Junkar[4], Petr Humpolíček[3], and Petr Sáha[1]

Abstract Collagen films (Atelocollagen from bovine Achilles tendon) were prepared in tissue culture dishes and their surfaces were modified by using air and nitrogen plasma treatment. The treated samples were characterised by surface probe techniques including attenuated total reflection Fourier transform infrared spectroscopy (ATR-FTIR), scanning electron microscopy imaging (SEM) and X-ray photoelectron spectroscopy (XPS). In addition, human immortalised non-tumorigenic keratinocyte cell line (HaCaT) was seeded on the treated and untreated films and cell proliferation was measured by using MTT assay test. The characterisation results confirmed physical and chemical changes on the collagen surface, such as increase in the extent of surface oxidation and surface roughness as well as, the treated samples showed better cell growth than untreated ones, and therefore this approach may be taken into account in the development of promising materials for tissue regeneration applications.

Keywords Atelocollagen • Thin films • Plasma treatment • Cell adhesion • Cell growth • Radio frequency discharge

Introduction

Collagen is a fibrillar protein, which has received remarkable interest by its abundance in the animal kingdom (*ca.* 25% of the whole-body protein content). It is involved in many important biological functions, such as tissue formation, cell adhesion and proliferation. In fact, collagen is present in the skin, tendons and cartilage [1]; thus, it affords extensive possibilities in designing materials for biomedical applications. Several authors have reported on different aspects of collagen research, *e.g.* polymer blends, drug delivery, polymer grafting, tissue engineering, and nerve regeneration amongst others [2, 3].

HaCaT (human adult low calcium high temperature) cells are spontaneously transformed human keratinocytes which have characteristics of basal epidermal keratinocytes; so that cell line may be used as an *in vitro* model for highly proliferative epidermis in tissue engineering [4].

Tissue engineering is a multidisciplinary and emerging field focused on providing substitutes that replace tissue and restore functions. It may be reached by combining synthetic/natural polymers with mammalian cells. There are three basic materials for the creation of a new tissue; cells, scaffold and growth factor. Cells synthesise matrices of the new tissue, while the scaffold provides an appropriate environment for cells, and growth factor assists and promotes cells to regenerate new tissue. Hence; the substrate-cells interaction is absolutely relevant and ubiquitous in clinical trials, such as skin transplants for patients with burns, skin ulcers, corneas, cartilage, bone, liver and other tissues [5, 6].

In this regard, plasma treatment is an effective and economical tool in the field of surface modification, which may be used quickly, easily and it does not require relatively expensive devices for its operation. The primary effect of plasma treatment is to convey reactivity to the treated surfaces via electrons, ions and UV-radiation confining the treatment to the top layer without affecting bulk properties. For these reason, plasma surface modification has been done on different materials, such as polymers, carbon fibres, ceramics, and proteins [7-9].

In this work, collagen surface modification was carried out by using air and nitrogen plasma treatment. The treated samples were characterised employing, attenuated total reflection

M. Lehocký (✉)
[1]Polymer Centre, Faculty of Technology, Tomas Bata University in Zlín, T.G.M Sq. 275, 76272, Zlín, Czech Republic
e-mail: lehocky@post.cz
[2]Institute of Experimental Biology, Faculty of Sciences, Masaryk University Brno, Kotlářska 2, 61137, Brno, Czech Republic
[3]Centre of Polymer Systems, Tomas Bata University in Zlín, T.G.M. Sq. 5555, 76001, Zlín, Czech Republic
[4]Department of Surface Engineering, Plasma Laboratory, Jožef Stefan Institute, Jamova cesta 39, SI-1000, Ljubljana, Slovenia

Fourier transform infrared (ATR-FTIR) spectroscopy, scanning electron microscopy imaging (SEM), and X-ray photoelectron spectroscopy (XPS).

In addition, keratinocyte cells (HaCaT) were seeded onto the treated and untreated collagen samples, and the cell proliferation was measured by MTT assay. The characterisation methods along with the corresponding biological assays confirmed physical and chemical changes as well as better cell proliferation on the plasma-treated samples thus, these materials may prospectively serve for tissue regeneration in medicine.

Materials and Methods

Preparation of Collagen Films

An atelocollagen emulsion from bovine Achilles tendon pH 3.5 which contents 1.43 % of collagen (Vipo A.S, Slovakia) was dissolved in 0.1M water solution of acetic acid to prepare a 0.1 % w/w solution using a stirring machine for 4 hours at 1,000 rpm. Then, 2 mL of this solution was poured into each of the tissue culture dishes. Finally, the solvent was evaporated at ambient conditions for three days.

Plasma Surface Treatment

The plasma treatment of such prepared collagen thin films was carried out by using plasmochemical reactor (Femto, Diener electronic, Germany) with a chamber of 100 mm diameter and 270 mm length operated at frequency of 40 kHz, pressure 40 Pa, and power input of 50 W. Air and nitrogen were used as carrier gases. The feed rate in all experiments was $5cm^3$/min. The duration of the plasma treatment was 5 minutes for each sample. Subsequently, the specimens were taken and normally manipulated for the next tests.

X-Ray Photoelectron Spectroscopy (XPS)

Measurements of the collagen samples were performed in a XPS microprobe instrument PHI Versaprobe (Physical Electronics, USA). The base pressure in the XPS analysis chamber was about 6×10^{-8} Pa. The samples were excited with X-rays over a 400 μm spot area with a monochromatic Al $K_{\alpha1,2}$ radiation at 1,486.6 eV. The photoelectrons were detected with a hemispherical analyser positioned at an angle of 45° with respect to the normal of the sample surface. The energy resolution was about 0.5 eV. And, survey-scan spectra were made at 187.85 eV, while for C1s and O1s individual high-resolution spectra were taken at 23.5 and 0.1 eV energy step. The concentration of different chemical states of carbon in the C1s peak was determined by fitting the curves with symmetrical Gauss–Lorentz functions. The spectra were fitted using MultiPak v7.3.1 software which was supplied with the spectrometer.

Attenuated Total Reflection Fourier-Transform Infrared Spectroscopy (ATR-FTIR)

The ATR-FTIR spectra of both treated and untreated samples were recorded on a FTIR spectrometer Avatar 320 (Nicolet, USA) equipped with a ZnSe crystal at an incident angle of 45°. For each sample 32 scans were recorded within the spectral range of 4,000–500 cm^{-1} in the absorbance mode with a resolution of 2 cm^{-1}.

Scanning Electron Microscopy (SEM)

SEM images were taken by Vega LMV (Tescan s.r.o, Czech Republic). The operating voltage of the Secondary Electron (SE) detector was 5 kV. All observed samples were coated with a sputtered thin layer of Au/Pd. In order to get higher resolution and observation of the surface topography, the specimens were 30 ° tilted and the images were taken at 5,000x magnification.

HaCaT Cell Cultivation

Human immortalised non-tumorigenic keratinocyte HaCaT cells (Cell Lines Service, Germany) were seeded onto the treated and untreated samples in the culture dishes and incubated at 37 °C for 4 days [10]. DMEM (high glucose) supplemented with 2mM L-glutamine solution and 10% fetal calf serum was used as the culture medium.

MTT Proliferation Assay

The cell proliferation was determined after 4 days of culturing employing the MTT cell proliferation assay kit on

each sample [reduction of 3-(4,5-dimethylthiazol-2-yl)-2,5-diphenyltetrazolium bromide, which is yellow, to a purple formazan product]. A volume of 10 μL of 12 mM MTT was taken for cell incubation performed at 37 °C for 4 hours in the darkness. The media were then decanted and washed with phosphate-buffered saline solution (PBS). The produced formazan salts were dissolved with dimethylsulphoxide (DMSO, Sigma-Aldrich, USA). The formazan concentration was measured in a spectrophotometer at 570nm [11].

Results and Discussion

The XPS survey spectra of the untreated and plasma treated films are given in fig. 1. In addition; Table 1 displays the relative peak areas of C1s, N1s and O1s along with O/C and N/C ratios for each experiment. The XPS data shows an increment of the oxygen content after air and nitrogen plasma treatment, besides a rise in the O/C ratio confirm the extent of surface oxidation after each treatment. This increment may be attributed to the oxidation of pendant groups present in collagen backbone. There are two reactions involved, the first ones occur directly in the plasma chamber and these are related to the oxygen and CO_2 content of air (*ca*. 20.94% and 0.031% respectively); on the other hand, the other reactions arise once the films are taken out from the plasma reactor through free-radical reactions. Either of these treatments introduces many radicals which may survive for several days, reacting with oxygen and other reactive species present in the atmosphere leading to surface functionalisation. It is particularly noticed on nitrogen plasma treatment. This gas is considered low reactive due to its molecular stability, and it only reacts spontaneously with few reagents. Nonetheless, oxygen functionalities are always incorporated in nitrogen plasma treatments [12-14]. Other kind of reactions specially centred on N-terminal and C-terminal of the protein might occur giving rise to Nitro R-NO_2, nitroso R-N=O, nitrosamine R_1-N(−R_2)-N=O, amide ($RCONH_2$) or amines (R-NH_2) entities, which may explain the increase in the N/C ratio after nitrogen plasma treatment. It should be noted that plasma treatment with any of these gases does not produce a unique functionality on collagen surface.

The ATR-FTIR spectrum of the untreated sample divided into two regions along with air and nitrogen plasma treated ones are presented in fig. 2. Peptide bond characteristic bands at ~3,300, 3,080, 1,645, 1,550, 1,240 and 695 cm^{-1} are identifiable and indeed, due to peaks overlapping, plasma treatment effects are rather masked. The amide I is a broad band around 1,640-1,630 cm^{-1} originated from C=O stretching vibrations coupled to N–H bending vibration. According to this absorption range, this band may come from collagen with high proline-proline-glycine sequences [15]. The amide II band ~1,550 cm^{-1} surges of N-H bending vibrations coupled to C-N stretching vibrations, and the amide III characteristics bands appear at ~1,280, 1,240 and 1,200 cm^{-1} which

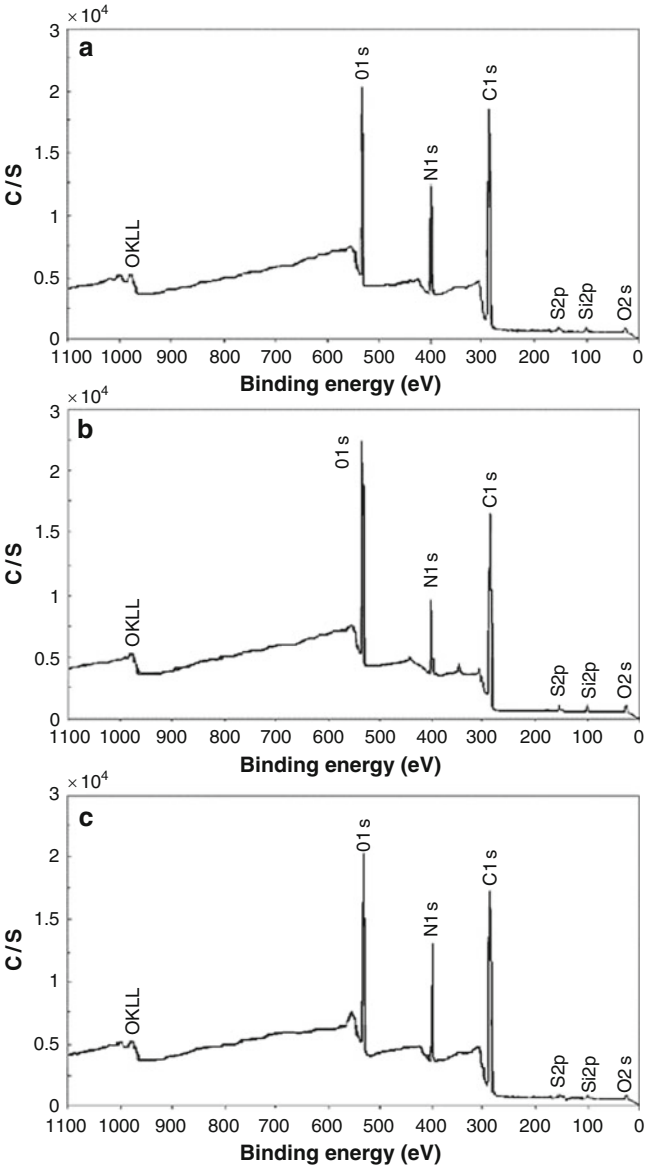

Fig. 1 XPS survey spectra of: (A) untreated; (B) air and (C) nitrogen plasma treated films

Table 1 Relative Peak Areas of C1s, N1s and O1s before and after the treatment

Sample	C1s%	N1s%	O1s%	N/C	O/C
Untreated	66.0	14.1	19.3	0.21	0.29
Air treatment	58.1	11.3	25.9	0.20	0.46
N_2 treatment	58.2	18.4	22.7	0.32	0.39

result from the interaction between N-H bending and C-N stretching. The band at 695 cm^{-1} is a usual amide vibration which arises from out of plane N-H wagging [16]. After each plasma treatment, the typical peptide bands remain visible which means that collagen is retained and its backbone is not drastically modified. Nevertheless, the intensity of the bands decreases after the treatments which is probably consequence of plasma-induced reactions. For instance, the characteristic amide N-H stretching at ~3,300 and 3,080 cm^{-1} shift down indicating of an alteration in the surface chemistry. This is particularly pronounced after treatment in nitrogen medium where the peaks within 2,950-2,850 cm^{-1} corresponding to methyl and methylene stretching deformation shift and change in strength. The intensity of some weak signals at ~1,485, 620 and 565 cm^{-1} increases following plasma treatment which may be assigned to nitro compounds 1,485 N=O stretching, 670 and 562 cm^{-1} NO_2 bending vibrations. Moreover, the bands within the 1,100-850 cm^{-1} spectral range associated with C-O stretching vibrations present clear alterations after both plasma treatments; and it may be observed on the peaks that appear at around 1,045, 1,000 and 905 cm^{-1} respectively. Therefore, it is found out through surface chemistry analysis that plasma treatment, either in air or nitrogen, is capable of affecting the surface chemistry via ablation and functionalisation.

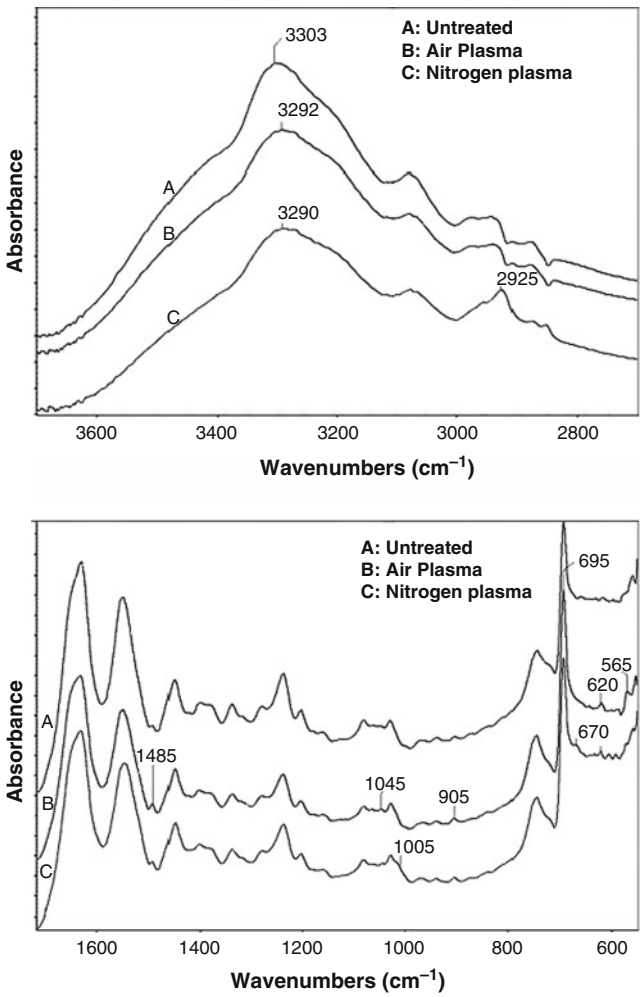

Fig. 2 ATR-FTIR spectra of: (A) untreated; (B) air and (C) nitrogen plasma treated films

Significant changes on the surface morphology after the plasma treatment may be observed in SEM images (fig. 3). The treated samples show relatively rougher surface topography and etched features, as long as the untreated film has a relatively smooth morphology.

This is in concordance with the spectroscopic results where regardless of the carrier gas, surface ablation was observed.

A rise in roughness and surface polar functionalities after exposing atelocollagen films to air and nitrogen plasma treatment promote cell attachment and proliferation, and it is in agreement with the HaCaT cell proliferation measurement (fig. 4) which was significantly higher for either of these treated samples than the untreated films.

This previous information is also supported qualitatively by the micrographs in fig. 5, where a higher amount of cell aggregates in form of ripple-like areas adhered on the surfaces is identified. The plasma-treated collagen surfaces offer several favourable sites and polar groups which poten-

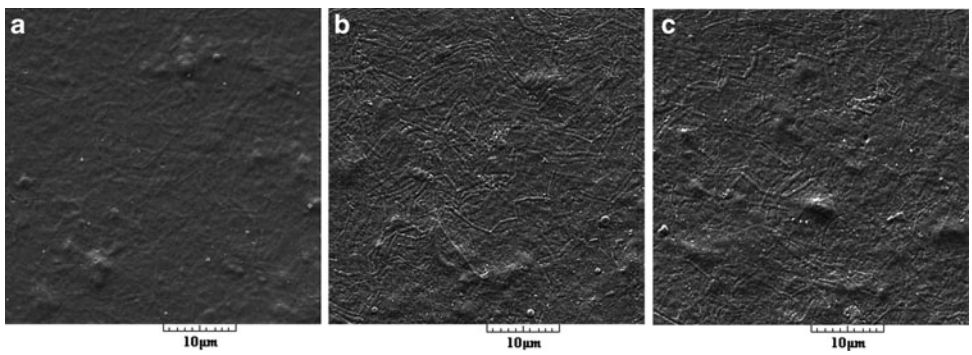

Fig. 3 SEM images of (A) untreated, (B) air and (C) nitrogen treated films

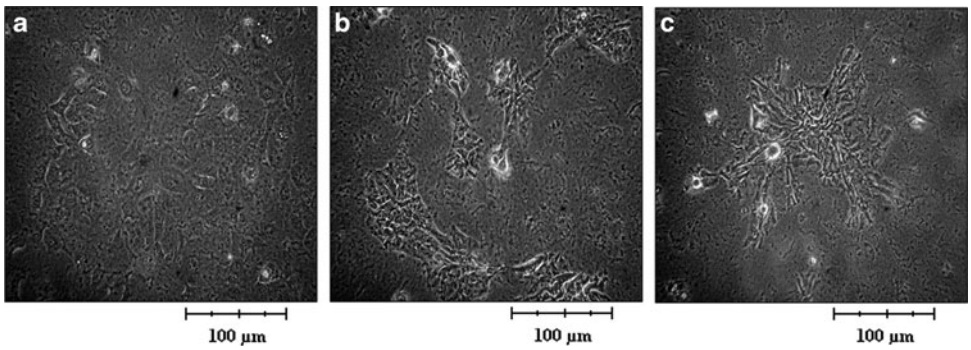

Fig. 5 Micrographs of human skin HaCaT keratinocytes in culture upon the collagen films. (A) untreated, (B) air and (C) nitrogen treated

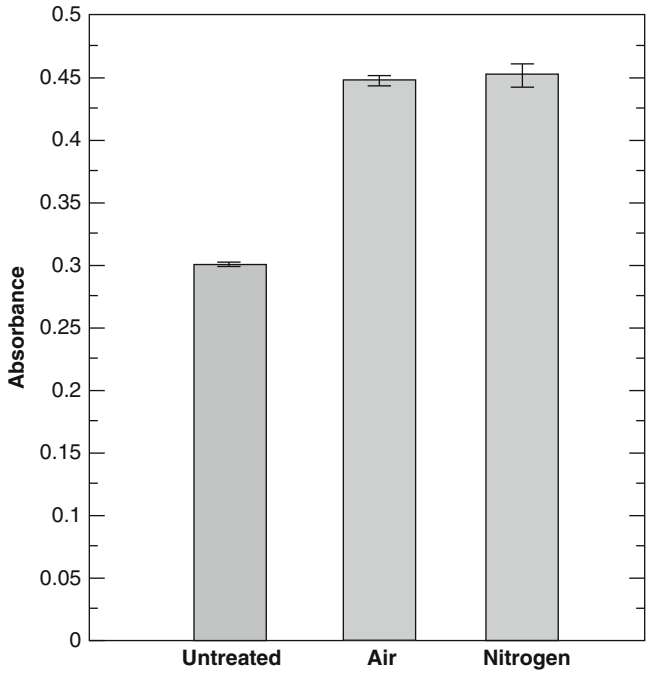

Fig. 4 Absorbance values of Formazan at 570 nm for determining the HaCaT cell proliferation by MTT assay (the error bars depict standard deviations)

tially link human cells. It is exactly the case of HaCaT keratinocytes whose cell growth tends to be favoured in hydrophilic surfaces, and their attachment is mainly concern of carbonyl and carboxyl groups along with hydrogen bonding and van der Waals forces, which reinforce the linking between cell and films [17-19].

Surface morphology is a key factor in cell attachment mechanism, since an increase in surface roughness lead to higher effective surface area and thus, more available sites for cells-substrate interaction. This information suggests that those plasma-treated films possess better condition for cell growth and are potentially suitable for tissue engineering applications likewise, the important role of organic entities and surface morphology on cell growth.

Conclusions

XPS and ATR-FTIR results indicated that plasma treatment is able to alter collagen thin films via chemistry surface modification. Other consequence of plasma surface modification was found microscopically. Air and nitrogen plasma treated samples showed an increase in surface roughness.

The keratinocytes HaCaT cell proliferation was remarkably improved after both treatments, pointing up the special connexion between physicochemical surface properties and cell growth. Thus, air and nitrogen plasma treatment are effective tools to increase organic entities (mainly O-containing functional groups) and surface roughness of collagen films providing chemical and physical features which enhance attachment and proliferation of keratinocyte cells.

Acknowledgements The authors are thankful to the Ministry of Education, Youth and Sports of the Czech Republic (MSM 70088352101) and (CZ.1.05/2.1.00/03.0111) for financial support. The author López JG would like to express his gratitude to the Internal Grant Agency (IGA/20/FT/11/D) of Tomas Bata University in Zlín, Czech Republic for financing of this research.

References

[1] Matthew HWT (2001) Polymers for Tissue Engineering Scaffolds. In: Dumitriu S (ed) Polymeric Biomaterials, vol 8. CRC Press, Boca Raton, pp 167-170
[2] Parenteau-Bareil R, Gauvin R, Berthod F (2010) Materials 3: 1863
[3] García JL, Asadinezhad A, Pacherník J, Lehocký M, Junkar I, Humpolíček P, Sáha P, Valášek P (2010) Molecules 15: 2845
[4] Lehmann B (1997) J Invest Dermatol 108: 78
[5] Langer R, Tirell DA (2004) Nature 18: 487
[6] Tabata Y (2009) J R Soc Interface 6: 311
[7] Chu PK, Chen JV, Wang LP, Huang N (2002) Mater Sci Eng Res 36: 143

[8] Desmet T, Morent R, De Geyter N, Leys C, Schacht E, Dubruel P (2009) Biomacromolecules 10: 2351
[9] Lehocký M, Drnovká H, Lapčíková B, Barros-Timmons AM, Trindade T, Zembala M, Lapčík L (2003) Colloids Surf A 222: 125
[10] Boukamp P, Petrussevska RT, Breitkreutz D, Hornung J, Markham A (1988) J Cell Biol 106: 761
[11] Mosmann T (1983) J Immunol Meth 65: 55
[12] Deslandes Y, Pleizier G, Poiré E, Sapieha S, Wertheimer MR, Sacher E (1998) Plasmas Polym 3: 61
[13] Vrlinič T, Vesel A, Cvelbar U, Krajnc M, Mozetič M (2007) Surf Interface Anal 39: 476
[14] Canal C, Gaboriau F, Richard A, Mozetič M, Cvelbar U, Drenik A (2007) Plasma Chem Plasma Process 27: 404
[15] Bryan MA, Brauner JW, Anderle G, Flach CR, Brodsky B, Mendelsohn R (2007) J Am Chem Soc 129: 7877
[16] Tiong WHC, Damodaran G, Naik H, Kelly JL, Pandit A (2008) Langmuir 24: 11752
[17] Paleos CM, Tsiourvas D, Sideratou Z (2004) Origins Life Evol Biosphere 34: 195
[18] Ji Y, Li XT, Chen GQ (2008) Biomaterials 29: 3807
[19] Lehocký M, Sťahel P, Koutný M, Čech J, Institoris J, Mráček A (2009) J Mater Process Technol 209: 2871

Progr Colloid Polym Sci (2011) 138:95–102
DOI: 10.1007/978-3-642-19038-4_17

Adsorption of Poly(Acrylic Acid)-Graft-Poly(Ethylene Glycol) on Polyelectrolyte Multilayers

Claus-Peter Klages, Sven Hartwig, and Hannah Schmolke

Abstract Graft copolymers PAA-g-PEG with poly(acrylic acid) (PAA, 200 kDa) backbone and poly(ethylene glycol) (PEG, 5 kDa) side chains with grafting ratios g = 5, adsorbed on stainless steel surfaces, were studied using FTIR-ATR spectroscopy. The amount of adsorbed PAA-g-PEG could strongly be increased with a polyelectrolyte multilayer (PEM) as an interlayer. Two independent calibration methods were used to calculate PEG chain areal densities σ_{PEG} or effective thickness values $d = \sigma_{PEG} \cdot n_{EG} / \rho_{EG}$ (n_{EG}: number of EG units in the chain, ρ_{EG}: assumed volume density of EG units) of the PEG component. With a suitable PEM interlayer a thickness of d = 34 nm, close to the theoretical length of a helical PEG chain with 114 EG units (32 nm), was obtained. In PEM-PEG coatings with appreciable contents of PEG, the dominance of vibrational bands with transition dipole moments parallel to the axis of helical PEG chains indicates that most PEG helices are oriented vertically on the substrate.

Keywords Polyelectrolyte multilayer PEM • poly (ethylene glycol) PEG • graft copolymer • FTIR-ATR • adsorption

Introduction

The present paper gives a concise account of selected results obtained during infrared spectroscopic investigations of poly (acrylic acid)-graft-poly(ethylene glycol) (PAA-g-PEG) copolymers adsorbed on bare stainless steel and on stainless steel precoated with polyelectrolyte multilayers (PEMs), respectively. The motivation of our studies was to control particle-wall interactions in microbioreactors consisting, generally, of polymers, glass, ceramics, and metals, and one special target was to prevent cell adhesion on the reactor surfaces. While designing a coating material and coating process suitable to generate a functional lining inside an already sealed multimaterial microfluidic device, several boundary conditions have to be observed: For example, the presence of metallic parts such as sensors or connectors generally precludes the utilization of atmospheric-pressure gas discharges (plasmas) which can otherwise be applied to treat or coat inner surfaces of microfluidic devices, consisting only of dielectrics (polymers, glass, ceramics) [1]. The presence of thermally sensitive materials sets an upper limit to temperatures which can be applied during a surface modification process. Due to the risks of debonding and destroying the device, extensive use of organic solvents for swelling of polymeric parts and subsequent incorporation of amphiphiles is also generally not possible. Last not least, radical polymerization processes *in situ*, as they are involved in "grafting from" approaches, are practically precluded because of the difficult deaeration of the microdevice.

Taking into account these and other prerequisites, our strategy was therefore to use the adsorption of PEMs from aqueous solution in order to cover all kinds of materials contributing to the inner surface of a hybrid microreactor. The deposition of PEMs using layer-by-layer (lbl) deposition was reported two decades ago by Decher and Hong in 1991 [2] and it was reviewed, among many others, by Tang et al. under the aspect of biomedical applications [3] and by Picart with a focus on the control of cellular behavior. In the latter article the physico-chemical factors favoring suppression of cell adhesion to the PEM surfaces were extensively discussed [4]. Mechanical properties and swellability of PEMs play an important role in cell adhesiveness. For example, PEMs based on the polyelectrolyte couple poly (acrylic acid) (PAA) and poly(allylamine hydrochloride) (PAH), deposited under conditions favoring highly swellable films, were found to be virtually bioinert against normally highly adhesive fibroblast cell lines [5].

However, as poly(ethylene glycol) (PEG) is commonly considered the material of choice for preventing bioadhesion

C.-P. Klages (✉)
Institut für Oberflächentechnik, Technische Universität Braunschweig, Bienroder Weg 54 E, D-38108 Braunschweig, Germany
e-mail: c-p.klages@tu-bs.de

in general and has frequently been shown to suppress adhesion of proteins and bacteria or cells on surfaces effectively, it is of interest to compare cell repellency performance of PEM coatings with that of surfaces obtained by PEGylation. For this purpose a graft copolymer was chosen with a polyelectrolyte backbone and PEG side chains. The preparation, adsorption and bioadhesive properties of graft copolymers of the type polyelectrolyte-g-PEG have already been reported in the literature [6-10]. However most of these papers are dealing with polymers with a polyamine backbone, such as poly(ethylene imine) or poly-L-lysine, because the corresponding graft copolymers, carrying a positive charge at not too high pH, will adsorb readily on negatively charged surfaces of silica [6] (or other materials with surface silanol groups such as glass or partially oxidized poly(dimethyl-siloxane)), stainless steel – actually carrying a chromium(III) oxide surface [7, 8], and other oxides such as titanium(IV) oxide or niobium(V) oxide [9, 10].

In the present paper the preparation and adsorption of poly(acrylic acid)-g-poly(ethylene glycol) (PAA-g-PEG) is described, a graft copolymer with a poly(carboxylic acid) backbone, forming a negative charge upon dissociation. This choice was made because of our special interest in attaching (PEGylated) PEMs firmly to stainless steel surfaces: PAA is known to have a high chemical affinity to metal oxides, among others Cr_2O_3, due to the formation of carboxylates with mono- or bisdentate chelating [11]. The paper focuses on surprising results obtained while investigating PAA-g-PEG coatings adsorbed on stainless steel surfaces which had been precoated with PEMs. Due to the importance of a determination of the adsorbed amount (PEG chain areal density or effective thickness) by FTIR-ATR spectroscopy, the corresponding calibration procedures will be explained in some detail in this paper. A comparison of different synthetic approaches to graft copolymer PAA-g-PEG with differing g is described in more detail in a forthcoming paper; only the optimum method is therefore reported in the following.

Experimental

Materials

1-Hydroxy-benzotriazole (HOBT), *N,N′*-diisopropylcarbodiimide (DIC), and *N,N*-dimethylformamide (DMF) were obtained from Sigma-Aldrich (Germany). Poly(allylamine hydrochloride) (PAH; M_w = 60 kDa) and poly(acrylic acid) (PAA; M_w = 200 kDa) were purchased from Polysciences Europe GmbH (Eppelheim, Germany). A methoxy-terminated poly(ethylene glycol)-amine (mPEG-NH_2) (M_w = 5 kDa) was obtained from Rapp-Polymere (Tübingen, Germany). All chemicals were used without further purification. All polyelectrolyte solutions were prepared with ultra pure water (TKA MicroPure purification stage, Niederelbert, Germany) using a polyelectrolyte concentration of 0.01 mol/L with respect to the monomer unit. Directly before the coating process, the polyelectrolyte solutions of PAH and PAA were carefully adjusted to a fixed pH using dilute NaOH or dilute HCl.

Preparative Methods

Synthesis of PAA-5-PEG

19 mg (0.15 mmol) DIC and 20 mg (0.15 mmol) HOBT were added to a solution of 7.2 mg PAA (0.1 mmol AA units) in 5 ml DMF. The solution was kept for 1 h at 40 °C under stirring; then 100 mg (0.02 mmol) mPEG-NH_2 was added and the reaction was allowed to proceed at 40 °C for another 20 h. The DMF was subsequently removed in a rotary evaporator, the resulting copolymer was dissolved in 5 ml water and dialysed against water for one week, using a 100 kDa molecular weight cut off filter (Spectra/Por CE Float-A-Lyzer G2, Spectrum Labs, purchased from Sigma-Aldrich, Germany). According to gel permeation chromatographic determination of the molecular weight, g = 4.8 (one PEG side chain per 4.8 AA units) is obtained by this procedure. In the following the designation PAA-g-PEG will always refer to this copolymer, PAA(200 kDa)-5-PEG (5 kDa).

Preparation of Stainless Steel Surfaces

Stainless steel foils (50 µm thickness, ASTM 304 (DIN 1.4301), Georg Martin GmbH, Germany) were manually mirror-polished using water-based diamond suspensions (MetaDi, Buehler, Germany) with particle sizes from 3 µm (polishing time 12 min) down to 1 µm (polishing time 5 min), and cleaned by repeated wiping with an acetone-soaked tissue. Among various cleaning methods (e.g. ultrasonic cleaning in ethanol or alkaline solution, treatment with H_2SO_4/H_2O_2 (*Piranha*) solution, cleaning with other organic solvents), evaluated by FTIR-ATR measurements and PAA adsorption experiments, this was the most effective one leading to sufficient cleaning, leaving the passivation layer of stainless steel surface intact, and yielding relatively large amounts of adsorbed PAA.

Deposition of PEMs and Adsorption of PAA-g-PEG

The deposition of PEM films was done using a dipping robot (Riegler & Kirstein GmbH, Berlin, Germany) by exposing stainless steel foils alternately to the two aqueous 10^{-2} M (based on the repeating unit) polymer solutions for 2 min with three rinsing steps with ultra pure water (2 min, 1 min and 1 min) in between. During one such cycle a polyelectrolyte double layer (DL) is created on the surface. To deposit PAA-g-PEG the copolymer was diluted to a concentration of approx. 5 mM (based on AA units), pH adjusted and then adsorbed for 10 min, either on bare stainless steel or PEM interlayers, followed by 10 min rinsing in water under agitation. In the following a word like "(PAH7.5/PAA3.5)x" signifies that the PEM was assembled from PAH and PAA solutions with pHs of 7.5 and 3.5, resp.; x denotes the number of double layers assembled; half-integral x indicates a PEM ending with a PAH layer.

Film Characterization

For FTIR-ATR measurements a Nicolet 5700 FT-IR spectrometer (Thermo Scientific) was used, equipped with a DuraSamplIR single-reflection 45° diamond ATR crystal. The IR beam had parallel polarization with respect to the plane of incidence. In order to provide good optical contact between the polished 50 µm stainless steel foils and the ATR crystal, a soft polymeric backing cushion was arranged behind the foil. Film thicknesses were also determined by ellipsometry (SE 850, Sentech GmbH, Berlin, Germany) of the coatings on stainless steel surfaces, preferably on polished small blocks instead of foils in order to guarantee planarity of the surface. In order to determine film thicknesses, an oscillator model was used to describe the optical properties of the substrate and a Cauchy model was applied for the organic film.

Quantification of FTIR-ATR Spectra of PEG-Containing Thin Films

FTIR-ATR spectra of thin PAA-g-PEG or PEM-PEG films on metal substrates can be used to gain information about the structure as well as the areal density of EG units or PEG chains on the surface, if the films contain primarily randomly oriented or aligned helical coils. The analysis can be made for ultrathin layers with thicknesses down to a few nanometers, because the metal substrate will not contribute signals interfering with vibrational bands of the organic coating. Near the metal surface the electric field of the infrared light has only a perpendicular component; therefore only vibrations with a transition dipole moment (TDM) component oriented perpendicular to the surface will be visible in the ATR spectrum [12]. The symmetry of the helical PEG coil with 7 EG units in two helical turns per one fibre period – a so-called (7/2) helix - of 19.48 Å length [13] allows a classification of infrared-active normal vibrations into bands with TDMs parallel to the coil axis (parallel bands, belonging to the irreducible representation A_2) and bands with TDM vertical to the coil axis (perpendicular bands, E_1). In most of the FTIR-ATR spectra of PEM-PEGs with an appreciable amount of PEG recorded in this study, parallel bands typical of crystalline PEG are dominating the spectra (Figure 1), indicating the presence of largely intact helical PEG coils with a high degree of vertical orientation relative to the metal substrate. These spectra look virtually identical (in line positions, peak absorbance ratios and line widths) to IRRAS spectra of 9 nm thick self assembled PEG monolayers on gold, reported by Herrwerth (ref. [14] and personal communication by R. Dahint).

In the present work two calibration methods (A and B) have been used to derive effective thickness values, i.e., thicknesses determined under the assumption that the PEG phase in the samples under investigation has the same density as the reference materials used.

Method A uses bulk ATR spectra of thick polycrystalline samples of PEG with a random orientation of helical coils: Using the SpectraRay 2 software package (SENTECH Instruments GmbH, Berlin, Germany), Drude-Lorentz oscillator parameters [15] were determined by spectral line fits to selected vibrational bands of an ATR spectrum, taken from

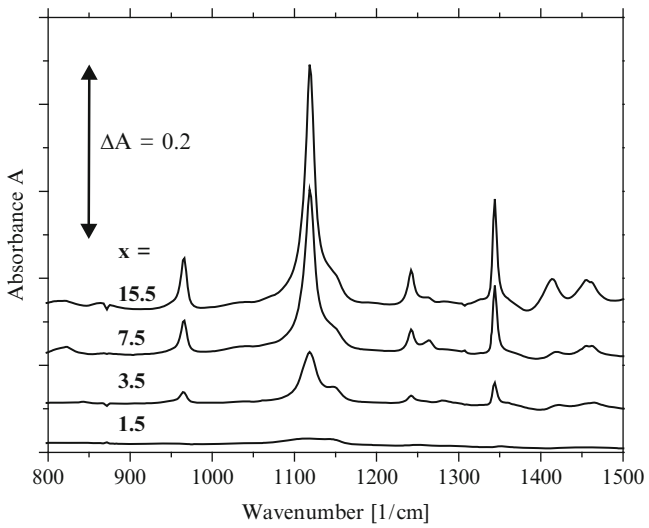

Fig. 1 FTIR-spectra of PAA-g-PEG adsorbed on (PAH7.5/PAA3.5)x at pH 3.2 (interlayer spectrum was subtracted). x is indicated at the corresponding spectra (The band at 1413 cm^{-1} in the spectrum of sample x = 15.5 is a residual PEM band; feature at 1263 cm^{-1} for x = 7.5 is probably due to contamination)

methoxy-terminated amino-PEG (5 kDa) (see above) by single-reflection diamond ATR (45°, p-polarization), see Figure 2. Then the oscillator parameters (Table 1) were used to calculate the spectrum of a hypothetical thin film with random coil orientation on a stainless steel, using optical parameters of iron in the infrared [16] for the substrate. To calculate the spectrum of a thin film with helices oriented vertically on the metal substrate, oscillator strengths of parallel bands were then multiplied by 3 in order to take into account the increase of absorption upon going from a random orientation of TDMs relative to $\hat{E}$ (absorption ~ $<\cos^2\alpha> = 1/3$, α = angle between TDM and E field) to the situation in which all TDMs are aligned parallel to $\hat{E}$ ($<\cos^2 0> = 1$). Correspondingly, oscillator strengths of perpendicular bands were set equal to 0. At room temperature, long chain methoxy-terminated PEGs (Carbowax PEGs) have densities of typically 1.13 g/cm^3, corresponding to ρ_{EG} = 15.5 EG units per nm^3. Thus, as an example, for the strong parallel band at 1341 cm^{-1} (antisymmetric CH_2 wagging vibration of CH_2-CH_2 in helices with gauche-trans-trans-gauche (GTTG) conformation of the sequence CH_2-CH_2-O-CH_2-CH_2 [17]) an absorbance A of 0.0040 (0.040) is calculated for a 2.5 nm (25 nm) thick film with random coils, corresponding to A = 0.012 (0.12) in vertically aligned films with the same thicknesses, if the EG unit density of ρ_{EG} = 15.5 nm^{-3} applies also to these films. For a lower assumed ρ_{EG}, higher thicknesses will be obtained for the given A and vice versa. The corresponding EG unit areal densities are ρ_{EG}·d = 38.8 nm^{-2} and 388 nm^{-2} for A = 0.0122 and 0.12, resp. In crystalline PEGs the 1341 cm^{-1} vibration is well separated from other bands and can therefore easily be used to calculate the effective thickness of random or vertically aligned PEG, i.e., the thickness which results if the unknown sample and the reference sample are assumed to have the same packing density of oscillators. Thanks to the virtually identical line widths of corresponding vibrations in the PEM-PEGs and the reference PEG, the calibration can be based on band peak absorbance values instead of band areas.

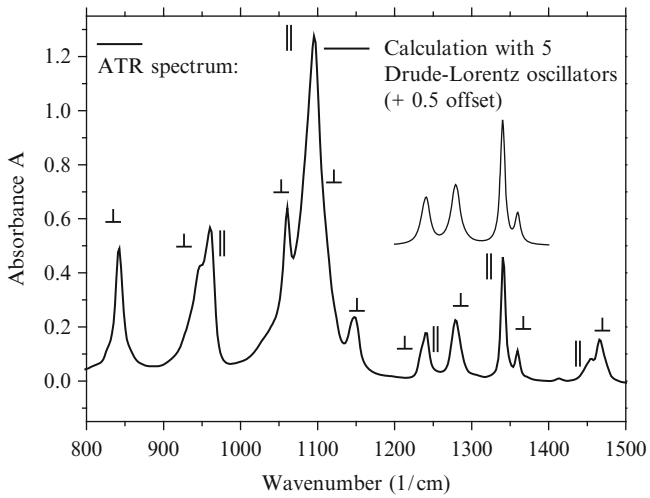

Fig. 2 Bold line: FTIR-spectrum of a thick layer of polycrystalline PEG; symbols are representing the TDM orientations of the corresponding bands. Faint line: Calculated spectrum between 1200 and 1400 cm^{-1} consisting of five Drude-Lorentz oscillators with parameters given in Table 1 (spectrum is offset by + 0.5 absorbance units)

Table 1 Oscillator parameters of selected CH_2 vibrations

Band #	1	2	3	4	5
Ω_0 (cm^{-1})	1237	1242	1280	1341	1360
Ω_p (cm^{-1})	28.0	45.0	66.0	70.0	38.0
Ω_τ (cm^{-1})	12.0	11.0	14.0	7.0	8.0
Assignment	CH_2 twist E_1	CH_2 twist A_2	CH_2 twist E_1	CH_2 wagg A_2	CH_2 wagg E_1

The table presents oscillator parameters of five selected CH_2 vibrations between 1200 and 1400 cm^{-1} used to fit the Drude-Lorentz spectrum calculation to an experimental spectrum of random polycrystalline PEG. See ref. [15] for the meaning of Ω_0, Ω_p, and Ω_τ. For the high-frequency dielectric constant ε_∞ = 2.10 was used, see text

A critical point in method A is the not exactly known refractive index n or, in terms of the Drude-Lorentz model, ε_∞ of PEG in the infrared region, because it enters the spectrum calculation but cannot be determined with sufficient accuracy from the spectral fit. Changes of ε_∞ have, other things being equal, opposite effects on ATR reflectivities calculated for bulk material and thin films on metal, respectively. In the present calculation, ε_∞ = 2.10 (n = 1.45) was used, somewhat smaller than the value n_D = 1.46 reported in the literature [18] in order to take into account the optical dispersion [19] in an approximate manner.

The second method (B) used is based on an equation for external reflection spectroscopy on metal substrates given in the paper of Chabal [12], covering both IRRAS spectra and ATR of thin films on highly reflective metal substrates:

$$\left.\frac{\Delta R}{R}\right|_{p-pol} = 8\pi\tilde{\nu}\cdot \mathrm{Im}\left[\frac{-1}{\tilde{\varepsilon}_z}\right]\cdot\left(n_1^3\frac{\sin^2\theta}{\cos\theta}\right)\cdot d \qquad \text{Eq.1}$$

$\tilde{\nu}$ and d are the wavenumber and film thickness, respectively. The method-dependent term in the round bracket, containing the refractive index of the dielectric medium and the angle of incidence, n_1 and θ, is a factor of 1.75 higher for our ATR method than for IRRAS on Au with an incidence angle of 80°, due to the higher n_1 (ATR: diamond with n_1 = 2.4 instead of IRRAS: air with n_1 = 1.0). For samples with the same molecular structure, the imaginary part of the material-dependent complex function in the square bracket should be identical. As the close similarity of the IRRAS spectrum of a PEG-SAM reported by Herrwerth et al. [14] suggests a very similar structure, it appears reasonable to take it as a

reference for PEM-PEG spectra with vertically oriented PEG coils. To a good approximation the properties of the metal substrates (Au and stainless steel, resp.) do not enter the equation because of the high absolute value of their dielectric function $|\varepsilon_m| > n_1^2 \cdot \tan^2\theta$ [12]. The sulfur-bonded PEG-SAMs on Au have a packing density of 4.67 nm^{-2} [20]; therefore a somewhat higher EG density, 16.8 nm^{-3}, corresponding to a density of 1.23 g/cm^3, is expected here, in reasonable accordance with the x-ray density of PEG (1.22 g/cm^3 [13]).

The evaluation of film thickness is done by plotting the band peak absorbances A_i of the five most prominent PEM-PEG bands in the range of 800 to 1500 cm^{-1} as ordinate values against the corresponding values of the 9 nm PEG-SAM on the abscissa (Figure 3). From the slope s of the linear fit the thickness of vertically aligned PEG with 16.8 EG units nm^{-3} can be determined by the simple equation

$$d_B/\mathrm{nm} = s \cdot \frac{9.0}{1.75} = s \cdot 5.14 \qquad \text{Eq.2}$$

For not too large absorbances $A = \log(1+\Delta R/R) \approx (\Delta R/R)/\ln(10)$, therefore plotting the A_i gives approximately the same slope as plotting $(\Delta R/R)_i$ as long as $A_i < 0.1$. Empirically, however, the linear correlation between A_i(PEM-PEG) and the A_i(PEG-SAM) extends to larger A_i (up to 0.4). The relative difference between thicknesses determined by methods A and B, d_A and d_B, is usually less than 15 %, see below.

Using at least one perpendicular band in addition to the parallel band at 1341 cm^{-1}, the principle of method A outlined here can easily be extended to more complicated situations where i) a mixture of a randomly oriented PEG phase and a phase with vertically aligned helices or ii) a PEG phase with coils inclined by a finite angle with respect to the surface normal is present. This quantitative analysis does not apply, however, to situations where the PEG chain conformations depart significantly from the ideal (7/2) helix. This is obviously the case in PAA-g-PEG films adsorbed directly onto stainless steel substrates, showing absorption bands near 1255, 1300, and 1325 cm^{-1} (Figure 4) which are not visible in crystalline PEG phases and are probably due to segments TGG O-CH_2-CH_2-O, GT CH_2-O-CH_2, and T OCH_2-CH_2O [17], not present in the ideal helix. The appearance of these conformations can be taken as an evidence of a strong interaction between the PEG chain and the chromium oxide layer on the stainless steel substrate.

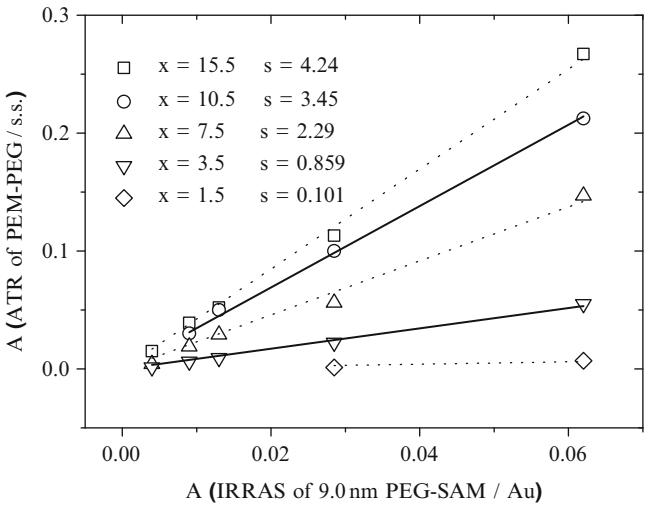

Fig. 3 Plots of peak absorbances of the five most prominent vibrational bands between 900 and 1500 cm-1 in FTIR-ATR spectra of PAA-g-PEG adsorbed on (PAH7.5/PAA3.5)x interlayers on stainless steel at pH = 3.2 against the corresponding values in an IRRAS spectrum of a 9.0 nm thick PEG-SAM on gold, taken from the literature [13]. The slopes s are determined by linear regression

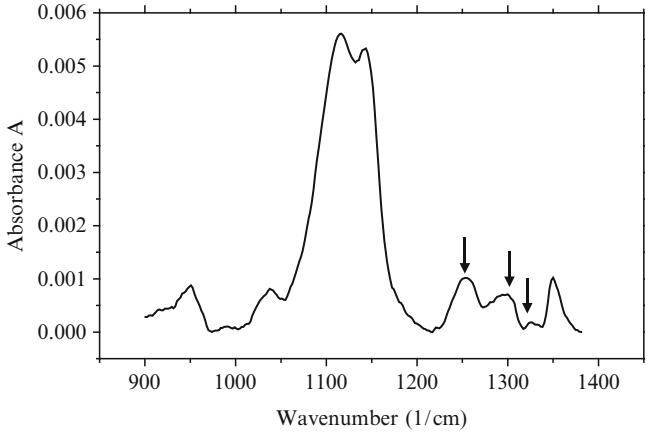

Fig. 4 FTIR-ATR spectra of PAA-g-PEG adsorbed on bare stainless steel. Arrows indicate features at 1255, 1300, and 1326 cm^{-1}, which are not present in spectra of crystalline PEGs with helical coils

Results and Discussion

Table 2 compiles results of ellipsometric and infrared spectroscopic determinations of dry thickness applied to PEM interlayers of the type (PAH7.5/PAA3.5)x and to the PEG component of PAA-g-PEG adsorbed to (PAH7.5/PAA3.5)x. Figure 5 shows a plot of d_{elli} (PEM) data in the 2nd column against the corresponding number of double layers x (1st column) (black squares). It exhibits a pronounced non-linearity indicating that the PEM deposition process is in the "exponential" regime [21, 22]. Figures in the 3rd column were obtained by subtracting the ellipsometric thicknesses d_{elli} (PEM) from d_{elli} (PEM-PAA-g-PEG) obtained after adsorption of the copolymer. The following two columns are effective thicknesses of the PEG components of PEM-PAA-g-PEG as determined by infrared spectroscopic methods A

and B outlined above, assuming $\rho_{EG} = 16.8\ nm^{-3}$. In the last column PEG chain densities are given, calculated for PEG (5 kDa) with $n_{EG} = 114$ EG units from $\sigma_{PEG} = \rho_{EG} \cdot d_B / 114$.

Surprisingly the amount of adsorbed PEG could be increased very strongly, compared to bare stainless steel (or Cr_2O_3), by using a suitable PEM as an interlayer. Although the ATR spectrum of PAA-g-PEG on stainless steel in Figure 4 cannot be evaluated quantitatively as reliably as the ATR spectra of PAA-g-PEG adsorbed on PEM, one can estimate that the adsorbed amount is roughly two orders of magnitude smaller without a PEM interlayer. On (PAH7.5/PAA3.5)x the adsorbed amount increases with x, see d_A, d_B and ρ_{PEG} in Table 2 and Figure 5. The close similarity of the PEM spectra, obtained after subtraction of the interlayer spectrum, to IRRAS spectra of PEG-SAMs leads to conclude that a crystal-like, highly ordered PEG phase is formed on top of the PEM interlayer.

Table 2 Thicknesses of (PAH7.5/PAA3.5)x and effective thicknesses of PEG components

Number of DLs x	d_{elli}(PEM) (nm)	d_{elli}(PEG) (nm)	d_A(PEG) (nm)	d_B(PEG) (nm)	σ_{PEG} (nm^{-2})
1.5	3.4	0.99	0.3	0.52	0.077
3.5	14.0	3.9	4.2	4.42	0.65
7.5	55.8	5.2	10.8	11.8	1.74
10.5	n.d.	n.d.	19.2	17.7	2.61
15.5	154.1	7.2	21.7	21.8	3.21

The table presents results of thickness determinations based on ellipsometry (d_{elli}) or infrared spectroscopy (d_A and d_B). DL =double layer. n.d. = not determined. d_{elli}(PEG) are differences in dry thicknesses after and before adsorption of PAA-g-PEG on the corresponding PEM. d_A and d_B were determined assuming a EG unit density of $\rho_{EG} = 16.8\ nm^{-3}$. Figures in the last column are the PEG chain densities calculated for PEG (5 kDa) with 114 EG units from $\sigma_{PEG} = \rho_{EG} \cdot d_B/114$

We attribute the high amount of PEG adsorbing on (PAH7.5/PAA3.5)x and the increase of PEG chain densities σ_{PEG} with x to the pronounced exponential growth of the PEM underlayer, see Figure 5. On another interlayer, (PAH9.0/PAA9.0)20.5, which is also known to grow in the exponential mode [23], the maximum density of chains obtained so far in these studies, 5.0 nm^{-2}, was found, close to the maximum possible packing density of parallel PEG chains, 4.67 nm^{-2} [13]. The effective thickness of the PEG component, assuming 16.8 EG units per nm^{-3}, is 34 nm (ellipsometric thickness: 25 nm), close to the lengths of the ideal PEG helix with 114 units (32 nm). On interlayers of the type (PAHy/PAAy)x with y = 2.0, 3.5, and 7.5, on the other hand, growing linearly in the zones I and III of the classification used by Bieker and Schönhoff [23], the adsorbed chain density stayed usually below 0.5 nm^{-2}, in spite of x attaining values up to 30.5 (y = 3.5) and 60.5 (y = 7.5), respectively.

An unequivocal interpretation of the findings reported here in terms of the growth mode and presumed structure of the (PAH/PAA) interlayer is hindered by the experimental procedure used to deposit the PEMs, involving in general three different pHs for adsorption of the polyanion, the polycation, and for rinsing, and a fourth pH value for adsorption of the PAA-g-PEG. The close relation of the adsorbed amount and the growth mode seems to suggest, however, that the observed strong increase of PEG chain density σ_{PEG} with the number of double layers x of exponentially growing (PAH/PAA) can be related to an increasing amount of free PAH chains which are able to diffuse to the film surface when it is brought into contact with the solution of PAA-g-PEG, in agreement with the generally accepted explanation of exponential PEM growth [21]. The failure of ellipsometric thickness determinations of adsorbed

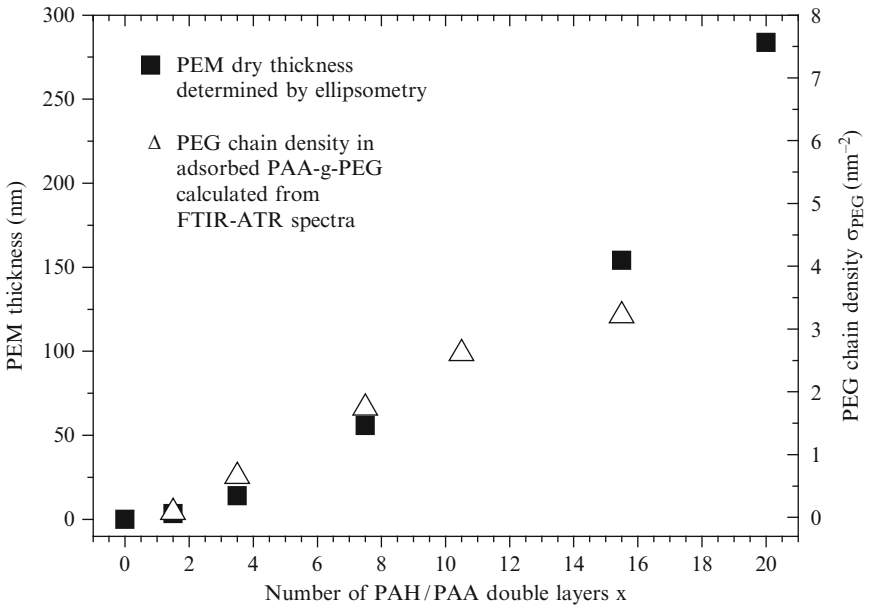

Fig. 5 Thickness of dry (PAH7.5/PAA3.5)x films on stainless steel substrates as determined by ellipsometry and PEG chain densities σ_{PEG} calculated from FTIR-ATR spectra using method B. Half-integral x signifies a film ending with a PAH layer

PAA-g-PEG as thickness difference after and before adsorption (see Table 2: d_{elli}(PEG) is always too small, compared to d_A and d_B) is probably due to a loss of previously adsorbed polyelectrolytes upon exposure to the copolymer solution, similar to what is observed in the system PAH/PAA itself [22].

Upon extended treatment with agitated water some of the adsorbed PEG is desorbed from the surface; the effect of extended H_2O rinsing on adsorbed PEG amount was investigated for (PAH7.5/PAA3.5)5.5-PAA-g-PEG: 67 % and 45 %, resp., of the coating were still present after 1 and 6 days, resp., in stirred water. With respect to cell anti-adhesiveness the PEM-PEG systems were found to be superior to PEG-free PEM as a wall coating in PDMS-based rectangular microchannels; PEM-PEG systems exhibited the lowest wall shear stress necessary to remove cells of a hydrophobic strain (DSM 2155) of *saccharomyces cerevisiae*. More details about adsorption behavior, stability in salt solutions, and cell repellency can be found in separate papers [24, 25].

Summary

Adsorption of PAA(200 kDa)-5-PEG(5 kDa) onto suitable PAH/PAA-based PEMs results in a drastically increased amount of surface-bound PEG, compared with adsorption on the Cr_2O_3 surface of stainless steel. FTIR-ATR spectra show a highly ordered structure with helical PEG coils orientated vertically to the substrate surface. Evaluation of FTIR-ATR spectra with respect to adsorbed chain densities reveal a very close chain packing up to 5 nm^{-2}. Suitable PEM-PEGs are very effective in suppressing wall adhesion of hydrophobic yeast cells.

Acknowledgement The authors thank the German Research Foundation (DFG) for support of this work in the framework of the Collaborative Research Group FOR 856 “mikroPART”.

References

[1] Klages CP, Hinze A, Lachmann K, Berger C, Borris J, Eichler E, v. Hausen M, Zänker A, Thomas M (2007) Plasma Process Polym 4: 208
[2] Decher G, Hong JD (1991) Ber Bunsenges Phys Chem 95: 1430
[3] Tang Z, Wang Y, Podsiadly P, Kotov, NA (2006) Adv Mater 18: 3203
[4] Picart C (2008) Curr Med Chem 15: 685
[5] Mendelsohn JD, Yang SY, Hiller J, Hochbaum AI, Rubner MF (2003) Biomacromolecules 4: 96
[6] Malmsten M, Emoto K, Van Alstine JM (1998) J Coll Interf Sci 202: 507
[7] Wei J, Bagge-Ravn D, Gram L, Kingshott P (2003) Coll Surf B Biointerfaces 32: 275
[8] Ngadi N, Abrahamson J, Fee C, Morison K (2009) Int J Biol Life Sci 1: 145
[9] Kenausis GL, Vörös J, Elbert DL, Huang N, Hofer R, Ruiz-Taylor L, Textor M, Hubbell JA, Spencer ND (2000) J Phys Chem B 104: 3298
[10] Pasche S, De Paul SM, Vörös J, Spencer ND, Textor M (2003) Langmuir 19: 926
[11] Wu HS, Jone HC (1997) Ind Eng Chem Res (1997) 36: 2006
[12] Chabal YJ (1988) Surf Sci Rep 8: 211
[13] Takahashi Y, Tadokoro H (1973) Macromolecules 6: 672
[14] Herrwerth S, Rosendahl T, Feng C, Fick J, Eck W, Himmelhaus M, Dahint R, Grunze M (2003) Langmuir 19: 88
[15] Tolstoy VP, Chernyshova IV, Skryshevsky VA (2003) Handbook of Infrared Spectroscopy of Ultrathin Films. John Wiley & Sons, Inc., Hoboken, New Jersey, USA, pp. 13-23
[16] Ordal MA, Bell RJ, Alexander Jr. RW, Long LL, Querry MR (1985) Appl Opt 24: 4493
[17] Matsuura H, Fukuhara K (1986) J Pol Sci B Pol Phys 24: 1383
[18] Aminabhavi TM, Banerjee K (1998) J Chem Eng Data 43: 852
[19] Ford JV, Sumpter BG, Noid DW, Barnes MD, Otaigbe JU (2000) Appl Phys Lett 77: 2515
[20] Harder P, Grunze M, Dahint R, Whitesides GM, Laibinis PE (1998) J Phys Chem B 102: 426
[21] Picart C, Mutterer J, Richert L, Luo Y, Prestwich GD, Schaaf P, Voegel JC, Lavalle P (2002) PNAS 99: 12531
[22] Elzbieciak M, Kolasińska M, Zapotoczny S, Krastev R, Nowakowska M, Warszyński P (2009) Colloid Surf A Physicochem Eng Asp 343: 89
[23] Bieker P, Schönhoff M (2010) Macromolecules 43: 5052
[24] Schmolke H, Demming S, Edlich A, Magdanz V, Büttgenbach S, Franco-Lara E, Krull R, Klages C-P (2010) Biomicrofluidics 4: 044113; doi:10.1063/1.3523059
[25] Schmolke H, Hartwig S, Klages C-P (2011) phys stat sol (c), accepted

Progr Colloid Polym Sci (2011) 138:103–108
DOI: 10.1007/978-3-642-19038-4_18

Phase Separation for Langmuir Monolayer in Binary System Based on a π-A Isotherm Measurement

Miyuki Kuramori, Takamasa Ishikawa, Takayuki Narita, and Yushi Oishi

Abstract The mixing behavior of binary monolayer of fatty acid was investigated on the basis of π-A isotherm measurements. The (palmitic acid(C_{16})/arachidic acid(C_{20})) and (C_{20}/lignoceric acid(C_{24})) mixed monolayers were in a miscible state, whereas the (C_{16}/C_{24}) mixed monolayer was an immiscible state. The (C_{16}/behenic acid(C_{22})) and (stearic acid(C_{18})/C_{24}) mixed monolayers were in an incomplete miscible state. The dependence of mixing behavior on the difference in the number of methylene group between components in monolayer is probably due to an enthalpic contribution based on the difference in cohesive energy between the monolayer components.

Keywords Monolayer • Fatty acid • Phase separation • Cohesive energy • Π-A isotherm

Introduction

The monolayer in a multi-component system has been attracting attention from the viewpoints of fundamental understanding on molecular self-assembly [1], as well as its applications for surface modifiers [2], biosensing [3-5], photoswitching [6] and electrical devices [7]. In this system, whether amphiphilic molecules are miscible or immiscible in the monolayer is important for its properties. Therefore, a systematic understanding on the phase separation mechanism in a mixed monolayer appears to be an essential step in the design and construction of functionalized structures in the system. The phase separation in a monolayer state depends on many factors involving electrostatic interaction, molecular chirality and so on besides thermodynamic parameters such as the subphase temperature and surface pressure. Hence, for a systematic understanding of phase separation in a monolayer, it is necessary to investigate a simple experimental system of fatty acid monolayer as a first step. The aggregation state of fatty acid monolayer depends mainly on the thermal molecular motion, the electrostatic interaction between hydrophilic groups and the cohesive energy between hydrophobic groups. Of these factors, little attention has been given to a systematic examination for the phase separation with respect to the difference in cohesive energy between those components. In this study, the mixing behavior of binary monolayer of fatty acids was investigated on the basis of π-A isotherm measurements with respect to the difference in cohesive energy of each alkyl chain.

Y. Oishi (✉)
Department of Chemistry and Applied Chemistry, Faculty of Science and Engineering, Saga University, 1 Honjo, Saga 840-8502, Japan
e-mail: oishiy@cc.saga-u.ac.jp

Experimental

Palmitic ($CH_3(CH_2)_{14}COOH$, C_{16}), Stearic ($CH_3(CH_2)_{16}COOH$, C_{18}), Arachidic ($CH_3(CH_2)_{18}COOH$, C_{20}), Behenic ($CH_3(CH_2)_{20}COOH$, C_{22}) and lignoceric ($CH_3(CH_2)_{22}COOH$, C_{24}) acids with a purity > 99.99 % were used as monolayer components. Benzene solutions of C_{16}, C_{18}, C_{20}, and (C_{16}/C_{20}) mixtures with molar fractions of 75/25, 50/50, 25/75 were prepared at a concentration of 2.0×10^{-3} mol L^{-1}, and those of C_{22}, C_{24}, and (C_{16}/C_{22}, C_{16}/C_{24}, C_{18}/C_{24}, C_{20}/C_{24}) mixtures with molar fractions of 75/25, 50/50, 25/75 were prepared at a concentration of 8.0×10^{-4} mol L^{-1}. The subphase water was purified by an Ultra High Quality Polishing System (Elgastat Co., Ltd.). The sample solution was spread on the water surface at a subphase temperature, T_{sp} of 293 K. The dimensions of the trough were 560 mm in length, 150 mm in width and 5 mm in depth. T_{sp} was adjusted to variation of ± 0.5 K by circulating constant-temperature water around the aluminum support of the trough. Also, the room temperature was adjusted to the same temperature as each T_{sp} by using an air-conditioner. After standing for 60 min, π-A isotherm of

each monolayer was measured under compression by two barriers at an area change rate of 8.6×10^{-5} nm^2 molecule^{-1} s^{-1} with a microprocessor-controlled film balance system (FSD-300, USI System).

Results and Discussion

Figure 1 (a) shows π-A isotherms of pure C_{16}, C_{20}, and of (C_{16}/C_{20}) mixed monolayers with different molar fractions on the water surface at a T_{sp} of 293 K. This figure was illustrated by sliding the abscissas corresponding to the five molar fractions for clarity. The π-A isotherms of the pure palmitic and arachidic acid monolayers (C_{16}/C_{20}: 100/0, 0/100) exhibited a sharp rise in surface pressure at a surface area of ca. 0.25 nm^2 molecule^{-1}. This increase in surface pressure results from contact between two-dimensional domains grown just after spreading a solution by surface compression. The π-A isotherms of the (C_{16}/C_{20}) mixed monolayers exhibited a characteristic shape at each molar fraction. Figure 1 (b) shows the composition dependence of surface pressure at the collapse and transition points from L_2 to LS of monolayer phase [8]. Collapse pressure linearly varied with the molar fraction. Surface pressure at the transition point decreased with an increase in C_{20} content to be a minimal value of 16.7 mN m^{-1} at the molar fraction of around 0.5. These indicate that the monolayer is composed of a single phase, and also that the aggregation state of monolayer changes with the monolayer composition. The miscibility behavior of the components in the mixed monolayer may be examined by the variation in the average molecular occupied area as a function of the composition. The following additivity rule is valid for a mixed system with ideal mixing or complete immiscibility of components [9-12]

$$A_{12} = N_1A_1 + N_2A_2,$$

where A_{12} is the average molecular area in a composite film, N_1 and N_2 are the molar fractions of the components, and A_1 and A_2 are the molecular area in the two single component films at the same surface pressure. A deviation from the additivity rule leads to the conclusion that the components of the system are miscible. The measured molecular areas for the mixed monolayer at constant surface pressures are plotted against the molar fraction of C_{20} in Figure 1 (c). Those plots revealed a negative deviation from the additive line, suggesting that the mixed monolayer is miscible. It is, therefore, reasonable to consider that the (C_{16}/C_{20}) mixed monolayer with the difference in the cohesive energy corresponding to four CH_2 groups (24-30 kJ mol^{-1}) is in a miscible state at 293 K.

Figure 2 (a) shows π-A isotherms of pure C_{16}, C_{24}, and of (C_{16}/C_{24}) mixed monolayers with different molar fractions at 293 K. For a pure lignoceric acid monolayer (C_{16}/C_{24}: 0/100), a plateau region was observed in an area range of 0.21 - 0.23 nm^2 molecule^{-1} on the π-A isotherm. The plateau region appears owing to the consumption of compression energy for the transition from a hexagonal system (L_2) to

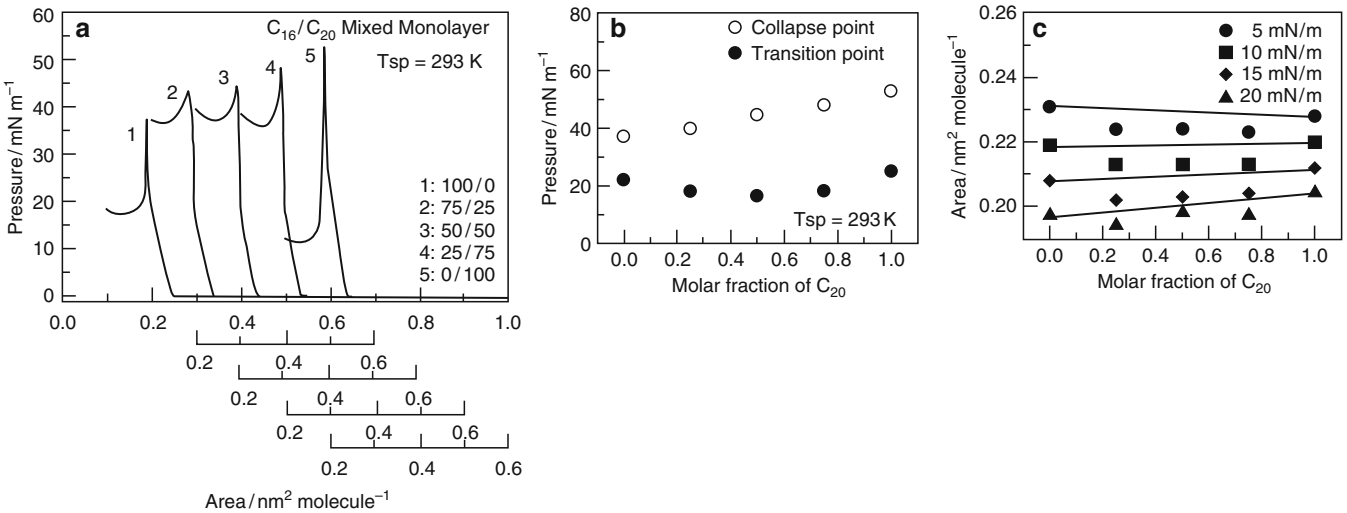

Fig. 1 (a) Π-A isotherms of pure C_{16}, C_{20} and of (C_{16}/C_{20}) mixed monolayers with molar fractions of 75/25, 50/50 and 25/75 on the water surface at T_{sp} of 293 K, (b) composition dependence of the collapse and transition pressures on the monolayer, (c) composition dependence of molecular occupied area at constant surface pressures of 5, 10, 15 and 20 mN m^{-1}

a rectangular one (CS) [13]. Transition and plateau pressures for the mixed monolayers containing C_{16} and C_{24} were almost constant, respectively, irrespective of monolayer composition, as shown in Figure 2 (b). The collapse pressure abruptly lessened by an addition of small amounts of C_{16} molecule and was almost constant except the pure C_{24} monolayer. These behaviors of characteristic pressures indicate that the aggregated regions of C_{16} and C_{24} molecules separately exist in the mixed monolayers. And also, the molecular areas, which were plotted against the monolayer composition, laid on the additive line (Figure 2 (c)). This additivity suggests that the components are ideal mixing or complete segregation. Hence, it is reasonable to consider that the (C_{16}/C_{24}) mixed monolayer with the difference in the cohesive energy corresponding to eight CH_2 groups (48 - 60 kJ mol^{-1}) is in an immiscible state at 293 K. The subphase was in the neutral pH range in this study, which corresponds to an unionized state of the carboxylic group of fatty acids [14]. Accordingly, the difference in cohesive energy of 48 - 60 kJ mol^{-1} reduces the interaction potential overcoming the entropic contribution, resulting in the immiscibility of the (C_{16}/C_{24}) mixed monolayer.

Figure 3 (a) shows π-A isotherms of pure C_{16}, C_{22}, and of (C_{16}/C_{22}) mixed monolayers with different molar fractions

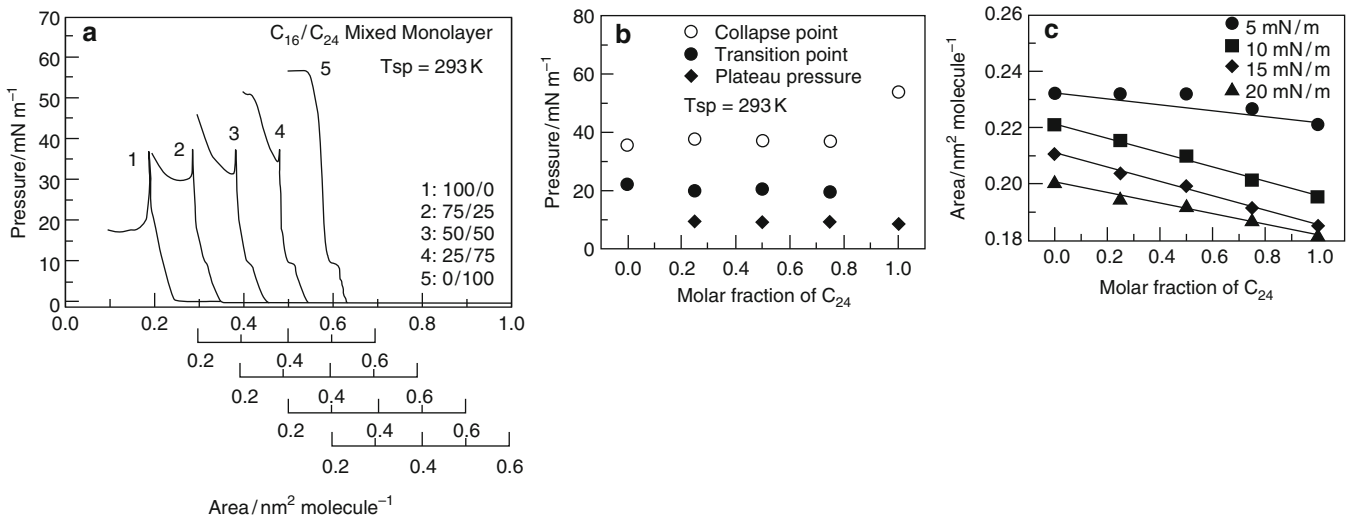

Fig. 2 (a) Π-A isotherms of pure C_{16}, C_{24} and of (C_{16}/C_{24}) mixed monolayers with molar fractions of 75/25, 50/50 and 25/75 on the water surface at T_{sp} of 293 K, (b) composition dependence of the collapse, transition and plateau pressures on the monolayer, (c) composition dependence of molecular occupied area at constant surface pressures of 5, 10, 15 and 20 mN m^{-1}

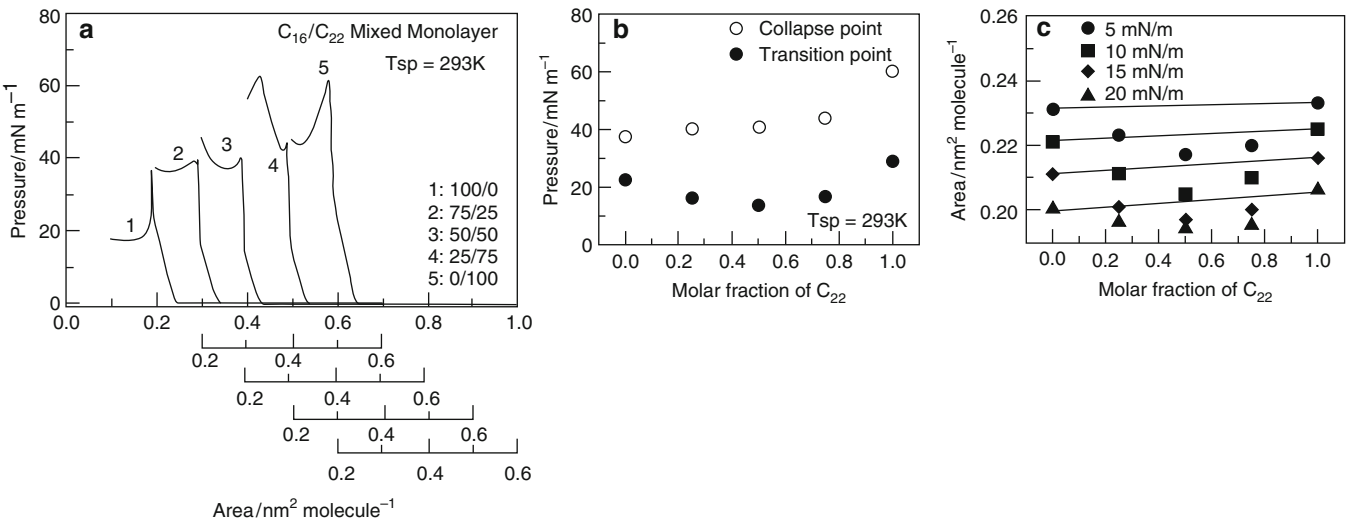

Fig. 3 (a) Π-A isotherms of pure C_{16}, C_{22} and of (C_{16}/C_{22}) mixed monolayers with molar fractions of 75/25, 50/50 and 25/75 on the water surface at T_{sp} of 293 K, (b) composition dependence of the collapse and transition pressures on the monolayer, (c) composition dependence of molecular occupied area at constant surface pressures of 5, 10, 15 and 20 mN m^{-1}

at 293 K. The π-A isotherms of the pure behenic acid monolayers (C_{16}/C_{22}: 0/100) exhibited a sharp rise in surface pressure at a surface area of ca. 0.25 nm^2 $molecule^{-1}$. Likely the (C_{16}/C_{24}) mixed system, the collapse pressure abruptly lessened by an addition of the small amount of C_{16} molecules and was almost constant except the pure C_{22} monolayer, as shown in Figure 3 (b). This indicates the existence of segregated regions with different mechanical properties in monolayer. On the other hand, the transition point decreased with an increase in C_{22} content to be a minimal value of 13.5 mN m^{-1} at the molar fraction of around 0.5. And also, as shown in Figure 3 (c), plots of the measured molecular areas for the mixed monolayer at constant surface pressures versus the monolayer composition revealed a negative deviation from the additive line. Putting the above-mentioned results together, it is reasonable to consider that the (C_{16}/C_{22}) mixed monolayer with the difference in the cohesive energy corresponding to six CH_2 groups (36 - 45 kJ mol^{-1}) is in an incomplete miscible state at 293 K.

Next, the mixing behavior of binary monolayer of fatty acid was investigated by using two kinds of combinaition of (C_{20}/C_{24}) and (C_{16}/C_{20}) in order to confirm the dependence of miscibility on the difference in cohesive energy, as discussed in Figures 1 – 3.

In the case of the (C_{20}/C_{24}) mixed monolayer with difference of four CH_2 groups, the behaviors of the transition point and the collapse pressure showed the same tendency of continuous variation as the (C_{16}/C_{20}) mixed monolayer, as shown in Figures 4(a) and 1(b). The composition dependence of the measured molecular areas for the mixed monolayer at constant surface pressures revealed a negative deviation at low pressure, whereas plots for higher pressures did the additivity, as shown in Figure 4 (b). Hence, the (C_{20}/C_{24}) mixed monolayer is in a miscible state at 293 K. On the other hand, the behavior of collapse pressure of the (C_{18}/C_{24}) mixed monolayer with difference of six CH_2 groups exhibited the same tendency of discontinuous variation as the (C_{16}/C_{22}) mixed monolayer, as shown in Figures 5(a) and 3(b). The composition dependence of the measured molecular areas for the (C_{18}/C_{24}) mixed monolayer at constant surface pressures revealed a negative deviation as same as the (C_{16}/C_{22}) mixed monolayer, as

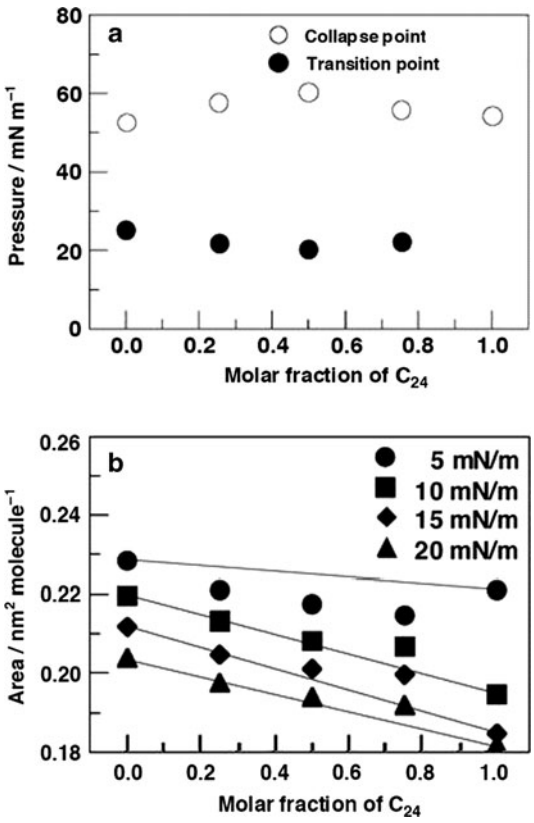

Fig. 4 (a) Composition dependence of the collapse and transition pressures of (C_{20}/C_{24}) mixed monolayers on the water surface at T_{sp} of 293 K, (b) composition dependence of molecular occupied area at constant surface of the monolayer

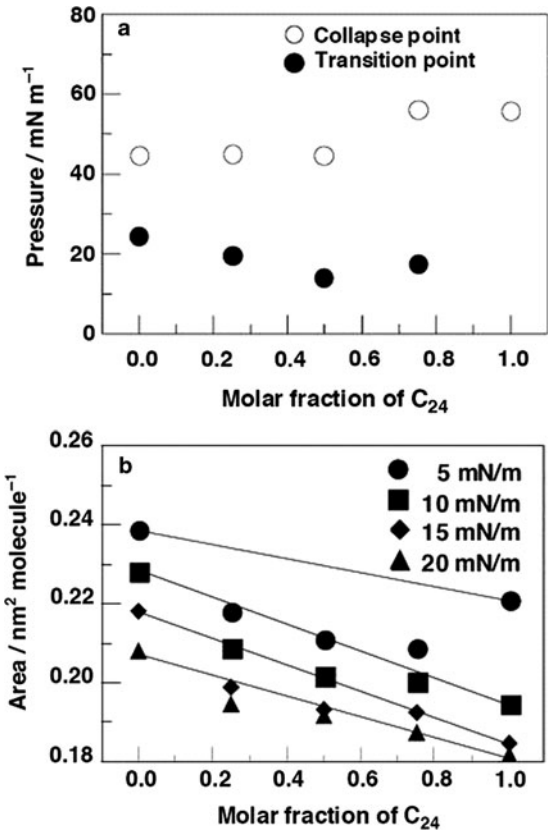

Fig. 5 (a) Composition dependence of the collapse and transition pressures of (C_{18}/C_{24}) mixed monolayers on the water surface at T_{sp} of 293 K, (b) composition dependence of molecular occupied area at constant surface pressures of the monolayer

shown in Figure 5 (b). Thus, the (C_{18}/C_{24}) mixed monolayer is not in a complete miscible state at 293 K. It is, therefore, clearly from the results of Figures 1–5 concluded that the mixing behavior of fatty acid mixed monolayer is governed by the difference in the cohesive energy based on a length of alkyl chain.

Conclusion

The present study suggests that the difference in cohesive energy between the hydrophobic groups in monolayer components was an important factor for determination of the mixing behavior. The mixing behavior may depend on various factors, such as the intermolecular interaction, particularly an electrostatic one, and the thermal molecular motion. A further systematic investigation is required to understand the aggregation mechanism in a multi-component monolayer.

Acknowledgments The authors thank Dr. Masao Suzuki (NOF Co.) for providing the samples of fatty acids used in this study.

References

1. Ariga K, Hill JP, Lee MV, Charvet VR, Acharya S (2008) Sci Technol Adv Mater 9: 014109
2. Kiss E, Vargha A, Vargha-Buttler EI (2004) Phys Chem Chem Phys 6:1575
3. Hou Y, Jaffrezic-Renault N, Martelet C, Tlili C, Zhang A, Pernollet JC, Briand L, Gomila G, Errachid A, Samlitier J, Salvagnac L, Torblero B, Temple-Boyer P (2005) Langmuir 21: 4058
4. Michinobu T, Shinoda S, Nakanishi T, Hill JP, Fujii K, Player NT, Tsukube H, Ariga K (2006) J Am Chem Soc 128: 14478
5. Mori T, Okamoto K, Endo H, Hill JP, Shinoda S, Matsukura M, Tsukube H, Suzuki Y, Kanekiyo Y, Ariga K (2010) J Am Chem Soc 132: 12868
6. Blonder R, Willner I, Buckman AF (1998) J Am Chem Soc 120: 9335
7. Yufang X, Zhongqi Y, Daosen J (1993) J Phys Chem 97: 8519
8. Peterson IR, Brzezinski V, Kenn RM, Steitz R (1992) Langmuir 8: 2995
9. Gaines Jr, GL (1966) J Colloid Interf Sci 21: 315
10. Demel RA, Van Deenen LLM, Pethica BA (1967) Biochim Biophys Acta 135: 11
11. Cadenhead DA, Demchak RJ (1969) J Colloid Interf Sci 30: 76
12. Bacon KJ, Barnes GT (1978) J Colloid Interf Sci 67: 70
13. Kuramori M, Uchida N, Suehiro K, Oishi Y (2000) Bull Chem Soc Jpn 73: 829
14. Oishi Y, Takashima Y, Suehiro K, Kajiyama T (1997) Langmuir 1997: 13 2527

Progr Colloid Polym Sci (2011) 138:109–114
DOI: 10.1007/978-3-642-19038-4_19

Rheological Behavior of Interfacial Layers Stabilized by Gelatin with Lecithin

S.R. Derkach[1], S.M. Levachov[2], T.A. Dyakina[1], and L.A. Petrova[1]

Abstract The effect of lecithin (natural surfactant) addition to gelatin on the surface rheological properties of the water/heptane interfacial layer and emulsion films formed by these liquids was studied. It was found that the gelatin/lecithin mixtures form complexes in the aqueous phase. Self-assembly of these complexes leads to the formation of viscoelastic interfacial adsorption layers characterized by a yield stress and elastic modules that provide stability of the emulsion films and emulsion systems. The above mentioned parameters evolve in time, though the formation of equilibrium interfacial layers proceeds during several hours; emulsion bilayer films require only several minutes.

Keywords Interfacial layer • gelatin • lecithin • surface rheology • emulsion film

Introduction

Water-soluble proteins as natural biopolymers are irreplaceable components in various technologies used in the development of new functional products in food, cosmetic, pharmaceutical medical application and so on. Gelatin occupies an important place in this case due to its unique capability to thermal reversible gel formation in the bulk as well as at liquid interfaces [1-3].

Physical modification of gelatin with different surfactants is an effective way for governing its colloid-chemical properties to achieve an optimum combination of solubility, rheology and stability of e.g., foams and emulsions [4-7]. Gelatin interacts strongly with synthetic surfactants. The surface tension plots and adsorption behavior of gelatin/surfactant mixtures at liquid interface indicate the formation of highly surface active macromolecular/surfactant complexes [2, 7-9]. These complexes are formed due to electrostatic interactions between charged residues of gelatin macromolecules and charged groups of surfactants and also due to hydrophobic interactions which happened between hydrophobic patches in the gelatin molecules and the hydrophobic chains of the surfactants [10-12]. The underlying behavior for gelatin and other polyelectrolyte/surfactant systems may be different from that of uncharged polymers and surfactants [13].

Natural surfactants like lecithin are of special interest for food and pharmaceutical industry. However properties of gelatin/lecithin mixtures are practically not described in current publications. Combinations of gelatin with lecithin as emulsifiers and stabilizers of traditional and new food recipes can provide new perspective products, and that is why studies of these systems are of actual importance. The interrelation between the rheological properties of interfacial absorption layers containing proteins and low-molecular-weight surfactants [14-21] and the behavior of emulsions (including its stability) is also of significant values.

This work is devoted to the study of thermodynamic and rheological properties of interfacial adsorption layers of gelatin and natural surfactants (lecithin) in a wide range of mixing ratios formed at interfaces between water and hydrocarbons.

Objects and Methods

Substances

Alkaline gelatin of the weight-average molecular weight $M_w \approx 1.0 \cdot 10^5$ Da was used. Isoelectric point is equal to 4.9.

A commercial grade of lecithin has the following content: mass share of the phospholipid complex equals 97% (including: phosphatidilcholin (lecithin by itself) 22%,

S.R. Derkach (✉)
[1]Chemistry Department, Murmansk State Technical University, Sportivnaya str. 13, Murmansk 183010, Russia
e-mail: derkachsr@mstu.edu.ru
[2]Department of Colloid Chemistry, M.V. Lomonosov Moscow State University, Vorobjevu Goru, Moscow 119899, Russia

phosphatilethanolamine 20%, phosphatidilinozitol 14%, glicolidids 15%, carbohydrates 8%, poly(unsaturated fatty acids) – linolec and lenolene 18%.

Lecithin (phosphatidilcholin) forms micellar solutions in hydrocarbons. For example, the CMC of lecithin in heptane is 10^{-5} mol/l [22]. Lecithin in water creates vesicles. Experiments performed in this study explored an aqueous phase containing gelatin and lecithin. Aqueous mixtures of gelatin with lecithin were obtained by adding the required volume of the *initial lecithin solution* into the aqueous gelatin solution at a temperature of 40-45°C. The lecithin concentration range was $1.0 \cdot 10^{-5}$ – $1.0 \cdot 10^{-2}$ mass.% which corresponds the domain of vesicles existence [22], pH 5.2 – 5.8. The formation of protein-lipid complexes as studied in [23, 24]. The *initial lecithin solution* (10% mass.) was prepared by dissolving a certain amount of a substance in a heptane/ethanol mixture (ratio of heptane to ethanol was 1:5 by mass).

Methods

The rheological parameters of adsorption layers and bilayer emulsion films at the water/hydrocarbon interface were measured by an interface rheometer, described in details in [25]. The apparatus is supplied with a system of horizontal concentric rings (Fig. 1). The inner and outer radii of the ring were R_1=2.56 cm and R_2=2.82 cm, respectively. A gap between the rings was 0.26 cm. The adsorption layers under consideration are formed in the gap between the rings. A bilayer emulsion films are formed within the gap between the coaxial rings when, lowering the funnel, they were displaced from the aqueous phase through the water/hydrocarbon interface into the hydrocarbon phase. The film is considered as stable if its lifetime was more than 10 min.

Investigation of the rheological properties of the adsorption layers and bilayer emulsion films was performed under shear [26]. A method of the sweep load was used [27]. The starting load τ_n was 0.056 mN/m and it increased by steps every 15 s.

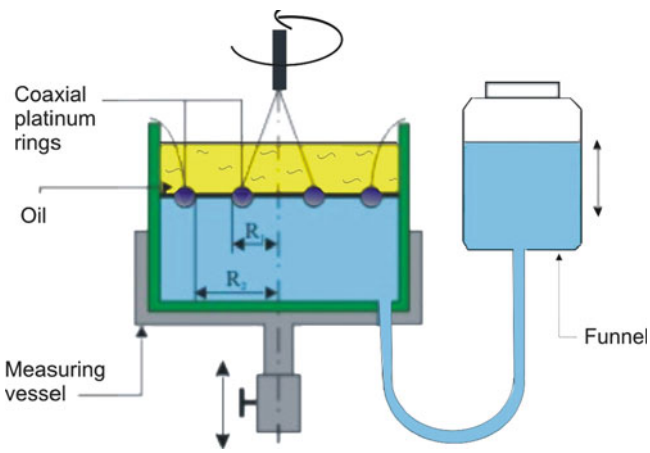

Fig. 1 Scheme of the interface rheometer set-up (description in the text)

Interfacial tension was measured by the Wilhelmy method [28], the traditional plate technique was used. The mean error of the results of measurements was ±0.5 mN/m.

The particle size in aqueous gelatin/lecithin solutions was determined by a light scattering dispersion method (method of turbidity spectrum) [29] using a spectrophotometer KFK-3 in the range of wave length from 450 till 550 nm.

Oil-in-water emulsions were prepared at ambient temperature using a laboratory homogenizer with 5 min continuous homogenization at the mixing speed 11000 rpm. Different heptane to aqueous phases ratios (volume) were used. After 24 hours aging, the volume fractions of the stable emulsion and the separated oil and aqueous phases were determined. These experimental data are the base for construction of the emulsion stability diagrams [30]. Aggregation stability against coalescence is characterized by the relative area on the diagram S(%) corresponding to stable emulsion.

Results and Discussion

Gelatin-Lecithin Interaction in Aqueous Bulk Phase

The results obtained by the light scattering method (Fig. 1) demonstrate that an average radius of nanoparticles in dilute gelatin solutions (C_{gel} = 0.10%) in absence of lecithin is of the order of 100 nm. The size of vesicles in lecithin dispersions in water in absence of gelatin lies in the range of 700-1100 nm (Fig. 2, curve 2). The latter results quite well correspond to literature data [22].

The addition of lecithin to a gelatin solution leads to the appearance of particles with a size larger than the gelatin particles but less than the lecithin vesicles. The typical size is in the range 250-550 nm.

It is proposed that particles appearing in the aqueous phase are the aggregates of micellar gelatin-lecithin complexes. The formation of such complexes [10, 11] happens as the result of ionic interaction due to charges and hydrophobic interaction between hydrophobic chains of the surfactant and respective hydrophobic residues in the gelatin.

Interface Tension

Low values of the interfacial tension as well as high values of the rheological parameters (elastic modules, yield stress)

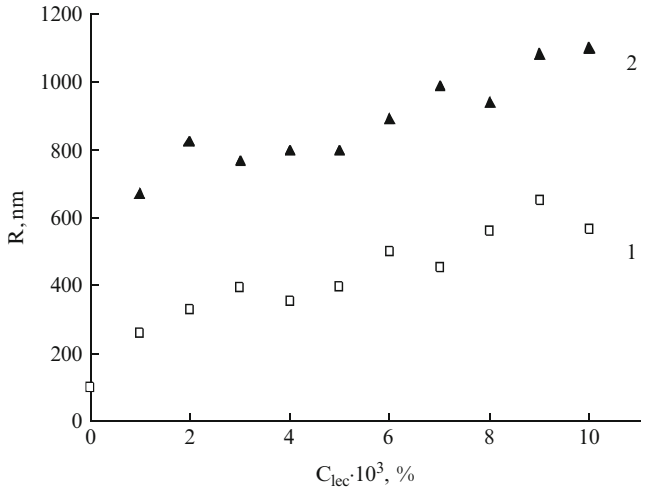

Fig. 2 Dependencies of the average particle radius in aqueous gelatin/lecithin mixtures (*1*) and in lecithin dispersions (*2*) on the lecithin concentration. T = 22 °C, the characteristic equilibration time was equal to 150 hours

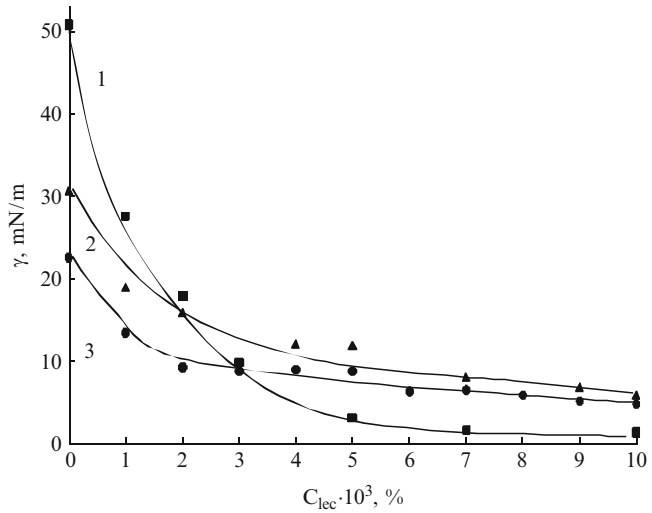

Fig. 3 Dependencies of the interfacial tension at the interface with heptane for aqueous gelatin/lecithin mixtures on the lecithin concentration. The gelatin concentration: C_{gel}, %: 0 (*1*), 0.10 (*2*), 0.50 (*3*). γ_0 (H_2O/heptane) = 50.85 mN/m, T = 25 °C

of interfacial gelatin layers at the water/hydrocarbon interface are the base of emulsion stability.

The isotherms of interface tension γ of aqueous lecithin dispersions in the absence of gelatin (Fig. 3, curve 1) as well as aqueous gelatin/lecithin mixtures at the interface with heptane are presented as functions of the lecithin concentration for two gelatin concentrations, C_{gel} = 0.10 % (Fig. 3, curve 2) and C_{gel} = 0.50 % (Fig. 3, curve 3). As seen in Fig. 3, the additions of lecithin to a gelatin aqueous solution results in a remarkable decrease in the equilibrium interface tension: the γ values decrease down to app. 5 mN/m at the lecithin concentration of C_{lec} = 0.010 %.

Rheological Properties of Adsorption Layers and Emulsion Films at the Water/Heptane Interface

The rheological properties of adsorption layers at the water/heptane interface formed from aqueous gelatin/lecithin mixtures were studies under shear.

In the beginning, the time has been established which is needed for reaching the quasi-equilibrium values of the rheological parameters. It is interesting to note that the time dependencies of the interfacial viscosity, the yield stress and the elastic modules are non-monotonous. Initially, during the first hours of layer formation, rheological parameters increase and reach their maxima for approximately 4 hours (Fig. 4 built for elastic modules). Then the rheological parameters decrease and they reach their asymptotic values in 6-8 hours.

This effect of non-monotonic increasing rheological parameters is apparently explained by phase transitions proceeding in time in the adsorption layer at the liquid/liquid interface.

The investigation of the lecithin adsorption [22, 31, 32] at the liquid/liquid interface showed that at the high lecithin concentration ($C_{lec.} > 10^{-4}$ mass.%) solutions the formation of none-monomolecular layers but layers of the complicated network structure changing in time takes place. The driving power of self-organization of these structures is hydration of phospholipid at the interfacial layer [31] leading to the decrease in solubility of lecithin in the non-polar bulk hydrocarbon phase. The mechanism of the interfacial processes taking place under the adsorption layer formation is based on the transformation of lecithin micelles with the addition of the trace amount of water [32]. These processes include the organic gel formation with its subsequent transition into a compact gel and its following transformation into the solid sediment of separate particles.

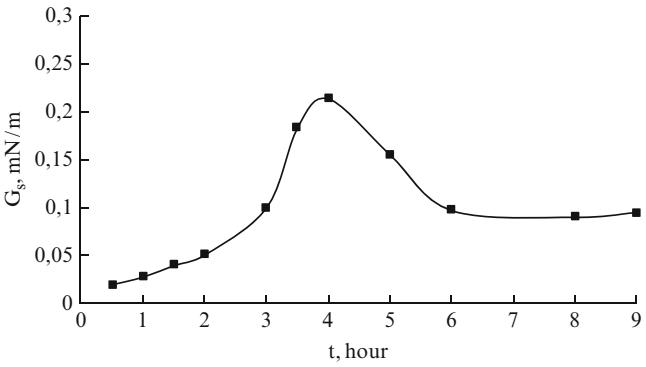

Fig. 4 Time dependence of elastic modules for interfacial adsorbed layers formed from aqueous mixtures of gelatin (C_{gel} = 0.10 %) and lecithin (C_{lec} = 0.0050 %) at the heptane interface. T = 22 °C

Such transitions have been observed at the interfacial layers formed by the gelatin-lecithin complexes during their adsorption from an aqueous phase in the present work too. In the beginning, complexes are concentrated in the gel-like layer (that is observed during first 4 hours). Then the gel-like structure transforms into flaky sediment. In the investigated systems, they become observed by sight even under small magnification.

Similar non-monotonic time-dependent interfacial shear viscosity data for protein solutions and protein-surfactant mixtures were described in literature [2, 14, 20]. They are explained by the very complex dynamic adsorption behavior which depends mostly on the composition of a mixture.

Fig. 5 shows the dependencies of rheological properties of adsorption layers on the lecithin concentration for two different situations: for gel-like layers formed after 4 hours (Fig. 5a) and for a separate particle layers formed after 6 hours (Fig. 5b).

In the first case, the interfacial adsorption layers are characterized by clearly expressed viscoelastic properties and plasticity reflected by the yield stress; Fig. 5a presents the interfacial shear viscosity, η_s, yield stress τ_{Ys} and surface elastic modules G_s. One can see that the elastic modules and the viscosity for gelatin layers without a surfactant ($C_{lec} = 0$) are equal to 1.2 mN/m and 8.3 mN·s/m, respectively. Upon addition of phospholipids at low lecithin-to-gelatin ratio these parameters do not change. However some threshold component ratio exists and the elastic modules and the yield stress sharply increase beyond this threshold. This is the evidence of the increase in the number of contacts between structure elements in a gel-like layer.

In the second case, when the time of layer formation is 6 hours; the quasi-equilibrium state is reached and a layer loses its gel structure, the addition of lecithin demonstrates an opposite effect. Fig. 5b shows that the increase in the lecithin concentration in the system leads to the monotonous decrease in the viscosity and elasticity in comparison with the gelatin layers in absence of phospholipid.

Fig. 6 illustrates the diagram of emulsion bilayer film stability. It has been shown that in the range of concentrations

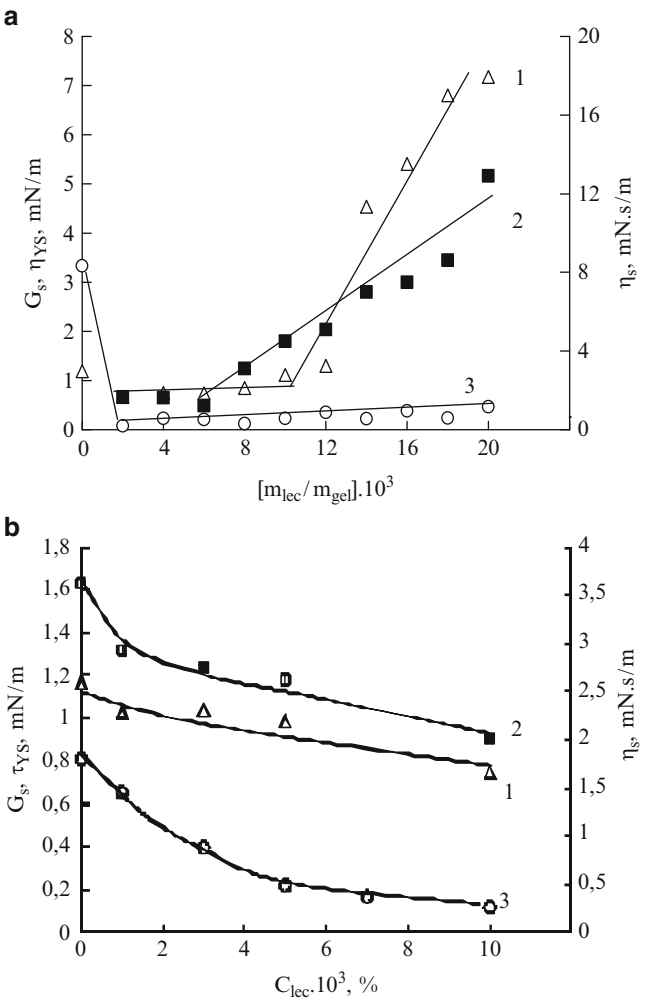

Fig. 5 Dependencies of some rheological parameters – elastic modules G_s (1), yield stress τ_{Ys} (2), viscosity η_s (3) of adsorption layers at the liquid interface (water/heptane) formed from aqueous gelatin/lecithin mixtures on the lecithin concentration. T = 22 °C. a) Layer formation time is 4 hours, C_{gel} = 0.50 %; b) Layer formation time is 6 hours, C_{gel} = 0.10 %

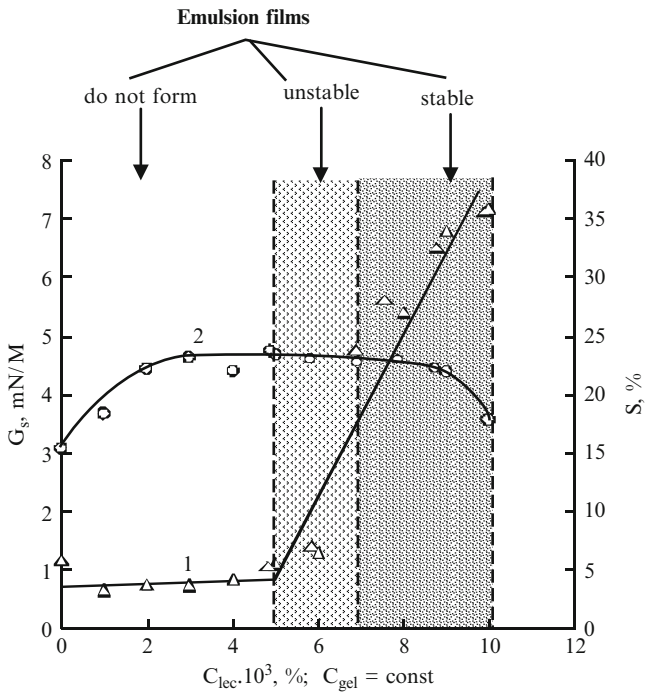

Fig 6 The diagram of emulsion bilayer films stability formed by gelatin/lecithin mixtures (C_{gel} = 0.50 %) at the water/heptane interface. 1 – dependence of the elastic modules on the lecithin concentration at C_{gel} = 0.50 %. 2 – dependence of the aggregation stability S of concentrated heptanes-in-water emulsions (φ=80%) stabilized by the gelatin/lecithin mixtures on the lecithin concentration (C_{gel} = 0.10 %)

Table 1 Elastic modules G_s, yield stress τ_{Ys} and viscosity η_s of emulsion bilayer films and interfacial adsorption layers formed at the interface with heptane from aqueous gelatin/lecithin mixed solutions

Parameter	Emulsion bilayer film		Interfacial absorption layer	
	C_{gel} = 0.50 % + C_{lec} %			
	0.0080	0.010	0.0080	0.010
G_s, mN/m	2.2	4.1	5.4	7.2
τ_{Ys}, mN/m	0.7	1.3	3.0	5.2
η_s, mN·s/m	1.0	3.8	1.0	1.5

under study, stable films appear if the lecithin-to-gelatin ratio exceeds 0.014 (by mass). It is interesting to mention that this domain coincides with the field of component ratios where the elastic modules of the corresponding interfacial layer in the process of formation (during 4 hours) sharply increases. Dependence of the aggregation stability (against coalescence) of concentrated emulsions of heptane in water stabilized by the gelatin-lecithin complexes on the lecithin concentration is also presented in Fig.6 (curve 2). It has been shown that the largest stability takes place in the range of stable emulsion films formation under the same lecithin-to-gelatin ratio.

Table 1 summarizes the values of rheological parameters of some studied emulsion films stabilized by the gelatin/lecithin complexes. These parameters were measured immediately after the film formation (at 1 min). It is worth noting that the yield stress, elastic modules and film shear viscosity increase in the increase of the lecithin concentration. Analysis of the experimental data demonstrates that the parameters of the films (when films have been formed during several minutes) have values in the same order as the analogous characteristics of the layer formed after 4 hours.

Conclusion

Gelatin (a denatured fibrillar protein collagen) is one of the most widespread natural high molecular mass surfactants in food, cosmetic, pharmaceutical, medicine, photographic industries as well as in the other fields. Addition of a low molecular mass component to gelatin provides the most effective influence on the surfactant properties. It is related to the formation of gelatin-surfactant complexes – a new type of surfactants.

Phospholipid lecithin is also one of the well-known natural surfactants. It is one of the structure components in the lipid matrix of biological membranes. Phospholipids are able to create complexes with proteins. Besides, lecithin is used in food, cosmetic industry and biotechnology as an effective emulsifying agent. There are many works dedicated to the investigation of lecithin, its self-organized structure in the bulk and at the immiscible liquid interface in the process of adsorption from the bulk non-aqueous solution.

Meanwhile the properties of aqueous gelatin/lecithin mixtures have not been investigated and not described in literature. At the same time, combined application of these natural surfactants (of high- and low-molecular masses) seems rather perspective for creating new stable emulsion systems, in particular in the food industry.

The results of investigation of the interfacial properties (thermodynamic and rheological) of the aqueous gelatin/lecithin mixtures in the wide range of component ratios are presented in this work for the first time. It has been shown that adsorption of gelatin/lecithin complexes (formed in the bulk aqueous phase) at the immiscible liquid interface leads to self-assembly of the interfacial viscoelastic layer. The non-monotonic time-dependent interfacial shear viscosity and elastic modulus evolution were observed. This effect was explained by the phase transitions proceeding in time at the liquid interface in the systems containing lecithin.

The formation of viscoelastic stabilizing layers of the gelatin/lecithin complexes results in the increase of the emulsion film stability. Emulsion bilayer films also display viscoelastic properties. In this case, the rheological parameters of the film are of the same order of values as the analogous parameters of the layer despite the difference in the formation time of the film and the layer. A possibility of increasing the coalescence stability of oil-in-water concentrated emulsions has been shown. This was considered as a result of the high stabilizing properties of gelatin/lecithin complexes. These properties depend mostly on the composition of a mixture.

Acknowledgement This work is supported by the Russian Foundation for Basic Research, project N 10-03-00310-a.

References

1. Ross-Murphy SB (1997) Imag Sci J 45:205;
2. Wüsteneck R, Krägel J (1998) In: Möbius D, Miller R (ed) Studies in Interface Science Series, V 7, Protein in liquid interfaces, Elsevier, Amsterdam, pp 433-490
3. Izmailova VN, Derkach SR, Sakvarelidze MA, Levachov SM, Voron'ko NG, Yapol'skaya GP (2004) Polymer Sci Series C 46:2216
4. Magdassi S, Kamyshny A (1996) In: Magdassi S (ed) Surface activity of proteins: chemical and physicochemical modifications, Dekker, New York Marcel, pp 1–38
5. Howe A.M, Wilkinst AG, Goodwint JW (1992) J Photogr Sci 40:234
6. Griffiths PC, Roe JA, Bales BL, Pitt AR, Howe AM (2000) Langmuir 16: 8248
7. Izmailova VN, Derkach SR, Levachev SM, Yampol'skaya GP, Tulovskaya ZD, Tarasevich BN (2000) Colloid Journal (Russian) 62:653
8. Knox WJ, O'Parshall T (1972) J Colloid Interf Sci 40:290

9. Muller D, Malmsten M, Bergenstahl B, Hessing J, Olijve J, Mori F (1998) Langmuir 14:3107
10. Congrove T, White SJ, Zarbakhsh A, Heenan RK, Howe AM (1996) J Chem Soc, Faraday Trans 92:595
11. Cooke DJ, Dong CC, Thomas RK, Howe AM, Simister EA, Penford J (2000) Langmuir 16: 6546
12. Griffiths PC, Fallis IA, Teerapornchaisit P, Grillo I (2001) Langmuir 17:2594
13. Goddard ED (1986) Colloids Surf 19:255
14. Miller R, Fainerman VB, Krägel J, Loglio G (1997) Curr Opin Colloid Interf Sci 2:578
15. Izmailova VN, Yampolskaya GN (2000) Adv Colloid Interf Sci 88:99
16. Murray BS (2002) Curr Opin Colloid Interf Sci 7:426
17. Mackie AR (2004) Curr Opin Colloid Interf Sci 9:357
18. Erni P, Fischer P, Windhab EJ (2005) Langmuir 21:10555
19. Dickinson E (2006) Soft Matter 2:642
20. Krägel J, Derkatch SR, Miller R. (2008) Adv Colloid Interf Sci 144:38
21. Krägel J, Derkatch SR (2010) Curr Opin Colloid Interf Sci 15:246
22. Shchipunov YuA (1997) Uspekhi khimii (Russian) 66:328
23. Nylander T (1998) In: Möbius D, Miller R (ed) Studies in Interface Science Series, V 7, Protein in liquid interfaces, Elsevier, Amsterdam, pp 385-431
24. Levachov SM, Izmailova VN (1994) Colloid Journal (Russian) 56:193
25. Zotova KV, Trapeznikov AA (1964) Colloid Journal (Russian) 26:158
26. Derkatch SR, Miller R, Krägel J (2009) Colloid Journal (Russian) 71:1
27. Derkatch SR, Petrova LA, Izmailova VN, Tarasevitch BN (1999) Colloid Surf A 152:189
28. Rusanov AI, Prokhorov VA (1996) In: Möbius D, Miller R (ed) Studies in Interface Science Series, V 3, Interfacial Tensiometry, Elsevier, Amsterdam
29. Klenin VI (1999) Thermodynamics of systems containing flexible-chain polymers. Elsevier, Amsterdam
30. Gurova NV, Gurov AN, Tokaev ES (1994) Methods of measurement of protein emulsion properties (Russian). AgroNIIT, Moscow
31. Shchipunov YuA, Kolpakov AF (1991) Adv. Colloid Interf Sci 35:31
32. Shchipunov YuA, Schmiedel P (1996) Langmuir 12:6443

Progr Colloid Polym Sci (2011) 138:115–120
DOI: 10.1007/978-3-642-19038-4_20

Computer Simulations of Quasi-Steady Evaporation of Sessile Liquid Droplets

S. Semenov[1], V. Starov[1], R.G. Rubio[2], and M.G. Velarde[3]

Abstract Instantaneous distribution of mass and thermal fluxes inside and outside of an evaporating sessile droplet is considered using computer simulations. The latter distribution is calculated in a self consistent way by considering an interconnected problem of vapour transfer in the vapour phase outside the droplet; heat transfer in vapour, liquid and solid substrate; and Marangoni convection inside the liquid droplet. The influence of thermal conductivity of the solid support on the evaporation process is evaluated. The deduced dependences of instantaneous fluxes can be applied for self-consistent calculations of time evolution of the evaporation processes of sessile droplets.

Keywords *evaporation* • *sessile droplets*

Introduction

Understanding the evaporation of droplets is essential for processes like painting, coating, ink-jet printing, premixing of fuel with oxygen in air [1], particle deposition applications (formation of ring-like spots on the substrate during droplets evaporation), DNA chip manufacturing [2], etc. The measurements of evaporation rate of droplets on different solid surfaces can be used for production of materials providing optimal regime of work in air conditioners, dryers and cooling systems [3]. On the other hand the investigation of evaporating droplets can reveal the influence of Derjaguin pressure in a vicinity of the apparent three-phase contact line [4] as well as the effect of latent heat of vaporization and Marangoni convection [5] on evaporation process.

Evaporation starts after the deposition of a liquid droplet on a solid substrate in a non-saturated vapour atmosphere. In the presence of contact angle hysteresis the latter process occurs in three steps [6, 7]: 1) constant contact line radius, L, and decreasing contact angle, θ; 2) constant receding contact angle, θ_r, and decreasing contact line radius, L; 3) both the contact line radius, L, and the contact angle, θ, decrease.

R.D. Deegan *et al* [8, 9] studied the distribution of vapour flux density over the spherical cap of a sessile droplet neglecting the latent heat of vaporization and the thermocapillary flow inside the droplet. Their solution shows an increased vapour flux in the vicinity of the three-phase contact line, which generates flow inside the droplet transporting suspended solid particles to the edge of the droplet and leading to a ring-like stain formation.

A.M. Cazabat *et al* [10] showed that the vapour flux density over the droplet is inversely proportional to the contact line radius. As a consequence the integration of flux density over the whole droplet surface gives a total vapour flux proportional to the contact line radius.

Theoretical and computer simulation studies [5, 11–15] give the following equation for the evaporation rate of a sessile droplet:

$$\frac{\mathrm{d}V}{\mathrm{d}t} = -2\pi \frac{DM}{\rho} \left(c_{sat}\left(T_{surf}\right) - Hc_{sat}(T_\infty)\right) F(\theta) L, \qquad (1)$$

where V is the droplet volume, t is time, D, ρ, and M are vapour diffusivity in air, density of the liquid and the molar mass, respectively; H is humidity of the ambient air, T_{surf} is the temperature of the droplet-air interface and T_∞ is the temperature of the ambient air, $c_{sat}(T_{surf})$ and $c_{sat}(T_\infty)$ are the molar concentrations of saturated vapour at the corresponding temperature; $F(\theta)$ is a function of the contact angle, θ, with value 1 at $\theta = \pi/2$. Eq. (1) was obtained for a model of evaporation which takes into account diffusion only of the vapour in the surrounding air and ignores the temperature distribution along

S. Semenov (✉)
[1]Dept. of Chemical Engineering, Loughborough University, LE11 3TU Loughborough, UK
e-mail: S.Semenov@lboro.ac.uk
[2]Dept. of Química Física I, Universidad Complutense, 28040 Madrid, Spain
[3]Instituto Pluridisciplinar, Universidad Complutense, 28040 Madrid, Spain

the droplet-air interface. In the case of θ independent of L (second stage of evaporation) Eq. (1) gives an evaporation rate directly proportional to the contact line radius, L.

Investigations of evaporation of droplets with contact angles $\theta < 120^\circ$ were performed by F. Girard *et al* [5, 12–15] and H. Hu and R.G. Larson [16–18]. The former investigated the influence of substrate heating [14–15], air humidity [14] and Marangoni convection [5]. They concluded that the contribution of Marangoni convection to the total vapour flux is negligible, whereas heating the substrate is significant. The other authors investigated the process of particle deposition and ring-like stain formation during droplet evaporation.

Ristenpart et al. [19] investigated the influence of the substrate conductivity on reversal of Marangoni circulation within evaporating sessile droplet. Despite of plenty assumptions made by the authors, their quantitative criteria for the circulation direction is confirmed by experiments.

Bhardwaj et al. [20] solved numerically a very complex problem of drying colloidal droplets and deposits formation. Their model takes into account the interaction of the free surface with the peripheral deposit and eventual depinning. The diffusion of vapour in the atmosphere is solved numerically, providing an exact boundary condition for the evaporative flux at the droplet-air interface. The formation of different deposit patterns obtained experimentally is explained well by their simulations.

Below we investigate all fluxes in the course of evaporation process in a self consistent way: we study the interconnected problem of vapour transfer, heat transfer in the vapour, the liquid and the solid substrate, and Marangoni convection inside the liquid droplet.

Mathematical Modelling and Approximations

The system under consideration is a pinned sessile droplet of a liquid (water in these simulations) on a solid substrate open to ambient air. The problem is taken axisymmetric with a cylindrical system of coordinates r and z (Fig. 1). We focus attention on relatively small droplets, neglecting gravity force. Thus the droplet is a spherical cap. Diffusion model of evaporation is taken to describe the quasi-steady process of droplet evaporation. The characteristic time scales of heat, $t_{heat} \sim 10$s, and momentum, $t_{mom} \sim 1$s, transfer processes inside the droplet are smaller than the droplet evaporation time (10^2s) at least by one order of magnitude. For this reason all those processes are taken as steady state processes. Convection in air caused by evaporation is neglected, because the experiments [21] did not reveal any difference in evaporation regimes with and without forced convection in the ambient air.

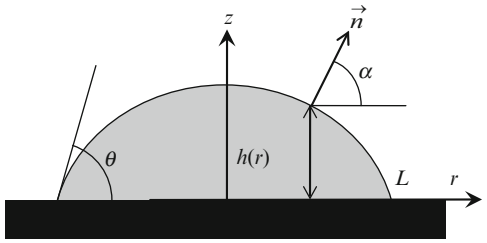

Fig. 1 Illustration of droplet parameters: L, h(r), θ and $\vec{n}$ in the case where $\theta < \pi/2$

Evolution Equations

Let us start considering the particular isothermal case with contact angle $\theta = \pi/2$. In this case we can solve the vapour diffusion equation, $\frac{1}{r^2}\frac{\partial}{\partial r}\left(r^2\frac{\partial c}{\partial r}\right) = 0$, analytically with boundary conditions: $c(L) = c_{sat}(T_{surf})$, $c(\infty) = c_\infty$, where $c_{sat}(T_{surf})$ and c_∞ are saturated and far-field vapour concentrations, respectively. We neglect the deviation of the $c_{sat}(T_{surf})$ from the actual one (according to the Kelvin's equation [22]). The solution gives the following local, $j_{\pi/2}(L,T_{surf})$, and total, $J_{\pi/2}(L,T_{surf})$, vapour fluxes at the droplet surface:

$$j_{\pi/2}(L,T_{surf}) = D\left(c_{sat}(T_{surf}) - c_\infty\right)\frac{1}{L}, \tag{2}$$

$$J_{\pi/2}(L,T_{surf}) = 2\pi D\left(c_{sat}(T_{surf}) - c_\infty\right)L, \tag{3}$$

This analytical solution, obtained for $\theta = \pi/2$, is used to validate the computer simulations below.

The quasi-steady-state solution of the problem corresponds to solving the problem with vanishing time-derivatives. Hence the problem is solved only for the *instantaneous* field values and for the fluxes in the system. Thus the problem is described with the following governing equations:

1) Vapour diffusion in the ambient air:

$$\frac{1}{r}\frac{\partial}{\partial r}\left(r\frac{\partial c}{\partial r}\right) + \frac{\partial^2 c}{\partial z^2} = 0; \tag{4}$$

2) The Navier-Stokes equations together with the continuity equation in the liquid bulk:

$$\begin{aligned} u\frac{\partial u}{\partial r} + v\frac{\partial u}{\partial z} &= -\frac{\partial p}{\partial r} + \eta\left(\frac{1}{r}\frac{\partial}{\partial r}\left(r\frac{\partial u}{\partial r}\right) + \frac{\partial^2 u}{\partial z^2} - \frac{u}{r^2}\right), \\ u\frac{\partial v}{\partial r} + v\frac{\partial v}{\partial z} &= -\frac{\partial p}{\partial z} + \eta\left(\frac{1}{r}\frac{\partial}{\partial r}\left(r\frac{\partial v}{\partial r}\right) + \frac{\partial^2 v}{\partial z^2}\right), \end{aligned} \tag{5}$$

$$\frac{1}{r}\frac{\partial (ru)}{\partial r} + \frac{\partial v}{\partial z} = 0, \tag{6}$$

where u and v are radial and vertical components of the velocity vector, respectively, p is the pressure, and η is the dynamic (shear) viscosity;

3) The heat transfer Fourier equation in all three phases (solid support, liquid droplet, and the ambient air):

$$u\frac{\partial T}{\partial r}+v\frac{\partial T}{\partial z}=\kappa\left(\frac{1}{r}\frac{\partial}{\partial r}\left(r\frac{\partial T}{\partial r}\right)+\frac{\partial^2 T}{\partial z^2}\right), \qquad (7)$$

where T is the temperature, κ is the thermal diffusivity of the corresponding phase. Note that $u=v=0$ inside vapour and solid phases.

Boundary Conditions

At the liquid-solid boundary no-penetration and no-slip boundary conditions are used for Navier-Stokes equations; and continuity conditions for the temperature and heat fluxes. At the air-solid boundary the no-penetration condition is used for the diffusion equation; and continuity for the temperature and the heat fluxes. Conditions of axial symmetry are applied at $r=0$. At the outer boundaries of the system vapour concentration and temperature are equal to their far-field values. The velocity component normal to the liquid-air boundary is negligible in comparison with its tangent component, caused by thermal Marangoni stress. Hence:

$$\vec{u}\cdot\vec{n}_{l,a}=0, \qquad (8)$$

where $\vec{n}_{l,a}$ is the unit normal vector to the liquid-air interface, subscripts l and a correspond to liquid and air. The Laplace and thermal Marangoni stresses are applied at the liquid-air interface: $\boldsymbol{\tau}\cdot\vec{n}_{l,a}=-\gamma K\vec{n}_{l,a}+\gamma'_T\nabla_{surf}T$, where $\boldsymbol{\tau}$ is the full stress tensor, γ and γ'_T are the surface tension and its derivative with respect to temperature, respectively, K is the surface curvature (positive for a sessile droplet), and $\nabla_{surf}T$ is the surface gradient of temperature. The concentration of saturated vapour, c_{sat}, at the droplet surface is defined by the local temperature according to the Clausius-Clapeyron equation and the ideal gas law. The influence of curvature on the concentration of saturated vapour is neglected below. The temperature at the liquid-air interface is continuous, however the heat flux experiences discontinuity because of the latent heat of vaporization: $k_a(\nabla T)_a\cdot\vec{n}_{l,a}-k_l(\nabla T)_l\cdot\vec{n}_{l,a}=j\cdot\Lambda$, where k is a thermal conductivity, j is the local evaporation flux, ∇T is a temperature gradient, Λ is the latent heat of vaporization. The whole problem is solved under quasi-steady approximation. As the normal velocity of the liquid across the liquid-gas interface (Eq. 8) is of the same order of magnitude as the normal velocity of the interface in itself (due to the global mass conservation law), then neglecting the former velocity (Eq. 8) allows us to neglect the velocity of the liquid-gas interface.

Numerical Simulations

The solution of the steady state problem described above was performed using the commercial software COMSOL Multiphysics v 3.5a. The numerical technique used by that software is the Finite Element Method (FEM). The shape functions, chosen for the simulation, are Lagrange quadratic shape functions.

Eqs. (4) – (7) are solved simultaneously at a given time. Gas, liquid and solid phases have their own simulation domains interconnected with each other via corresponding boundary conditions. In the present study the equation for heat transfer (7) is connected to the vapour diffusion equation (4) by calculating the saturated vapour concentration at the liquid-gas interface as a function of local temperature.

The size of the air domain is chosen to be one hundred times bigger than the contact line radius L. This choice prevents numerical artefacts caused by the proximity of the outer boundary [14], and provides a good approximation (less than 1% error bar) for the problem of droplet evaporation into a semi-infinite space.

To reduce the influence of singularities the size of mesh elements at the droplet edge is chosen to be one hundred times smaller than the contact line radius, L. In all our computer simulations the liquid used is water and the solid substrate is made of copper if other materials are not mentioned. T_∞=20°C is used below.

Results and Discussion

Unlike lab experiments computer simulations allow to switch off and on any physical effects in the system under consideration. Initially we switch off both the Marangoni convection and the effect of latent heat of vaporization. It allows comparing our simulation results with earlier published results on evaporation of droplets.

Local Normal Vapour Flux over the Droplet Surface

The distribution of local normal vapour flux, j, over the droplet surface is shown in Fig. 2. It is done using a rescaled, normalised vapour flux $j/j_{\pi/2}(L,T_\infty)$, where $j_{\pi/2}(L,T_\infty)$ is defined by Eq. (2). The line with triangles (Fig. 2), gives the result, which coincides with the analytical solution (the straight line): $j/j_{\pi/2}(L,T_\infty)=1$ within the simulation error bar.

Latent heat of vaporization (LHV) reduces the local flux of evaporation, j, over the whole surface (due to heat con-

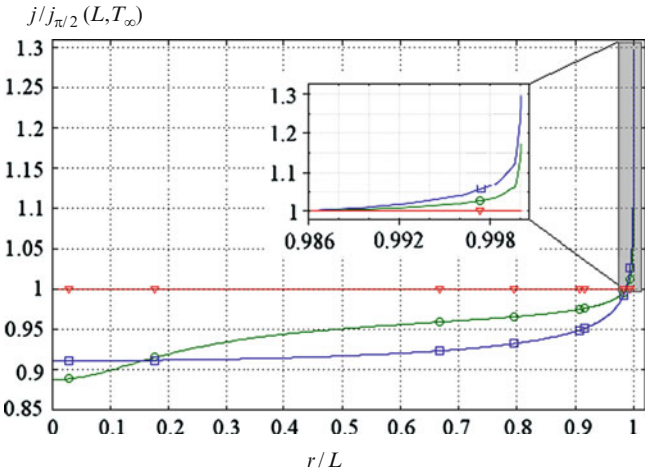

Fig. 2 Calculated distributions of local normal vapour flux, j, over the droplet surface, $\theta=\pi/2$, $L=1$ mm. Circles - both Marangoni convection (MC) and latent heat of vaporization (LHV) are taken into account; squares - LHV is included, but MC is excluded; triangles - both MC and LHV are excluded. The insertion represents the shaded rectangle with a changed scale

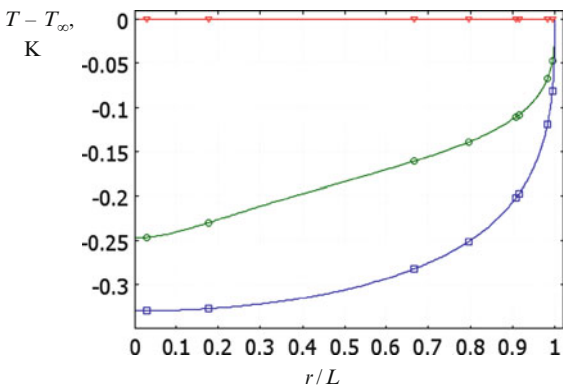

Fig. 3 Calculated temperature distributions over the droplet surface: $\theta=\pi/2$, $L=1$ mm. T_∞ is the ambient temperature. Circles - MC and LHV are taken into account; squares - LHV is included, but MC is excluded; triangles - both MC and LHV are excluded

sumption by the evaporation) except at the droplet edge, where it increases (squares in Fig. 2) due to proximity of highly heat conductive substrate.

Inclusion of Marangoni convection (MC) inside the droplet provides a convective heat flux in addition to the conductive flux. The flow along the liquid surface from the edge of the droplet, where the temperature is higher, to the droplet apex increases the temperature at the droplet surface (Fig. 3, circles). It results in the local vapour flux changes (Fig. 2, circles).

To check the validity of the above given relationship for the local vapour flux, $j\sim1/L$, (Eq. 2) the ratio of fluxes $j_{apex}/j_{\pi/2}(L,T_\infty)$ was plotted against the inverse value of L (Fig. 4) for the case $\theta=\pi/2$. Proportionality $j\sim1/L$ is valid, according to Fig. 4, only when the Marangoni convection is neglected:

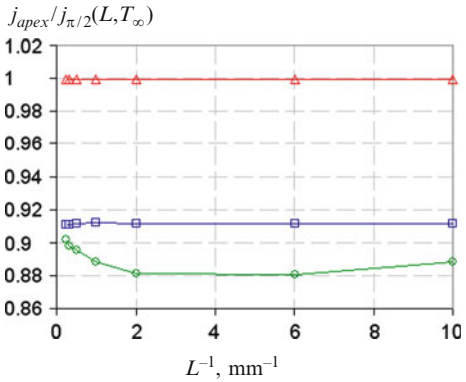

Fig. 4 Calculated dependences of a local vapour flux at the droplet apex, j_{apex}, on contact line radius, L; $\theta=\pi/2$. Circles - MC and LHV are taken into account; squares - LHV is included, but MC is excluded; triangles - both MC and LHV are excluded

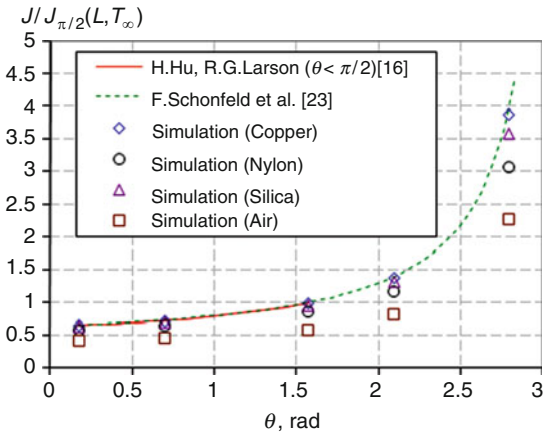

Fig. 5 Rescaled dependence of the total vapour flux from the droplet surface, J, on contact angle θ, $L=1$ mm. Both LHV and MC are taken into account

the presence of the Marangoni convection makes non-linear this dependence (circles in Fig. 4).

Total Vapour Flux from the Droplet Surface

Let us now study the dependence of the total vapour flux, J, on the contact line radius, L, and the contact angle, θ (Fig. 5). It appears that J increases nonlinearly with contact angle. All calculations were performed with both LHV and MC included. The results (Fig. 5) were obtained for substrates made of different materials and compared to those calculated for the isothermal case by H. Hu and R.G. Larson [16] and F. Schonfeld *et al* [23]. In the case of highly heat conductive solid support (copper) the difference between the present simulations and the results from [16, 23] for an isothermal case do not exceed 3%. However, if other materials are used

with lower heat conductivity (down to the heat conductivity of air), then the evaporation flux is substantially reduced (Fig. 5). Such flux reduction is connected to the noticeable temperature reduction of the droplet surface.

Let us now introduce the mean temperature of the droplet surface: $T_{av} = \frac{1}{S}\int_S TdS$, where S is the droplet surface area. We have plotted the dimensionless total flux $J/J_{\pi/2}(L,T_{av})$, (Fig. 6). All calculated total fluxes for all substrates are on one universal dependence of total vapour flux, J, versus contact angle, θ. Accordingly, the variation of the surface temperature is the major phenomenon influencing the evaporation rate.

The total vapour flux, J, varies linearly with L only in the case of absence of Marangoni convection. That can be seen from Fig. 7, where the triangles show the ratio $J(L)/J_{\pi/2}(L,T_\infty)$ to be constant for the isothermal model while the squares illustrate the constancy for the model with LHV and without MC. The difference between these two is only quantitative: the total evaporation rate is smaller, if LHV is included into the model. The addition of Marangoni convection changes the character of the above dependence. It becomes non-linear (circles in Fig. 7). For any value of L the evaporation is enhanced if Marangoni convection is included. This evaporation enhancement is due to surface temperature increase (Fig. 3).

As the size of the droplet decreases, the total evaporation flux, J, tends to the value attained without Marangoni convection. The reason is as follows: as the droplet size decreases the conductive regime of heat transfer becomes dominant. As a result (Fig. 7) the reduction of the contact line radius, L, changes the value of total vapour flux, J, to that corresponding to the regime of heat conduction only.

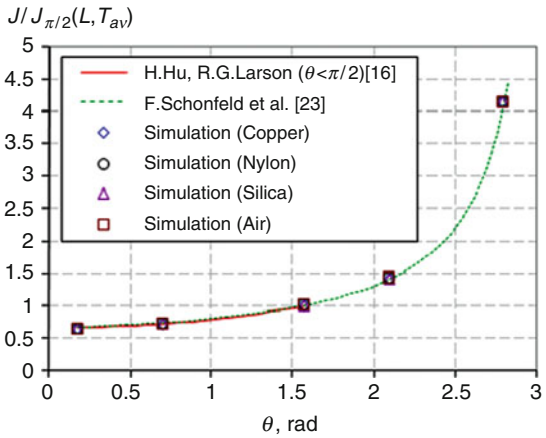

Fig. 6 Rescaled dependence of the total vapour flux from the droplet surface, J, on contact angle θ, $L=1$ mm. Both LHV and MC are taken into account

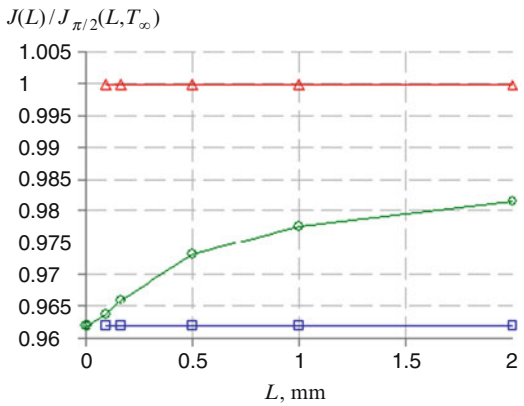

Fig. 7 Dependence of the total vapour flux from the droplet surface, J, on contact line radius, L, at $\theta=\pi/2$. Circles - MC and LHV are taken into account; Squares - LHV is included, but MC is excluded; Triangles - both MC and LHV are excluded from the model

Conclusions

Under a number of reasonable approximations the evaporation of small enough sessile droplets has been investigated in a self consistent way by considering the interconnected problem of vapour transfer; heat transfer in vapour, liquid and solid support; and the Marangoni convection inside the liquid droplet. The influence of the thermal conductivity of the solid support on the evaporation process has been analyzed. The calculated total evaporation flux has been compared with the result in the case of isothermal evaporation. It has been shown that the lower the thermal conductivity of the solid support the higher the deviations appear from the isothermal case. However, if the mean temperature of the droplet surface is used instead of the temperature of the surrounding air for the vapour concentration on the droplet surface then the results found coincide with those known for the isothermal case.

It has also been found that the latent heat of vaporization does not change the qualitative dependence of the total vapour flux, J, on the droplet size, L, that remains linear: $J \sim L$. The presence of the thermal Marangoni convection inside the droplet makes all relationships non-linear.

When the rescaled dimensionless total flux is plotted, $J/J_{\pi/2}(L,T_{av})$ where T_{av} is the mean surface temperature, then all calculated total fluxes for solid substrates of different heat conductivity fall on a single universal relationship between the total vapour flux, J, and the contact angle, θ. Accordingly, the variation of the surface temperature is the major element influencing the evaporation rate.

Acknowledgement This research was supported by the European Union under Grant MULTIFLOW, FP7-ITN-2008-214919. The work of R.G. Rubio was supported in part by the Spanish Ministerio de Ciencia e Innovación through grant FIS2009-14008-C02-01, and by ESA through project MAP-AO-00-052.

References

[1] M. Burger, R. Schmehl, K. Prommersberger, O. Schafer, R. Koch, S. Wittig (2003) Int. J. Heat Mass Transfer 46: 4403–4412.

[2] V. Dugas, J. Broutin, E. Souteyrand (2005) Langmuir 21: 9130–9136.

[3] Hyungmo Kim, Joonwon Kim (2010) J. Micromech. Microeng. 20: 045008

[4] S. Moosman, G.M. Homsy (1980) J. Colloid Interface Sci. 73: 212–223.

[5] F. Girard, M. Antoni, K. Sefiane (2008) Langmuir 24: 9207–9210.

[6] C. Bourges-Monnier, M.E.R. Shanahan (1995) Langmuir 11: 2820–2829.

[7] K. Sefiane, L. Tadrist (2006) Int. Commun. Heat Mass Transfer 33: 482–490.

[8] R.D. Deegan (2000) Phys. Rev. E 61: 475–485.

[9] R.D. Deegan, O. Bakajin, T.F. Dupont, G. Huber, S.R. Nagel, T.A. Witten (2000) Phys. Rev. E 62: 756–765.

[10] G. Guena, C. Poulard, M. Voue, J.D. Coninck, A.M. Cazabat (2006) Colloids Surfaces A 291: 191–196.

[11] R.G. Picknett, R. Bexon (1977) J. Colloid Interface Sci. 61: 336–350.

[12] F. Girard, M. Antoni, S. Faure, A. Steinchen (2006) Langmuir 22: 11085–11091.

[13] F. Girard, M. Antoni, S. Faure, A. Steinchen (2006) Microgr. Sci. Technol. XVIII-3/4: 42–46.

[14] F. Girard, M. Antoni, S. Faure, A. Steinchen (2008) Colloids Surfaces A 323: 36–49.

[15] F. Girard, M. Antoni (2008) Langmuir 24: 11342-11345.

[16] H. Hu, R.G. Larson (2002) J. Phys. Chem. B 106: 1334–1344.

[17] H. Hu, R.G. Larson (2005) Langmuir, 21: 3963–3971.

[18] H. Hu, R.G. Larson (2005) Langmuir, 21: 3972–3980.

[19] W.D. Ristenpart, P.G. Kim, C. Domingues, J. Wan, H.A. Stone (2007) Physical Review Letters 99: 234502.

[20] R. Bhardwaj, X. Fang, D. Attinger (2009) New Journal of Physics 11: 075020.

[21] K.S. Lee, C.Y. Cheah, R.J. Copleston, V.M. Starov, K. Sefiane (2008) Colloids Surfaces A, 323: 63–72.

[22] K.P. Galvin (2005) Chem. Eng. Sci. 60: 4659–4660.

[23] F. Schonfeld, K.H. Graf, S. Hardt, H.J. Butt (2008) Int. J. Heat Mass Transfer 51: 3696–3699.

Progr Colloid Polym Sci (2011) 138:121–126
DOI: 10.1007/978-3-642-19038-4_21

FTIR ATR Study of Adsorption of Trisiloxanes and Hydrocarbon Surfactants at Hydrophobic Solids from Aqueous Solutions

Boris Bezuglyi, Natalia Ivanova, and Victor Starov

Abstract Kinetics of the integrated absorbance in C−H stretch region for ethoxylated trisiloxane and alkyl polyethoxylate surfactants on low- and highly hydrophobic surfaces has been measured by Fourier-Transform Infrared spectroscopy (FTIR) in the attenuated total reflection (ATR) mode. It has been found that regardless of the surface energy of substrate the absorbance of trisiloxanes continuously increases during the experiment (characteristic time scale is ten minutes), while the absorbance of alkyl polyethoxylate surfactants reaches equilibrium for tens of seconds on low hydrophobic and for a few minutes on the highly hydrophobic surfaces. The continuous growth of absorbance with increasing bulk concentration of surfactants has been detected in the case of trisiloxanes on both substrates even at concentrations above critical wetting concentration; while hydrocarbon surfactants attained the constant values of absorbance at concentrations above critical aggregation concentration. The results for alkyl polyethoxylate surfactants obtained from FTIR-ATR spectra are consistent with the results obtained by other authors used neutron and optical reflectometry. Influence of the length of hydrophilic chains on the value of the absorbance of surfactants has been analyzed. In the case of alkyl polyethoxylate surfactants the absorbance decreases with increasing the length of hydrophilic ethoxy groups. However, in the case of trisiloxane surfactants studied the above trend cannot be clearly traced. Some aspects associated with the relationship between adsorption of trisiloxanes at hydrophobic solid/liquid interfaces and spreading kinetics are discussed.

Keywords Fourier-Transform Infrared Spectroscopy • Adsorption of surfactants • Trisiloxane surfactants • AMTIR • Teflon AF

V. Starov (✉)
Department of Chemical Engineering, Loughborough University, Leics, LE11 3TU, UK
e-mail: V.M.Starov@lboro.ac.uk

Introduction

Adsorption and self-aggregation of surfactant molecules at solid liquid interfaces is a subject of great interest [1-9] because of its importance in many technological processes including coatings, surface modification, flotation and agrochemical applications. Knowledge of interaction of surfactant molecules with low energetic surfaces is required for understanding of superspreading behavior of silicon-based trisiloxane surfactants [10, 11]. Trisiloxanes were found to possess an unusual ability to induce water to spread out over hydrophobic surfaces [10, 11]. It was found that conventional hydrocarbon surfactants are also capable of promoting rapid spreading of water on hydrophobic surfaces [12]. Using optical and neutron reflectometry [1, 6], AFM [2, 7, 8] and FTIR spectroscopy [3-5, 9] some progress has been made in understanding of surface adsorption of surfactants. It was revealed [7, 8] that on a given hydrophobic solid trisiloxanes do not show any features in the adsorption behavior as compared with hydrocarbon surfactants, but the rate of formation of surface aggregates was different for those surfactants. In the case of trisiloxanes the latter rate was found very slow and took up to several hours, although the presence of the adsorption layer was detected soon after the solution was placed onto the solid. At concentrations above critical wetting concentration (CWC) [8, 13, 14] trisiloxanes form multilayer aggregates at hydrophobic solids, which were supposed [8] to be responsible for superspreading. However, the "superspreading" of trisiloxane surfactant solutions takes from only a few seconds to a few minutes on those hydrophobic surfaces [8, 12-14, 15], that is, much faster than multilayer formation process. Kumar et al [9] showed that trisiloxane molecules replace water with free OH bonds near the solid and build hydrogen bonds, which make favorable its further adsorption and promotes spreading. However, in this case also adsorption process is very slow and takes tens of minutes.

Below we focus on studying using FTIR-ATR spectroscopy the spectral characteristics and the absorbance kinetics

of aqueous solutions of trisiloxanes and hydrocarbon surfactants on different hydrophobic solid surfaces.

Experimental

Trisiloxane surfactants $[(CH_3)_3SiO]_2Si(CH_3)(CH_2)_3(OCH_2CH_2)_nOH$, denoted below as TEO_n, differ from hydrocarbon surfactants $CH_3(CH_2)_{11}(OCH_2CH_2)_nOH$ ($C_{12}EO_n$ notation used below) by their hydrophobic moiety. TEO_n consists of a flexible Si−O−Si framework with attached hydrophobic methyl ($-CH_3$) groups [10], while hydrophobic part of $C_{12}EO_n$ is mostly composes of less surface active methylene ($-CH_2$) groups [10]. Hydrophilic heads of both trisiloxanes and hydrocarbon surfactants are polyoxyethylene chains (EO_n), where "n" is a number of EO groups. We studied aqueous solutions of both surfactants with n = 4 – 8, and a commercial silicon-based surfactant Silwet® L-77 (Momentive Performance Materials, Germany).

A Nicolet-6700 FTIR spectrometer with liquid nitrogen cooled MCT/A detector and KBr beam splitter, multireflection ATR accessory with the AMTIR crystal trough plate (45° angle of incidence, Pike Technologies) were used for the collection of IR spectra. A depth of penetration of an evanescence wave into a sample in a case of air above the AMTIR increases from 0.37 μm to 1.09 μm in the range of 2800 - 1000 cm^{-1}. The clean exposed surface of the AMTIR which is characterized by a contact angle of pure water $\theta_w \approx 80°$, and the same surface coated with a thin Teflon AF film with $\theta_w = 118°$ were used as low hydrophobic and highly hydrophobic surfaces, respectively. A spectrum of pure water (Millipore filter, 18.2 MΩcm) was subtracted from the sample spectra. Series of absorbance spectra of surfactant solutions were collected for 10 minutes with 4 cm^{-1} resolution.

Characteristics of IR Spectra of Trisiloxanes and Hydrocarbon Surfactants in Aqueous Solutions

Figure 1(a-b) shows IR spectra of solutions of both types of surfactants at concentration CAC (the critical aggregation concentration) at 5 minutes after the deposition. Figure 1 shows that IR spectra of trisiloxanes studied (as well as other trisiloxanes) are quite similar to each other and show three distinctive bands of adsorption regardless of the properties of substrates, Figure 1 (curves 1-2). In the range of 2800 – 3000 cm^{-1} there is an intensive wide adsorption band of C–H bond stretching (str.) with two peaks: at 2962 cm^{-1} asymmetric str. (AS) mode of $–CH_3$ group, and at 2872 cm^{-1} symmetric str. (SS) mode [16], Figure 1a. A very sharp intensive band covering the range of 1230 – 1280 cm^{-1} is related to $Si–CH_3$ SS deformation mode [16-18]. A more intensive band 1130 – 1000 cm^{-1} in the spectra, belongs to Si–O–Si AS (1050 cm^{-1}) and $Si–O–CH_3$ modes (1100 cm^{-1}). Two others peaks should be also noted: an appearance of a sharp peak at 845 cm^{-1} (Figure 1b) in the fingerprint region indicates trimethyl group attached to the silicon [17]; a very weak peak at 1350 cm^{-1} belongs to $–CH_2O–$ deformation showing a hydrophilic head of a trisiloxane molecule [19].

Spectra of hydrocarbon surfactants $C_{12}EO_n$ are also quite similar to each other, but unlike to trisiloxanes, they show

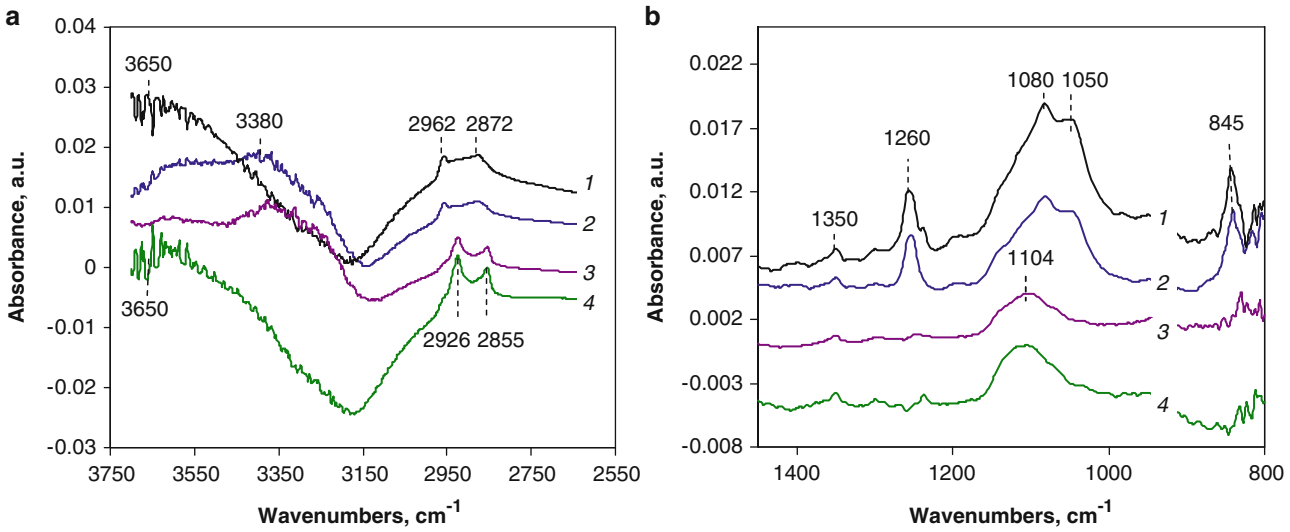

Figure 1 The typical spectra in (a) high wavenumbers and (b) low wavenumbers areas of trisiloxane solutions at 1CAC (L-77, curves 1,2) and hydrocarbon surfactant solutions at CAC ($C_{12}EO_5$, curves 3,4) on AMTIR surface (2, 3) and Teflon AF surface (1, 4). Spectra 3 and 4 are shifted relative to the base line for better discerning peaks

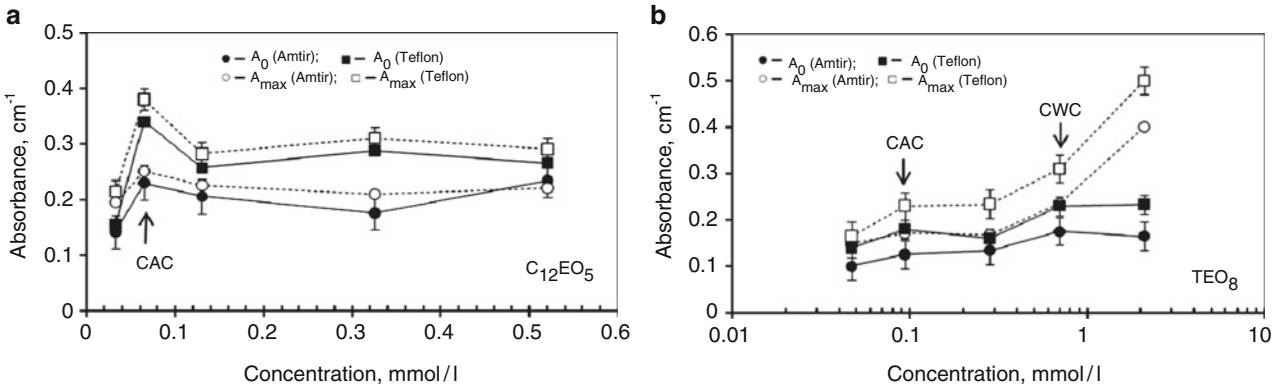

Figure 2 Dependencies of integrated absorbance of C-H stretching region (A_0 at the beginning of process, A_{max} at the equilibrium state) on bulk concentration of surfactants in aqueous solutions. (a) $C_{12}EO_5$ and (b) TEO_8 both on AMTIR (circles) and Teflon AF (squares). The solid and dashed lines were drawn to guide the eye

two intensive peaks at ~ 2926 cm^{-1} and ~ 2855 cm^{-1} corresponding to -CH_2 SS and AS modes [16] and a complex peak at 1104 cm^{-1}. As in the case of trisiloxanes the weak peak at 1350 cm^{-1} appears in the spectra [19]. Another feature of the hydrocarbon surfactants spectra is a hardly detectable peak at around 2958 cm^{-1}, which corresponds to AS mode of only single $-CH_3$ groups of hydrophobic moiety of $C_{12}EO_n$.

Kinetic Studies of Adsorption Process on Solid/Solution Interface

It is known [5] that an integrated absorbance (A) obtained from FTIR-ATR spectra is proportional to the amount of surfactant adsorbed at the solid liquid interface; hence, it can be used for qualitative analysis of surfactant adsorption. As far as adsorption to hydrophobic surfaces occurs by attaching $-CH_3$ and $-CH_2$ groups of surfactant molecules then A is calculated as the area under the peak corresponding to C−H str. mode (see the paragraph above) of FTIR-ATR spectra.

We found that regardless of the surface energy of substrate the absorbance kinetics of all trisiloxanes studied show a continuous growth during the whole time of spectra collection (10 minutes) and no equilibration is reached over that time; while the absorbance of $C_{12}EO_n$ surfactants reaches equilibrium state after less than a minute after the beginning of collection on the AMTIR and after a few minutes on Teflon AF surface. Furthermore, all surfactants studied on both surfaces show a non-zero initial value (A_0) of absorbance in the FTIR-ATR spectrum. This is probably due to the following simultaneous processes taking place at the solid surface: (1) immediate transfer and adsorption of surfactant molecules in the zone of contact from solution/air interface onto solid/solution interface. Those molecules were pre-adsorbed at air/solution interface when solution was released from a pipette; (2) a fast adsorption of surfactant molecules from adjacent layers. We observed that the A_0 for a given surfactant on Teflon AF is larger than on AMTR surface, and the value of A_0 accounts for more than a half of a total (A_{max})* absorbance (see below Figures 2 and 3). The latter observations allow us to conclude that contribution of pre-adsorbed molecules in absorbance formation at the solid/solution interface is not the only process, which takes place at the initial moment of the deposition. Another important consequence from our data is that trisiloxane and hydrocarbon surfactants form an adsorbed layer on hydrophobic surfaces within a few seconds, but their further adsorption behavior is very much different. The latter is in an agreement with AFM measurements by Svitova et al [8].

An influence of bulk concentration of TEO_8 and $C_{12}EO_5$ surfactants on the integrated absorbance in C–H stretching region on both AMTIR and Teflon AF surfaces is shown in Figure 2. Figure 2 shows that regardless of hydrophobicity of substrates TEO_8 exhibits nearly linear increase in absorbance with the bulk concentration (even at C > CWC [8, 13, 14]), while the absorbance of $C_{12}EO_5$ at C > CAC no longer increases. It interesting to note that absorbance behavior of $C_{12}EO_5$ is consistent with its spreading behavior; e.g. at C > CAC no further decrease of advancing contact angle was observed [20]. However, for TEO_8, as well as for other trisiloxanes studied, absorbance behavior at hydrophobic solid/liquid interfaces and their advanced contact angle behavior [13-15, 21] cannot be matched.

* In case of $C_{12}EO_n$ A_{max} was the equilibrium value of adsorbance, however, in case of TEO_n the value of adsorbance after 10 minutes was adopted as A_{max}.

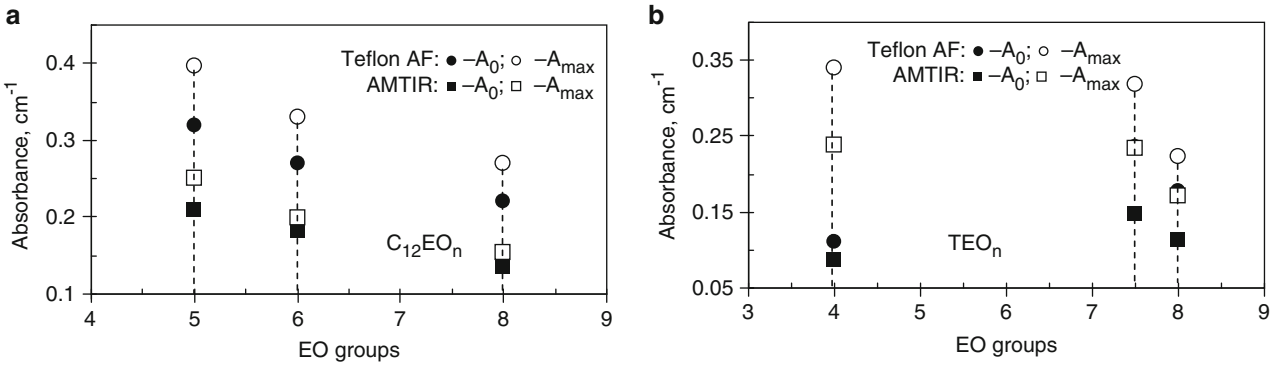

Figure 3 Absorbance values against the numbers of EO groups of trisiloxane and hydrocarbon surfactants on both AMTIR (squares) and Teflon AF (circles) substrates. (a) $C_{12}EO_n$; (b) TEO_n. The dashed lines are to guide the eye

Note also that absorbance of surfactants on Teflon AF is larger as compared with that on low hydrophobic AMTIR. Those observations are quantitatively in line with results by other authors, who showed that adsorption layers of hydrocarbon and commercial nonionic surfactants are thicker on more hydrophobic polystyrene [1] and PTFE [22] surfaces in compare with low hydrophobic PMMA [1, 22].

The considerable adsorption on Teflon AF could be explained by a strong hydrophobic interaction between individual $-CF_3$ groups of Teflon AF surface and $-CH_3$ and $-CH_2$ hydrophobic groups of trisiloxane and hydrocarbon surfactant molecules in water phase. On the other hand, spreading or wetting dynamics is a cumulative macroscopic process which is widely interpreted in terms of surface energies of two surfaces brought into a contact. For instance, Teflon AF surface is determined by $-CF_3$ groups and a surfactant solution droplet, whose liquid/air interface covered by $-CH_3$ groups. Those two surfaces have different surface energies around 16 mN/m [23] and 20 mN/m [24] for Teflon AF and trisiloxane, respectively. The latter clearly shows that spreading in this case is not favorable as a process of lowering of surface energy of the substrate, that is also supported by experiments on spreading kinetics [13-15, 20, 21].

Based on the results of our study we would assume that adsorption of surfactant molecules at hydrophobic solid/liquid interfaces does not play a decisive role in spreading processes.

The length of EO groups influences the adsorption of surfactants mainly through an ability of surfactant molecules to pack densely on solid/solution interfaces. It is known [25] that the EO chains of hydrocarbon surfactants being adsorbed on interfaces form a spiral-like shape to increase an area in contact with water. The latter means that the longer the EO chain the wider the gyration area and, hence, less dense the coverage of the interface due to hydrophilic repulsion between adjacent EO spirals. Figure 3a shows that in the case of $C_{12}EO_n$ the absorbance on both AMTIR and Teflon AF surfaces decreases with increasing length of the EO chain. Regarding trisiloxanes (Figure 3b) the effect of the EO area on absorbance can also be noticed especially by comparison of Silwet® L-77 ($n \approx 7.5$) with TEO_8. However, the absorbance values of TEO_4 are dropped from this trend. That might be explained by low solubility of TEO_4 in water that results in molecules of TEO_4 tend to be adsorbed mostly at air/liquid interface preferably at the initial moment and, therefore, do not contribute noticeably to solid/liquid adsorption at the same initial moment. Note, that Silwet® L-77 reaches nearly the same absorbance value as TEO_4, but starts at a higher A_0 and exhibits a slow increasing absorbance. This behavior might be due to a strong polydispersity of Silwet® L-77 in respect to the number of the EO units (which is a mixture of the EO_n with n varying from 3 to 16, average $n \approx 7.5$ [26]). The latter results in a selective adsorption of molecules with the shorter polyoxyethylene chains at the interface.

Conclusions

FTIR-ATR spectroscopy was used to study the absorbance kinetics of trisiloxane and hydrocarbon surfactants on different hydrophobic solids from aqueous solutions. The surface of AMTIR (the internal reflection element) was used as low hydrophobic surface, and Teflon AF coated AMTIR surface was chosen as a highly hydrophobic surface. It has been shown that the absorbance of all surfactants studied on Teflon AF is considerably higher than that on AMTIR surface. Irrespectively of the surface energy of solid substrates the absorbance of trisiloxanes increased over 10 minutes of the experiment, while the absorbance of hydrocarbon surfactants reached equilibrium in seconds on AMTIR and in a few minutes on Teflon AF surfaces. The continuous growth of absorbance with increasing bulk concentration of surfactants has been detected in case of trisiloxanes on both substrates even at $C > CWC$; while hydrocarbon surfactants

attained the constant values of absorbance at C > CAC. The length of hydrophilic chains of surfactants affects the absorbance remarkably in the case of hydrocarbon surfactants: the absorbance decreases with an increase in the length of ethoxy groups. However, for trisiloxanes studied the latter trend was traced for so called superspreader trisiloxanes with moderate lengths of ethoxy chains, but trisiloxane with short ethoxy chain (EO_4) and, hence, low soluble, is dropped out from this tendency. Despite some trends observed in our study are consistent with the results obtained by other authors using different experimental techniques, the relationship between absorbance kinetics of trisiloxanes at hydrophobic solid/liquid interfaces and spreading behaviour remains to be understood.

Acknowledgement This research was supported by Engineering and Physical Sciences Research Council, UK (Grant EP/D077869/1) and MULRYFLOW Marie-Curie grant.

References

1. J.R. Howse, R. Steitz, M. Pannek, P. Simon, D.W. Schubert, G.H. Findenegg, PCCP **3**, 4044 (2001)
2. H.N. Patrick, G.G. Warr, S. Manne, I.A. Aksay, Langmuir **13**, 4349 (1997)
3. R.F. Tabor, J. Eastoe, P. Dowding. Langmuir **25**, 9785 (2009)
4. D.J. Neivandt, M.L. Gee, M.L. Hair, C.P. Tripp, J. Phys. Chem. B **102**, 5107 (1998)
5. R.P. Sperline, S. Muralindharum, H. Freiser, Langmuir **3**, 198 (1987)
6. C. Geffroy, M.A. Cohen, K. Wong, B. Cabane, V. Bergeron, Langmuir **16**, 6422 (2000)
7. J. Dong, G. Mao, R.M. Hill, Langmuir **20**, 2695 (2004)
8. T. Svitova, R.M. Hill, C.J. Radke, Colloids Surf. A **183–185**, 607 (2001)
9. N. Kumar, Ch. Maldarelli, A. Couzis, Colloids Surf. A **277**, 98 (2006)
10. R.M. Hill, Silicone surfactants. Vol 86. 1999, Marcel Dekker
11. R.M. Hill, Current Opinion in Colloid & Interface Sci. **7**, 255 (2002)
12. T. Stoebe, Z. Lin, R.M. Hill, M.D. Ward, H.T. Davis, Langmuir **12**, 337 (1996).
13. T. Svitova, R.M. Hill, Yu. Smirnova, A. Stuermer, G. Yakubov, Langmuir **14**, 5023 (1998)
14. N. Ivanova, V. Starov, R. Rubio, H. Ritacco, D. Hilal, D. Johnson, Colloids Surf. A **354**, 143 (2010)
15. S. Zhu, W.G. Miller, L.E. Striven, H.T. Davis, Colloids Surf. A **90**, 63 (1994)
16. Infrared spectral interpretation: a systematic approach/ Smith B.C. CRC Press LLC, 1999
17. Analysis of silicones / edited by A. Lee Smith, Chemical Analysis, v. 41, Wiley-Interscience, 1974.
18. N. Wright, M.J. Hunter, Organosilicon polymers. III. Infrared spectra of the methylpolysiloxanes. J. Am. Chem. Soc. **69**, 803 (1947)
19. T.M. Schmitt, Analysis of surfactants. 2nd edition. Revised and explained. 2001. Marcell Pekker, Inc.
20. V. Dutschk, K.G. Sabbatovskiy, M. Stolz, K. Grundke, V.M. Rudoy, J. Colloid Interfaces Sci **267**, 456 (2003); V. Dutschk, B. Breitzke, Tenside Surf Det **42**, (2005)
21. N. Ivanova, V. Starov, D. Johnson, N. Hilal, R. Rubio, Langmuir **25**, 3564 (2009)
22. A. Zdziennicka, Applied Surf. Sci. **255** 3801, (2009).
23. Zisman, W. A. In *Advances in Chemistry Series 43*; Gould, R. F., Ed.; American Chemical Society; Washington, DC, 1964.
24. H.A. Ritacco, F. Ortega, R.G. Rubio, N. Ivanova, V.M. Starov, Colloids Surf. A **365**, 199 (2010).
25. Nonionic Surfactants. Schick, M. J., Ed.; Marcel Dekker Inc.: New York, 1987.
26. L.S. Bonnington, W. Henderson, J.A. Zabkiewicz, Appl. Organometal. Chem. **18**, 28 (2004)

Progr Colloid Polym Sci (2011) 138:127–130
DOI: 10.1007/978-3-642-19038-4_22

Effectiveness of Polymer Sheet Layer to Protect Hydrogel Dressings

Niladri Roy[1], Nabanita Saha[1], Takeshi Kitano[1], Eva Vitkova[2], and Petr Saha[1]

Abstract Two kinds of polymer sheet layers: breathable film (BF) and breathable laminate (BL) were chosen to cover hydrogel dressings (PVP-CMC and PVP-CMC-BA). The upper and lower surfaces of the polymer sheets were designated as BF (U) and BF (L) for BF and BL (U) and BL (L) for BL, respectively. Water vapor transmission (WVT) test reveals that both BL and BF have oxygen diffusion property, i.e. they are breathable. Microbial penetrability test shows that BF has more resistant property against microbial penetrability. Moisture retention capability proves that polymer sheets effectively reduce the tendency of rapid moisture loss from the hydrogels. According to all the results BF could be considered as more effective layer to protect the properties of hydrogel dressings.

Key words Antibacterial • breathable • hydrogel • wound dressings • polymer sheet

Introduction

Hydrogels are widely used for healing of skin lesions in the form of bandages, adhesives or as burn wound dressings, as moist environment can enhance the wound healing process [1]. Beside that, hydrogel dressings are tissue compatible materials, preventing the wound from microbial contamination, inhibiting the loss of body fluids, and moreover providing free flow of oxygen to the wound [2], hydrogels are generally soft and tender material and loose moisture through evaporation in a faster rate if left open to air. So, the wound dressing hydrogels need proper protection during handling and storing. Furthermore, as the hydrogels are biomaterials, they have higher risk to get contaminated by microbes. Thus, from the medical application point of view, it is required to implement some biologically important and bio-inspired system to protect the important pharmaceutical properties and physical characteristics of the hydrogel. The aim of this study is to select appropriate covering material for the hydrogels to protect the hydrogels from rapid moisture loss, bacterial contamination and to provide extra strength during handling and storing. Some secondary layer of polymeric sheet may improve the mechanical strength of hydrogels as well. Breathable film (BF) or breathable laminate (BL) may be the suitable one as layered material or covering sheet. This article evaluates mainly the oxygen diffusion and microbial penetrability of BF and BL polymer sheets individually as well as their effectiveness to protect the polymeric hydrogel from water loss.

N. Saha (✉)
[1]Polymer Centre, Faculty of Technology, Tomas Bata University in Zlin, TGM-275, CZ-76272, Zlin, Czech Republic
e-mail: nabanita@ft.utb.cz
[2]Fatra a.s, Tr. T. Bati 1541, 76361 Napajedla, Czech Republic

Experimental

Materials

Polymer sheets and hydrogels were used to investigate this study. Polymer sheets: Medical grade polymer sheets (a) Sontek® F Breathable Film (BF) and (b) Sontek® L Breathable Laminate (BL), were supplied by Fatra a.s., Czech Republic. Breathable film (BF) was prepared with the mixture of linear low density polyethylene (LLDPE) and calcium carbonate ($CaCO_3$) and marked as upper (U) and lower (L) though both the sides appear similar (smooth surface and white). Breathable laminate (BL) was prepared with LLDPE, $CaCO_3$ and nonwoven polypropylene (PP) and also marked as upper (U, smooth and white) and lower (L, nonwoven, rough and white). Hydrogels were prepared at Polymer centre laboratory, Tomas Bata University in Zlin, Czech Republic with biodegradable and biocompatible polymers: Polyvinylpyrrolidone (PVP) and carboxymethyl

cellulose (CMC) and without and with boric acid (BA). Finally, these hydrogels are termed as PVP-CMC and PVP-CMC-BA respectively [3-5].

Methods

Water Vapor Transmission (WVT)

The water vapor transmission (WVT) of breathable BF and BL was determined gravimetrically. Each aluminium foil dish (internal diameter of 5.5 cm and height 1 cm) was filled with 10 ml of distilled water (100% RH). A circular piece of polymer sheet [upper, BF (U)/BL (U) or lower, BF (L)/BL (L)] was placed on the dish and sealed with glue. Samples were accurately weighed, and then placed in a desiccator containing calcium chloride ($CaCl_2$) as a desiccant, and filled with silica gel (0% RH) and incubated at 40°C. At specific intervals (24, 48, 72, 96 and 120 hours) the dishes were weighed and the profile of mass change was plotted versus time, for each side of every cover sheet. The amounts of water vapor transmission through the sheets were measured using the following equation [6, 7].

$$WVT = \frac{Wx}{tAP_0(RH_1\text{-}RH_2)} \quad (1)$$

In this equation, WVT is the water vapor transmission. W/t is the mass change (flux, mg/h) resulted from the slope of profile of the mass change versus time. Wx is product of variables where x is the thickness of the film used in the scale of μm. A is the area of the film in the scale of m^2, which is equal to the surface of the dish. P_0 is the vapor pressure of pure water vapor transmission that is equal to 7.4 kPa at 40°C. RH_1-RH_2 is the relative humidity gradient of the inside and outside moisture contact of the examined dish, here this value is considered to be 100. The average values of three specimens of a sample are represented here.

Microbial Penetrability

The bacterial penetration ability in polymer sheets (BF and BL) was examined in presence of *Staphylococcus aureus (S. aur) and Escherichia coli (E.coli)* [7, 8]. The sheets were first cut into rectangular pieces of size 30 × 30 mm and placed on sterile nutrient agar medium in the petri dishes (diameter 85 mm). The open surface of each polymer sheet was contaminated with 0.02 ml of culture inoculums (10^7 CFU/ml) and then incubated at 37°C up to 120 hrs. Polymer sheets were removed every 24 hr interval and examined the formation of colony on the surface of nutrient agar plate where the contaminated sheets were placed. In each case, two specimens from the same sample were measured.

Moisture Retention Capability

Both PVP-CMC and PVP-CMC-BA hydrogels (thickness ~2.8 mm, diameter = 85 mm) without and with cover (BF and BL) were weighed and incubated at 40°C. The weights of the samples were measured in every 2 hr intervals and the moisture retention capability was measured by the water loosing rate of the samples [9]. In each case, an average value of three specimens has been represented in the graph and table.

Results and Discussions

Water Vapor Transmission (WVT) of Polymer Sheets

The oxygen diffusion property of polymer sheets was confirmed by measuring water vapor transmission (WVT) rate and loss of water in time under controlled environment and the results are presented in Table 1 and Figure 1. Rate of water vapor loss is uniform for BF for both side, but the value through BL (U) is lower than BL (L). It is desirable that the covering material for hydrogel should be breathable; it will provide flow of oxygen to the hydrogel and will help to evaporate the water accumulated at the junction of hydro-

Table 1 Water vapor transmission of the polymer sheets

Sample index	Film thickness (μm)	Mass change (mg/h)	WVT (mean±S.D.; n=3) (mg mm/m^2 h kPa)
BF (U)	60	76.25	2.60±0.11
BF (L)	60	77.08	2.62±0.62
BL (U)	190	60.20	6.52±0.56
BL (L)	190	76.45	8.29±0.54

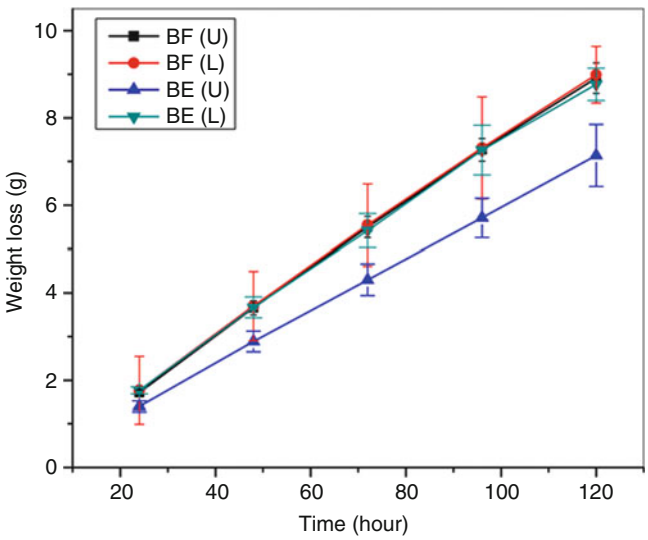

Fig. 1 Profile of water vapor transmission through polymer sheets

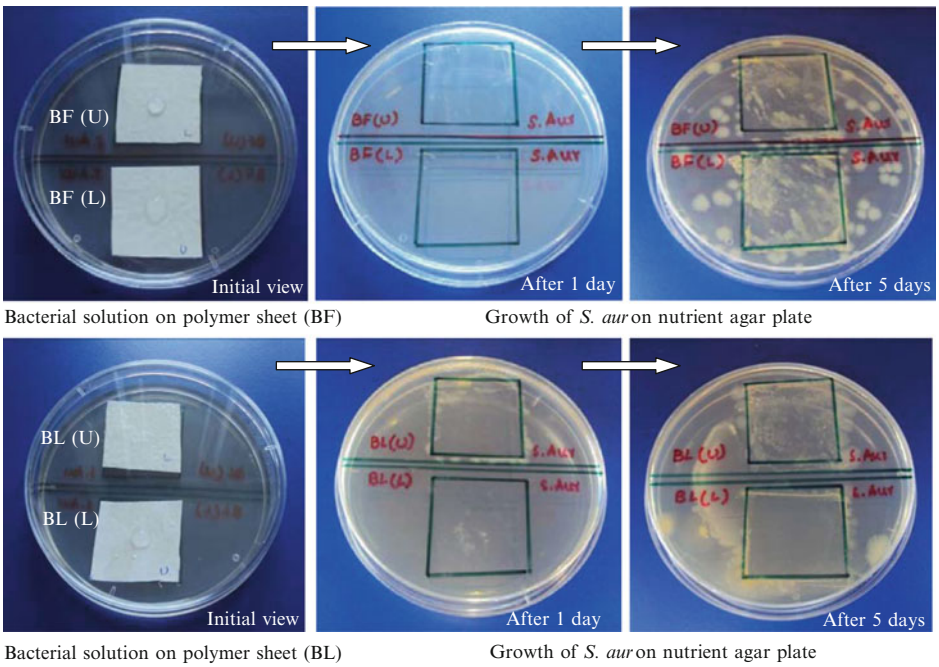

Fig. 2 Visual image of microbe penetration test through polymer sheets in presence of *Staphylococcus aureus*

gel and the cover. Otherwise the cover layer will slip from the surface of the hydrogel.

Microbial Penetrability of Polymer Sheets

One of the important characteristics of the cover of hydrogel wound dressing material is that the covering material must have adequate microbe barrier property to protect the hydrogel from microbial contamination. The penetrability of microbial agents through the polymer sheets has been examined qualitatively on the basis of observed microbial growth using the strain *Staphylococcus aureus* (*S.aur*) and *Escherichia Coli (E.coli)* on nutrient agar plates. It is clearly visible from Figure 2 that bacteria can penetrate through the polymer sheets of BF or BL but more bacteria can pass through BL than BF until 24 hour. From the growth of bacterial colonies on the nutrient agar plates, it seems that the entry of bacteria is higher in presence of BL rather than BF. A same phenomenon was also observed in presence of *E. coli*. It gives the impressions that BF shows better resistant property against bacterial penetrability. But, after penetration, the growth of bacterial colonies on nutrient agar plate increases in time, as presented the results on 5th day of investigation.

Moisture Retention of Hydrogels by Polymer Sheets

Moisture retension capacity is a very important factor for wound dressing hydrogels. Thus, moisture retention ability of the hydrogels were measured without cover (Figure 3 (a)) and with cover (covered both sides with polymer sheets, Figure 3 (b) & (c)) samples and the results are depicted in Figure 4 and Table 2. Both PVP-CMC and PVP-CMC-BA hydrogels (without cover) show high rate of moisture loss with time, but the rate of moisture loss is significantly reduced when covered with polymer sheets (BF or BL). The hydrogels when covered with polymer sheets the hydrogel surface no longer remain exposed to the air. But, as BF and BL are

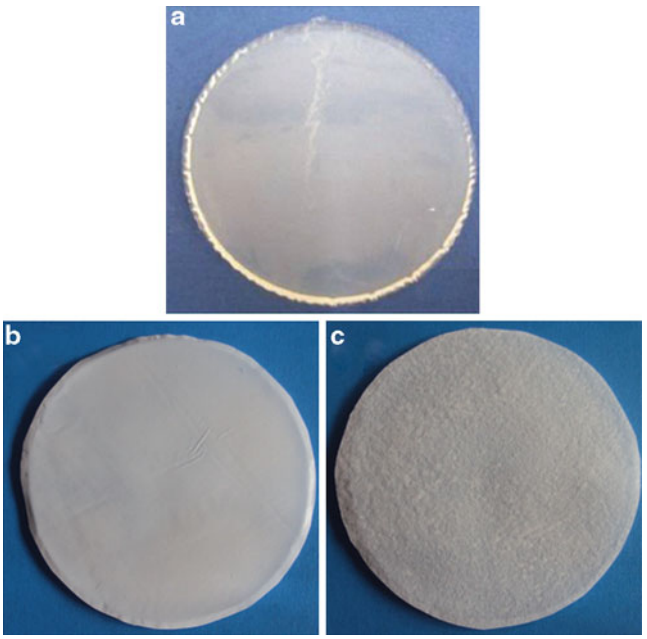

Fig. 3 Images of hydrogel (a) without covering, (b) covered with breathable film [viewed smooth surface of BF], (c) covered with breathable laminate [viewed rough surface of BL]

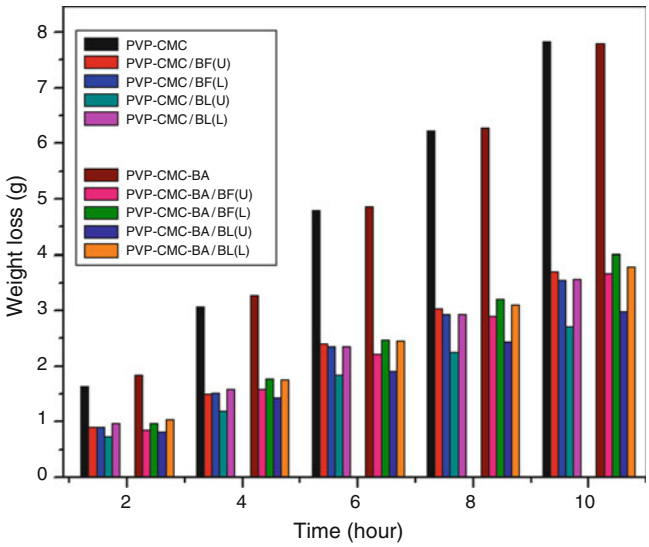

Fig. 4 Moisture retention capability of PVP-CMC and PVP-CMC-BA hydrogels without and with polymer sheet layer

Table 2 Moisture retention capability of PVP-CMC and PVP-CMC-BA hydrogels without and with polymer sheet

Sample index	Weight loss (g)				
	2hrs	4hrs	6hrs	8hrs	10hrs
PVP-CMC	16.7	32.2	48.6	63.5	79.1
PVP-CMC /BF(U)	8.5	15.0	24.7	31.5	36.0
PVP-CMC /BF(L)	8.5	15.3	24.1	30.1	35.1
PVP-CMC /BL(U)	7.1	12.3	18.9	23.2	26.5
PVP-CMC /BL(L)	9.0	15.9	24.1	30.0	26.6
PVP-CMC-BA	18.1	33.1	48.5	63.7	78.3
PVP-CMC-BA /BF(U)	8.1	15.4	23.2	29.5	35.9
PVP-CMC-BA /BF(L)	9.0	16.5	25.0	31.8	40.0
PVP-CMC-BA /BL(U)	7.5	14.6	18.5	23.8	28.2
PVP-CMC-BA /BL(L)	9.9	16.3	24.8	31.1	37.5

breathable, thus less amount of water evaporate through the polymer sheets. Furthermore, the thin layer of water between polymer sheets and hydrogels may help to interact between polymer sheets and hydrogels and to form some temporary physical bondings, which helps the polymer sheets to adhere on the surfaces of the hydrogels and to prevent the rapid water loss as well. As a result, both the polymer sheets effectively help the hydrogels to retain the moisture.

Conclusion

Both polymer sheets (BF and BL) show more or less similar properties in case of water vapor transmission as well as moisture retention capability. Furthermore, both polymer sheets and hydrogels are chemically innert in presence of each other, so it is effective to cover the hydrogels by these polymer sheets. In addition, the polymer sheets do not affect on the texture of the hydrogels but, provide some extra stability during handling. The polymer sheet covers easily adhere on the surfaces of the hydrogels, but do not stick, thus it is easy to remove them before applying the hydrogels on patients skin. Among these two polymer sheets, BF shows better role against microbial penetrability during first 24 hour which is a very important factor to protect the wound dressing hydrogels. Thus, considering all the above mentioned results, it can be concluded that between these two polymer sheets BF could be the better one as a covering material for the hydrogel dressings to protect and preserve the quality of the hydrogel.

Acknowledgements Authors are thankful to Internal Grant Agency (IGA/1/FT/10/D) of Tomas Bata University in Zlin, The Czech Republic for financial support.

References

1. Winter GD, Scales JT (1963) Nature 197: 91
2. Higa OZ, Rogero SO, Machado LDB, Mathor MB, Lugao AB (1999) Radiat Phys Chem 55: 705
3. Saha P, Saha N, Roy N (2008) Hydrogel Wound Covering, Patent (UPV CR) File No: PV 2008-306.
4. Roy N, Saha N, Kitano T, Saha P (2010) J Appl Polym Sci 117: 1703
5. Roy N, Saha N, Kitano T, Saha P (2010) Soft Materials 8 (2): 130
6. Akhgari A, Farahmand F, Garekani HA, Sadeghi F, Vandamme TF (2006) Eur J Pharm Sci 28:307
7. Roy N, Saha N, Humpolicek P, Saha P (2010) Soft Materials 8 (4): 307
8. Tomic SL, Micic MM, Dobic SN, Filipovic JM, Suljovrujic EH (2010) Radiat Phys Chem 79: 643
9. Wang M, Xu L, Hu H, Zhai M, Peng J, Nho Y, Li J, Wei G (2007) Nucl Instrum Methods Phys Res. Sect. B 265: 389

Progr Colloid Polym Sci (2011) 138:131–138
DOI: 10.1007/978-3-642-19038-4_23

Membrane Affinity of New Antitubercular Drug Candidates Using a Phospholipid Langmuir Monolayer Model and LB Technique

D. Schnöller[1], Cs. B. Pénzes[1], K. Horváti[2], Sz. Bősze[2], F. Hudecz[2,3], and É. Kiss[1]

Abstract Tuberculosis is a major problem throughout the world causing 1.9 million deaths annually, and induces a major global public health problem. The pathogen responsible for the disease is *Mycobacterium tuberculosis*. Drug candidates expected to be specific inhibitors of dUTPase an essential enzyme of *Mycobacterium tuberculosis* were identified *in silico*. A phospholipid Langmuir monolayer formed at the liquid/air interface as a simple but versatile model of the cell membrane was applied to assess the membrane affinity of the drug candidates. The interaction of three different potential drug molecules TB501, TB502, and TB505 with lipid monolayer was characterised by tensiometry, and atomic force microscopy at different temperatures. The degree of penetration of drug candidates into the lipid film and the structural variation of drug penetrated lipid films revealed by atomic force microscopic images were compared.

Keywords Langmuir monolayer • AFM • LB film • Penetration • Antituberculotics

Abbreviation

Mtb	Mycobacterium tuberculosis
LB	Langmuir-Blodgett
AFM	Atomic force microscopy
MIC	Minimum inhibitory concentration

D. Schnöller (✉)
[1]Laboratory of Interfaces and Nanostructures, Institute of Chemistry, Eötvös Loránd University, Budapest 112, P.O. Box 32, H-1518 Hungary
[2]Research Group of Peptide Chemistry, Hungarian Academy of Sciences, Eötvös Loránd University, Budapest 112, POB 32, H-1518 Hungary
[3]Department of Organic Chemistry, Institute of Chemistry, Eötvös Loránd University, Budapest 112, P.O. Box 32, H-1518 Hungary

Introduction

Tuberculosis is a chronic disease which is one of the leading causes of death in the world. The pathogen responsible for the disease is *Mycobacterium tuberculosis* (*Mtb*) causes 8 million infected people and nearly two million deaths every year [1]. The difficulties of the therapy for tuberculosis are: the long duration of treatment, the drug toxicity which is increasing with the dose, and heavy side effects like the damage of liver and kidney, furthermore the emergence of drug resistance. The aim is to shorten the duration of treatment hence reducing harmful side effects.

A new method to find effective drug candidates is the "*in silico*" identification of chemical species able to block vital bacterial enzymes. Numerous possible specific inhibitors of dUTPase an indispensable enzyme of *Mtb* for cell viability, [2-4] were identified with a technique based on computer simulation [5]. The introduction of the best drug candidates, which were selected and characterized physico-chemically, biologically and pharmaceutically, might be effective in treatment of tuberculosis infections. The Frigate program generated docking energies for each of the more than 2 million small molecules. The best 1000 scored molecules were filtered according to log P and predicted solubility properties. We also checked for their drug likeness and ranked them according to their binding affinities. *In vitro* functional characteristics of the compounds (MIC values against mycobacterial species, cytotoxicity on human cells, cellular uptake profile) were carefully analysed.

Drugs have to be transported through various membranes to reach the infected target cell. The focus of our interest is the investigation of the molecular interaction of the drug candidates with the lipid membrane. Lipid Langmuir monolayer is one of the simplest model of cell membranes. It is much less complex than any biological membrane but a well defined system allowing many parameters like packing, density, nature of lipids just as the subphase composition and temperature to be varied [6, 7]. The monolayer technique is a current method to characterize the molecular interaction

between drug candidates and membrane forming lipids and other components [8-10]. The monomolecular layer of ordered and close packed, amphiphylic lipid molecules with constant thickness is prepared at the air-water surface in a Langmuir balance. It is possible to assess the membrane affinity of the drug molecules getting quantitative information on their adsorption/penetration ability into lipid layer.

Three of new drug candidates which were identified "*in silico*" and expected to be specific inhibitor of dUTPase were investigated and compared in this study. Langmuir monolayer was made of phospholipon and penetration ability of the drug candidates were evaluated at 24 and 36 °C by measuring the change of the surface pressure of the Langmuir film.

Penetrated lipid monolayers were transferred to solid support (mica) by Langmuir-Blodgett (LB) technique. Their surface topography was investigated by atomic force microscopy (AFM) which is a promising method for imaging the surface details of a molecular film. By means of AFM it is possible to study the structures and structural changes of model membranes due to the incorporation of drug molecules.

Experimental

Materials

Phospholipon 100H a pure phosphatidylcholine with fatty acid composition of approx. 85 wt% stearic acid 15 wt% palmitic acid, was purchased from Nattermann GmbH (Germany).

The *in silico* identified selective inhibitor molecules of the dUTPase are marked as TB501 (M: 436.5), TB502 (M: 294.3) and TB505 (M: 343.2). The molecular structure of the three drug candidates is given in Fig 1.

Chloroform (purity $>$ 99.9%) from Promochem Optigrade HPLC was used for preparing lipid solution. Dichloromethane (purity $\geq$ 99.8%) and methanol (purity $\geq$ 99.9%) obtained from Promochem Optigrade HPLC were used for cleaning the Langmuir trough. Dimethyl sulfoxide (purity $>$ 99.9%) from Sigma-Aldrich A.C.S. reagent was used to dissolve TB502 and TB505 drug candidates. Purity of double distilled water was checked by its conductivity ($<$ 5 mS) and surface tension ($>$ 72.0mN/m at 24 °C) values.

Methods

Antibacterial Properties of Drug Candidates

The antitubercular effect of TB501, TB502 and TB505 was characterized by the determination of the minimum inhibitory concentration (MIC) on *M. tuberculosis* $H_{37}Rv$ strain (ATCC 27294). Briefly: *In vitro* antimycobacterial activity of the compounds was determined in Sula semi-synthetic medium, which was prepared in-house [11-13] at pH 6.5. MIC values were determined after incubation at 37 °C for 28 days. MIC was the lowest concentration of a compound at which the visible inhibition of the growth of *M. tuberculosis* $H_{37}Rv$ occurred. The sterility of these tubes and the activity of the compounds were confirmed using a colony forming unit (CFU) determination by subculturing from the Sula medium onto drug-free Löwensten-Jensen solid medium. The samples were incubated for further 28 days [12, 14, 15]. The experiments were repeated two times.

Langmuir Film Experiments

The experiments were performed by a computer controlled KSV MiniMicro Langmuir balance (KSV Instruments, Finland). The trough (51×169×4 mm) was made of Teflon while the material of the barrier was polyoxymethylene recommended for work with lipid layers [16]. Trough was cleaned with dichloromethane and double distilled water, while the barriers with methanol and double distilled water. Lipid dissolved in chloroform (1g/L) was spread on the water surface. 15μL of solution was applied dropwise by a Hamilton syringe to form the monolayer. Prior recording the isotherms the solvent was let to evaporate for 10 minutes.

The lipid layer was compressed into a dense monolayer by the two movable barriers while the surface pressure and

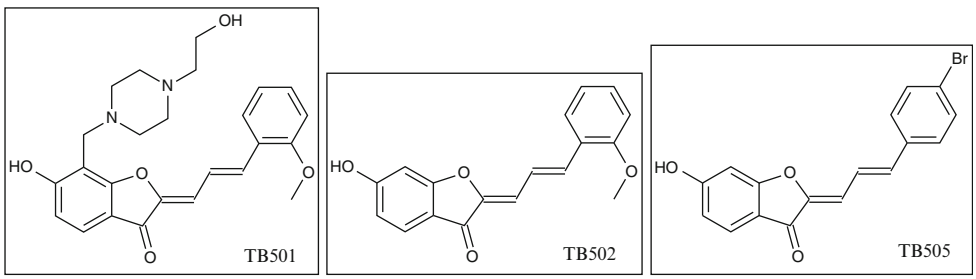

Figure 1 Molecular structure of TB501, TB502 and TB505

the area were continuously recorded. The surface pressure was measured tensiometrically by a KSV force transducer with an accuracy of ±0.05mN/m using chromatography paper (Whatman Chr1) as a Wilhelmy plate. Surface pressure-area isotherms of lipid monolayers were recorded at a barrier speed of 2.22Å^2/molec/min.

The trough was mounted on an aluminum base with built-in channels for temperature control of the subphase and enclosed in an environment chamber. The surface pressure-area isotherms were determined at two different temperatures 24.0±0.2 and 36.0±0.2°C. Three compression-expansion isotherms were recorded consecutively. There was no awaiting time between compression and expansion. There was a small deviation between the first and the second isotherms but the third one presented no difference against the second one.

Penetration of Drug Candidates

Three variations of a potential drug molecule were tested in penetration experiments. TB501, TB502 and TB505 were dissolved and injected into the water subphase below the lipid layer. TB502 and TB505 were dissolved in dimethylsulfoxide (DMSO). Effect of corresponding amount of pure DMSO was checked on the surface pressure in a separate experiment and found to be negligible.

As a first step pure lipid monolayer was formed than following two compression-expansion cycles the layer was compressed to a given value of surface pressure 15, 20, or 25mN/m which are consistent with property of lipid bilayer [17]. At that position the barrier was stopped and a fixed amount of solution of the drug was injected into the subphase to obtain a final drug concentration of 2×10^{-6}mol/L. The change in surface pressure was recorded as a function of time for one hour. Adsorption/penetration of the drugs into the lipid layer was indicated by the increase of surface pressure. To determine the degree of penetration the surface pressure of pure lipid film was compared to the surface pressure obtained for lipid monolayer interacting with the injected drug. Three independent measurements were performed and the average values with the SD are displayed in the Figures.

Langmuir-Blodgett Film

Langmuir films were transferred to freshly cleaved mica solid support by a KSV film lift with Langmuir-Blodgett (LB) technique at a film lift speed of 2 mm/min to keep the surface pressure constant during the transfer. 1 mm/min barrier speed was applied to allow the smooth transfer and the transfer ratio of 1. LB films were kept under vacuum for 24 hours before AFM measurements.

Atomic Force Microscopy (AFM)

The morphology of the LB film was studied with multimode atomic force microscope instrument (Park System, XE-100, South Korea) in the contact mode. Cantilever CSC38 (MicroMash, Estonia) made of Si_3N_4 was used with a tip curvature radius less than 10 nm, an average spring constant of 0.03 N/m, resonance frequency of 10 kHz and with Al coated reflective side. The AFM studies were conducted at 1.0 Hz scanning rate and a scan window of 5 x 5 μm. 4-5 images were collected for every specimen at randomly selected locations. The image analysis was performed by the XEI 1.6 program (Park System, South Korea).

Results and Discussion

Antimycobacterial Evaluation of Drug Candidates

dUTPase is essential for DNA integrity and thymidylate biosynthesis. *Mycobacterium tuberculosis* apparently lacks any other thymidylate biosynthesis pathway, therefore dUTPase is a promising antituberculotic drug target [2-4]. New promising drug candidates were identified by a new molecular dynamic docking method using RS-PDB (highly structured and repaired version of PDB) and Zinc (a free database of commercially-available compounds for virtual screening) [5]. Antimycobacterial activity of compounds in vitro was characterized by the determination of MIC with 4-week exposure period. All of the three drug candidates were effective against H_{37}Rv bacterial strain. The MIC was 20 μg/ml, 20 μg/ml, and 5 μg/ml, for TB501, TB502 and TB505, respectively. The MIC values were in the same concentration range suggesting that the structural variation of the molecule did not alter its *in vitro* antimicrobial effect to a great extent.

Monolayer Experiments

The shape of the isotherms reflects the molecular interaction and the packing of the lipid molecules in the monolayer varying with the temperature as shown in Figure 2.

The lipid monolayer is less condensed at 36 °C than at 24 °C in a wide range of surface density. Above surface pressure of 20 mN/m approaching the close packed condition the difference become small and the state of the lipid monolayers does not differ significantly in the compressed range.

Fluidity or compressibility which is an important property of the monolayer [18] can be shown by their compressibility modulus (K):

$$\mathrm{K} = -A\frac{\mathrm{d}\pi}{\mathrm{d}A}$$

The lipid layer is highly compressible with almost zero compressibility modulus at 24°C until the molecular surface area reaches the value of 75 A^2/molecule (Figure 3). From that point the modulus rises intensely while increases further as the film got into the condensed state. Contrary to that the lipid layer presents a significant compressibility modulus at 36°C from the beginning of the isotherm which is getting higher approx. at the same density as the layer at the lower temperature. The moduli increase almost parallel in the condensed range of the isotherm but the value determined at 36°C remains smaller e.g. the layer is more fluid than that was observed at the lower temperature.

Penetration of Drug Candidates

Molecular interaction between the drug candidates and the lipid layer is characterized by the increase of surface pressure ($\Delta\pi$) of the lipid film due to the penetration of the drug molecules into the lipid film.

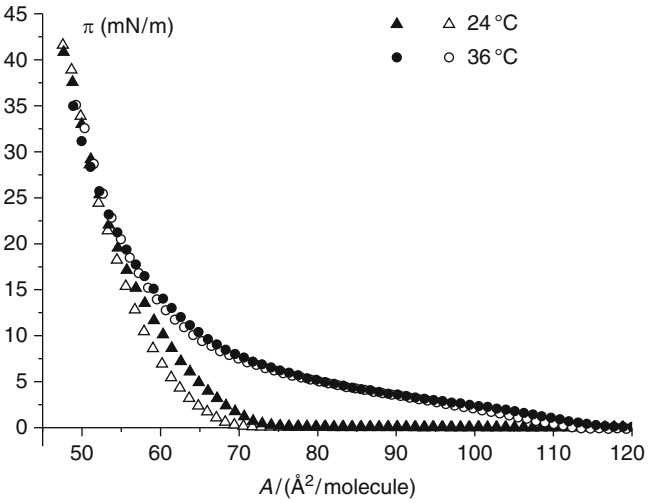

Figure 2 Compression (filled symbols) and expansion (open symbols) surface pressure-area isotherms of phospholipon film at 24 (●) and 36 °C (▲)

The phospholipon monolayer was compressed to various degrees characterized by the surface pressure as 15, 20 and 25mN/m. As an example, the penetration results for TB501 at three different surface pressures at 24°C are shown in Figure 4. The penetration ability of TB501 is higher into less dense lipid monolayer (15mN/m), but it is important to note, that detectable changes in surface pressure were observed at 20 or even at 25 mN/m. This is a clear evidence for membrane-drug interaction.

The penetration results for drug candidates are collected in Figure 5 (at 24°C) and Figure 6 (at 36°C) as a function of initial surface pressures of lipid monolayer. Since TB505

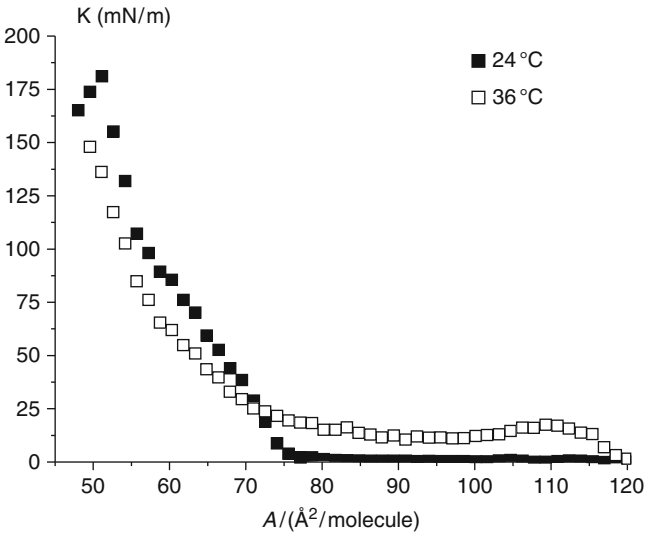

Figure 3 Compressibility modulus (K) of phospholipon monolayer as a function of molecular area (A) at 24 (■) and 36°C (□)

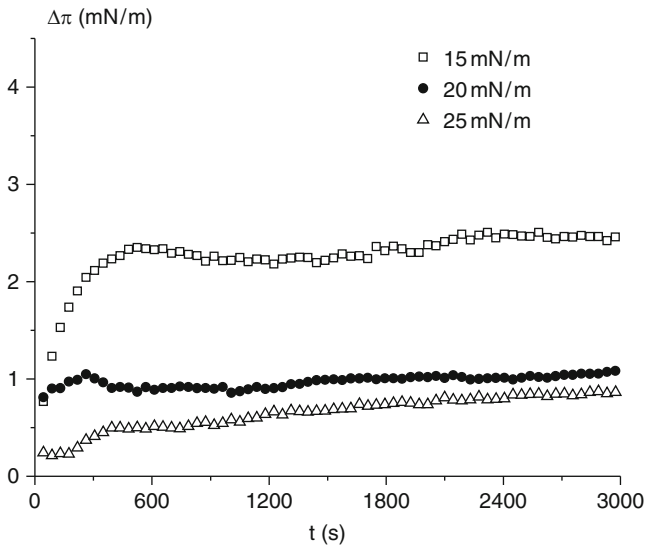

Figure 4 Penetration ($\Delta\pi$) of drug candidate TB501 into phospholipon monolayer at different beginning surface pressures of 15 (□), 20 (●) and 25mN/m (Δ) as a function of time (t) at 24 °C

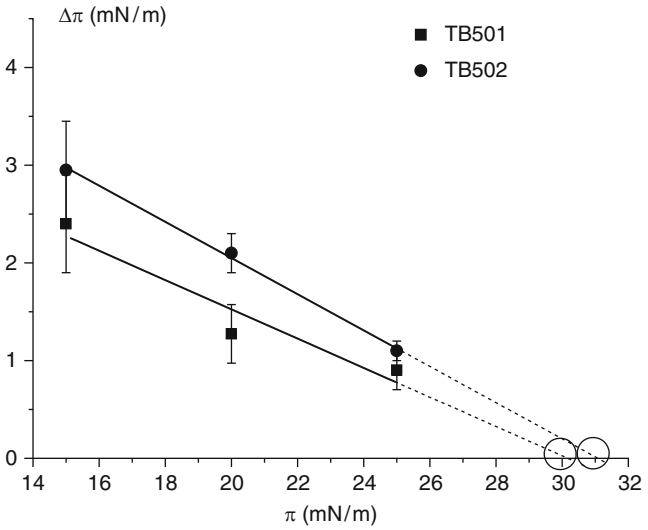

Figure 5 Degree of penetration ($\Delta\pi$) as a function of the surface pressure of phospholipon monolayer (π) and the threshold values of TB501 (■) and TB502 (●) at 24 °C

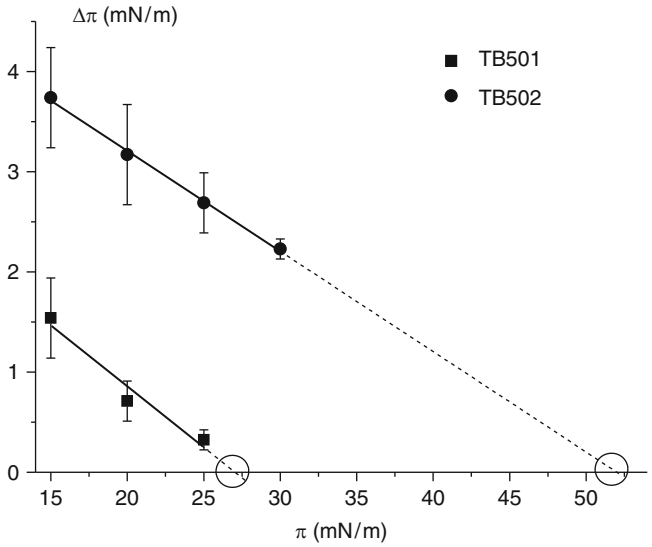

Figure 6 Degree of penetration ($\Delta\pi$) as a function of the surface pressure of phospholipon monolayer (π) and the threshold values of TB501 (■) and TB502 (●) at 36 °C

does not show detectable penetration at 24 or 36 °C the effect of TB505 is not presented in figures.

TB501 and TB502 exhibit a significant and similar membrane affinity at 24°C whereas the penetration is getting weaker into the more dense lipid layers with 20 and 25mN/m. Great difference was found to be however, at 36°C in the penetration behavior of TB502 and TB501. TB502 shows definitely more intense penetration, than the other compound. To test this property the experiment was extended to lipid layer with surface pressure of 30mN/m and a considerable affinity was obtained even in that case.

The threshold of the penetration ability is the highest surface pressure of lipid monolayer which the drug candidate is able to penetrate into. Above that critical value no penetration is expected. It is accessibly illustrated by the extrapolation of penetration ($\Delta\pi$) as a function of surface pressure (π) to the surface pressure (π) axis (Figure 5 and 6). The threshold values are typically about 30 mN/m for TB501 and TB502 drug candidates at 24°C and somewhat smaller for TB501 at 36°C. Contrary to that, the greatly enhanced penetration ability found for TB502 at 36°C led to high threshold value above 50mN/m. That finding might indicate an effective potential transfer through the monolayer. This is a remarkable property of that molecule, which probably can not be explained just by the higher fluidity of phospholipid film at the temperature of 36°C.

AFM Investigations

Phospholipon films penetrated by TB501 or TB502 at 24 and 36°C were transferred to muscovite mica solid support by the LB technique at a surface pressure of 15mN/m. The surfaces of these one-layer films were characterized by AFM images taken at contact mode. The morphology of the complex layers and that of pure phospholipon films as comparison was illustrated in Figure 7.

The pure phospholipon layer at 24 °C presented a highly homogeneous surface with extended islands. Line section analysis reveals a rather smooth surface with a roughness of 0.1-0.2nm. The thickness of the domains was found to be 2.4 nm corresponding to the length of alkyl chains with nearly perpendicular orientation in the monolayer. Phospholipon layer shows similar homogeneity at 36 °C although the grooves are wider between the islands and the thickness of the monolayer is smaller (approx. 1.5nm) reflecting the less oriented structure of the lipid molecules at the higher temperature (Figure7 a, d).

AFM micrographs show important differences at both temperatures depending on whether TB501 or TB502 interacted with phospholipon monolayer. Penetration of TB501 into lipid film at 24 °C and 36 °C is illustrated in Figure 7 b and e. The TB501 penetrated films show topography with considerable lateral heterogeneity. The domain structure is recognizable but perturbed by presence of penetrated molecules leading to increased surface roughness at 24°C or large aggregates in the case of higher temperature (Figure 7 e). The structural change of two types shown on the lipid monolayers clearly represents the effect of interaction of lipid layer with the drug candidate molecule.

The domain structure is basically sustained following the penetration of TB502 (Figure 7 c and f) while the characteristic change is the significant decrease of uncovered areas between the lipid domains comparing to the pure lipid film.

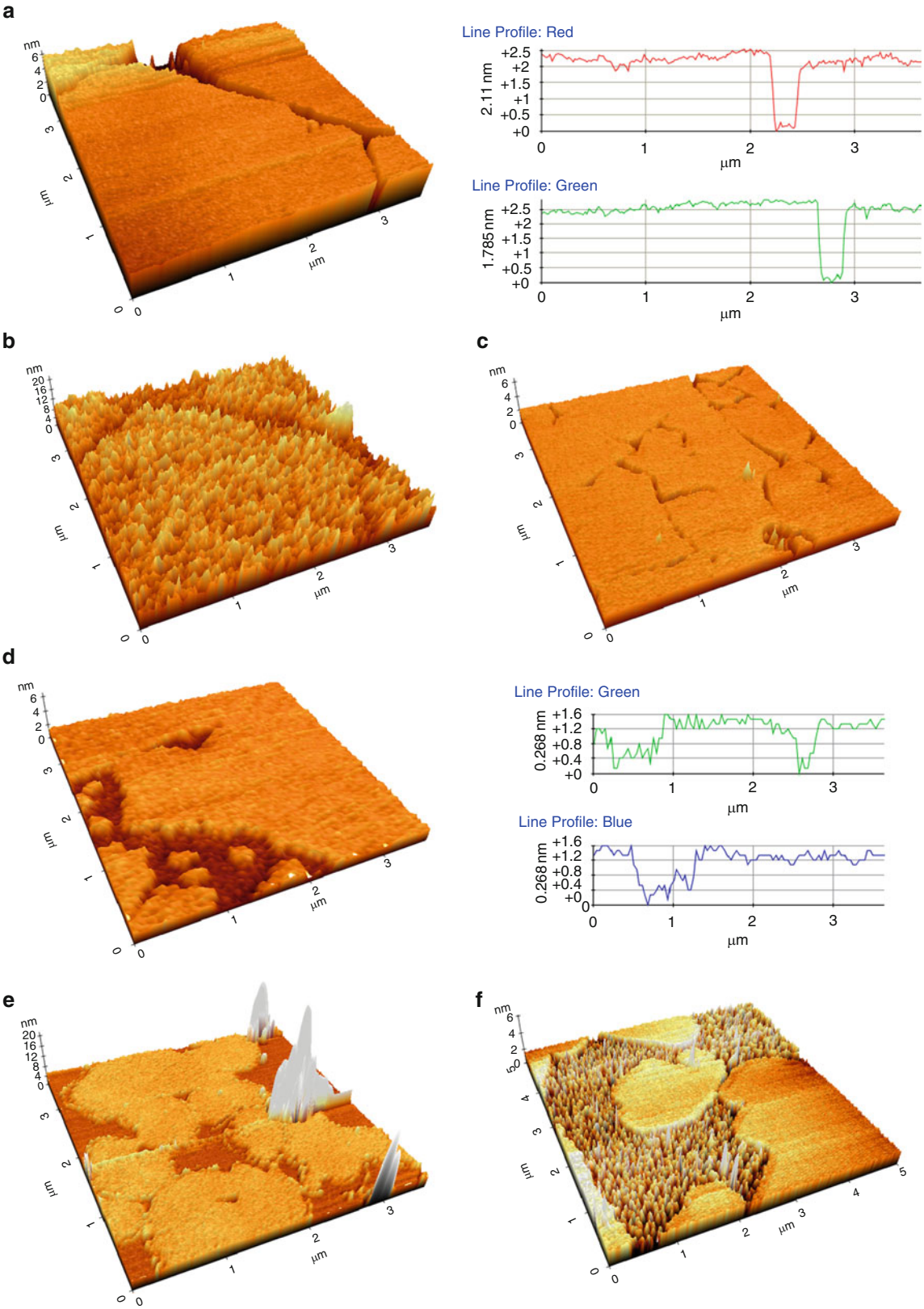

Figure 7 Phospholipon monolayer at 24 °C (a) and 36°C (d), and the phospholipon monolayer after penetration of TB501 (b) and TB502 (c) at 24 °C and of TB501 (e) and TB502 (f) at 36°C

Especially the image of TB502 penetrated film at 36°C (Figure 7f) exhibits important structural alteration with areas of higher density between the islands of considerable roughness.

Comparing the surface imaging results with that of penetration experiments we can conclude that the penetration of a dissolved drug candidate molecule into the lipid monolayer leads to a considerable visible disturbance of the monolayer structure. Depending on the molecular size and structure the interaction implies various mechanisms and hence causes different structural changes. Although the degree of penetration for TB501 and TB502 were similar the appearance of structural changing effect of TB502, which is a smaller molecule, is less observable on the lipid domains. It is rather concentrated to the region between the domains according to the AFM images of the complex LB films.

Conclusion

High performance *in silico* docking method is a cost-effective computational approach to find new promising inhibitors against a crucial enzyme of *Mycobacterium tuberculosis*. Lipid membrane affinity of various drug candidates were compared using monolayer model system. This behaviour is possibly related to nonspecific transport of bioactive species through the cell membrane and requires a certain amphiphilic character and appropriate steric properties of the drug candidate molecules as well.

Acknowledgements Dr. K. Hill is thanked for valuable consultation. The work was supported by Hungarian Research Found (OTKA 68120, OTKA 68358, OTKA 68285) and by the National Office for Research and Technology: BIOSPONA TeT-08-SG-STAR, NKFP 07 TB_INTER-HU, FP7-228490.

References

1. World Health Organization (2002) Report 2002
2. Chan S, Segelke B, Lekin T, Krupka H, Cho US, Kim M, So M, Kim CY, Naranjo CM, Rogers YC, Park MS, Waldo GS, Pashkov I, Cascio D, Perry JL, Sawaya MR (2004) J Mol Biol 341: 503
3. Barabás O, Pongrácz V, Kovári J, Wilmanns M, Vértessy BG (2004) J Biol Chem 279: 42907
4. Varga B, Migliardo F, Takacs E, Vértessy BG, Magazù S, Mondelli C (2008) J Chem Phys (2008) 345: 250
5. Ördög R, Grolmusz V (2008) Bioinform Res Appl 4983: 402
6. Maget-Dana R (1999) Biochem Biophys Acta 1462:109
7. Kiss É, Dravetzky K, Hill K, Kutnyánszky E, Varga A (2008) J Colloid Interf Sci 325: 337
8. Agasøsler A V, Tungodden LM, Čejka D, Bakstad E, Sydnes LK, Holmsen H (2001) Biochem Pharmac 61: 817
9. Jabłonowska E, Bilewicz R (2007) Thin Solid Films 515: 3962
10. Hill K, Pénzes CsB, Vértessy BG, Szabadka Z, Grolmusz V, Kiss É (2008) Progr Colloid Polym Sci 135: 87
11. Sula L (1963) Bull World Health Organ 29: 589
12. Sula L (1963) Bull World Health Organ 29: 607
13. Vinsova J, Cermakova K, Tomeckova A, Ceckova M, Jampilek J, Cermak P, Kunes J, Dolezal M, Staud F (2006) Bioorg Med Chem 14: 5850
14. Jensen KA (1932) Zentralb Bakteriol Parasitenkd Infektionskr Hyg Abt I Orig 125: 222
15. Löwenstein E (1931) Zentralb Bakteriol Parasitenkd Infektionskr Hyg Abt I Orig 120: 127
16. Hardy NJ, Richardson TH, Grunfeld F (2006) Colloid Surf A 202: 284
17. Marcelja S (1974) Biochim Biophys Acta 367: 165
18. T-H. Chou, C-H. Chang (2000) Colloids Surf A 17: 71

Progr Colloid Polym Sci (2011) 138:139–142
DOI: 10.1007/978-3-642-19038-4_24

Scattering from Dilute and Lamellar Phase Solutions of Aerosol-OT Simultaneous Probe of Surface Structures and Bulk

Maja S. Hellsing[1], Adrian R. Rennie[1], Lionel Porcar[2], and Carl-Johan Englund[1]

Abstract The benefits of simultaneous studies of adsorbed layers and bulk structures are shown for solutions of the surfactant Aerosol-OT. Above the critical micelle concentration, Aerosol-OT forms an aligned lamellar phase at the sapphire/solution interface which is in equilibrium with a bulk phase that consists of coexisting micellar solution and dispersed lamellar phase. Measurements of the aligned surface layers and the bulk scattering from a 2% wt solution by grazing incidence and small-angle neutron scattering show that the bulk consist of lamellar structures with the same *d*-spacing as seen at the surface but without the surface induced alignment. The surface lamellar structure corresponds to a 10% volume fraction for a 2% wt bulk which implies that there must be coexistence of regions of different concentration. Scattering patterns measured in grazing incidence geometry clearly show the relative contributions from small-angle scattering and specular reflectivity.

Keywords sodium bis 2-ethylhexyl sulfosuccinate • lamellar phase • scattering

Introduction

Neutron reflectivity (NR) and small-angle and grazing incidence neutron scattering (SANS and GiSANS) are efficient tools to study the surface and bulk structures and compositions of surfactant solutions. For systems where the structure at the surface may penetrate deep into the bulk, or where the system comprises of a dynamic equilibrium between surface and bulk, it is often useful to measure both NR and SANS or GiSANS in order to get a complete understanding of the whole system. To get reliable and comparable results with these complementary techniques, we have developed a cell that can be used for both on the same sample. We present data for the surfactant sodium bis 2-ethylhexyl sulfosuccinate, Aerosol-OT, at a sapphire (Al_2O_3) interface. The critical micellar concentration (cmc)[1] is about 0.11 wt%. Aerosol-OT adsorbs as a single dense bilayer[2] with a plateau of about 2.6 mg m^{-2} at concentrations between 0.1 and 0.3 wt%. Above 1.0 wt% this system readily forms lamellar structures at the interface and in the bulk.[3]

Experimental and Technique

Experiments were performed on D22 at the Institut Laue Langevin, France.[4] The novel sample cell is shown in Figure 1. For the experiment a Knauer HPLC pump was used for automatic sample injections. The volume of the cell is about 3 ml and has a sample injection inlet at the bottom, and an outlet diagonally opposite at the top. The thickness of the sample is about 2 mm, and it is held in place in between two crystals, one polished sapphire surface for reflection and one non-polished silica back surface. The neutron beam can enter the cell from the side in reflection. A wavelength of 6 Å was chosen and reflectivity and grazing incidence scattering measurements made at a range of incident angles up to 2.4 degrees. By rotating the cell by 90 degrees, the neutron beam can go through the cell from the front and is in SANS geometry to give information from the bulk of the sample. The temperature of the cell was controlled and set to 25°C.

M.S. Hellsing (✉)
[1]Department of Physics and Astronomy, Ångström Laboratory, Uppsala University, Box 516, 751 20, Uppsala, Sweden
[2]Institut Laue Langevin, Grenoble, France

[1] Li ZX, Lu JR, Thomas RK, Penfold J (1997) J Phys Chem B 101: 1615-1620
[2] Hellsing MS, Rennie AR, Hughes AV (2010) Langmuir 26: 14567-14573
[3] Hellsing MS, Rennie AR, Hughes AV (2011) Langmuir - in Press
[4] www.ill.fr/YellowBook/D22/

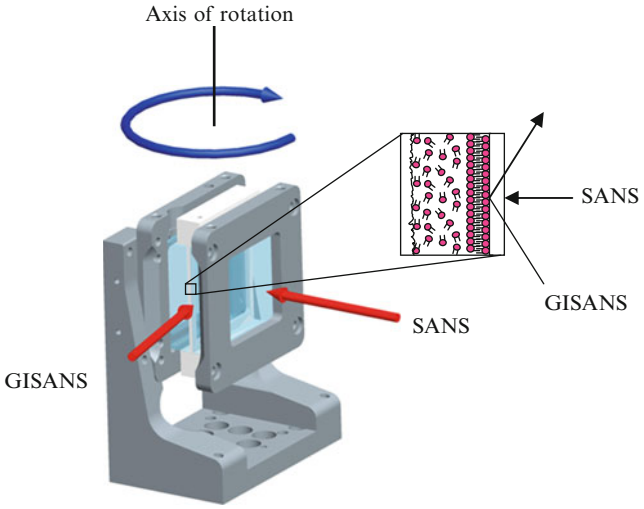

Figure 1 Schematic representation of the cell that can be used for neutron reflection, GiSANS and SANS measurements

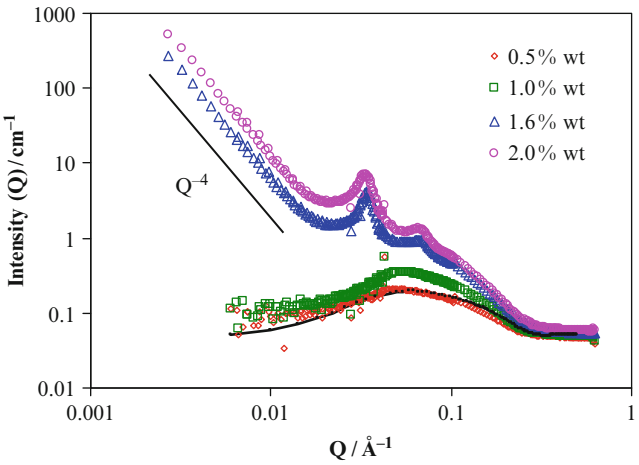

Figure 2 Small-angle neutron scattering from Aerosol-OT in D_2O at 25°C. The error bars are generally smaller than the data points and are not shown. The continuous line shows a fit to the 0.5% wt data

For comparison additional SANS measurements were made later in conventional fused silica cells.

Sodium bis 2-ethylhexyl sulfosuccinate (98% purity) was purchased from Sigma-Aldrich and purified by liquid-liquid extraction using the procedure of Li *et al.*[5] Pure water (18 MΩ cm) was obtained from a Millipore system and D_2O from EURISOTOP, CEA, Saclay and from Sigma-Aldrich. The (0001) sapphire surface used for reflection measurements was purchased from PiKem and cleaned with a 'dilute piranha' solution.[6] The other parts of the sample cell and connecting tubing were cleaned with Decon 90 followed by extensive rinsing with Millipore water.

Neutron reflection gives information of structures normal to the surface, SANS measures the structure in the bulk of the system and GiSANS scattering probes the near surface structures in the solution. Neutron scattering experiments gives information on molecular length scales, the theory described elsewhere, see for example Penfold and Thomas.[7] Briefly, in neutron reflection the momentum transfer, Q, normal to the reflecting surface is described by

$$Q = (4\pi/\lambda) \sin\ \theta$$

where λ is the incident neutron wavelength and θ is the angle of incidence. Systems that contain repeating structures give rise to Bragg diffraction peaks, where the position of the Bragg peak gives information about the interlayer spacing, d, by

$$d = 2\pi/Q_p$$

Results and Discussion

Conventional SANS measurements in fused silica cells of Aerosol-OT in D_2O shows that when the surfactant concentration is increased from 0.5 to 2.0% wt, which corresponds to 5 to 20 × cmc, the system changes from micellar to lamellar structures, as shown in Figure 2. This is in agreement with previous studies[8] on the phase behaviour of Aerosol-OT in H_2O. Model fits show that a solution of concentration 0.5% wt of Aerosol-OT forms micelles with a 27 Å diameter hydrophobic core and an interaction potential of about 50 mV, in agreement with what has been observed previously.[9] For concentrations above 1.2% wt a lamellar phase can be observed with Bragg scattering peaks from the repeating structures. The Q^{-4} slope at lower Q indicates that there are dispersions of large objects with sharp interfaces. A simple analysis of the Bragg peak positions for 2.0% wt Aerosol-OT shows the lamellar structure to have a d-spacing of 190 Å. The lower boundary between isotropic and lamellar structures of bulk Aerosol-OT has been reported previously[8,10,11]

[5] Li ZX, Lu JR, Thomas RK (1997) Langmuir 13: 3681-3685

[6] Turner SF (1998) PhD Thesis, Cambridge University, United Kingdom

[7] Penfold J, Thomas RK (1990) J Phys: Condens Matter 2: 1369-1412

[8] Rogers J, Winsor PA (1969) J Colloid Interf Sci 30: 247-256

[9] Sheu EY, Chen S-H, Huang JS, (1987) J Phys Chem 91: 3306-3310

[10] Fontell K (1973) J Colloid Interf Sci 44: 318-329

[11] Ekwall P, Mandell L, Fontell K (1970) J Colloid Interf Sci 33: 215-235

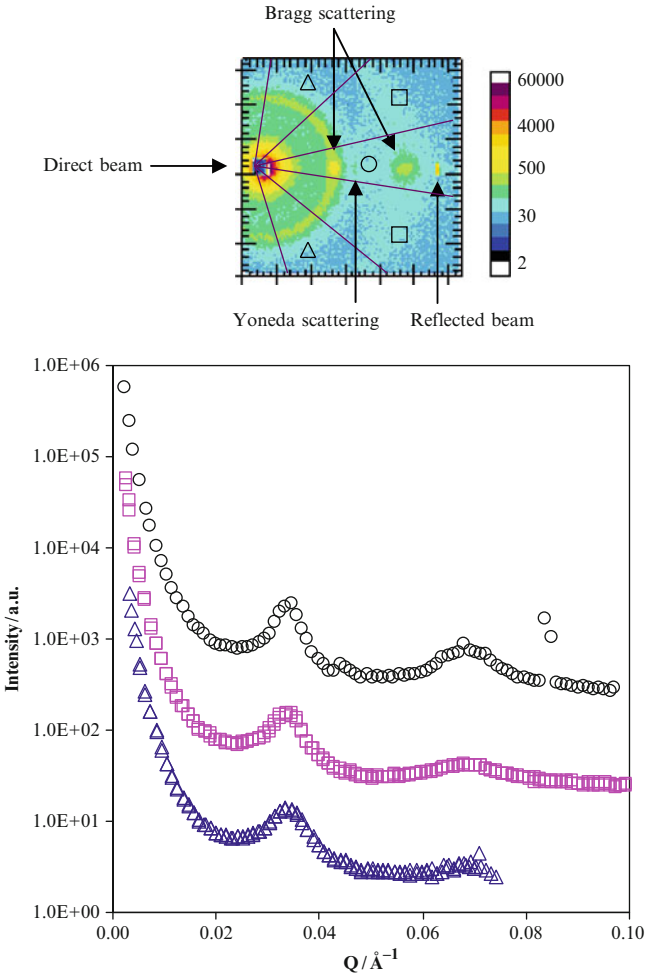

Figure 3 2D scattering pattern(a) from GiSANS geometry of 2.0% wt Aerosol-OT in D_2O at 25°C and a plot of intensity from the different sectors (b) with the symbols corresponding to the sectors marked in (a). The specular reflection is clearly visible as a sharp peak at 0.084 $Å^{-1}$ in the horizontal sector. This sector also shows the Yoneda scattering at 0.042 $Å^{-1}$. The peaks in grazing incidence scattering arising from lamellar order are seen in all sectors. Curves with symbols square and triangle are offset by factor 10

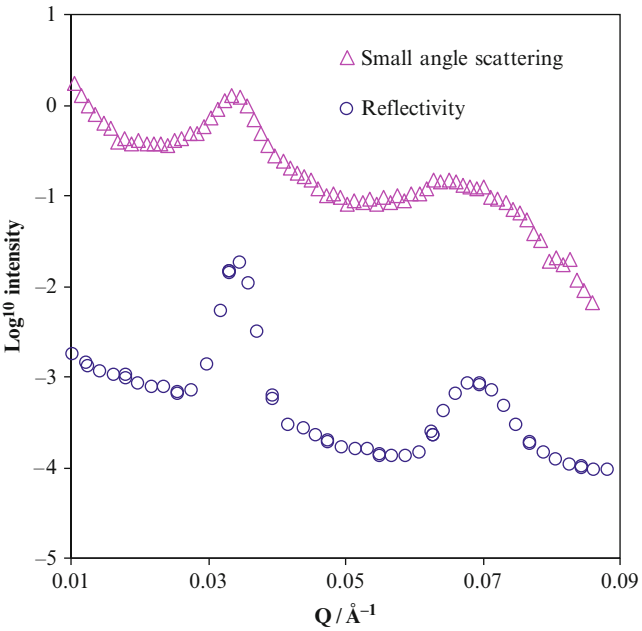

Figure 4 Neutron small-angle scattering for 2.0% wt Aerosol-OT in D_2O at 25°C and reflectivity extracted from GiSANS measurements for the sapphire/solution interface

to lie somewhere between 8–17% wt. Co-existence of micelles and dispersed lamellar phase requires model fits for surfactant lamellae[12] to be combined with that for micelles and must include the instrumental resolution.

In order to clarify in more detail the behaviour of 2.0% wt Aerosol-OT, complementary measurements in GiSANS geometry were made. Data were collected for angles of incidence between 0 and 2.4 degrees and the 2.4 degree measurement is shown in Figure 3. From these measurements one obtains the specular reflectivity from the interface by integrating the peak that is seen on the detector at a different position, corresponding to 2θ in each data set. There is further information about the relative contribution of surface and bulk scattering. In the image of intensity on the two-dimensional detector, the partly blocked direct beam is visible and two orders of Bragg scattering can be seen. However, due to the limited range of Q that can be measured at one detector position, the higher order Bragg scattering seen in other measurements[3] is not visible here. The very sharp specular reflection peak is clearly visible at Q=0.084 $Å^{-1}$. The integrated intensity of the specular peak determined for each measured angle gives the reflectivity curve that is shown in Figure 4. Again, from the peak positions in Q we can identify a lamellar structure with a d-spacing of 190 Å. Similar reflectivity data measured over a wider range in previous experiments[3] has indicated a bilayer thickness of about 33 Å. This structure would correspond to a 10% volume fraction of Aerosol-OT at the sapphire surface which is much higher than the bulk concentration of 2% wt. The scattering from the bulk of the sample shows diffraction peaks in similar positions implying coexistence of regions of high concentration with a lower concentration, micellar dispersion. The coexistence of phases for higher concentration solutions of Aerosol-OT has been reported.[13] The second peak in the SANS scattering curve in Figure 4 is broad and may include a significant contribution to the scattering from micelles. The similarity of the surface and bulk structures indicates that the main driving force for adsorption of Aerosol-OT is

[12] Nallet F, Laversanne R, Roux D (1993) J Phys II 3: 487-502

[13] Hamilton WA, Porcar L, (2010) J. Phys.: Conf. Ser. 251: 012034

self-assembly dominated by hydrophobic interactions rather than a surface effect as previously suggested by comparison of various chemically different substrates.[2,14]

The shape of the background is visible in the 2D scattering pattern and this is important in order to subtract the correct level of background in reflection measurements.[3] In the GiSANS measurements, it is possible to see enhanced scattering near the 'horizon', known as a Yoneda peak[15] which arises from roughness. This was not visible in measurements of the bare sapphire/H_2O interface and can thus be attributed to fluctuations and density variations in the adsorbed surfactant layers. The SANS curve in Figure 4 differ slightly from those in Figure 2 and this may arise from the slightly different thermal history of the sample in Figure 4. This emphasises the advantage of simultaneous measurements.

Conclusions

At concentrations above the cmc Aerosol-OT forms spherical micelles with a hydrophobic core of 27 Å diameter in the bulk. By increasing the concentration to above 1.2 %wt Aerosol-OT forms a lamellar system with a *d*-spacing of 190 Å. The position of Bragg peaks seen in surface reflection and bulk measurements is the same, implying the lamellar spacing is constant throughout the system. However, the bulk solution lacks the alignment found at the surface. For a 2.0 %wt bulk solution, the concentration found at the surface is higher by a factor of five. This in turn indicates that the bulk of the system must contain regions with very little material, a biphasic lamellar system.

In order to obtain comparable data from such complex systems we have developed a cell with the ability of use for measurements both in reflection and small-angle neutron scattering geometry. This cell allows studies of adsorbed surface layers and the equilibrium bulk structures for one sample in the same experiment by simple rotation of the cell. This is a particular advantage when studying surfactants above the cmc or liquid crystals which may show one type of order at a surface and another in the bulk.

Scattering patterns from measurements of 2.0 %wt Aerosol-OT in GiSANS geometry give information about the relative contributions from specular reflection, small angle bulk scattering, near surface fluctuations and background scattering. This information is useful for an overall understanding of the system, as well as in obtaining detailed information of the molecular structure at different co-existing regions.

Acknowledgements We are grateful to the Institut Laue Langevin for allocation of beam time for these measurements.

[14] Li ZX, Lu JR, Fragneto G, Thomas RK, Binks BP, Fletcher PDI, Penfold J (1998) Coll Surf A 135: 277-281

[15] Yoneda Y (1963) Phys Rev 131: 2010-2013

Progr Colloid Polym Sci (2011) 138:143–146
DOI: 10.1007/978-3-642-19038-4_25

The Effect of Chemical Modification on Mechanical Properties of Carbon Black Filled Elastomer

Tomasz Pingot, Martyna Pingot, and Marian Zaborski

Abstract The aim of the work was to modify the acrylonitrile-butadiene rubber (NBR) in order to improve mechanical properties by enhancing filler-polymer interactions. Following compounds were used as the coupling agents: 2-isopropenyl-2-oxazoline (OKS), 1-allyl-3-methylimidazolium chloride (AMC), 1-vinyl-2-pyrrolidinone (NWP). Two types of carbon black were used as a reinforcing filler: pigment black FW200 and FEF N550. The fillers were characterized by dibutylphtalate (DBP) absorption analysis, aggregates size, rheological properties of filler suspensions and zeta potential analysis. The compounding was carried out in a laboratory rolling mill. Samples were prepared through the vulcanization process at 160°C. The vulcanization kinetics of rubber compounds, crosslink density and mechanical properties of vulcanizates were also measured.

Keywords elastomer • carbon black • grafting • coupling agent • filler

Introduction

Elastomers are presently used in wide areas of application, such as wires, cables and automobiles, due to their light weight, hydrophobicity, easy maintenance and processing. This materials have been usually applied in the filled state because of fillers reinforcing effect [1]. Fillers are inorganic or organic powders with a considerable granularity. They exhibit high tendency to mix and uniformly disperse in plasticized rubber. Fillers can be divided into three groups depending on their influence on mechanical properties of polymers: active fillers (reinforcing effect), semi active (semi-reinforcing effect) and inactive (non reinforcing effect). The mechanism of reinforcing is to a large extent associated with the chemical and physical interactions between the polymer matrix and a filler. The reinforcing effect of a filler depends on its characteristics such as: size and shape of the particles, specific surface area, surface activity, hydrodynamic effect and on the strength of polymer-filler interactions. Typical example of an active filler is carbon black. It is the most commonly used active filler in elastomer technology. There are several chemical groups on the surface of filler particles. The most common groups on the carbon black surface are: carboxyl, hydroquinone, quinine, and lactone groups [2,3]. One of the methods to enhance reinforcement of the filler is the improvement of polymer-filler interactions. In the past, the nitrosoaniline derivatives were used as coupling agents but due to their cancerogenic effect they were withdrawn from usage [4].

In our work we used new modifiers in order to improve polymer-filler interactions. The modification process was carried out in Brabender mixer. During this process the coupling agent was grafted on the polymer macromolecule and then the reaction with chemical groups on the carbon black surface took place [5].

Experimental Section

Materials

The object of our study was acrylonitrile-butadiene rubber PERBUNAN 2845 F (LANXESS), acrylonitrile content: 28%. Two types of carbon black were used: Colour Black FW 200 (Evonik Degussa GMbH) and FEF N550 (Evonik Degussa GMbH). The elastomer was crosslinked by sulphur vulcanization system. The following compounds were used as accelerators: mercaptobenzothiazole (MBT) and

T. Pingot (✉)
Institute of Polymer and Dye Technology, Technical University of Lodz, Stefanowskiego 12/16, 90-924, Lodz, Poland
e-mail: tomasz.pingot@gmail.com

N-cyclohexyl-2-benzothiazole sulfenamide (CBS), (Chemical Plants Organika). To improve filler dispersion the following dispersing agents were used: nonylphenyl poly(ethylene glycol)ether (NF-PEG), (Chemical Plants Rokita S.A.); triethanolamine (TEA), (Chempur). In order to improve polymer-filler interactions several compounds were used as coupling agents: 2-isopropenyl-2-oxazoline (OKS), (Sigma-Aldrich); 1-vinyl-2-pyrrolidinone (NWP), (Sigma-Aldrich); 1-allyl-3-methylimidazolium chloride (AMC) (Sigma-Aldrich). Rubber compounds with the following composition were prepared (parts by wt.): acrylonitrile-butadiene rubber 100 phr, filler 30 phr, dispersing agent 3 phr, coupling agent 5 phr.

Preparation and Testing of Elastomeric Composites

Rubber compounds were prepared by the common manufacturing method using laboratory rolling mill with roll dimensions: D = 150 mm, L = 300 mm. The temperature of rolls was 27 - 37°C. The vulcanization kinetics of rubber blends were determined according to standard PN-ISO 3417:1994 by the use of a "Monsanto" vulcameter made by ZACH METALCHEM, at constant temperature of 160°C. The rubber blends were vulcanized in steal moulds placed between electrically heated shelves of a hydraulic press. The vulcanization temperature was 160°C. The vulcanization time was determined from vulcanization kinetics study. Crosslinking density of vulcanizates was calculated based on the rapid solvent-swelling measurements in toluene from the Flory-Rehner equation. Tensile strength was determined in accordance with standard PN-ISO 37:1998, using w-3 dumbbell samples. Tear resistance was measured in accordance with PN-ISO 34–1, using rectangular shapes. These tests were performed using a universal "Zwick" tester, model 1435, connected to a computer with appropriate software. Particle size was measured in paraffin oil using Zetasizernano S90 (Malvern Instruments) analyzer. Zeta potential of filler dispersion in water was studied by the means of Zetasizer 2000 (Malvern Instruments) apparatus. Rheological properties of filler suspensions in paraffin oil were determined by viscometer RM500 (Rheometric Scientific). Dibutylphtalate (DBP) absorption was measured by means of an Absorptometer "C" (Brabender). The modification process was carried out in Brabender Measuring Mixer N50 at following parameters: temperature: 125°C; rotor speed: 40 RPM; duration: 0,5 h.

Results and Discussion

Filler's Characteristics

From Fig. 1 it follows that both FW200 and FEF N550 carbon blacks revealed a high tendency to agglomerate in paraffin oil (a model of elastomer matrix). The addition of dispersing agents reduced this effect considerably.

The analysis of rheological properties (Fig. 2) of filler suspensions in paraffin oil showed that the carbon black FW200 revealed stronger tendency to create a structure in elastomer matrix than N550 carbon black (the higher values of φ in Table 1). High viscosity of suspension at γ=120 s^{-1} was due to the high hydrodynamic effect caused by the branched structure of carbon black FW200 (Table 1).

High dibutyl phtalate absorption of FW200 showed that this carbon black had a large amount of free spaces between the aggregates (Table 2). Macromolecules of elastomers can be trapped in this pores or voids of the aggregates which increases the reinforcing effect of the filler.

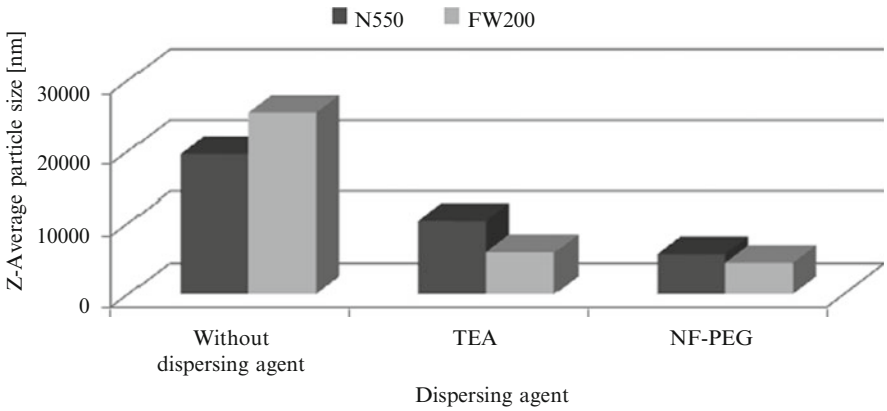

Fig. 1 Filler's agglomerates size in paraffin oil

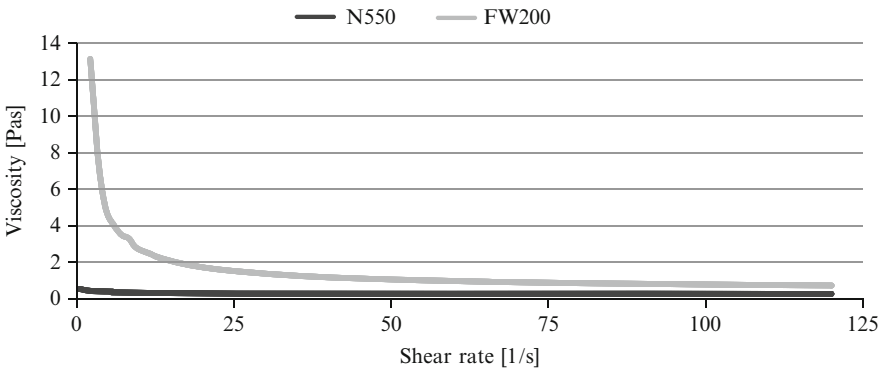

Fig. 2 Apparent viscosity of filler suspensions in paraffin oil

Table 1 Volume fraction of carbon black agglomerates (φ) and the viscosity of suspension (η) at γ=120 s^{-1}

Filler	φ_0 *[% v/v]*	φ *[% v/v]*	η *[mPas]*
N550	2.85	12.00	273
FW200	2.85	28.79	730

φ-volume fraction of carbon black agglomerates
η-the viscosity of suspension at γ=120 s^{-1}
φ_0-volume fraction of carbon black in suspension

Table 2 Dibutylphtalate absorption analysis

Filler	*DBP absorption [ml/100g]*
N550	109.2
FW200	172.6

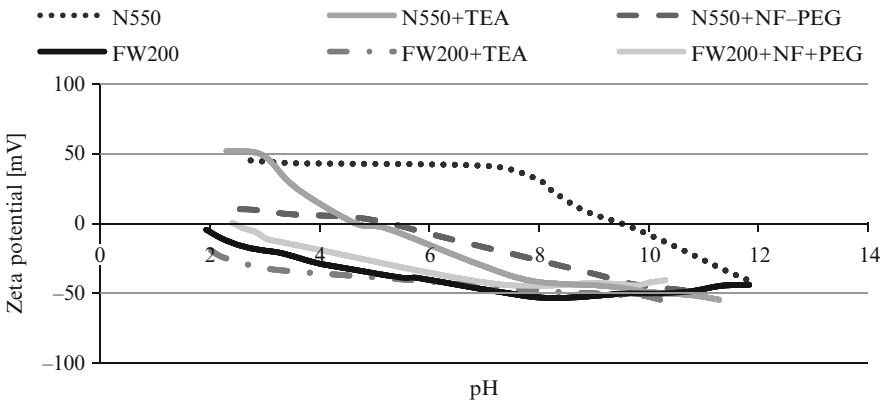

Fig. 3 The zeta potential curves of fillers dispersed in water

The surface of FW200 carbon black exhibited an electron acceptor (acidic) characteristics. On the other hand, the N550 showed electron donor (basic) character which was reflected by the zeta potential analysis. The addition of dispersing agents changed the character of filler's surface as shown in Figure 3.

Characteristics of Vulcanizates

The crosslink density of the majority of samples was within the range of 6,61-7,32 [mol/cm^3]*10^{-4}. The vulcanizates with the addition of coupling agent: 1-allyl-3-methylimidazolium chloride exhibited much lower crosslink density (Fig. 4).

The addition of modifiers influenced to a high extent the mechanical properties of vulcanizates. Samples with N550 carbon black revealed the highest tensile strength with the addition of 2-isopropenyl-2-oxazoline or 1-vinyl-2-pyrrolidinone. On the other hand, the highest tensile strength of vulcanizates filled with FW200 was achieved by addition of 1-vinyl-2-pyrrolidinone to samples with TEA and by addition of 1-vinyl-2-pyrrolidinone or 1-allyl-3-methylimidazolium chloride mixed with NF-PEG dispersing agent (Fig. 5). Tear resistance was also improved by the presence of coupling agents. In the case of vulcanizates filled with N550, the best results exhibited vulcanizates with 1-allyl-3-methylimidazolium chloride. Samples filled with FW200 carbon black revealed the highest tear resistance for following modifiers: 1-vinyl-2-pyrrolidinone or 1-allyl-3-methylimidazolium chloride. Addition of 2-isopropenyl-2-oxazoline did not improve this parameter (Fig. 6).

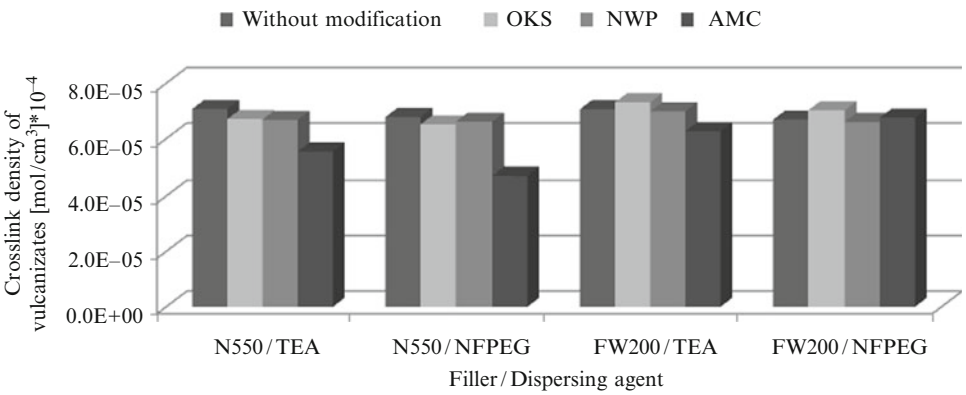

Fig. 4 Crosslink density of vulcanizates

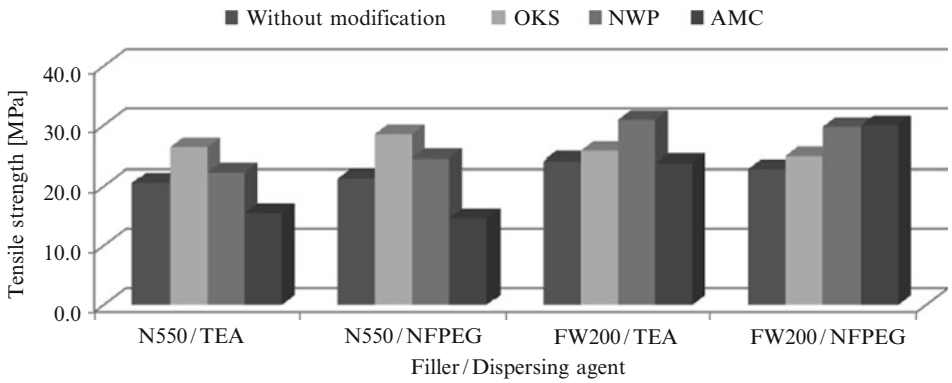

Fig. 5 Tensile strength of vulcanizates

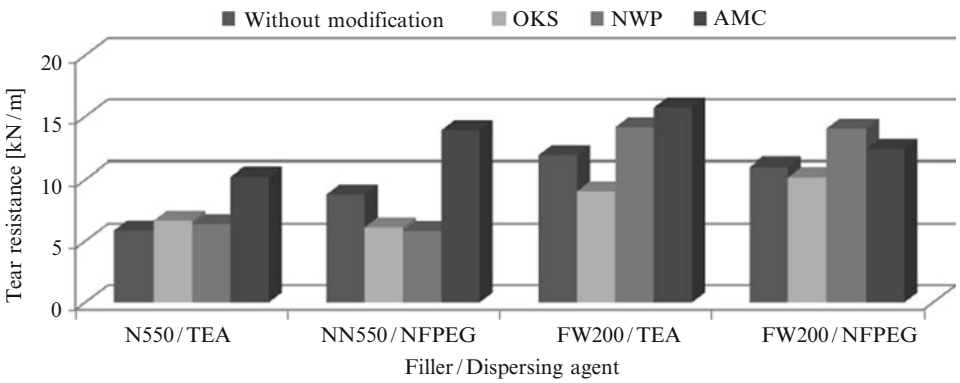

Fig. 6 Tear resistance of vulcanizates

Conclusions

The investigation showed that carbon black FW200 had a higher tendency to form a three dimensional network in elastomer matrix than N550 carbon black. Both N550 and FW200 had a high tendency to agglomerate in paraffin oil. The addition of dispersing agents reduced this effect considerably. In most cases the modification process improved the tensile strength and tear resistance of vulcanizates.

References

[1] Li ZH, Zhang J, Chen SJ (2008) Express Polymer Letters 10:695
[2] Frohlich J, Niedermeier W (2005) Composites:Part A 36: 449
[3] Kohls DJ, Beaucage G (2002) Current Opinion Solid State Mater Sci 6: 183
[4] Gonzales L, Rodriguez A, De Benito L (1996) Rub Chem and Tech 69: 266
[5] Pigłowski J, Gancarz I, Wlaźlak M (2000) Polymer 41: 3671

Progr Colloid Polym Sci (2011) 138:147–150
DOI: 10.1007/978-3-642-19038-4_26

Nanostructured Metal Oxide and Unsaturated Acid as a New Co-agent in Peroxide Cross-Linking of Hydrogenated Butadiene-Acrylonitrile Rubber

Martyna Pingot, Tomasz Pingot, and Marian Zaborski

Abstract Blends of hydrogenated butadiene-acrylonitrile rubber (HNBR) with nanostructured metal oxides: magnesium oxide (MgO), calcium oxide (CaO), zinc oxide (ZnO) and unsaturated acids: monoallyl maleate (MM) or acrylic acid (AA), as co-agents, were prepared. Dicumyl peroxide (DCP) was used as a vulcanizing agent. The rheometrical properties of rubber mixes and cross-link density of vulcanizates were measured. Mechanical properties of the samples were investigated. Agglomeration degree of metal oxides in the elastomer matrix was also studied by SEM images. It was found that the addition of new co-agents improves the cross-link density and tensile strength of elastomer composites. The obtained elastomer networks consist of covalent bonds and ionic bonds. To conclude, we discovered new type of elastomeric material, cured with high efficiency by dicumyl peroxide and revealing good mechanical properties.

Keywords peroxides • co-agents • cross-linking • rubber compounds • properties of vulcanizates

Introduction

Peroxides are probably the most common materials used instead of sulfur for rubber vulcanization, because of their ability to cross-link a variety of unsaturated and saturated elastomers and also their ability to produce thermally stable carbon-carbon cross-links. There are also some disadvantages of peroxide cross-linking. The most important are the poor mechanical properties of vulcanizates and low cross-link efficiency [1,2]. The use of co-agents coupled with peroxides to cure elastomers has been a common practice in the rubber industry for many years. Co-agents are typically multifunctional monomers that are highly reactive in the presence of free radicals and readily graft onto elastomer chains to form a complex cross-link [3,4].

In this work new type of co-agents for hydrogenated butadiene-acrylonitrile rubber (Therban A3407), cured by dicumyl peroxide (DCP), are presented.

M. Pingot (✉)
Institute of Polymer and Dye Technology, Technical University of Lodz, Stefanowskiego12/16, 90-924, Lodz, Poland
e-mail: martyna.pingot@gmail.com

Experimental Section

Materials

Hydrogenated acrylonitrile-butadiene rubber (HNBR)-Therban 3407, containing 34 % of acrylonitrile units; and residual double bonds max 0.9 %, Mooney viscosity 70; was purchased from Lanxess. Dicumyl peroxide obtained from Aldrich was used as cross-linker. Co-agents consisted of: nanostructured metal oxides: magnesium, zinc or calcium oxide provided by Aldrich and unsaturated acids: acrylic acid (Aldrich) or monoallyl maleate (synthesized by Department of Organic Chemistry- Technical University of Lodz). The composition of a typical elastomer blend was: HNBR-100 phr, DCP- 3 phr, metal oxide- 3 phr, unsaturated acid-1 phr.

Preparation and Testing of Elastomeric Composites

Particle size in water and paraffin oil were measured with Zetasizernano S90 (Malvern Instruments). Cure characteristics were measured at 160°C using a Monsanto rheometer. The rubber mixes were prepared on a laboratory two-roll mill at about 30°C, with roll dimensions of D = 200 mm and L = 450 mm. The rotational speed of a front roll (Vp) was $2s^{-1}$

with a friction coefficient f = 1.1, total time of mixing was 10 minutes. The duration of rubber plasticizing was 4 minutes. After this period, the other components were added. The process of vulcanization was carried out using a hydraulic press with electrical heating. The samples were vulcanized at 160^0C for 30 minutes. The plates obtained had a thickness of about 1 mm. Cross-link density of vulcanizates was determined on the basis of solvent-swelling measurements and calculated using the Flory-Rehner equation.

The mechanical properties were measured in accordance with ISO 37. The tensile tests were carried out using a Zwick 1435 Universal Testing Maschine with the cross-head 500 mm/min. The samples had the standard dumbbell shape. The microstructure of the vulcanizates surface was observed by scanning electron microscopy (SEM) LEO 1530 Zeiss. The samples of cured sheets were fixed on the sample holder, then gold-coated and secondary electron images were recorded.

Results and Discussion

Metal oxides exhibit different tendency toward agglomeration in water and paraffin oil (model of elastomer matrix). This is reflected in the aggregates size, as shown in Table 1. The highest tendency to agglomeration in water, as well as in paraffin oil, shows calcium oxide and the lowest, magnesium oxide.

Based on data in Table 2 it is evident that co-agents have an influence on the increment of torque in rubber compound during vulcanization. It was observed that dG increased from 58.3 dNm to 75.1 dNm for the rubber compound containing acrylic acid and calcium oxide as co-agent. The application of the new co-agents leads to a reduction of optimal vulcanization time in comparison with the sample containing monoallyl maleate and calcium oxide. There was no significant changes in the vulcanization rate constant. However, it slightly increased for the systems with co-agent.

The apparent structural parameters of the three-dimensional networks are presented in Table 3. Cross-link density analysis showed that vulcanizates contained both ionic bonds and covalent bonds. As we expected, addition of co-agents led to an increase of cross-link density (v_T) of vulcanizates. The highest value was obtained for the sample containing acrylic acid and zinc oxide ($7.55 \cdot 10^{-5}$ mol/cm^3) in contrary to the sample without co-agents ($4.77 \cdot 10^{-5}$ mol/cm^3). Thus, also the cross-link efficiency increased. It was found that non-covalent bonds are formed in the network structure and then break under the influence of ammonia vapours. It reveals in a decrease of cross-link density measured on the basis of equilibrium swelling in toluene and ammonia vapours (v_{T+A}).

As it can be seen from Figure 1, the addition of new co-agents to the rubber compund resulted in improvement of tensile strength of vulcanizates. The tensile strength of vulcanizate containing magnesium oxide and monoallyl maleate increased almost threefold in comparison with the system without co-agents.

To correlate the mechanical properties of vulcanizates with their morphology, the composites were investigated by SEM. The dispersion of metal oxides CaO, ZnO, and MgO in the elastomer matrix is shown in Figures 2;3; and 4, respectively. As can be seen, metal oxides have a strong tendency to agglomeration, which imparts significant reinforcing effect towards the vulcanizate.

Table 1 The characteristic of metal oxides

Type of metal oxide	Aggregates size in water [nm]	Aggregates size in paraffin oil [nm]
MgO	223	4478
ZnO	267	5298
CaO	488	7114

Table 2 Cure characteristic of HNBR compounds containing 3 phr of metal oxide and 1 phr of unsaturated acid

Rubber compound	dG [dNm]	t_{90} [min]	$k \cdot 10^{-3}$ [s^{-1}]
HNBR/DCP	*58.3*	*23*	*0.77*
HNBR/DCP/CaO/MM	65.1	28	1.06
HNBR/DCP/CaO/AA	75.1	22	0.96
HNBR/DCP/MgO/MM	64.3	21	1.27
HNBR/DCP/MgO/AA	74.5	17	1.24
HNBR/DCP/ZnO/MM	67.2	22	0.96
HNBR/DCP/ZnO/AA	71	19	1.20

dG- the increment of torque in rubber compound during vulcanization
t_{90}- optimal vulcanization time
k- constant of the vulcanization rate

Table 3 Cross-link density of HNBR vulcanizates containing 3 phr of metal oxide and 1 phr of unsaturated acid

Vulcanizate	$v_T \cdot 10^{-5}$ [mol/cm^3]	$v_{T+A} \cdot 10^{-5}$ [mol/cm^3]	$\Delta v/v_T$ [%]	E
HNBR/DCP	*4.77*	*4.77*	-	*0.43*
HNBR/DCP/CaO/MM	6.71	5.8	13.6	0.6
HNBR/DCP/CaO/AA	7.49	6.67	10.9	0.67
HNBR/DCP/MgO/MM	7.05	4.61	34.6	0.57
HNBR/DCP/MgO/AA	7.2	6.04	16.1	0.65
HNBR/DCP/ZnO/MM	6.46	5.6	13.3	0.58
HNBR/DCP/ZnO/AA	7.55	6.09	19.3	0.68

v_T- cross-link density measured on the basis of equilibrium swelling in toluene
v_{T+A}- cross-link density measured on the basis of equilibrium swelling in toluene and ammonia vapours
$\Delta v/v_T$- non-covalent bonds content
E- cross-link efficiency

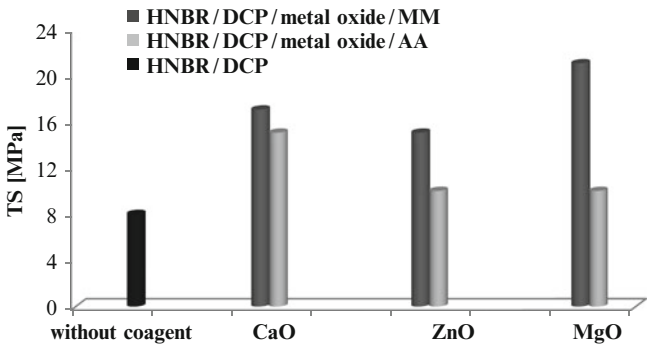

Fig. 1 Tensile strength (TS) of dicumyl peroxide (DCP) cured HNBR vulcanizates containing 3 phr of metal oxide and 1 phr of unsaturated acids: monoallyl maleate (MM) and acrylic acid (AA)

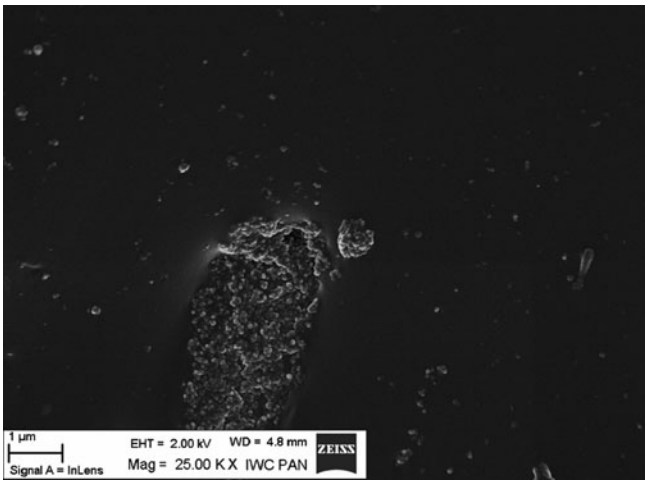

Fig. 2 SEM image of HNBR vulcanizate containing coagent: CaO/MM

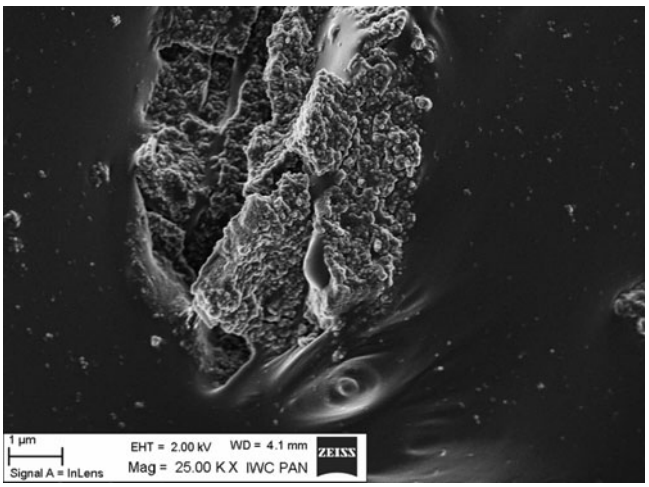

Fig. 3 SEM image of HNBR vulcanizate containing coagent: ZnO/MM

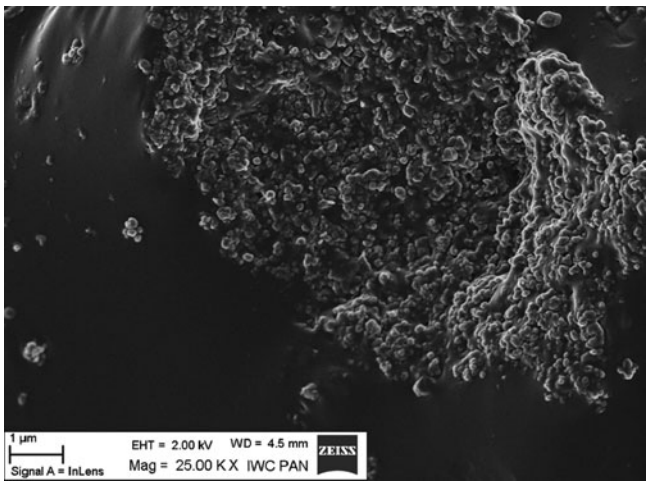

Fig. 4 SEM image of HNBR vulcanizate containing coagent: MgO/AA

Conclusion

The new co-agents revealed high tendency to agglomeration in elastomer matrix what had a beneficial effect on vulcanizates mechanical properties. Application of unsaturated acids and metal oxides as the new co-agents in peroxide vulcanization of HNBR caused mostly a decrease of vulcanization time, considerable improvement of vulcanizates mechanical properties, as well as the increase of cross-link efficiency. Thus, they may be used successfully in rubber technology.

References

1. Grima Alvarez M. M, Talma A. G, Datta R. N, Noordermeer J. W. M (2006) Rubber Chem. Technol. 79:694
2. Zaborski M, Skurska M, Przybyszewska M, Pingot T, Zawadiak J, Orlińska B, Gillner D (2010) Polimery 55:293
3. De Risi F. R, Noordermeer J. W. M (2007) Rubber Chem. Technol. 80:83
4. Dluzneski P.R (2001) Rubber Chem. Technol. 74:451

Progr Colloid Polym Sci (2011) 138:151–154
DOI: 10.1007/978-3-642-19038-4_27

Effect of Ionic Liquids on the Mechanical Properties of Methylvinylsilicone Rubber

Anna Strąkowska and Marian Zaborski

Abstract The influence of hydrophobic ionic liquids on cross-link density, mechanical properties, hysteresis and relaxation rates of the methylvinylsilicone rubber vulcanizates were investigated. Imidazolium salts with bromide, chloride and hexafluorophosphate groups were applied, resulting in shortening of the rubber vulcanization time, as well as decrease of the torque increment during cross-linking. Their presence reduced crosslinks decomposing under the influence of ammonia vapour. The most significant changes of methylvinylsilicone rubber properties were observed in a case of ionic liquid with 1-methyl-3-octylimidazolium cation and hexafluorophosphate anion.

Keywords silicone rubber • ionic liquids • mechanical properties • reinforcement

Introduction

Methylvinylsilicone rubber is an inorganic synthetic elastomer which demonstrates unique properties making it a very attractive material for numerous applications. Generally it is non-reactive, stable, and resistant to extreme environment conditions and temperatures (−55°C to +300°C), while still maintaining its useful properties [1-3]. Unfortunately, due to very poor intermolecular interactions silicon networks are week and its composites show much worse mechanical properties than other synthetic rubbers. Therefore, it is necessary to incorporate reinforcing fillers into the silicone matrix. Fumed silicas are commonly used fillers for silicone rubber. Their reinforcing effect is the effect of hydrogen bonding between silanol groups on silica surface and oxygen atoms in polysiloxane chains [4-6]. Recently, it has been shown that ionic liquids can interact with silanol groups on silica surface as well as with silicone rubber leading to the increase of polymer – filler interactions and improvement of filler dispersion [7].

A. Strąkowska (✉)
Institute of Polymer and Dye Technology, Technical University of Lodz, Stefanowskiego 12/16, 90-924, Lodz, Poland
e-mail: anna.k.strakowska@gmail.com

Materials

The object of this study was methylvinylsilicone rubber, "POLIMER MV 0.07", containing 0.07 % of vinyl groups (Chemical Plant "Silikony Polskie", Nowa Sarzyna). The rubber was cross-linked with dicumyl peroxide (DCP, Aldrich), deposited on chalk carrier. The filler was fumed silica, "Aerosil 380", (Degussa, Germany). 1-methyl-3-octylimidazolium (1-m-3-oim) salts with bromide, chloride and hexafluorophosphate (HFF) groups were applied as ionic liquids. The composition of blends was as follows (parts by wt.): POLIMER MV 0,07 – 100 phr, DCP – 2 phr, Aerosil 380 – 30 phr, Ionic Liquid – 3 phr.

Methods

Methylvinylsilicone composites, containing ionic liquids, were prepared by the common manufacturing procedures of rubber. Firstly, fumed silica was mixed with the rubber using two – roll mill at 30 °C. Secondly, injection and stirring of ionic liquids into the elastomer composites were performed in Brabender measuring mixer N50 (temp. 50 °C, speed range 40 min^{-1}, time of the process 10 min.) Finally two – roll mill was used again to mix the blend with the cross-linking agent (dicumyl peroxide). The vulcanization kinetics of rubber blends were determined using an oscillating disk rheometer produced by Zach Metalchem, at a constant temperature of 160°C. Then the rubber blends were vulcanized in a steal mould placed between electrically

heated shelves of a hydraulic press. The vulcanization temperature and time were 160°C and 30 min., respectively.

The crosslinking density of vulcanizates was determined by equilibrium swelling in toluene and toluene under ammonia vapours, based on the Flory-Rehner equation. The parameter of rubber-toluene interaction at a temperature of 20°C was μ = 0.45 [8].

Tensile strength was determined according to ISO-37 with a universal machine Zwick 1435. This testing machine was also used to test the hysteresis and relaxations properties of vulcanizates. Based on the results obtained from the measurement of the hysteresis, Mullins' effect was also calculated.

Results and Discussion

In order to assess the effect of ionic liquids on the cross-linking process, the kinetics of elastomeric blend vulcanization was examined. The obtained results are shown in Figure 1.

It appeared that ionic liquids caused the reduction of the minimal torque, indicating a reduction in viscosity at high temperature. This phenomenon could improve filler dispersion in elastomer matrix as well as facilitate the processing of blends. Additionally, ionic liquids reduced vulcanization time of rubber compounds compared to the conventional blend.

The ionic liquids affected the cross-link density of vulcanizates, as shown in Table 1. The vulcanizate containing HFF 1-m-3-oim had a lower degree of crosslinking than vulcanizate filled with fumed silica, what was also confirmed by the results of rheometric measurements. Moreover, a decrease in the concentration of non-covalent crosslinks was also observed in the blends containing ionic liquids.

The use of ionic liquids clearly affects the mechanical properties of the vulcanizates (Figure 2 and 3). The blends containing ionic liquids were demonstrated higher tensile strength and a higher elongation at break than those containing only pyrogenic silica. The vulcanizate containing HFF 1-m-3-

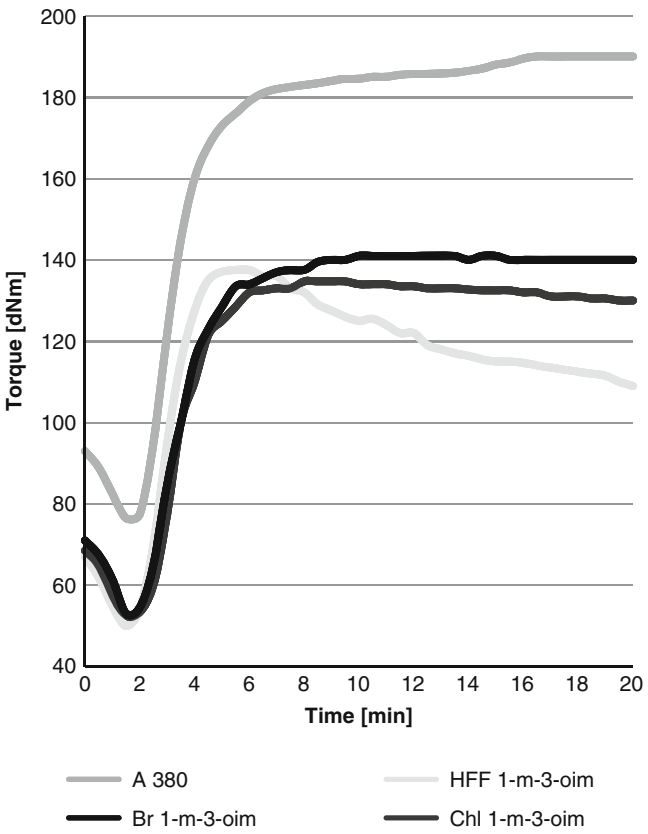

Fig. 1 The rheometric curves of silicone rubber blends containing the ionic liquids

Table 1 Cross-link density of silicone rubber vulcanizates containing ionic liquids

	Toluene		Toluene+Ammonia		$\Delta\nu/\nu$ [%]
	Q_w [mol/dm^3]	$\nu_e 10^{-5}$ [mol/dm^3]	Q_w [mol/dm^3]	$\nu_e 10^{-5}$ [mol/dm^3]	
A 380	2.04	21.93	3.85	6.10	72
HFF 1-m-3-oim	2.30	17.20	2.53	14.27	17
Br 1-m-3-oim	2.00	22.70	3.27	8.50	63
Cl 1-m-3-oim	2.07	21.22	3.52	7.29	66

(v– crosslink density, Q_w – equilibrium swelling, Δv – the amount of non-covalent crosslinks decomposing under the influence of ammonia vapour)

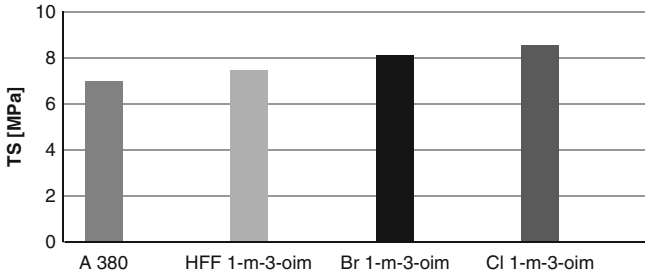

Fig. 2 The effect of ionic liquids on the tensile strength (TS) of methylvinylsilicone vulcanizates

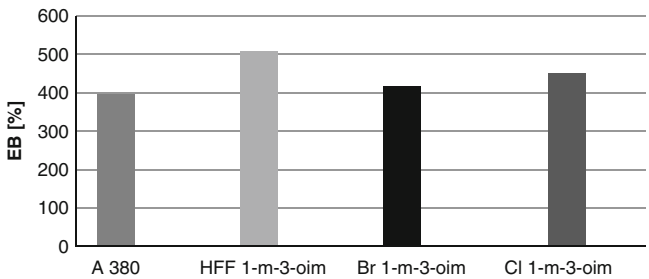

Fig. 3 The effect of ionic liquids on the elongation at break (EB) of methylvinylsilicone vulcanizates

oim revealed the highest elastic properties, as confirmed by the value of elongation at break, resulting from the lowest crosslink density.

In order to establish damping properties, the hysteresis of vulcanizates and Mullins' effect were determined (Table 2, Figure 4). The addition of ionic liquids to the blend affected the changes in hysteresis in comparison with the reference vulcanizate. Mullins' effect also changed. Higher influence was observed for 1-methyl-3-octylimidazolium hexafluorophosphate, then by other ionic liquids, as its addition coused a decrease in the work required for the first stretching of the sample, for which the amount of heat emitted due to strains increased. Therefore one can conclude that the use of HFF 1-m-3-oim considerably contributes to increasing the rubber-filler and/or filler-filler interactions. Therefore, damping properties of the vulcanizate were improved. This was also confirmed by the high values of Mullins' effect, showing high amounts of aggregates which broke down under stress.

Table 2 Hysteresis of the silicone rubber vulcanizates containing the ionic liquids

	W_1 [Nmm]	ΔW_1 [Nmm]	$\Delta W_1 / W_1$ [%]	W_5 [Nmm]	ΔW_5 [Nmm]	$\Delta W_5 / W_5$ [%]
A 380	146.7	92.6	63	67.6	17.8	26
HFF 1-m-3-oim	129.8	124.5	96	20.3	17.3	85
Br 1-m-3-oim	186.2	106.8	57	97.9	24.3	25
Cl 1-m-3-oim	131.8	91.6	69	56.8	22.6	40

(W_1, W_5 – work needed to stretch samples for the first and fifth time; ΔW_1, ΔW_5 – hysteresis of the first and fifth stretching cycle; E_M - Mullins' effect [%] – defined as: $E_M = (W_1 - W_5 / W_1) * 100\%$)

Figure 5 illustrates the stress relaxation of methylvinylsilicone vulcanizates containing ionic liquids. Addition of ionic liquids to the rubber caused the lower stress during the relaxation process. However, those stresses decreased more significantly for ionic liquids containing samples, which was reflected by relaxations rates (Table 3). The

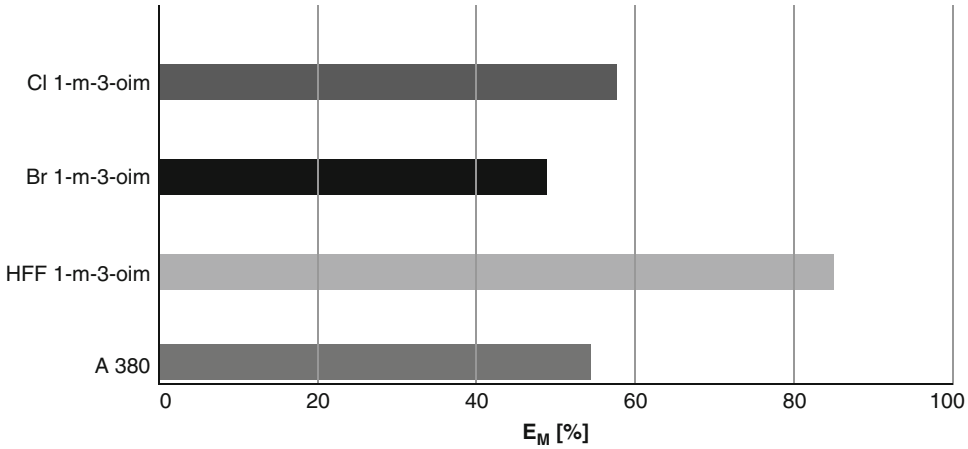

Fig. 4 Mullins' effect (E_M) of the methylvinylsilicone rubber vulcanizates containing the ionic liquids

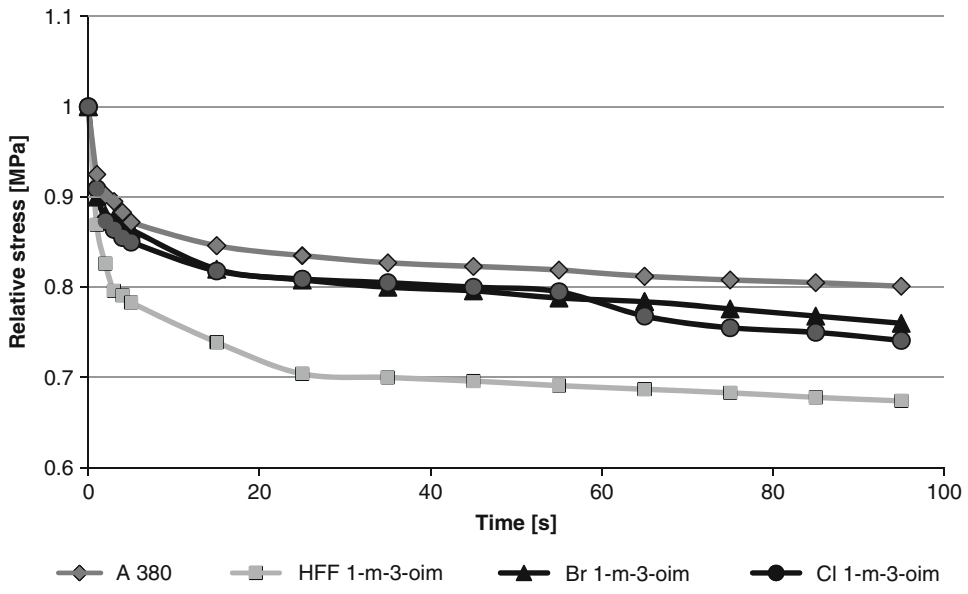

Fig. 5 Relaxation curves for the silicone rubber vulcanizates

Table 3 Relaxation rates of silicone rubber vulcanizates

	$n_1 *10^{-2}$ [− 1/s]	$n_2 *10^{-2}$ [− 1/s]	$n_3 *10^{-2}$ [− 1/s]
A 380	14.34	3.42	2.57
HFF 1-m-3-oim	30.53	6.09	5.04
Br 1-m-3-oim	19.44	4.27	2.95
Cl 1-m-3-oim	20.44	4.45	2.44

(n_1, n_2, n_3 - relaxation rates at the following time periods: 0–10 s, 10-100s, 100-1000s)

vulcanizate with HFF 1-m-3-oim showed the higher relaxation rates, that could be associated with the breakdown of the filler-filler structure and weak polymer-filler networks.

Conclusions

Application of ionic liquids in vulcanizates of methylvinyl-silicone rubber caused a decrease of torque increment during cross-linking, considerable improvement of vulcanizates mechanical properties as well as the increase of relaxation rates. The most effective ionic liquid was 1-methyl-3-octylimidazolium hexafluorophosphate. It decreased vulcanization time and reduced the amount of crosslinks decomposing under the influence of ammonia vapour. Additionally, vulcanizate containing HFF 1-m-3-oim demonstrated by good dumping absorption properties confirmed by high hysteresis and the high values of Mullins' effect.

References:

[1] Fang S, Hu Y, Song L, Zhan J, He Q (2008) J Mat Sci 43: 1057
[2] Jia LY, Du ZJ, Zhang C, Li CJ, Li HQ (2008) Polym Eng Sci 48: 74
[3] Park ES (2008) J Appl Polym Sci 110: 1723
[4] Wojtas A, Zaborski M, Kosmalska A (2010) Polimery 3: 208
[5] Xu Q, Pang M, Zhu L, Zhang Y, Feng S (2010) Mat Des 31: 4083
[6] Basuli U, Chaki TK, Naskar K (2008) J Appl Polym Sci 108: 1079
[7] Ueno K, Imaizumi S, Hata K, Watanabe M (2009) Langmuir 25: 825.
[8] Frounchi M, Dadbin S, Panahinia F (2006) Nucl Instr Meth.Phys Res B 243: 354

Progr Colloid Polym Sci (2011) 138:155–160
DOI: 10.1007/978-3-642-19038-4_28

A Simulation Study on the Structure of Bimetallic Nanoparticles Synthesized in Microemulsions

M. de Dios, F. Barroso, and C. Tojo

Abstract Monte Carlo simulations were carried out to study the different structures showed by bimetallic nanoparticles synthesized in microemulsions. It is observed that the difference in reduction rates of both metals is not the only parameter to determine the metals segregation, playing the interdroplet channel size a relevant role. The reduction rates difference determines nanoparticle structure only in two extreme cases: when both reactions take place at the same rate a nanoalloy structure is always obtained; if both reactions have very different rates, the nanoparticle shows a core-shell structure. But in the large interval between both extreme cases, the nanoparticle structure is strongly dependent on the intermicellar exchange, which is mainly determined by the surfactant film flexibility, and on reactants concentration. This result is very promising for the preparation of bimetallic nanoparticles with a given structure.

Keywords bimetallic nanoparticles • nanomaterials • microemulsions • reduction rate • microheterogeneous reaction media

Introduction

Studies of bimetallic nanoparticles received great attention from both scientific and technological communities because of most of the nanoparticle catalytic activity depends on their structural aspects [1]. Among the various structural aspects it is of most important to control the homogeneity, dispersion and alloying extent as they have profound influence on the surface properties which affect to catalytic activity and stability of the bimetallic nanoparticles. Therefore, control of composition distribution of bimetallic nanoparticles is crucial to the improvement of particle properties.

The bimetallic particles will be in a core-shell structure or alloy form, depending on the preparation route, miscibility and reduction kinetics of metal ions. As an example, bimetallic particles like Au/Ag are reported to exhibit Ag core and Ag/Au alloyed-shell type of structure by the seed-growth method [2]. However, if the reductions are simultaneous in presence of a capping agent, Au/Ag nanoparticles form homogeneous alloy [3]. When they are reduced simultaneously by the microemulsion method, Au/Ag nanoparticles can form homogeneous alloy [4] or an enriched in Au core-enriched in Ag shell structure [5], depending on the preparation conditions.

Among the methods used for nanosized particle synthesis, the microemulsion route is one of the most important methods to control the particle size, because the surfactant-stabilized droplets provide a microenvironment for the preparation of nanoparticles by exchanging their contents and preventing the excess aggregation of particles. But microemulsion itself is a very complicated system, and different simulation results show that the dynamics of intermicellar exchange plays an important role in the kinetics [6-9]. Likewise, experimental data supports this result. For example, Au/Pt alloys [10] and Au/Pt core-shell particles [11] had been prepared using different microemulsions. It seems fair to say that no definitive conclusions may be established about the control of particle structure. In line with our ongoing effort to evaluate the particles synthesis in microemulsions [7-9,12,13] we have aimed here to study the factors affecting nanoparticle structure.

Model Formulation

The computer simulation of the formation of nanoparticle in microemulsions was carried out using the model previously reported [7-9]. Briefly, each simulation began with a random

C. Tojo (✉)
Physical Chemistry Department, Faculty of Chemistry, University of Vigo, E-36210, Vigo, Spain
e-mail: ctojo@uvigo.es

distribution of three microemulsions droplets randomly located on a three-dimensional lattice: one microemulsion contains molecules of the metal salt A, other the metal salt B, and another the reductor R. The reactants are distributed throughout the droplets using a Poisson distribution.

Two micelles chosen randomly are allowed to collide (due to Brownian motion), fuse and redisperse. Upon collision and they can establish a water channel forming a transient dimmer (fusion), exchanging their contents (reactants, products and/or growing particles). Exchange criteria depend on the species inside the droplets (see Ref. [8,12] for details). The micellar dynamics is affected by changing the surfactant, the chain length of the oil phase and the cosurfactant [6,7,14-19]. The surfactant film flexibility is the ability to depart from the optimal curvature. Surfactants can be flexible or rigid, depending on the strength of the interactions at both sides of the interface. To simulate this phenomenon the surfactant film flexibility around the droplets is related to the ease with which channels communicating colliding droplets can form. Film flexibility also places a limit on the size of the particles traversing the interdroplet channels. The flexibility parameter (f) is the maximum size of the particle which can be exchanged: particles with more than f products are not allowed to pass from one droplet to another. In this way, a highly flexible film allows the interchange of larger particles than a rigid one. The ripening relies on mass transport from smaller to larger droplets: if a droplet containing a small particle collides with another droplet containing a greater one, the smaller particle will traverse the interdroplet channel to be added to the larger one. The species inside micelles, reactants and growing particles, can be exchanged if the droplets stay long enough together and if the size of the channel communicating colliding droplets is large enough [12]. Since a reactant molecule is smaller than a particle, it is assumed that the main factor determining the reactant interdroplet transfer is the dimer stability, and the channel size would not be so important. On the contrary, the channel size will be relevant when the exchanged material is a particle (products aggregate), which has to be transferred as a whole. The k_{ex} simulation parameters govern the exchange of reactants and non-aggregated products and they are related to the dimer stability. The larger the dimer stability the longer two water pools stay together and more molecules can be transferred during a collision. The material exchange parameters (f and k_{ex}) rise together: an increase of the flexibility implies not only the exchange of larger particles, but also a quicker exchange of reactants.

In order to include different reaction rates, only a percentage v of reactants inside the colliding droplets leads to products. The fastest reaction is v=1 (100% reactants transform in products). Because there are two different metal salts, two different reaction rate parameters have to be considered: the reduction rates of the metal salt A^+ ($A^+ + R \rightarrow A$) and B^+ ($B^+ + R \rightarrow B$) are determined by v_A and v_B respectively.

The nanoparticles growth may be limited by the size of the drops. The influence of droplet size was studied previously [20], so in this work we present results without restriction by droplet size.

Consistency between experimental and simulation results [8,9,13,20] show the validity of the simulation model.

Results and Discussion

Reduction Potential and Nanoparticle Structure

It is well-known that in homogeneous media, the higher reduction potential ions usually have the priority in reduction. Consequently, the difference in reduction potential of two metal ions may be the major factor to decide what structure the particles should be. It is assumed that a large difference in the reduction potential usually results in a core-shell structure, and a small difference in the reduction potential leads to an alloy one [21]. In order to study if this assumption can be used in a microheterogeneous media as a microemulsion, Figure 1 shows simulation results for two different reduction rate ratios v_A/v_B, being v_A and v_B the A and B metal reduction rates, and keeping constant the synthesis variables. The number of particles containing different percentage of one of the metals (A) is monitored from the nanoparticle core to the outside (layer by layer). When both reduction rates are equal (see Figure 1.A), an alloy structure of nanoparticle is observed from the core/beginning. Although the inner layers of some particles are mainly composed by only one of the metals, the composition shows a progressive improvement towards a perfect mix of both metals from the inner to the outer layers. At the end of the process, the composition of most of the particles is 50% in each metal. On increasing the difference between the chemical reaction rates, a progressive change from an alloy to a core-shell structure is observed, as in homogeneous media. Previous studies [9] allowed us to propose a detailed explanation of this result based on the interplay between the ripening contribution to nanoparticle growth (which is strongly dependent on intermicellar exchange) and the difference in reduction rate of both metals. The conclusion was that only for small differences in the reduction rates the

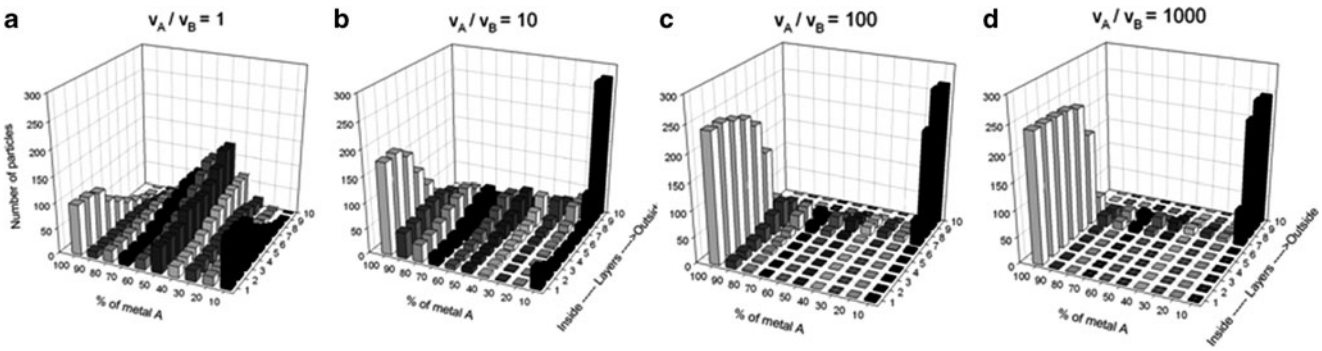

Figure 1 Number of particles versus the percentage of one of the products (a), from the nanoparticle core to the outside (layer by layer) for different reduction rate ratios. Synthesis conditions: reactant concentration $\langle c_A \rangle = \langle c_B \rangle = 32$, f=30, k_{ex}=5. A) v_A/v_B=1; b) v_A/v_B=10; c) v_A/v_B=100; d) v_A/v_B=1000

Table 1 Bimetallic nanoparticles prepared by simultaneous reduction in microemulsions

Metals	Structure	Microemulsionreductor agent; metal precursor	f	Ref
Au-Ag	Au core-enriched in Ag shell	water/AOT/isooctane N_2H_5OH; Ag^+, $AuCl_4^-$	rigid	[5]
	nanoalloy	water/TritonX-100/cyclohexane $NaBH_4$, Ag^+, $AuCl_4^-$	flexible	[4]
Au-Pt	core-shell	water/AOT/isooctane N_2H_5OH, $AuCl_4^-$, $PtCl_6^{2-}$	rigid	[11]
	nanoalloy	water/Tergitol 15-S-5/isooctane N_2H_5OH, $AuCl_4^-$, $PtCl_6^{2-}$	flexible	[10]

intermicellar exchange affects to nanoparticle structure. This conclusion was supported by a comparison study between experimental and simulation results, on the basis of electrochemical arguments [9].

Microemulsion Composition and Nanoparticle Structure

Table 1 shows experimental data of Au-Ag [4,5] and Au-Pt [10,11] nanoparticles. It is observed that a given bimetallic nanoparticle can be obtained in alloy form if the surfactant film flexibility is high, or in a core-shell structure using a rigid film. In agreement with experimental results, our simulation model shows that the nanoparticle structure can be modified by changing the parameters which control the interdroplet channel size and the dimer stability, i.e. by changing the microemulsion composition. As the film flexibility increases the degree of alloying increases too, and a transition from core-shell to alloy structure is obtained for moderate differences in reduction rate (v_A/v_B=10). These results allow us to propose that it is possible, even when the chemical reaction rates are different, to obtain nanoalloyed nanoparticles just by changing the microemulsion composition. On the contrary, if both reduction rates take place at similar rates or if the difference between rates is large enough, the structure is not modified by changing the surfactant flexibility (see Ref. [9] for details).

Reactants Concentration and Nanoparticle Structure

A new set of computer experiments were carried out to study the influence of reactants concentration on the nanoparticle structure. Figure 2 shows the structures obtained using different number of atoms/molecules of reactants (two metal salts and reducing agent) initially contained inside a microemulsion droplet. When both reduction rates are equal a homogeneous alloy is obtained for all values of concentrations and flexibilities. Likewise, when the chemical reaction rates are very different (v_A/v_B=1000), concentration does not modify the structure, being always a core-shell. But the intermediate cases (v_A/v_B=10,100) show structural changes as increasing reactant concentration, as can be observed in Figure 2. In the left column (v_A/v_B=10) one can observe that the core enrichment in the faster product diminishes as increasing concentration (from the top to the bottom), giving rise to a higher degree of mixture in the inner layers. In addition the shell is enriched in the slower product with the increase of concentration. Right column shows results using a higher reduction rate ratio (v_A/v_B=100), which presents a better separation of both metals in the middle layers as increasing concentration. Qualitatively similar results are obtained using lower or higher values of the flexibility parameters. It seems that when the reduction rates are not very different the nanoparticle structure is also affected by changing reactants concentration.

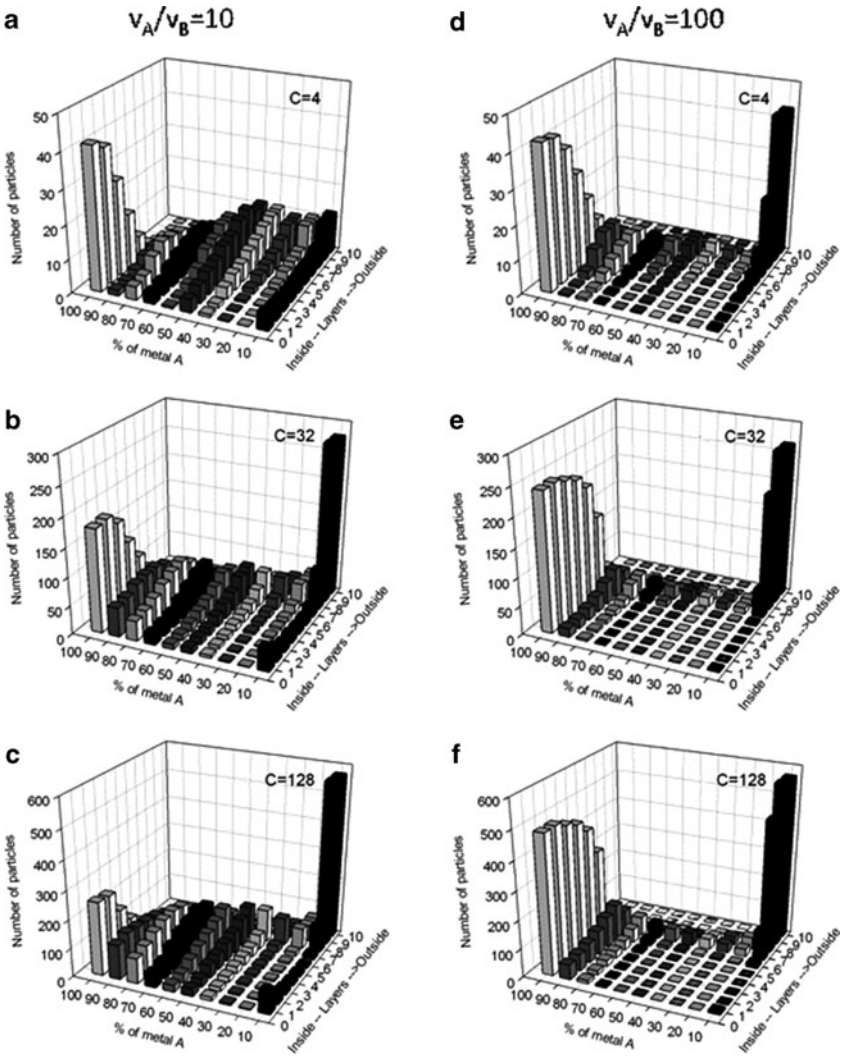

Figure 2 Number of particles versus the percentage of one of the products (A), from the nanoparticle core to the outside for different concentrations and keeping constant the film flexibility (f=30, k_{ex}=5). Left column: v_A/v_B =10; right column: v_A/v_B=100. Reactant concentration: a) and d) $\langle c_A \rangle = \langle c_B \rangle$ = 4; b) and e) $\langle c_A \rangle = \langle c_B \rangle$ = 32; c) and f) $\langle c_A \rangle = \langle c_B \rangle$ = 128 reactants per droplet

Conclusions

The main conclusion is that nanoparticle structure is determined by the chemical reaction rates ratio, as in homogeneous media, only if both reactions take place at the same rate and if the reaction rates are very different. The first case leads to a nanoalloy and the second one to a core-shell structure. But in the common case of a nanoparticle composed by two metals with a moderate difference in reduction potentials, the dynamics of the intermicellar exchange causes that the synthesis variables, such as surfactant film flexibility or initial reactants concentrations, become more relevant, modifying the nanoparticle structure: An increase of flexibility gives rise to alloys, and an increase of concentration implies a higher degree of mixture in the inner layers and an enrichment in the slower product in the outer layers.

Acknowledgements The authors are grateful for the finantial support of the Regional government of Galicia (Project INCITE09 314 261 PR) and Ministerio de Ciencia e Innovación (project CTQ2009-08676).

References

[1] Toshima N, Yonezawa T (1998) New J Chem 22: 1179
[2] Srnová-Sloufov I, Vlcková B, Bastl Z, Hasslett TL (2004) Langmuir 20: 3407
[3] Mallin PM, Murphy C (2002) Nano Lett 2: 1235
[4] Pal A, Shah S, Devi S (2007) Coll Surf A 302: 483
[5] Chen D, Chen C (2002) J Mater Chem 12: 1557
[6] Bagwe RP, Khilar KC (2000) Langmuir 16: 905
[7] López-Quintela MA, Tojo C, Blanco MC, García-Río L, Leis JR (2004) Curr Opin Colloid Int Sci 9: 264
[8] Tojo C, Blanco MC, López-Quintela MA (1997) Langmuir 13: 4527
[9] Tojo C, de Dios M, López-Quintela MA (2009) J Phys Chem 113: 19145
[10] Hernández-Fernández P, Rojas S, Ocón P, Gómez de la Fuente JL, San Fabián J, Sanza J, Peña MA, García-García FJ, Terreros P, Fierro JL (2007) J Phys Chem B 111: 2913
[11] Wu M, Chen D, Huang T (2001) Chem Mater 13: 599
[12] Quintillán S, Tojo C, Blanco MC, López-Quintela MA (2001). Langmuir 17: 725.
[13] Tojo C, Barroso F, de Dios M (2006) J Colloid Int Sci 296: 591
[14] Bagwe RP, Khilar KC (1997) Langmuir 13: 6432

[15] Curri ML, Agostiano A, Manna L, Della Monica M, Catalano M, Chiavarone L, Spagnolo V, Lugará M (2000) J Phys Chem B 104: 8391
[16] Cason J, Miller ME, Thompson JB, Roberts CB (2001) J Phys Chem B 105: 2297
[17] Kitchens CL, McLeod MC, Roberts CB (2003) J Phys Chem B 107: 11331
[18] López-Quintela MA (2003) Curr Opin Colloid Int Sci 8: 137
[19] Szleifer I, Kramer D, Ben-Shaul A, Roux D, Gelbart WM (1988) Phys Rev Lett 60: 1966
[20] Tojo C, Blanco MC, López-Quintela MA (1998) J Non-Crys. Solids 235-237: 688
[21] Feng J, Zhang C (2006) J Colloid Int Sci 293: 414

Progr Colloid Polym Sci (2011) 138:161–164
DOI: 10.1007/978-3-642-19038-4_29

Preparation of Porous Magnetic Nanocomposite Materials Using Highly Concentrated Emulsions as Templates

G. Ghosh[1,†], A. Vílchez[1], J. Esquena[1], C. Solans[1], and C. Rodríguez-Abreu[1,2,#]

Abstract Iron oxide nanoparticles (NPs) with a size of 3 and 10 nm were used to prepare porous hybrid magnetic nanocomposite materials via polymerization in highly concentrated water-in-oil (w/o) emulsions. The NPs were dispersed in a monomer mixture (styrene-divinylbenzene), which was then polymerized to obtain porous solid monoliths with embedded magnetic nanoparticles. The NPs were characterized using x-ray diffraction (XRD), scanning electron microscopy (SEM) and transmission electron microscopy (TEM). The results showed that the nanocomposites contain a high pore volume fraction, with pores of size around 1-10 μm, surrounded by thin polymer walls containing homogeneously distributed nanoparticles. Porous nanocomposites can be attracted to a strong permanent magnet.

Keywords Nanocomposites • emulsion polymerization • porous materials

Introduction

With great advancement of research in polymer science in recent years it is now possible to prepare a variety of materials with controllable mechanical, thermal, and electroactive properties for various applications. Such materials are readily available in the market. However, in spite of numerous works by different groups, still the preparation of an organic polymeric material with high magnetic moment and susceptibility comparable to an inorganic system remains a great challenge. There are several reports describing different synthetic routes of fabrication of magnetic polymer nanocomposites combining organic polymers and inorganic magnetic nanoparticles [1]. For example, polymerization in emulsion and in dispersed media have been used to encapsulate iron oxide nanoparticles into polymeric micro and nanospheres [2]. These methods are helpful to synthesize many more polymeric materials. In this work, we prepared porous hybrid magnetic nanocomposite (NC) materials using highly concentrated emulsions (HIPRE) as reaction media. This type of emulsions are characterized by a volume fraction of dispersed phase higher than 0.74, the critical value of the most compact arrangement of uniform, undistorted spheres [3,4]. Consequently, their structure consists of deformed and/or polydisperse droplets separated by a thin film of continuous phase, a structure resembling gas-liquid foams. The characteristic properties of highly concentrated emulsions are of particular interest for their use as reaction media [5], namely for the preparation of solid macroporous foams (aerogels) by polymerization in the continuous phase. [6-11].

Experimental

Materials

Iron (III) chloride hexahydrate ($FeCl_3$, $6H_2O$) and anhydrous Iron (II) chloride ($FeCl_2$) were purchased from Sigma-Aldrich. Ammonium hydroxide (32 wt% NH_3) and oleic acid were purchased from Merck and Fluka, respectively. Styrene and divinylbenzene (DVB), either from Merck or Aldrich, were purified by passing through neutral

[†]On leave from UGC-AE CSR, Trombay, Mumbai, 400 085 India
[#]Current affiliation: International Iberian Nanotechnology Laboratory (INL), Avda. Central n°100, Edificio dos Congregados, 4710-229 Braga, Portugal
C. Rodríguez-Abreu (✉)
[1]Instituto de Química Avanzada de Catalunya (IQAC), Consejo Superior de Investigaciones Científicas (CSIC), Jordi Girona, 18-26, 08034 Barcelona, Spain
e-mail: crodriguez@inl.int
[2]International Iberian Nanotechnology Laboratory (INL), Avda. Central nº100, Edificio dos Congregados, 4710-229 Braga, Portugal

chromatographic aluminum oxide, in order to eliminate polymerization inhibitors. Acrylic acid was obtained from Merck. 2,2′-azodi-(2,4-dimethylvaleronitrile) (ADVN, soluble in oil phase), courtesy of DuPont Ibérica S.A. ,was used as initiator in the case of bulk polymerization. Potassium persulfate 99%, used as initiator in emulsion polymerization, was obtained from Merck. Hexaethylene glycol n-hexadecyl ether and octaethylene glycol n-dodecyl ether nonionic surfactants, abbreviated as $C_{16}(EO)_6$ and $C_{12}(EO)_8$ respectively, were purchased from Nikko Chemicals Co (Japan). The poly(ethylene glycol)-poly(propylene glycol)-poly(ethylene glycol) $(EO)_{13}$-$(PO)_{30}$-$(EO)_{13}$ triblock copolymer surfactant (Synperonic L64) was obtained from Uniqema (United Kingdom). All surfactants were used without further purification. Tetradecane 99% was obtained from Aldrich. Milli-Q water was used in all the experiments.

Methods

Synthesis of nanoparticles: Iron oxide nanoparticles (NPs) were synthesized using water-in-oil (w/o) microemulsion droplets as templates [12], as well as by a co-precipitation method [13], following the literature.

Synthesis of porous nanocomposite materials: To prepare porous nanocomposite (NC) materials, the oil phase consisting of styrene, divinylbenzene (DVB) and oleic acid coated iron oxide NPs was polymerized in the continuous phase of water-in-oil (W/O) highly concentrated emulsions prepared using the phase inversion temperature (PIT) method [10]. Emulsions were prepared in the system H_2O / $K_2S_2O_8$ / $C_{16}(EO)_6$ / $C_{12}(EO)_8$ / Synperonic L-64 / styrene / divinylbenzene / tetradecane following weight ratios given in the literature [10]. Acrylic acid was added to the oil phase for better dispersion of NPs. Samples were mixed thoroughly in an ice bath and then put directly in a 70 ^{o}C bath with strong shaking until the mixture became highly viscous. Samples were then kept in that bath at 70 °C for 48 hours for polymerization. The final porous NCs were washed with ethanol and water and then freeze-dried to remove the aqueous dispersed phase. The nanoparticle concentration used in these porous nanocomposites was 6.4 wt% with respect to the polymer content in the final product.

Results and Discussion

Figures 1, (a) and (b) show the X-ray diffraction (XRD) patterns of the dried NPs prepared using microemulsion droplets as templates, and the coprecipitation method, respectively. The XRD peaks in Fig. 1a are quite broad, while those in Fig. 1b are sharper and they can be matched with both Fe_2O_3 and Fe_3O_4 phases [14,15]. Both XRD patterns contain a strong background, which could be due to the oleate coating on the NP surfaces. The Debye-Scherrer equation, $D = 0.9\lambda / \beta \cos\theta$, was used to calculate the crystalline grain size (D), where λ = 1.54 Å (X-ray wavelength) and β is the full-width at half maximum of a peak at θ (we selected the peak at $2\theta \approx 62$ ° corresponding to the 4 4 0 reflection). The values of D estimated for the NPs obtained using the microemulsion and coprecipitation methods were around 2.8 and 7.3 nm, respectively. These values are very close to the particle diameters (3 and 8 nm) obtained from TEM measurements for the two NPs, indicating that these NPs are single-crystalline.

Figures 2, (a) and (b) show the Scanning Electron Microscopy (SEM) images of porous NCs with (a) 3 nm and (b) 10 nm NPs, respectively. Interconnected pores with 1 – 10 μm size can be observed. These pores (voids) were created

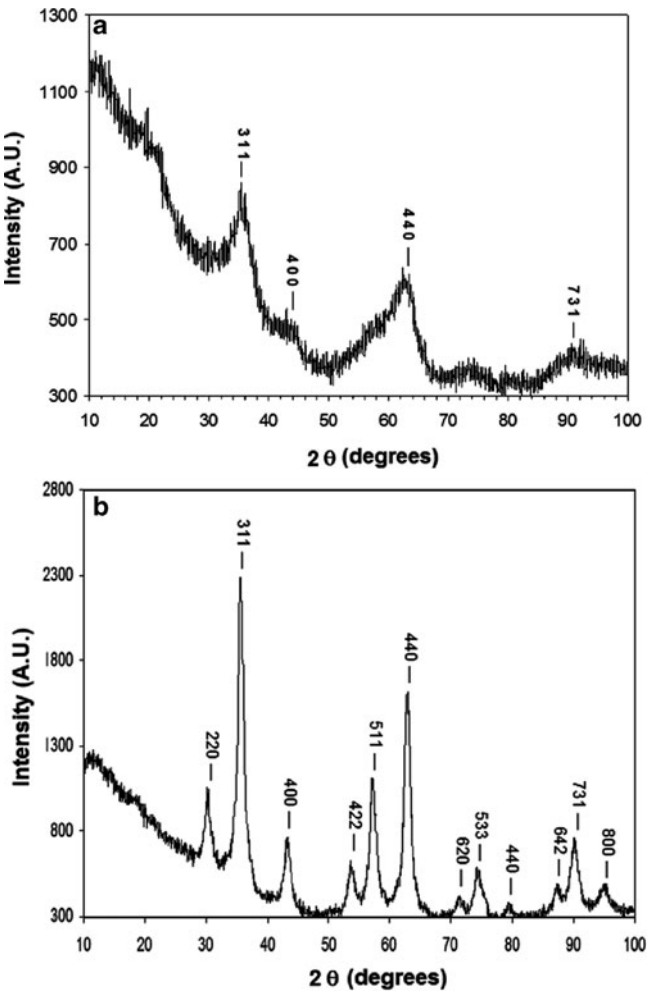

Fig. 1 XRD patterns of nanoparticles of size (a) 3 nm and (b) 10 nm

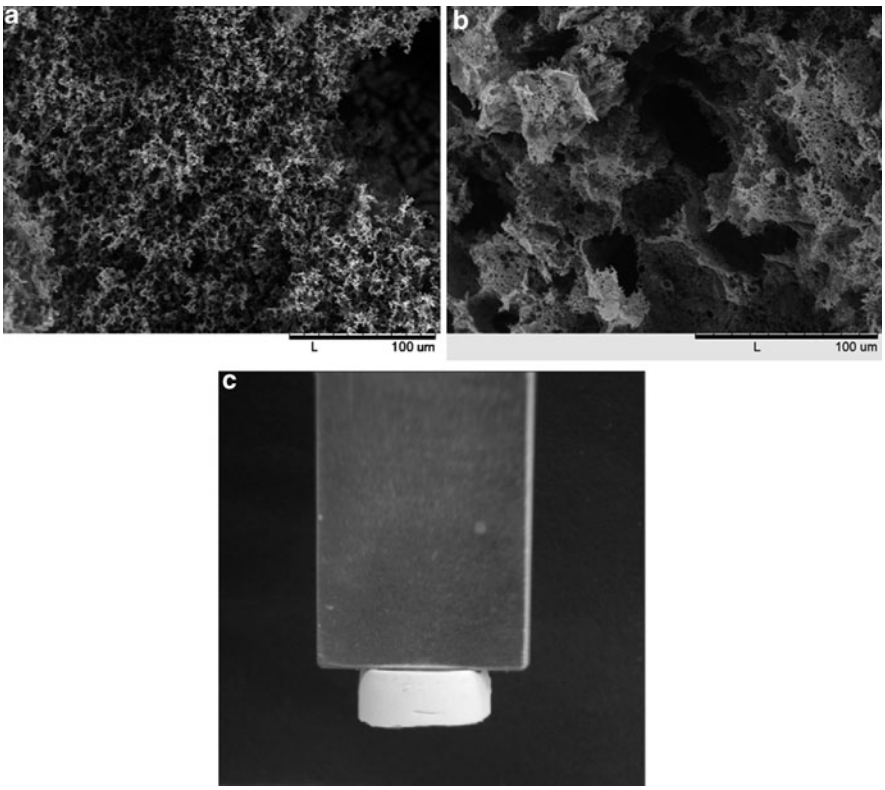

Fig. 2 SEM images of porous NCs with 6.4 wt% of (a) 3 nm and (b) 10 nm nanoparticles. Black zones represent pores surrounded by white polymer walls. (c) Image of a porous NC attracted to a magnet. SEM images were taken with a Hitachi TM-1000 instrument

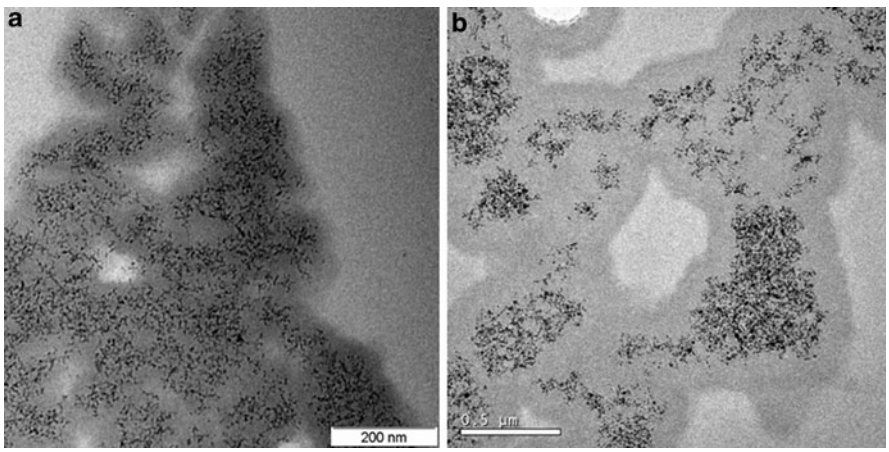

Fig. 3 TEM images of ultramicrotomed slices of porous NCs with with 6.4 wt% of (a) 3 nm and (b) 10 nm nanoparticles. Small black dots are nanoparticles, dark gray regions covering nanoparticles are polymer walls. Light gray zones surrounded by polymer walls are pores. Images were collected with a JEOL JEM 1010 microscope

by removing the water drops from the polymerized W/O emulsions. The polymer pore walls contains embbeded NPs. The density of these porous NCs were measured to be 0.05-0.07 g / cm^3, which is about 20 times less than the non-porous NCs (e.g., density of non-porous polystyrene monolith is 1.1 g / cm^3).

The distribution of NPs inside the polymer walls of ultramicrotrome sliced porous NCs were observed by Transmission Electron Microscopy (TEM). Figures 3 (a) and (b) show the distribution for (a) 3 nm and (b) 10 nm NPs, respectively. Black dots are nanoparticles embedded in the dark gray regions which are the polymer walls. The light grey regions represent the pores. Nanoparticles are homogeneously distributed inside the polymer walls. Due to their light weight, the obtained NCs are attracted to a strong magnet even at low (6.4 wt%) NP concentration (see Figure 2c). Results on magnetic properties of these materials will be published elsewhere.

Conclusions

Hybrid magnetic nanocomposite materials have been prepared by using polymerization in highly concentrated water-in-oil emulsions of styrene-divinylbenzene mixtures. The emulsion polymerization produced ultra-light porous nanocomposites of density around 0.05-0.07 g / cm^3, which is about 20 times lighter than the non-porous nanocomposite material with similar magnetic properties. In these porous nanocomposite materials the nanoparticles are distributed homogeneouly in the polymer walls providing an uniform magnetic moment over the entire material. Therefore these nanocomposites are easily attracted to a strong, permanent magnet.

Acknowledgement G. Ghosh acknowledges a JAE-Doc 2008 post-doctoral grant from CSIC, Spain. C.R-A is grateful to the Ministerio de Ciencia e Innovación, Spain (Project CTQ2008-01979/BQU) and the bilateral cooperation program "Luis Santaló" between Spain (CSIC) and Argentina(CONICET) for financial support. Authors are grateful to Prof. Francisco Rivadulla, Jorge Vidal and Manuel Bañobre (Universidad de Santiago de Compostela, Spain) and Roberto Zysler (Centro Atomico Bariloche, Argentina) for useful discussions and help on nanoparticle synthesis and magnetic measurements.

References

1. Leslie-Pelecky D and Rieke R D (1996) Chem Mater 8: 1770.
2. Bao H, Chen Z, Xu W, Wu P, Wang Y, Gao B and Liu J (2006) Colloid J 68: 644.
3. Lissant K J, (1966) J Colloid Interface Sci 22:462.
4. Princen H M (1979) J Colloid Interface Sci 71:55.
5. Solans C, Esquena J, Azemar N (2003) Curr Opin Colloid Interfece Sci 8: 156.
6. Barby D, Haq Z (1982) European Patent No. 0060138 (Unilever).
7. Ruckenstein E and Park J S (1992) Polymer 33:405.
8. Williams J M (1988) Langmuir 4:44.
9. Cameron N R, Sherington D C, Albiston L and Gregory D P, (1996) Colloid Polym Sci 274:592.
10. Esquena J, Ravi Sankar G S R Solans C (2003) Langmuir 19: 2983.
11. Solans C and Esquena J (2009). In: Platikanov, D and Exerowa, D (ed) Highlights in Colloid Science, Wiley VCH, Weinheim, Germany.
12. Vidal-Vidal, J, Rivas, J, López Quintela, MA (2006) Colloid Surf A 288: 44.
13. Ramirez, L P and Landfester, K (2003) Macromol. Chem Phys 204: 22.
14. Andersson, N, Corkery, RW and Alberius, PCA. (2007) J Mater Chem 17: 2700.
15. Sun, YK, Ma, M, Zhang, Y, Gu, N (2004) Colloids Surf A 245: 15.

Progr Colloid Polym Sci (2011) 138:165–172
DOI: 10.1007/978-3-642-19038-4_30

2-Mercaptobenzothiazole as a Corrosion Inhibitor in Low Temperature Ionic Liquids

K. Marczewska-Boczkowska and M. Kosmulski

Abstract The corrosion of metals (copper, zinc, and plain carbon steel) in dialkylimidazolium tetrafluoroborates depends on the presence of traces of impurities in the ionic liquids. Water, chlorides, and especially simultaneous presence of the both impurities enhances the pitting corrosion of metals. The products of corrosion contain the metal of interest as well as nitrogen, boron, chlorine, fluorine, carbon, and oxygen.

The rate of corrosion of metals in both pure and water- and/or chloride-containing tetrafluoroborates can be substantially reduced in the presence of 2-mercaptobenzothiazole. In 0.001 M 2-mercaptobenzothiazole the rate of corrosion drops by 70 % at 25 °C and by 60 % at 200 °C with respect to the corrosion rate in absence of corrosion inhibitor. We speculate that the other derivatives of azoles and thiazoles, which have been successful as corrosion inhibitors in aqueous media, can also be efficient in low temperature ionic liquids.

Key words corrosion • electrochemistry • adsorption • surface reaction • self assembled monolayer

Introduction

Dialkylimidazolium tetrafluoroborates belong to the most well-known ionic liquids, and they have been studied with respect to their possible applications in organic synthesis [1,2], biocatalysis [3,4], extraction [5,6], as electrolytes in chemical power sources including electrochemical capacitors [7,8], as heat-transfer media [9,10], in chemical analysis [11,12] as lubricants [13,14], etc.

M. Kosmulski (✉)
Lublin University of Technology, 38 Nadbystrzycka St., 20-618, Lublin, Poland
e-mail: mkosmuls@abo.fi

Dialkylimidazolium tetrafluoroborates are hygroscopic, and the commercially available specimens often contain water, which affects their physical and chemical properties [15,16]. Chlorine (in a form of chloride anions) is another common impurity of commercial specimens of ionic liquids [15]. Both water and chlorides substantially enhance the corrosion of metals in ionic liquids, and the pitting corrosion may be a serious problem in practical applications of ionic liquids [17–24]. Water- and chloride-free ionic liquids are desired in applications involving contact with metals, but such products are rather expensive. Therefore we are looking for an alternative solution, which is addition of corrosion inhibitors to ionic liquids. Derivatives of azoles and thiazoles as benzotriazoles, mercaptobenzothiazoles, benzoimidazoles, and imidazoles, which have been successful as corrosion inhibitors in aqueous medium, are considered as the candidates for corrosion inhibitors in ionic liquids**.** SAM (Self Assembled Monolayers) of these compounds on the surfaces of metals are stable, and they protect metal surfaces from aggressive ions [25]. Similar inhibition mechanism is expected in ionic liquids. The 2-mercaptobenzothiazole (MBT) was selected as a corrosion inhibitor for this study of corrosion of plain steel, copper and zinc in 1-butyl-3-methyloimidazolioum tetrafluoroborate ($BMIBF_4$) in presence and absence of water and chlorides.

Experimental

Ionic Liquids

$BMIBF_4$ was obtained in our laboratory by means of a well-known recipe [15,26]. A mixture of $BMIBF_4$ with BMICl was prepared from pure compounds (outgased and protected from atmospheric moisture) gravimetrically. MBT was added as 0.1 M solution in acetone, and acetone was subsequently evaporated. Water was added volumetrically in a

final step to produce desired composition (0.87 mass % of Cl; 1.3 mass % of water).

Electrochemical Study

The electrochemical measurements were carried out in a 3-electrode system. A working electrode, s = 0.196 cm^2 was made from a metal rod (Cu, 99.9 % pure, composition according to Polish standard PN-EN 13599:2002; Zn, 99.99 % pure, composition according to Polish standard PN-EN 1179:1998 or plain steel, type S235JRG2, composition: C<0.17 %; Mn<1.4 %; P<0.045 %; S<0.045 %; N<0.009 %, according to Polish standard PN-EN 10025–2:2005) in a Teflon housing. The electrodes were polished with #1200 abrasive paper, washed with water, with acetone, with water again, and dried. A platinum sheet (s = 1.5 cm^2) was used as a counterelectrode. A platinum wire φ = 0.5 mm was used as a reference electrode. The reaction vessel of 10 cm^3 was thermostated, and Teflon separators were used to keep a constant geometry for all measurements. The reaction vessel was kept in a dry box to protect the ionic liquid from atmospheric moisture.

The polarization study was carried out by means of ATLAS 0531 electrochemical analyzer (Poland), and the corrosion current j_{corr} and Tafel coefficients b_a, b_k were calculated using the standard approach discussed in detail elsewhere [27,28].

Gravimetric Studies

Copper, zinc and plain steel were studied in form of disks, 3.5 cm in diameter, and 1 mm thick, and the exposed surface area was 20.33 cm^2. The disks for gravimetric studies were prepared in the same way as for electrochemical studies. The reaction with ionic liquids was carried out at 50 and 200 °C for 150 h in an air-proof glass container. After heating in ionic liquids the specimens were washed with 2-propanol and with water, and dried.

Surface Morphology and Surface Composition

Surface morphology and surface composition were studied by means of scanning electron microscope TESLA BS-304 with X-ray probe Microanalyser EDS (Thermo Electron Co. USA) with NORAN 300 system. The results reported in this paper were obtained using a 20 kV beam at 25 °, and the Proza correction function was applied.

The specimens described in the previous section (ionic liquids without MBT and with 10^{-3} M MBT) were studied. The surface composition reported in this study is a result of measurement from 9 different spots: the extreme results were rejected and an average was taken from the other results. A standard deviation in a set of concentrations from different spots of one specimen was below 30 %.

Results and Discussion

Fig. 1 and 2 illustrate the inhibition of corrosion by MBT. Interestingly enough, the corrosion currents in dry and chloride-free $BMIBF_4$ (Fig. 1) were in the same range for all

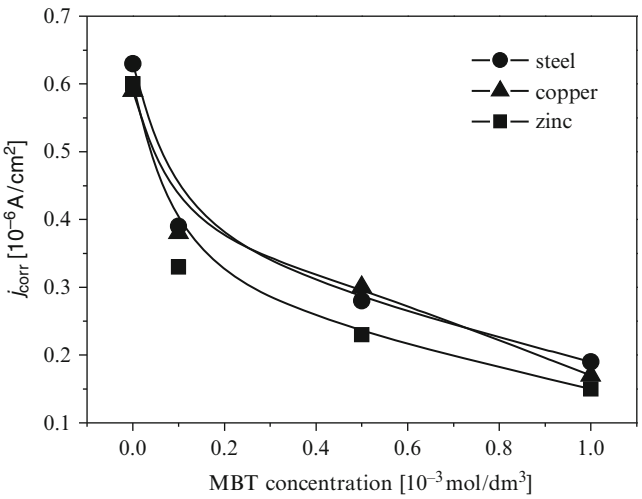

Fig. 1 Corrosion rate of metals in dry and chloride-free $BMIBF_4$ at 25 °C, at different MBT concentrations

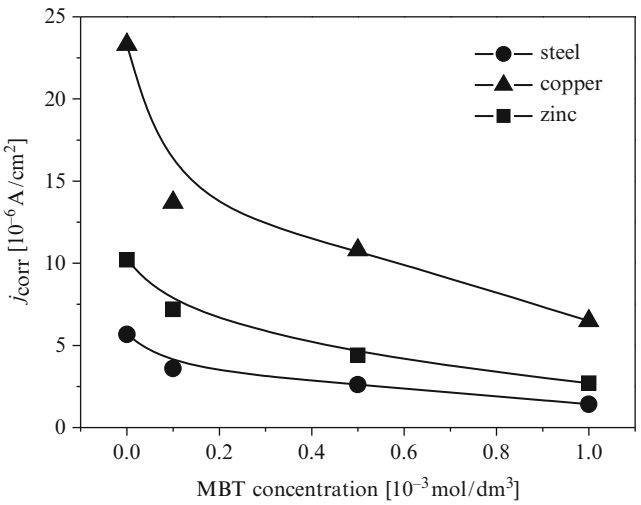

Fig. 2 Corrosion rate of metals in $BMIBF_4$ containing 0.87 mass % of Cl and 1.3 mass % of water at 25 °C, at different MBT concentrations

3 metals. The coincidence is accidental, and there is no fundamental reason why 3 different metals should behave alike. Addition of 10^{-3} M MBT depressed the corrosion rate by a factor of about 4 for all 3 metals. The corrosion currents in the presence of water and chlorides are higher by an order of magnitude than in dry and chloride-free ionic liquids (Fig. 2). The enhancement of corrosion rate of Cu was more pronounced than for the other two metals, probably because of the stability of Cu-Cl complexes in ionic liquid medium. Also fluoride anions produced by hydrolysis of tetrafluoroborate anions in the presence of water show different affinities to particular metals.

Fig. 3 shows that the corrosion potentials of steel in dry and chloride-free $BMIBF_4$ in the presence of MBT shift to more positive values, and that both anodic and cathodic currents are depressed by MBT. This indicates that MBT is a mixed corrosion inhibitor (that acts in both a cathodic and an anodic manner). Qualitatively similar shifts in corrosion potential and depression of corrosion currents on the both sides of corrosion potential are reported in Fig. 4-8 for steel, zinc and copper in the presence and absence of water and chlorides.

Plain steel corrodes in active-passive state in the ionic liquid. Near the corrosion potential the corrosion current increases abruptly by two orders of magnitude. At about 100 mV above the corrosion potential, the anodic current is observed, which only slightly changes with the potential. This indicates a passive layer. At about 400 mV above the corrosion potential, the passive layer is destroyed, and the anodic current abruptly increases again to reach another plateau. The shape of the corrosion curves suggests that a diffusion-limited current is measured, and the fluctuations may be due to formation of surface layer with some protective properties. The protective layer is stable over a 1

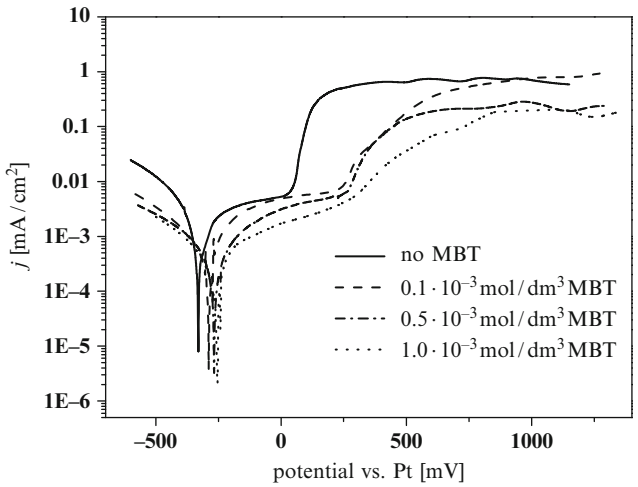

Fig. 3 Voltammetric curves of plain steel in dry and chloride-free $BMIBF_4$ at 25 °C, at different MBT concentrations

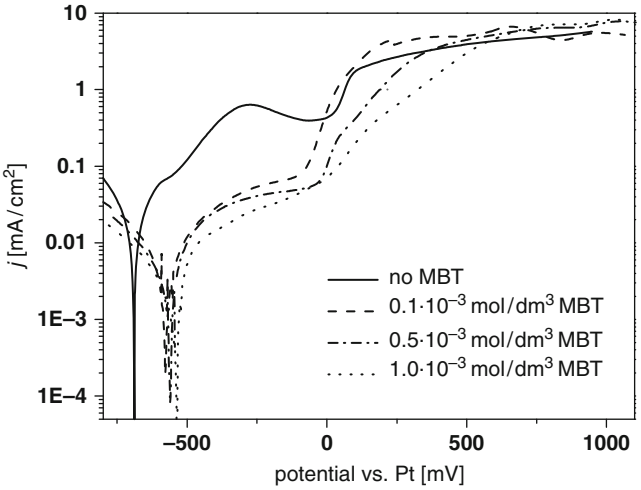

Fig. 4 Voltammetric curves of plain steel in $BMIBF_4$ containing 0.87 mass % of Cl and 1.3 mass % of water at 25 °C, at different MBT concentrations

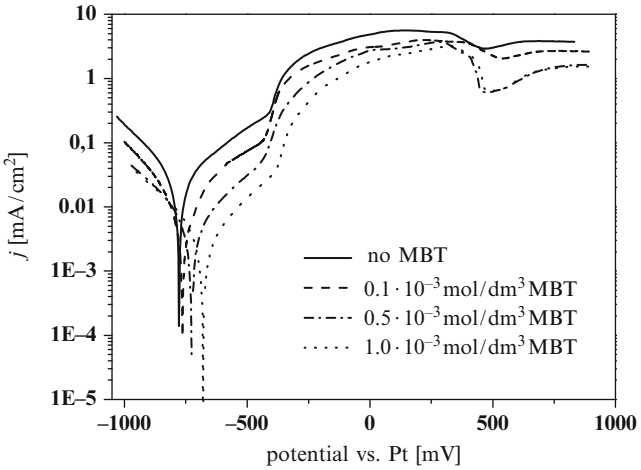

Fig. 5 Voltammetric curves of Zn in dry and chloride-free $BMIBF_4$ at 25 °C, at different MBT concentrations

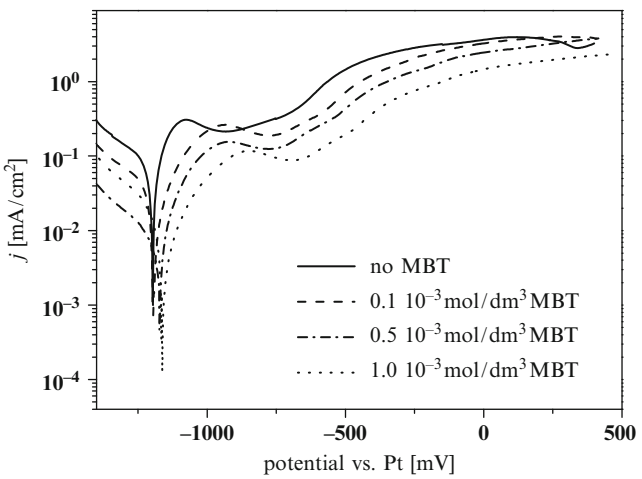

Fig. 6 Voltammetric curves of Zn in $BMIBF_4$ containing 0.87 mass % of Cl and 1.3 mass % of water at 25 °C, at different MBT concentrations

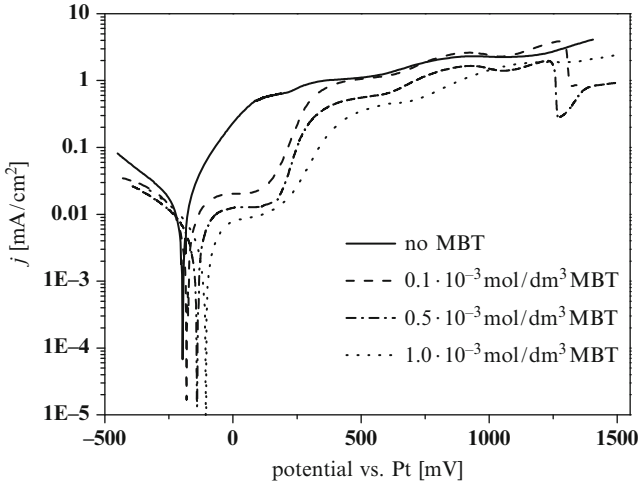

Fig. 7 Voltammetric curves of Cu in dry and chloride-free $BMIBF_4$ at 25 °C, at different MBT concentrations

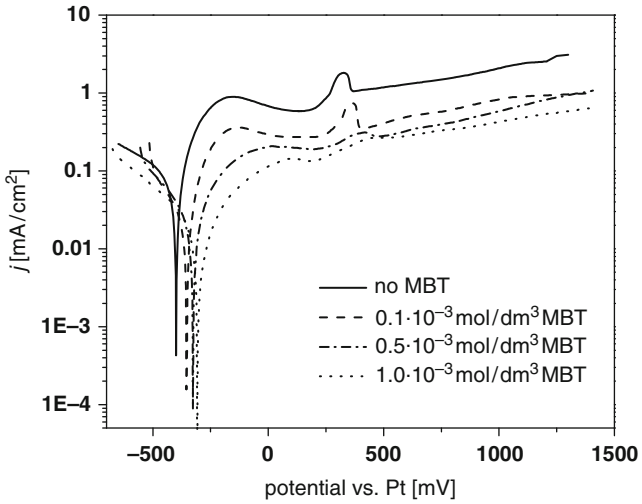

Fig. 8 Voltammetric curves of Cu in $BMIBF_4$ containing 0.87 mass % of Cl and 1.3 mass % of water at 25 °C, at different MBT concentrations

V-wide range. The both plateaus differ in the current by 2 orders of magnitude. Similar series of passivation and transpassivation ranges were found by Arenas and Reddy [17] and by Qu et al. [23,24].

In the presence of chlorides (as an impurity in an ionic liquid) or of fluorides (which are formed as a result of hydrolysis of tetrafluoroborate anion in a wet ionic liquid) the passive layer is destroyed and pitting corrosion develops. This is why the first plateau discussed above for dry and chloride-free $BMIBF_4$ (Fig. 3) almost disappears in the presence of water and chlorides when the corrosion inhibitor is absent (Fig. 4). In contrast, in the presence of MBT the first plateau in wet and chloride-containing $BMIBF_4$ (Fig. 4) is almost as wide as in dry and chloride-free $BMIBF_4$ (Fig. 3). Apparently the MBT layer protects the surface from chloride- and fluoride attack.

Table 1 Mass loss (in mg) of metals treated with ionic liquids at 50°C and 200 °C

metal	Steel		Cu		Zn	
t [°C]	50	200	50	200	50	200
$BMIBF_4$	14.5	14.0	23.5	18.0	17.0	15.0
$BMIBF_4$+ 10^{-3} M MBT	4.0	6.0	7.5	7.5	5.0	5.0
$BMIBF_4$ + 0.87% Cl	-	28.0	-	54.0	-	45.0
$BMIBF_4$ + 0.87% Cl + 10^{-3} M MBT	-	11.0	-	20.0	-	17.0
$BMIBF_4$ + 0.87% Cl + 1.3% water	64.0	-	103	-	119.5	-
$BMIBF_4$ + 0.87% Cl + 1,3% water+10^{-3} M MBT	17.0	-	28.5	-	34.0	-

The voltammetric curves for Zn in $BMIBF_4$ presented in Fig. 5 (dry and chloride- free $BMIBF_4$) and 6 ($BMIBF_4$ containing 0.87 mass % of Cl and 1.3 mass % of water) also indicate layers of corrosion products, which depress the corrosion rate, but unlike for steel (Fig. 3) the first plateau is absent, and the protective layer is not a passive laver.

MBT depresses the corrosion rate over the entire potential rate, but without a substantial change in the shape of corrosion curves.

The voltammetric curves for Cu in $BMIBF_4$ presented in Fig. 7 (dry and chloride- free $BMIBF_4$) and 8 ($BMIBF_4$ containing 0.87 mass % of Cl and 1.3 mass % of water) show, that in the absence of MBT a protective layer is only formed at very positive potentials. A complex shape of voltammetric curves of Cu with characteristic peaks has been interpreted in terms of two-step oxidation to Cu (I) and then to Cu(II) [28].

In contrast, in the presence of MBT, a clear plateau is observed in dry and chloride-free $BMIBF_4$ (Fig. 7, but not in wet and chloride-containing ionic liquid) at potentials about 100 mV above the corrosion potential indicating a layer of corrosion products, which substantially depress the corrosion rate.

The results of gravimetric study are summarized in Table 1. Surprisingly the increase of temperature from 50 to 200 °C does not substantially accelerate the mass loss. Addition of MBT depressed the mass loss of all 3 metals irrespective of the temperature. It should be emphasized that the ionic liquids underwent a partial thermal decomposition at 200 °C, but this process was rather slow except for chloride-containing ionic liquid in contact with Cu, in which the thermal decomposition was faster than in other studied systems.

The literature is full of misleading informations regarding the thermal stabilities of tetrafluoroborate ionic liquids. The results obtained by fast TGA lead to substantial overestimation of the temperature stability of ionic liquids [29-30]. Actually the long-term stability does not exceed 200 °C for most ionic liquids [21, 22, 31]. The metal ions produced in

corrosion process may accelerate the thermal decomposition. On the other hand, the thermal decomposition products block the metal surface, depress the diffusion and depress the corrosion rate [22]. The present results support this interpretation. MBT is stable up to 260 °C [32] that is at higher temperature than the ionic liquids studied in this paper. MBT depressed the mass loss of plain steel by a factor of about 3 irrespective of the temperature in the presence and absence of chlorides.

The SEM images of steel treated with ionic liquids are presented in Fig. 9-12. Corrosion damages are visible as deposits, crevices, holes and spots. The SEM images confirm

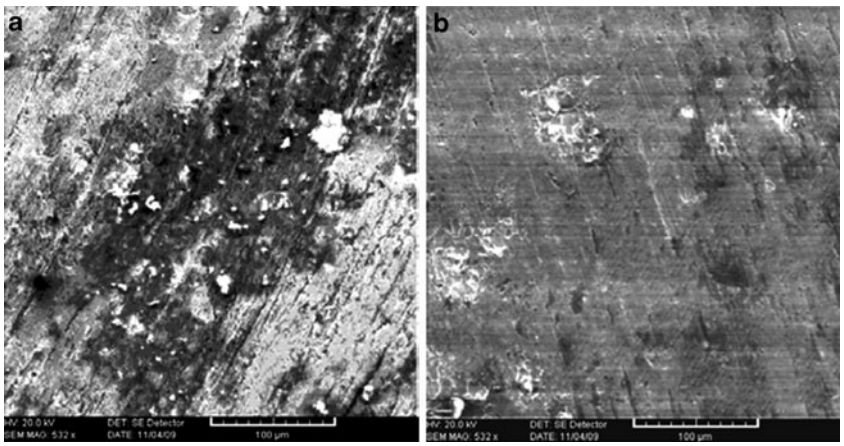

Fig. 9 Morphology of plain steel treated with $BMIBF_4$ at 50°C for 150 h : a/ no MBT b/ 10^{-3} M MBT

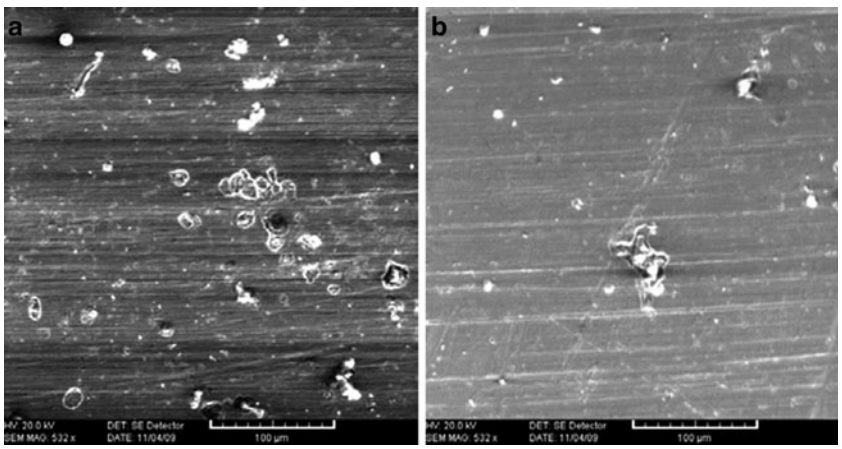

Fig. 10 Morphology of plain steel treated with $BMIBF_4$ at 200 °C for 150 h : a/ no MBT b/ 10^{-3} M MBT

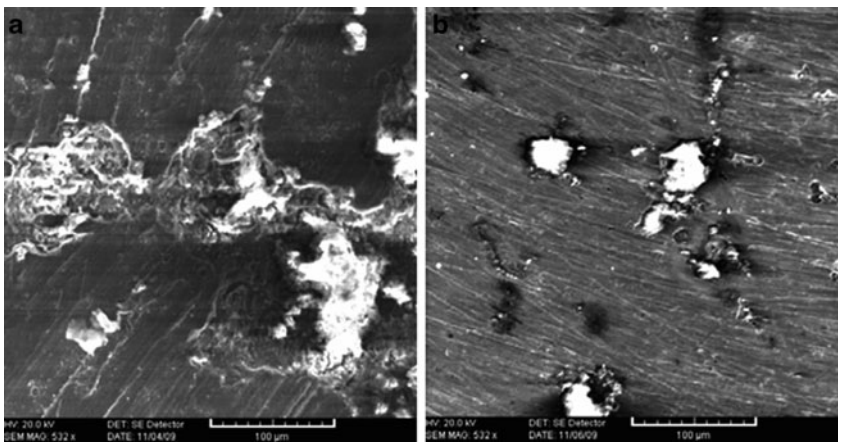

Fig. 11 Morphology of plain steel treated with $BMIBF_4$ containing 0.87 mass % of Cl and 1.3 mass % of water at 50 °C for 150 h : a/ no MBT b/ 10^{-3} M MBT

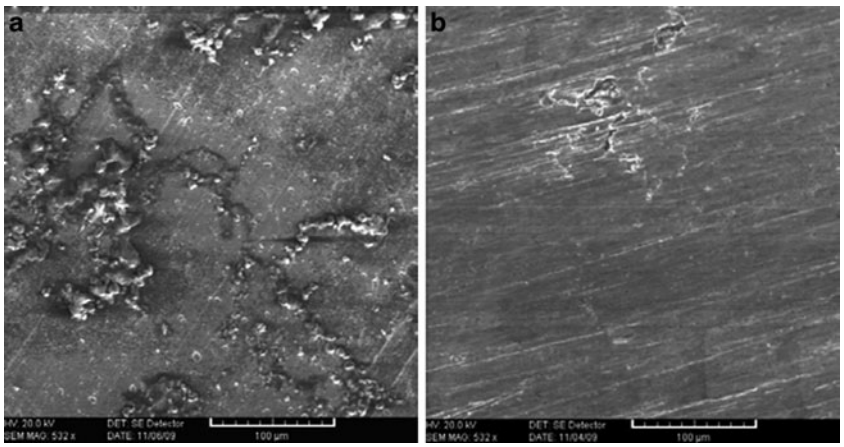

Fig. 12 Morphology of plain steel treated with $BMIBF_4$ containing 0.87 mass % of Cl and 1.3 mass % of water at 200 °C for 150 h : a/ no MBT b/ 10^{-3} M MBT

Table 2 Composition of corrosion products of plain steel at 25°C

	Corrosion medium				
		$BMIBF_4$		$BMIBF_4$ + 0.87 % Cl + 1.3 % water	
Element	Original sample	No MBT	10^{-3} M MBT	No MBT	10^{-3} M MBT
Fe	97.3	58.9	57.4	46.8	54. 9
C	0.20	21.2	27.5	19.5	15.7
S	0.05	b.d.l.	0.3	0.01	0.3
P	0.04	b.d.l.	b.d.l.	0.01	0.01
Si	0.14	0.1	0.09	0.08	0.05
Mn	0.6	0.3	0.3	0.3	0.3
Cr	0.04	0.01	b.d.l.	0.03	0.01
B	b.d.l.	2.2	1.9	3.5	3.0
N	b.d.l.	7.9	4.8	9.4	8.3
O	1. 7	6.6	5.5	12.7	13.7
F	b.d.l.	2.7	2.1	3.6	3.2
Cl	b.d.l.	0.13	0.05	4.0	0.7

b.d.l. = below detection limit

the above results obtained by means of other methods, especially the enhancement of corrosion in the presence of chlorides, and depression of corrosion rate in the presence of MBT.

Figure 9 shows that in the presence of MBT, the layer of corrosion products is more uniform while in absence of MBT local corrosion occurs.

Figure 10 shows the steel covered with a layer of products of thermal decomposition of ionic liquid. In the presence of MBT that layer is more stable while in absence of MBT numerous pits are visible.

Figure 11a indicates pits about 100 μm in diameter produced by an aggressive environment containing chlorides. Similar pits are observed in the presence of MBT (Fig. 11 b), but they are less numerous and smaller.

Figure 12 shows the steel covered with a layer of products of thermal decomposition of ionic liquid. Several pits in that layer are visible but in the presence of MBT they are less numerous and smaller.

The composition of corrosion products obtained on steel at 25°C is summarized in Table 2. Irrespective of the conditions of corrosion that layer contained all elements-constituents of ionic liquid.

Wet and chloride-containing ionic liquid leads to higher concentration of B and F in the corrosion products. The presence of MBT induces a substantial decrease in the concentration of the products of decomposition of ionic liquid in the corrosion products in spite of relatively low concentration of MBT (cf. the concentration of S reported in Table 2). This result proves a strong interaction between MBT and steel and suggests that MBT adsorption occurs directly on the surface.

Conclusion

MBT is an efficient corrosion inhibitor of steel, Cu and Zn in pure and in wet and chloride-containing $BMIBF_4$ at concentration on the order of 10^{-3} M. Further increase in MBT concentration is unlikely to substantially improve the protective properties. We demonstrated that MBT works for pure ionic liquid and for 3 mixtures containing relatively high concentrations of water and/or chlorides, which are higher than typical concentrations of those impurities in commercial ionic liquids. We speculate that MBT works also for lower concentrations of water and/or chlorides than the concentrations studied in this paper.

References

[1] Olivier-Bourbigou H, Magna L, Morvan D (2010) Appl. Catal. A 373: 1
[2] Wasserscheid P, Welton T (2008) Ionic liquids in synthesis, Wiley-VCH, Weinheim.

[3] van Rantwijk F, Sheldon RA (2007) Chem. Rev. 107: 2757
[4] Park S, Kazlauskas RJ (2003) Curr. Opin. Biotechnol. 14: 432
[5] Domańska U (2008) Ionic Liquids in Chemical Analysis, Chapter 1, General Review of Ionic Liquids and Their Properties CRC Press, Taylor & Francis Group, Abingdon, UK.
[6] Li Z, Chang J, Shan H, Pan J (2007) Rev. Anal. Chem. 26: 109
[7] Galiński M, Lewandowski A, Stępniak I (2006) Electrochim. Acta 51: 5567
[8] Hagiwara R, Lee JS (2007) Electrochemistry 75: 23
[9] Van Valkenburg ME, Vaughn RL, Williams M, Wilkes JS (2005) Thermochim. Acta 425: 181
[10] Reddy RG, Zhang Z, Arenas MF, Blake DM (2003) High Temp. Mat. Process. 22: 87
[11] Sun P, Armstrong DW (2010) Anal. Chim. Acta 661: 1
[12] Pandey S (2006) Anal. Chim. Acta 556: 38
[13] Minami I (2009) Molecules 14: 2286
[14] Bermudez MD, Jimenez AE, Sanez J, Carrion FJ (2009) Molecules 14: 2888
[15] Seddon KR, Stark A, Torres MJ (2000) Pure. Appl. Chem. 72: 2275
[16] Jarosik A, Krajewski SR, Lewandowski A, Radzimski P (2006) J. Mol. Liq. 123: 43
[17] Arenas MF, Reddy RG (2003) J. Min. Met. 39: 81
[18] Uerdingen M, Treber C, Balser M, Schmitt G, Werner C (2005) Green Chem. 7: 321
[19] Predel T, Pohrer B, Schluckre E (2010) Chem. Eng. Technol. 33: 132
[20] Perissi I, Bardi U, Caporali S, Lavacchi A, Corr. Sci. 48 (2006) 2349
[21] Perissi I, Bardi U, Caporali S, Frossati A, Lavacchi A (2008) Sol. Energ. Mater. Soll. Cell 92: 510
[22] Bardi U, Chenakin SP, Caporali S, Lavacchi A, Perissi I, Tolstogouzov A (2006) Surf. Interface Anal. 38: 1768
[23] Qu J, Truhan JJ, Dai S, Luo H, Blau PJ (2006) Tribol. Lett. 22: 207
[24] Qu J, Blau PJ, Dai S, Luo H, Meyer HM, Truhan JJ (2009) Wear 276: 1226
[25] Ulman A (1996) Chem. Rev. 96: 1533
[26] Huddleston JG, Visser AE, Reichert WM, Willauer HD, Broker GA, Rogers RD (2001) Green Chem. 3: 156
[27] Lorenz W, Mansfeld F (1981) Corr. Sci. 21: 647
[28] Marczewska-Boczkowska K, Kosmulski M, Mat. Manuf. Proc. (2009) 24: 1173
[29] Ngo HL, LeCompte K, Hargens L, McEwen AB (2000) Termochim. Acta 357-358: 97
[30] Fredlake CP, Crosthwaite JM, Hert DG, Aki SNVK, Brennecke JF (2004) J. Chem. Eng. Data 49: 954
[31] Kosmulski M, Gustafsson J, Rosenholm JB (2004) Thermochim. Acta 412: 47
[32] Zhang J, Liu W, Xue Q (1999) Wear 231: 65

Progr Colloid Polym Sci (2011) 138:173–178
DOI: 10.1007/978-3-642-19038-4_31

A Soft Method for Developing Nanostructured Organic Biomaterials

M. Al Helou[1], M-A. Guedeau Boudeville[1], N. Sanson[2], C. Gérardin[3], and A. Mourchid[1]

Abstract We study new methods for the elaboration of nanoporous biomaterials intended to deliver encapsulated molecules via diffusion. The strategy consists of casting a polylactide biopolymer around templating micelles strictly using soft preparation methods. The micelles are polyion complex micelles prepared from double hydrophilic block copolymers and hydrosoluble polyamines in aqueous solution. We show that when the aqueous solvent is switched to an organic one, the complexes remain stable, although dynamic light scattering measurements show a larger micellar size. The data is compatible with a much extended brush of the micelles in the organic solvent. The study is in progress with the aim to produce porous structures on a nanometric scale by casting biopolymer films around the micellar entities in chloroform.

Keywords Biomaterial • Biopolymer • Micelle • Micellization • Complexes

Introduction

Considerable interest exists in developing implantable and injectable biomaterials for drug delivery, tissue reconstruction and engineering [1]. In particular, biopolymer-based materials are the most attractive choice for such medical applications. This is primarily because they are easily processable, which could allow less or non-invasive therapeutic procedures. Most biomaterials produced as carriers for drug delivery or scaffolds for tissue reconstruction are intended for a fixed period of use. The optimal interval corresponds to the duration of drug release or tissue growth. Hence the remaining structure might be left in place, be removed surgically, or have to degrade. Of course, degradation is preferred. The biomaterials synthesized for drug delivery must allow for fine-tuning of the device properties by adjusting the kinetic of release and degradation time. Nevertheless the release of active molecules from drug carriers developed so far is solely controlled by erosion of the bulk material [2]. Therefore, porous biomaterials could present an alternate and promising pathway to produce tunable devices for controlled release. Such biomaterials are studied for the encapsulation of drugs intended for a long period treatment (cancer, hormonal disorders, tissue engineering. . .) [3]. The research in the field of biomaterials is largely directed towards macro and microporous structures [4]. Several techniques were proposed for the elaboration of porous structures. They include phase separation [5], emulsion-solvent evaporation [6], spray drying [7], and solvent casting/salt leaching [8]. However some difficulties have been encountered in the structures obtained through these methods such as pore size, non connectivity of the pores, inactivation of active molecules, and most importantly, uncontrolled release usually referred to as the burst effect [9]. On the other hand, considerable developments have been made in the field of elaboration of nanostructured inorganic materials. The materials are fabricated by combining the sol-gel chemistry for the synthesis of inorganic matrices and physico-chemistry of surfactant assemblies for the formation of organic mesophases as templates of the inorganic structure [10]. The method allowed better control on the pore size, from few to tens of nm. It is worth adding that the fabrication procedure of these structures involves the use of aggressive treatment steps such as calcination or surfactant removal in organic solvent, which are both highly expensive and environment non-friendly. New strategies were proposed to avoid calcination or the use of unsustainable chemicals by employing soft physical processes. An interesting method was recently proposed which consists in the use of reversible

M. Al Helou (✉)
[1]Matière et Systèmes Complexes, UMR 7057 CNRS/Université Paris Diderot, Paris
e-mail: milad.al-helou@univ-paris-diderot.fr
[2]Physico-chimie des Polymères et Milieux Dispersés, UMR 7615 UPMC/ESPCI/CNRS, Paris
[3]Institut Charles Gerhardt, UMR 5253 CNRS/ENSCM/UM2/UM1, Montpellier

assemblies of hydrosoluble polymers as new recyclable templating systems [11]. The used polymers are double hydrophilic block copolymers (DHBC) that can reversibly assemble upon the change of solution parameters such as temperature, *p*H or ionic strength [12]. The ability to dissociate the micelles within the material allows liberating the porosity. The method has been successfully used for the synthesis of inorganic mesoporous materials.

The aim of the present study is to develop new methods for the fabrication of nanoporous biopolymer materials by combining recent advances in the field of elaboration of nanostructured inorganic materials and biodegradable polymer. For this purpose we synthesized poly(DL-lactide) (PDLLA) copolymerized with poly(ethylene oxide) (PEO).

PEO monomethyl ether was used to initiate the ring-opening polymerization of lactide monomers on its free side chain hydroxyl. The polymerization route was thoroughly discussed in a previous study by our group [13].

We chose the method described above in order to structure our organic materials using soft routes. We investigate the combination of DHBCs with oppositely charged polycations that are able to form stable polyion complexes, PIC, of nanometric size in both aqueous and organic solvents. It is expected that DHBCs will yield the formation of stable complexes in aqueous solution. The PICs will enable us to have a better control on the size and shape of nanopores through the variation of DHBCs characteristics and solution parameters. Thus, for practical and methodological questions, a more systematic investigation of their dispersion and stability in organic media is needed in order to assess their effectiveness for nanostructuring organic materials. Our goal herein is to investigate whether the double hydrophilic poly(methacrylic acid-*block*-ethylene oxide) (PMAA-*b*-PEO) and PEI homopolymers can form soluble complexes and to analyze the shape and size of the morphology in both H_2O and chloroform solvents.

Experimental Section

The homopolymers polyethyleneimine (PEI, $Mn \approx 600$ g/mol) and chitosan ($Mn \approx 5000$ g/mol), the dry organic solvents and D_2O were purchased from Sigma-Aldrich (France). The DHBC PEO-b-PMAA, was purchased from Polymer Source (Canada). The diblock copolymers and homopolymers were used as received unless otherwise specified. Dry chloroform, diethyl ether and deuterated chloroform ($CDCl_3$, Cambridge Isotope) were used as received.

Complexes of PEO_{177}-b-$PMAA_{23}$/polycation were prepared in aqueous solution (deionized water) by electrostatic bonding between PMAA and the polyamine (PEI or chitosan) at a *p*H between 4.5 and 7. In this range of *p*H both the polyacid block and the polyamine are in their ionized form. Typically 100 mg of the PEO-b-PMAA were dissolved in H_2O under magnetic stirring. Then 2.51 ml H_2O solution of PEI (or chitosan), at a NH^+ concentration of 0.1 M is prepared and added to the PEO-b-PMAA solution in order to have a stoechiometric loading ratio defined as $R = \frac{[NH^+]}{[COO^-]} = 1$. This ratio was later varied in this study. The *p*H was then adjusted to 5.5. The final suspension was left under magnetic stirring for 2 hours. The excess salt in solution was removed by dialysis against deionized water for 1 week. Then the samples were freeze-dried and stored at 4°C prior to use.

The freeze-dried complexes and PEO-b-PLA copolymer were dissolved in chloroform to a concentration of 0.1 g/ml. The solution was vortexed and sonicated to ensure total dispersion and homogeneity. Then it was poured onto glass microslide and left to dry under room conditions for 2 days to cast copolymer films with approximately 0.1 mm thickness. The resulting dried film was immersed in an aqueous solution at a *p*H > 8 to initiate the disassembly of the polymeric micelles and promote their elimination. The films were later placed under vacuum for 24 h to ensure total evaporation of the solvent. However, the study of the films' structure and morphology is still in a preliminary stage and thus no results will be shown in this study regarding the films.

Sample solutions for dynamic light scattering, DLS, were filtered three times on 0.45 μm filters. Measurements were carried out with a BI-9025AT goniometer and correlator (Brookhaven) at a wavelength of $\lambda = 633$ nm and fixed scattering angle of 90°.

Small angle neutron scattering, SANS, experiments were performed at Laboratoire Léon Brillouin (Saclay, France), on the PAXY beamline at scattering wave vectors q in the range of 0.005 and 0.4 $Å^{-1}$. Polymer solutions for SANS were prepared in D_2O or $CDCl_3$ to enhance the scattering length density contrast between the polymers and the solvent. The scattering intensity per unit volume $I(q)$ of a monodisperse system can be expressed as the product of the contrast, form and structure factors. In dilute systems, the structure factor is reduced to unity and $I(q)$ records the evolution of the form factor. We used the core-shell model described by Pedersen and Gerstenberg [14] with a lognormal distribution to model the scattering intensities in absolute scale (in cm^{-1}) of dilute samples. To maintain consistency between the results a maximum number of parameters were fixed, such as scattering length densities and concentrations.

Results and Discussion

In figure 1a the normalized autocorrelation function obtained on an aqueous solution of PEO-b-PMAA/PEI at $C = 0.001$ g/ml, ratio $R = 1$ and pH = 6 is shown. This DLS data show typical behavior of a micellar solution in the dilute regime whose correlation function is easily fitted to a standard second order cumulant expression, with the quality factor taken as a measure for the single exponential transient decay [15]. We checked that the first cumulant is a quadratic function of the wave vector for all the sample concentrations studied. The exponential fit to data in figure 1a yields a mean hydrodynamic diameter $D_h = 44$ nm. DLS experiments were also carried out on aqueous PEO-b-PMAA/PEI solutions after freeze-drying of the sample and redispersion in water. This procedure was performed in order to ensure that the freeze-drying operation does not alter the shape and size of the PIC. In both cases we obtained similar hydrodynamic diameter values within experimental uncertainty. The stability of the micellar complexes as a function of solution pH, at fixed micellar concentration, was studied by recording the absolute light scattering intensity, I, and measuring D_h. Dynamic light scattering data show similar evolution of I and D_h for complexes formed with either PEI or chitosan. In the following only data on PICs with PEI are discussed.

Figure 2a shows the variation of I and D_h as a function of the solution pH at $R = 1$. We note that, as the pH increases from 2, both I and D_h increase, reach a peak value at pH = 6 and then decrease when the pH increases from 6 to 10.

The evolution of the hydrodynamic diameter and absolute scattering intensity with the solution pH shows the expected behavior for this specific PIC. Indeed, when the solution pH is set between 5 and 7, both PMAA and PEI (or chitosan) exist in their ionized form since the $p\mathrm{K_a}$ of PMAA = 5.5, $p\mathrm{K_b}$ of PEI = 7-9 ($p\mathrm{K_b}$ of chitosan = 6.5) [16]. Therefore all the negative and positive sites on the polyelectrolyte backbone are accessible in this pH range. When PMAA and PEI are mixed together there is complete and strong association of the two polyelectrolytes due to charge neutralization. The formation of the electrostatic complex triggered by the pH yields PIC micelles with a finite size and stabilized by a corona of PEO chains in water.

The effect of R on the PIC size, at fixed pH = 6 is presented in figure 2b. We notice that when R increases from 0.2 to 1, the data show an increasing dependency of D_h and I. Such behavior further enhances the evidence of the role of charge neutralization in the formation of PIC micelles. This result shows that at low polyamine content, the PMAA block still interacts with the cationic polyamine to form small PIC micelles whose hydrodynamic diameter is mainly controlled by the PEO surrounding corona.

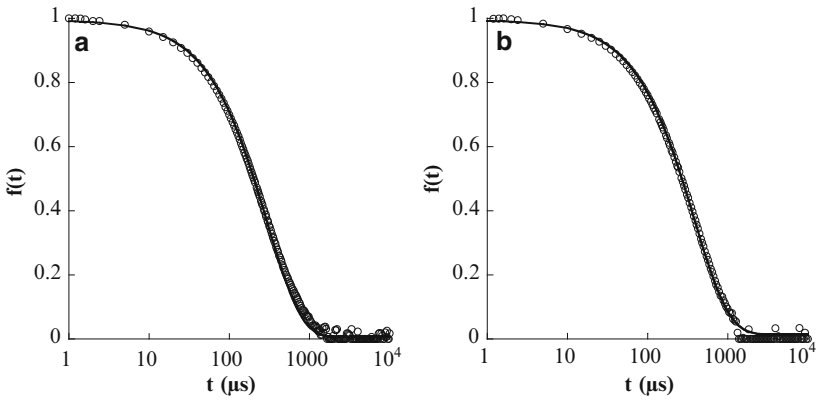

Figure 1 DLS intensity of PEO-b-PMAA/PEI micelles in H_2O and $CHCl_3$ (a and b) respectively): (○) experiment, (—) model

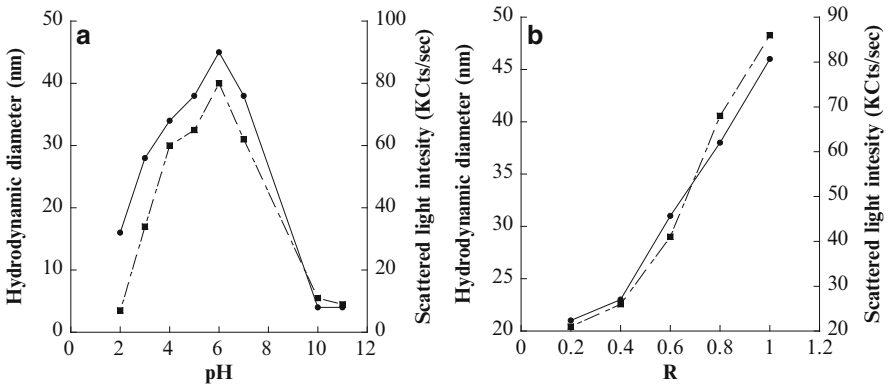

Figure 2 Variation of (●) hydrodynamic diameter and (■) scattering light intensity of PEO-b-PMAA/PEI micelles as a function of the pH at a molar ratio $R = 1$ and as a function of R at pH 6 (a and b respectively)

In the following a charge ratio R of 1 will be chosen to study the stability of the PIC micelles in chloroform. For this purpose, the PICs formed in H_2O at pH = 6 were freeze-dried and redispersed in anhydrous chloroform. The solutions were filtered and studied by DLS in the dilute regime. In figure 1b the normalized autocorrelation function obtained on a solution of PEO-b-PMAA/PEI at C = 0.001 g/ml is shown. Similarly to the data in water, the DLS data show the expected behavior for the correlation function of micellar solutions which is easily fitted to a standard second order cumulant expression with the quality factor taken as a measure for the exponential decay. We also checked that the first cumulant is a quadratic function of the wave vector for all the samples studied in chloroform. The exponential fit to data, also shown in figure 1b, yields a mean hydrodynamic diameter D_h = 125 nm. The large increase of the micellar hydrodynamic size from 44 nm in water to 125 nm in chloroform could be due to partial aggregation of PIC seen as single large objects by DLS. However a calculation of the stretch length of the PEO-b-PMAA chain, which is the upper limit possible micelle radius, can be calculated as 75 nm which indicates that the measured D_h of 125 nm could also suggest that the coronal PEO layer in the organic solvent is fully stretched. This point will be discussed in more detail below.

SANS measurements were performed to shed light on the morphology of the PIC during the varying steps of the elaboration process. Figure 3a shows the scattering intensity as a function of the wave vector q of micellar complexes in aqueous solution (D_2O) at a concentration C = 0.03 g/ml. The scattering intensity shows a typical behavior of non-interacting objects. The data display a q^{-2} variation at high q values, q^{-4} variation at intermediate q values and plateau in the scattering intensity in the low q domain investigated. This evolution is typically observed for spherical core-shell morphologies of block copolymers and surfactants in the dilute regime. To get more insights into the shape and size of the PICs, we used the core-shell model proposed by Pedersen and Gerstenberg for copolymer micellar solutions [14]. In this model, the copolymer micelles are assumed to have an inner dense core (PMAA/PEI) surrounded by brushes (PEO) which obey Gaussian statistics. It yields the core-shell form factor of the spherical micelles with four different terms that are mainly dependant on the morphology parameters of the PIC, i.e., core radius, R_c, aggregation number, N_{agg}, and the PEO brush gyration radius, R_g. The size polydispersity (log-normal distribution of core radii) has a standard deviation σ. The scattering data are perfectly fitted by this model as it can be seen in figure 3a. The parameters of the model are displayed in Table 1. It yields a core radius R_c = 4.4 nm, a shell radius of gyration R_g = 4 nm and an aggregation number N_{agg} = 28. The standard deviation of the log-normal distribution of core radii σ = 0.01. Such low standard deviation is typically observed for copolymer micelles with low polydispersity index of molecular weight distribution (~ 1.1 for the DHBC used here). The radius of gyration of the PIC can further be estimated by using the Guinier approximation in the domain of low wave vector q [17]. The estimated radius of gyration of the micelle is 10.5 nm which is in agreement with the micelle core diameter. The ratio $2R_g/D_h$ for these PICs in aqueous solution is equal to 0.47. Such a small ratio (below 0.77) is expected for a core-shell morphology with a rapidly varying radial density within the micelle [18]. From the experimental data and the fit parameters we envision the PIC as electrostatic aggregates of oppositely charged polyelectrolytes forming the core and stabilized by PEO chains in water.

The SANS experiments were carried out on PIC in d-chloroform for C between 0.005 and 0.2 g/ml. It is worth adding that it was necessary to study more diluted d-chloroform than D_2O solutions because the scattering curves on

Table 1 SANS (DLS) fitting parameters for micelles in D_2O and $CDCl_3$ (H_2O and $CHCl_3$ respectively)

SANS data (lengths are in nm)						DLS data
Solvent	R_c	R_g	N_{agg}	σ	R_g(Guinnier)	D_h (nm)
D_2O	4.4	4	28	0.01	10.5	44
$CDCl_3$	3.1	4.6	28	0.35	~12.5	125

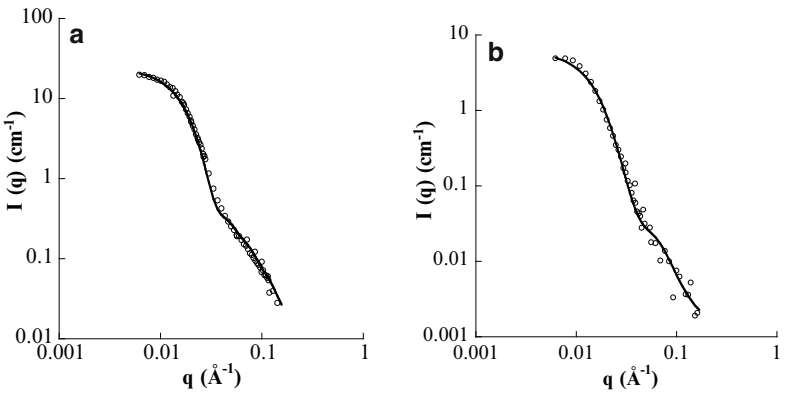

Figure 3 SANS intensity of PEO-b-PMAA/PEI micelles in D_2O, C = 0.03 g/ml, and $CDCl_3$, at C = 0.005 g/ml (a and b respectively): (○) experiment, (—) model

organic solutions showed the existence of correlation peaks down to $C = 0.03$ g/ml which contrasts with samples in D_2O. For the most diluted sample ($C = 0.005$ g/ml) the scattering intensity presented in figure 3b does not show the existence of any structure peak thus the correlations between the PIC can be neglected. The scattering intensity shows a similar behavior to that of samples in D_2O with a q^{-2} and q^{-4} variations at high and intermediate q values respectively, and a plateau in the low q domain investigated. We performed a similar procedure to model the scattering data to the form factor by setting the aggregation number to that found for the micellar complexes in D_2O in order to maintain consistency between the two sets of data. The model curve is also displayed in figure 3b and the parameters of the fit are reported in Table 1.

The core radius was estimated to be $R_c = 3.1$ nm and the PEO gyration radius $R_g = 4.6$ nm. The small decrease in the core radius compared to the value found for the samples in D_2O is most likely due to the dehydration of the polyelectrolyte forming-core in $CDCl_3$. The log-normal distribution of core radii yields a standard deviation $\sigma = 0.35$. This standard deviation value, which is higher than that found for the samples in D_2O, could be a consequence of the deformation of the cores upon dehydration. The increase of the shell gyration radius in comparison with that found in samples for D_2O is in agreement with the results obtained from DLS measurements in both chloroform and water.

It has been reported before that PEO chains have a larger expanded conformation in $CHCl_3$ than in H_2O [19]. The authors in this reference studied PEO homopolymers in various organic solvents and in water by measuring the intrinsic viscosity in the low polymer concentration domain. The highest value for the intrinsic viscosity was found for PEO solubilized in chloroform while the lowest value was measured in water. Since the intrinsic viscosity only depends on the hydrodynamic diameter of the polymer, the results suggest that the PEO chains have a more stretched conformation in chloroform than water. These findings are in agreement with our DLS data which show systematically larger hydrodynamic diameters in chloroform than in water. On the other hand, the results obtained here from the SANS experiments suggest that the freeze-dried PIC micelles redispersed in *d*-chloroform maintain the same aggregation number since the core-shell model describes well the scattering intensities in absolute scale. This is a strong indication that the PICs exist in both solvents as isolated micelles thus excluding aggregation.

We plotted the scattering data in the form of q^4I/C as a function of q in Figures 4a and 4b for the micellar solutions in both D_2O and $CDCl_3$ respectively, for different sample concentrations. This representation of the concentration normalized scattering intensity, called Porod plot, is known to enhance the features of the form factor in the scattering data. In both solvents, the observed oscillations of the normalized scattered intensity superimpose in intensity and position, within experimental uncertainties, demonstrating that this feature is a form factor independent of concentration and that the shape and size of the individual scattering objects do not vary upon concentration. Furthermore, the scattering intensity on organic solutions, at concentration $C \geq 0.05$ g/ml, exhibit a structure peak (the correlation peak on samples in D_2O is apparent only when $C > 0.1$ g/ml). The scattering data on concentrated samples in $CDCl_3$ are shown in the inset of figure 4c for $C = 0.05$, 0.1 and 0.2 g/ml. The data clearly show that the position of the peaks, q_0, shifts toward high q values as the micellar concentration increases. The position of the correlation peak is related to $d_0 = \frac{2\pi}{q_0}$, which represents the distance between two scattering neighboring spheres assuming a random close packing structure [20]. For core-shell scattering spheres having a constant core radius, R_c, the dilution law which describes the evolution of the correlation distance as a function of the polymer concentration, is given by the general formula: $d_0 = \frac{2\pi}{q_0} = AR_c\phi_c^{-1/3}$, where A is a constant that depends on the structure considered and ϕ_c is the volume fraction of the micellar core. We plotted in figure 4c the volume fraction of the PIC micellar core as a function of $(q_0/\pi)^3$. The dotted line in this figure represents the linear least-squares fit to experimental data.

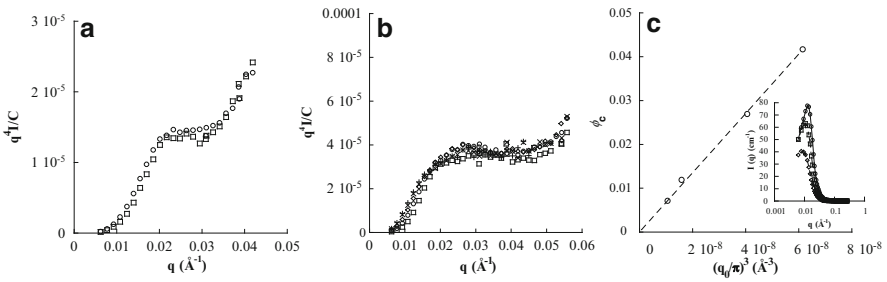

Figure 4 SANS plot of the concentration normalized intensity q^4I/C (Porod plot) in D_2O and $CDCl_3$ (a and b respectively); a) (+)0.005 g/ml, (×) 0.01 g/ml, (◇) 0.05 g/ml, (○) 0.1 g/ml, (□) $C = 0.2$ g/ml. b), (○) 0.1 g/ml, (□) $C = 0.2$ g/ml. c) Evolution of volume fraction with the position of correlation peak: (○) experimental data, (- -) linear least-squares fit. Inset: SANS intensity of PEO-b-PMAA/PEI micelles in $CDCl_3$ at $C = 0.05$, 01 and 0.2 g/ml

As expected for a three dimensional swelling, the volume fraction depends linearly on $(q_0/\pi)^3$ and decreases to zero as ${q_0}^3$ decreases to zero.

Both the superimposition of the data in the Porod representation and the linear variation of volume fraction with ${q_0}^3$, which is indicative of a 3 dimensional swelling law, strongly suggest that these PIC micelles are homogeneously distributed in space. These last data give an additional support on the good dispersion and stability of the PIC micelles in both water and organic solvent investigated in this study.

Conclusions

Polyion complex micelles were prepared in aqueous solution by using double hydrophilic block copolymers PEO-b-PMAA and polyamines. The formation of the complexes is triggered by electrostatic attraction between PMAA and the polyamine because they are oppositely charged. The PEO block forms the sterically stabilizing brush and prevents the aggregation of the polyion complexes. We studied the micellar characteristics as a function of *p*H and complexing ratio between the two polyelectrolytes. We demonstrated that the complexes are stable after freeze-drying and redissolution in chloroform although the hydrodynamic diameter of the PIC micelles was found to depend on the solvent. The neutron scattering data suggest that this dependence is due to favorable expansion of the PEO brush in the organic solvent. Further investigations are underway in order to shed more light on the structure of the films prepared by mixing both the biopolymer and the micelles.

Acknowledgement We acknowledge the support of the CNRS/CEA Léon Brillouin laboratory in providing the neutron facilities used in this study. We especially thank Dr A. Lapp for his assistance with the SANS measurements.

References

[1] Jeong B, Bae YH, Lee DS, Kim SW (1997) Nature 388: 860.
[2] Reed AM, Gilding DK (1981) Polymer 22: 494.
[3] Senuma Y, Franceschin S, Hilborn JG, Tissieres P, Bisson I, Frey P (2000) Biomaterials 21: 1135.
[4] McGuigan AP, Sefton MV (2007) Biomaterials 28: 2547.
[5] Zhao CS, Liu XD, Nomizu M, Nishu N (2004) J Colloid Interface Sci 275: 470.
[6] Dhanaraju MD, Vema K, Jayakumar R, Vamsadhara C (2003) Int J Biomed Mater Res 66A: 441.
[7] Wang L, Chaw CS, Yang YY, Moochhala SM, Zhao B, Ng S, Heller J (2004) Biomaterials 25: 3275.
[8] Mikos AG, Sarakinos G, Leite SM, Vacanti JP, Langer R (1993) Biomaterials 14: 323.
[9] Fu K, Harrell R, et al. (2003) J Pharma Sci 92: 1582.
[10] Tanev PT, Pinnavaia TJ (1995) Science 267: 865.
[11] Baccile N, In M, Gérardin C, Reboul J, Luck F, Van Donk S. Patent WO2009081000.
[12] Baccile N, Reboul J, Blanc B, Coq B, Lacroix-Desmazes P, In M, Gérardin C (2008) Angewandte Chemie Int Ed 47: 8433.
[13] Al Helou M, Anjum N, Guedeau-Boudeville M-A, Rosticher M, Mourchid A (2010) Polymer 51:5440.
[14] Pedersen J; Gerstenberg M (1996) Macromolecules 29: 1363.
[15] Kops-Werkhoven M M, Fijnaut H M (1981) J Chem Phys 74: 1618.
[16] Reboul J (2009) Assemblage induit et réversible de copolymères à blocs double hydrophiles. PhD thesis. University of Montpellier II.
[17] Guinier A. Fournet G (1955) Small-angle scattering of X-rays; Wiley: New York
[18] Pispas S, Hadjichristidis N (2003) Langmuir 19: 48.
[19] Son K W, Youk J H, Lee T S, Park W H (2004) Polymer 45: 2959.
[20] Grandjean J, Mourchid A (2005) Phys Rev E 72:041503.

Progr Colloid Polym Sci (2011) 138:179–182
DOI: 10.1007/978-3-642-19038-4_32

Interfacial Tensiometry of Tracheal Aspirate from Infants with Neonatal Respiratory Distress Syndrome

A. Jordanova[1], A. Tsanova[2], G. As. Georgiev[3], and D. Chakarov[4]

Abstract The interfacial properties of tracheal aspirate from infants with untreated neonatal respiratory distress syndrome (NRDS), and NRDS infants after therapy with the exogenous surfactant *Curosurf*® were assessed. The interfacial characteristics of the aspirate (equilibrium surface tension, maximal and minimal surface tension during lateral compression-decompression cycles) were determined with the pendant drop method. Our results show that the tracheal aspirate of infants with untreated NRDS had high equilibrium, maximal and minimal surface tension values. In contrast, the samples from infants, treated with *Curosurf*®, showed lower surface tension values, suggesting that the application of *Curosurf*® improves the composition and the properties of the pulmonary surfactant in the infant lung.

Keywords *Alveolar surfactant* • *Curosurf*® • *Pendant drop method* • *Surface tension*

Introduction

The lung alveolar surfactant (AS) is a complex lipid-protein mixture, essential for the normal respiratory activity [1-4]. The main AS function *in vivo* is to reduce the alveolar surface tension (γ, mN/m) and to provide alveolar stability [5, 6]. The absence of a "mature" AS in the lungs is the main reason for the development of neonatal respiratory distress syndrome (NRDS) that often has a lethal outcome [7].

The modern NRDS therapy includes the use of different native or synthetic exogenous surfactants (ES), like the native surfactant *Curosurf*®. ES function as analogues for normal human AS. The main characteristics of these preparations are their strong surface activity upon spreading at the air/water interface and their specific respiratory dynamic mechanical and physical characteristics during alveolar contraction and expansion [8-12].

In order to determine the infants' lung maturity and the necessity of surfactant therapy it is of great importance to substantiate the functionality of the alveolar surfactant, derived via invasive techniques [13]. Several techniques and models have been largely used to investigate interfacial physicochemical properties *in vitro* and to assess clinical efficiency of ES *in vivo*: the Langmuir monolayer technique in combination with Wilhelmy plate method for surface tension measurements and black foam film method for determination of the ability of ES for stable film formation [14]. The pendant drop method combined with the Axisymmetric Drop Shape Analysis (ADSA) has been also used for similar purposes [4, 15-18].

The aim of the work presented is to evaluate the physiological status of tracheal aspirate from infants with NRDS before and after *Curosurf*® therapy via interfacial tensiometry. The measurements are made by the pendant drop method, which requires a minimal volume of the clinical samples.

Materials and Methods

***Curosurf*® (Chiesi Farmaceutici, Parma, Italy)** is a natural surfactant extract, prepared from porcine lung, containing almost exclusively polar lipids, in particular phosphatidylcholine (about 70% of total phospholipid content), phosphatidylglycerol (about 30% of total phospholipids content) and about 1% of surfactant associated hydrophobic proteins SP-B and SP-C. The surfactant was suspended in 0.9 % sodium chloride solution. The pH was adjusted as required

A. Jordanova (✉)
[1]Institute of Biophysics and biomedical engineering, Bulgarian Academy of Sciences, 1113 Sofia, Bulgaria
e-mail: albena@biofac.uni-sofia.bg
[2]Faculty of Medicine, St. Kl. Ohridski University of Sofia, 1407 Sofia, Bulgaria
[3]Faculty of Biology, St. Kl. Ohridski University of Sofia, 1164 Sofia, Bulgaria
[4]Sheinovo Hospital, 1504 Sofia, Bulgaria

with sodium bicarbonate to a pH of 6.2 to aid mimicry of the lung environment.

Tracheal aspirate (TA) was obtained by low volume lavage (1 ml) from intubated newborns with NRDS. Exogenous surfactant was administered in accordance with international protocols for *Curosurf*® in the sixth postnatal hour. TA was obtained prior to and 12 hours after surfactant administration. For control the pure *Curosurf*® dispersion was also tested.

The pendant drop method allows study of extracted moiety surface behavior of small aliquots of the tracheal aspirate. A KSV CAM 101 (KSV Instruments Ltd., Finland) was used for tensiometry. The determination of surface tension was performed using the Axisymmetric Drop Shape Analysis (ADSA) software programme. The entire setup was controlled by a Windows-integrated program, including the ADSA surface tension calculation algorithm. The sampling volume was 50µl in which 15 minutes were allowed to elapse after the axisymmetric drop formation to obtain an adsorption equilibrium and the surface tension values $\gamma_{equilibrium}$ (γ_{eq}, mN/m) can thus be determined. Post formation 10 successive cycles of drop compression/decompression were performed in which the drop surface area was modified five-fold (from 100% to 20%). During these "dynamic" conditions the surface characteristics, maximal surface tension (γ_{max}, mN/m) at 100% of the drop surface, and minimal surface tension (γ_{min}, mN/m) at 20% of the drop surface, were determined. With the aid of a camera connected to the apparatus a series of images with different timeframe of measurement (from 60 to 300 pictures per minute) were taken and the surface parameters were determined. All experiments were performed at 22 °C.

Results and Discussion

The exogenous surfactant *Curosurf*® is indicated clinically for the treatment of NRDS in premature infants. The product has been shown to reduce mortality associated with NRDS [19–22]. Shortly after administration, the surfactant rapidly coats the alveoli to safeguard the lung against collapse. By reducing surface tension, *Curosurf*® helps facilitate lung expansion and gas exchange in premature infants which improves the functioning of the alveoli.

Our *in vitro* results showed a significant difference in surface tension values before (10 samples) and after *Curosurf*® therapy (12 samples). In premature infants (with body mass from 600 to 2500 grams) high equilibrium surface tension values (45 mN/m) were detected, while after treatment with *Curosurf*® this value decreased to 33 mN/m (which approached the equilibrium value of the pure *Curosurf*® preparation, 25 mN/m) (Fig. 1).

The dynamic characteristics of the samples studied also showed a significant improvement after the exogenous surfactant preparation application: γ_{max} reduced from 52 mN/m before the therapy to 32 mN/m after treatment with *Curosurf*®. The maximal surface tension of the pure preparation was 25 mN/m, i.e. tracheal aspirate values approached the parameters of the exogenous surfactant. The results are shown in Fig. 2.

A similar tendency (of improvement the dynamic characteristics of the samples after *Curosurf*® application) was observed regarding the γ_{min} values monitored. During the drop compression to 20% of its initial surface a minimal surface tension value of the clinical samples before the

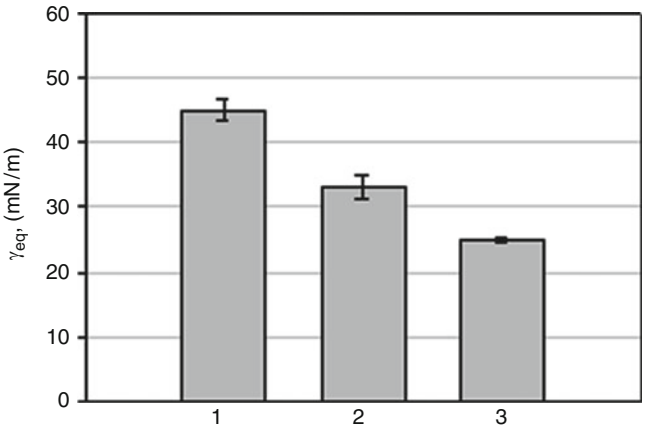

Figure 1 Surface tension equilibrium values, γ_{eq} (mN/m) of clinical samples from infants with NRDS: 1. before *Curosurf*® therapy, n=10; 2 – after *Curosurf*® therapy, n=12. 3 - *Curosurf*® pure dispersion for control. n-number of clinical samples. Data are presented as mean values ± SD (minimum three different drops of each sample)

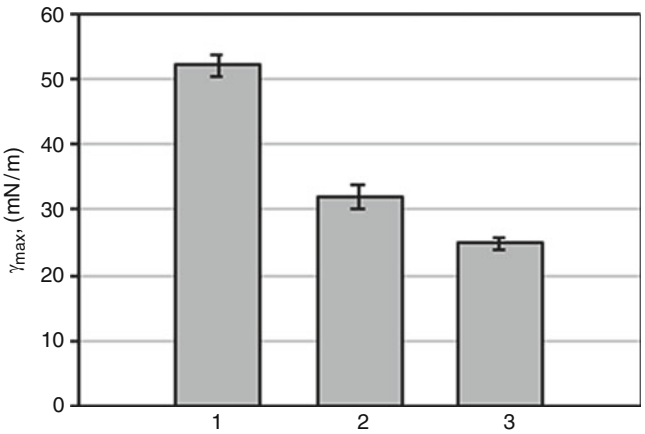

Figure 2 Surface tension maximal values, γ_{max} (mN/m) at 100% of the drop surface of clinical samples from infants with NRDS: 1. before *Curosurf*® therapy, n=10; 2 – after *Curosurf*® therapy, n=12. 3 - *Curosurf*® pure dispersion for control. n-number of cinical samples. Data are presented as mean values ± SD (minimum three different drops of each sample)

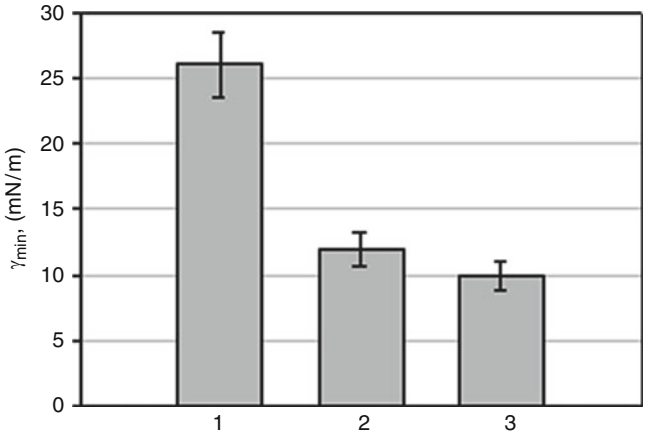

Figure 3 Surface tension minimal values, γ_{min} (mN/m) at 20% of the drop surface of clinical samples from infants with NRDS: 1. before *Curosurf*® therapy, n=10; 2 – after *Curosurf*® therapy, n=12. 3 - *Curosurf*® pure dispersion for control. n-number of clinical samples. Data are presented as mean values ± SD (minimum three different drops of each sample)

therapy with *Curosurf*® of 26 mN/m was measured. After treatment γ_{min} decreased significantly to 12 mN/m, which resembled the pure surfactant parameter studied (γ_{min} = 10 mN/m, Fig. 3).

The results showed that the infants with untreated NRDS had high equilibrium, maximal and minimal γ values of the tracheal aspirate. In contrast, the clinical samples from infants after surfactant therapy with *Curosurf*® showed low surface tension values, suggesting that the application of the exogenous surfactant improved the composition and the properties of the pulmonary surfactant in the infants. These results are in agreement with previous reports regarding the efficiency of surfactant application [14].

The findings presented in this note represent a physicochemical proof *in vitro* of the efficiency of the *Curosurf*® treatment *in vivo*. On the other hand, they demonstrate the applicability of the pendant drop ADSA, which requires a minimal amount of tracheal aspirate, as a fast, informative and useful technique for in-time alveolar surfactant diagnostics.

Acknowledgement We acknowledge the valuable help of our mentors Prof. Emilia Christova (Faculty of Public Health, Medical University of Sofia), Prof. Christian Vassilieff (Faculty of Chemistry, St. Kl. Ohridski University of Sofia) and Prof. Zdravko Lalchev (Faculty of Biology, St. Kl. Ohridski University of Sofia).

This work was financially supported by the Bulgarian Ministry of Education, Youth and Science, project N D002-107/08.

References

1. Schurch S, Lee M, Gehr P (1992) Pure Appl Chem 64: 1745
2. Griese M (1999) Eur Respir J 13: 1455
3. Saxena S (2005) Research News 91-96
4. Zuo YY, Veldhuizen RAW, Neumann AW, Petersen NO, Possmayer F (2008) BBA 1778: 1947
5. Veldhuizen EJ, Haagsman HP (2000) BBA 1467: 255
6. Whitsett JA, Weaver TE (2002) N Engl J Med 347:2141
7. Stevens TP, Sinkin RA (2007) Chest 131:1577
8. Goerke J (1997) Curr Opin Colloid Interface Sci 2: 526
9. Lalchev ZI (1997) Monograph: Surface Properties of Lipids and Proteins at Bio-Interfaces, Chapter N 17. In: KS Birdi (ed) Handbook of surface and colloid chemistry, CRC Press: Boca Raton New York Tokyo, pp 625
10. Exerova D, Kruglyakov P (1998) Foam and Foam Films, Elsevier
11. Poulain FR, Clements JA (1995) West J Med 162: 43
12. Hennes HM, Lee MB, Rimm AA, Shapiro DL (1991) Am J Dis Child 145: 102
13. Hallman M (1991) Acta Anaesthesiol Scand, 35 [Suppl 95]: 15
14. Lalchev Z, Georgiev G, Jordanova A, Todorov R, Christova E, Vassilieff CS (2004) Coll Surf B 33: 227
15. Kwok DY, Tadros B, Deol H, Vollhardt D, Miller R, Cabrerizo-Vilchez MA, Neumann AW (1996) Langmuir 12: 1851
16. Li JB, Miller R, Vollhardt D, Weidemann G, Moehwald H (1996) Colloid Polym Sci 274: 995
17. Wege HA, Holgado-Terriza JA, Gálvez-Ruiz MJ, Cabrerizo-Vlchez MA (1999) Coll Surf B 12: 339
18. Zuo YY, Neumann AW (2005) Tenside Surf Det 42: 126
19. Verder H, Albertsen P, Ebbesen F, Greisen G, Robertson B, Bertelsen A, Agertoft L, Djernes B, Nathan E, Reinholdt J. (1999) Pediatrics 103: E24.
20. Brower RG, Matthay MA, Morris A, Schoenfeld D, Thompson TB, Wheeler A (2000) N Engl J Med 342: 1301.
21. Darkin J, Griffiths M (2002) Thorax 57: 79
22. Dani C, Bertini G, Pezzati M, Cecchi A, Caviglioli C, Rubaltelli FF (2004) Pediatrics 113: e560

Progr Colloid Polym Sci (2011) 138:183–188
DOI: 10.1007/978-3-642-19038-4_33

Micellar and Solvent Effects on Electrochemical Behaviour of Antioxidants

J. Narkiewicz-Michalek[1], M. Szymula[1], and C. Bravo-Díaz[2]

Abstract We have carried out an electrochemical study of a number of relevant hydrophilic and hydrophobic antioxidants in the micellar sodium dodecyl sulphate, (SDS), solutions to determine the effects of solvent polarity, acidity and SDS concentration on their diffusion coefficients. Cyclic voltammograms show that both peak currents, i_p, and peak potentials, E_p, are affected by SDS concentration reaching a plateau region where with the further increase in the surfactant concentration i_p and E_p remain unchanged which indicates the existence of the saturated surfactant adsorption layer on the GC electrode surface. For the hydrophilic antioxidants: ascorbic acid and propyl gallate the diffusion coefficients vary only by a factor of ~0.8-2.0 in the presence of SDS micelles related to their values in the buffer solution due to the fact that they did not associate with the anionic micelles. For their hydrophobic derivatives the diffusion coefficients in the SDS micellar aqueous solution are very low compared to their values in the mixed aqueous-organic solvents. It suggests that in the mixed solvents antioxidant molecules are in a singly dispersed state whereas in the aqueous SDS solution they are strongly incorporated into the micelles.

Keywords Antioxidants • Electrochemical oxidation • Micellar systems

Introduction

There has been substantial interest in the electrochemistry in the colloidal systems during the last years because solubilisation of electrochemically active compounds in, for instance, micellar systems might significantly change their redox parameters as well as the stability of the electrochemically generated radicals [1-4]. Rusling and co-workers [3] suggested that the micelle-bound systems are attractive candidates for future designs that mimic redox events in such complex systems as biological membranes or food products.

This is the case of antioxidants, which are widely applied for the control of lipid oxidation reactions that lead to the development of undesirable off flavours, nutrient loss, and potential formation of toxic products [5-7]. The effectiveness of antioxidants depends on their polarity, lipid substrate, pH, temperature, concentration of antioxidants, and physical properties of food [7-10].

Here we have undertaken a study of the effects of SDS micellar systems and added organic solvents on the electrochemical behaviour of relevant antioxidants. In the last years we have taken great interest in determining the distribution of antioxidants in the emulsified systems, and for that purpose we have developed a novel kinetic method based on the reaction between a hydrophobic arenediazonium ion and the antioxidants which allows to determine the partition constants of the antioxidant between the oil, water and interfacial regions of the emulsified system [10-12]. The kinetic results are interpreted using the pseudophase kinetic model based on the hypothesis that the rates of chemical reactions are not limited by transport of reactants, i.e., that all reactants are in the dynamic equilibrium throughout the reaction. This hypothesis was experimentally proved by fitting the kinetic data to the equations derived from the pseudophase model, but determination of the diffusion coefficients of the reactants in the studied system will be very useful from the conceptual point of view to confirm or discard the mentioned idea.

The aim of the manuscript is to determine the diffusion coefficients and other relevant electrochemical parameters of antioxidants in water, micellar systems and organic solvents. As the first approach, we employed vitamin C (L-ascorbic acid, AA) and propyl gallate, (PG), and their lipophilic derivatives: ascorbyl-6-palmitate (AA16) and lauryl gallate, (LG), because they are well-known bioactive

M. Szymula (✉)
[1]Faculty of Chemistry, Maria Curie-Skłodowska University, Lublin, 20-031, Poland
e-mail: szymula@hektor.umcs.lublin.pl
[2]Facultad de Quimicas, Universidad de Vigo, 36-200, Vigo-Pontevedra, Spain

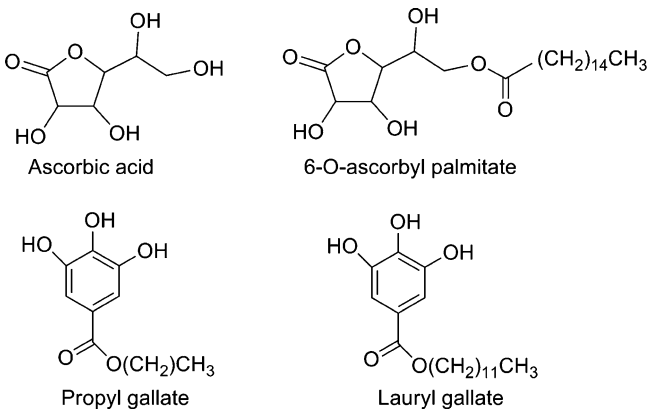

Scheme 1 Chemical structures of the antioxidants employed in this work. All compounds are widely used as antioxidants in the food industry

reducing agents whose electrochemistry was extensively studied [13-19] and substantial knowledge on their reactivity in the micellar systems is available [20-23]. Their chemical structures are displayed in Scheme 1.

A variety of techniques can be employed to determine the diffusion coefficients including ionic conductivity, optical methods, dispersion techniques and electrochemical methods [1, 24, 25]. We employed the cyclic voltammetry method, CV, because it is rapid, affordable and sensitive enough for determination of physiological concentrations of the electroactive molecules and was previously used to determine the diffusion coefficients [26].

Experimental

Materials

The reagents were of high grade purity and were used as received. Ascorbic acid (AA), propyl gallate (PG) and their hydrophobic derivatives: 6-O-ascorbyl palmitate (AA16) and lauryl gallate (LG), sodium dodecyl sulphate SDS and acetonitrile (ACN) were from Fluka, Germany. The other chemicals were from POCh, Poland.

Instrumental

CV electrochemical experiments were carried out by using a μ-Autolab analyzer (Eco Chemie, the Netherlands) and an electrode stand (mtm-anko, Poland) with a conventional three-electrode system attached to a computer for the data analyses and storage. The working electrode was made of glassy carbon (GC, ϕ 2mm, A = 0.0314 cm^2). Prior to each measurement, it was hand-polished for 30s with Al_2O_3 (0.3μm) on the alumina polishing pad (Buehler) and sonicated in water just before the use for a minimum of 30 seconds. A platinum wire was employed as an auxiliary electrode. All potentials were recorded in relation to the Ag/AgCl reference electrode.

Methods

All solutions were bubbled in the electrochemical cell with purified nitrogen (99.999%) to remove molecular oxygen from the voltammetry cell for at least 5 min before each measurement and kept under a nitrogen atmosphere during the electrochemical runs. All runs were carried out within a potential range (0 - 1V) where the background currents of the solutions were negligible at T = 22 ± 0.1°C. The voltammograms were recorded for four antioxidants in the SDS aqueous solutions at two pH values (pH 3.9 - acetate buffer and pH 6.88 - phosphate buffer) and in the mixed aqueous-organic systems: water+ACN (3:2 v/v) and water+EtOH (1:1 v/v) containing SDS and NH_3, pH 11. All solutions were prepared by using Milli-Q grade water.

Results and Discussion

In aqueous solutions, the EC mechanism proposed by Ruiz [13] for the oxidation of AA at low pH is widely accepted. It involves two consecutive one-electron transfer processes to form dehydroascorbic acid immediately followed by irreversible hydration to give the final product 2-3 diketogluconic acid. Although the electrochemical reaction is reversible at Hg electrodes [13], the large overpotential needed at carbon electrodes renders the oxidation of AA to be irreversible and the anodic potential (~300 mV at pH 3.9) is considerably higher than its standard value [14, 27], Figure 1.

The addition of SDS significantly alters the i_p of AA as shown in Figure 2a, decreasing i_p upon increasing [SDS] and reaching a plateau region (~ $1x10^{-3}$ M). The E_p values are also affected, Figure 2b, shifting E_p to more positive values reaching a plateau region similar to the variation of i_p. Analogous behaviour was found for PG. Finding these plateau regions indicates the saturated adsorption surfactant layer at the electrode surface, and is in accordance with the results published in the previous reports by our group and others [8, 9, 14, 17-19, 28].

The lipophilic AA16 and LG molecules are water-insoluble but they behave as amphiphilic ones capable of adsorbing on the electrode surface and forming mixed micelles

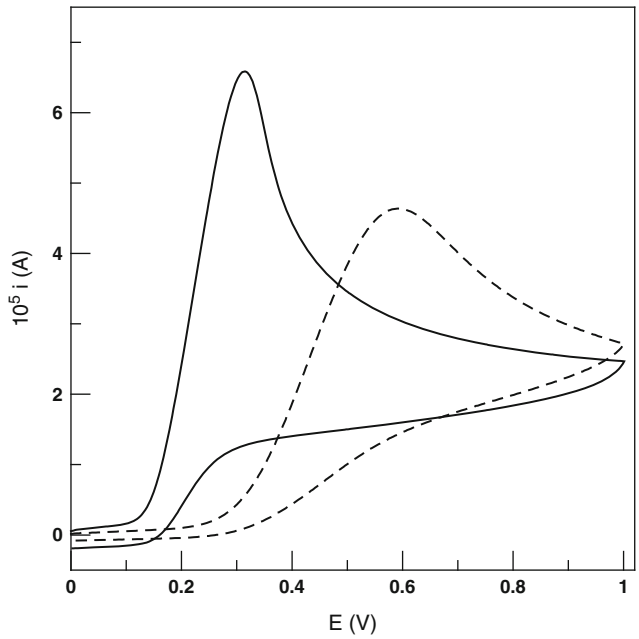

Figure 1 Cyclic voltammograms of AA in the absence (full line) and in the presence of 0.01 M SDS (dashed line). [AA] = $5x10^{-3}$ M, pH = 3.9, T = 22 °C, scan rate: 100 mV s^{-1}

with SDS [20]. For this reason, the effects of [SDS] on E_p and i_p for AA16 and LG were not investigated for the aqueous SDS solutions below CMC. However, they are soluble in the mixed aqueous-organic solvents. The presence of SDS does not influence much the AA16 and LG electrochemical oxidation parameters because no SDS micelles are formed in the aqueous-organic solvents.

Cyclic voltammetry experiments allow determining a number of relevant parameters to characterize the antioxidants as reducing agents, including their diffusion coefficients in a given system, their charge transfer coefficient βn_β and their apparent heterogeneous rate constant k^o. For irreversible anodic oxidations, Eq. 1 is applicable, which predicts a linear relationship between i_p and $v^{1/2}$ as can be seen in Figure 3. Such relationship is typical of the diffusion-controlled processes.

$$i_p = 3 \cdot 10^5 n(\beta n_\beta) A D^{1/2} c^0 v^{1/2} \quad (1)$$

where i_p is the peak current in A, n is the number of electrons involved in the oxidation, A is the area of the electrode (cm^2), c^0 is the concentration of the electroactive species (mmol dm^{-3}), ν is the scan rate (V s^{-1}) and D is the diffusion coefficient of the electroactive species (cm^2 s^{-1}).

The charge transfer coefficient βn_β can be determined from the E_p and $E_{p/2}$ values, which stand for the oxidation peak potential and the potential at which the current equals one half of the peak current, Eq. 2, which, in turn, are found from the CV plots, Figure 1.

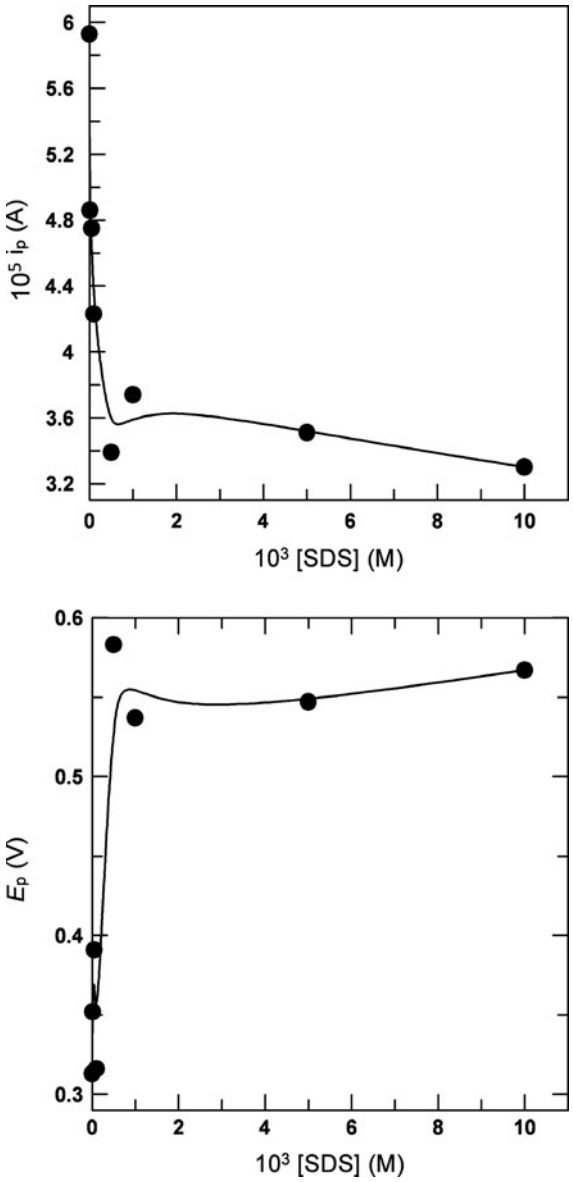

Figure 2 Illustrative plots showing the effects of [SDS] on the peak current i_p and the peak potential E_p of AA. In both cases, a plateau region is reached. pH=3.9, v = 100 mV s^{-1}, T = 22 °C, [AA] = $5x10^{-3}$ M

$$\beta n_\beta = \frac{0.048}{E_p - E_{p/2}} \quad (2)$$

Once the charge transfer coefficients are determined, diffusion coefficients are readily calculated by means of Eq. 3, which is obtained after rearrangement of Eq. 1,

$$D = \left(\frac{i_p}{3 \cdot 10^5 n(\beta n_\beta) A c^0 v^{1/2}} \right)^2 \quad (3)$$

The calculated values for the oxidation parameters of the investigated antioxidants are displayed in Table 1. As

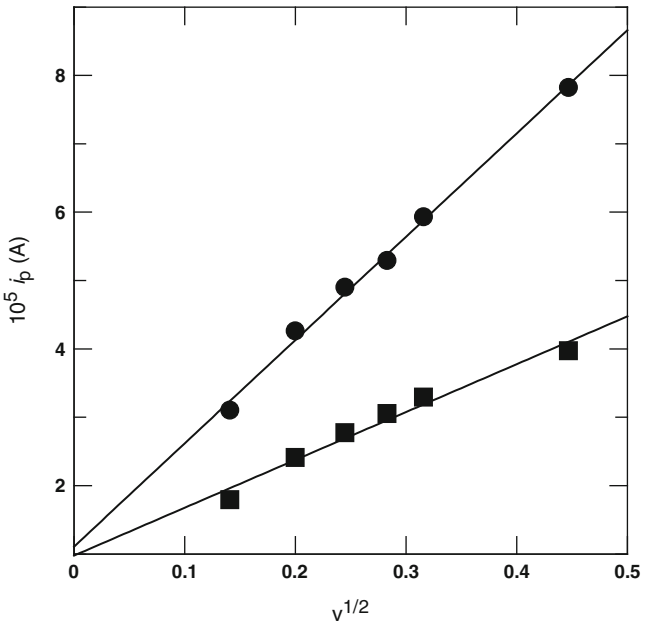

Figure 3 Representative plots showing the linear dependence of i_p for AA in the absence of SDS (●) and in the presence of [SDS] = 0.01 M (■) with the square root of the scan rate v (V s^{-1}) according to Eq. 1, pH = 3.9, T = 22 °C, [AA] = $5x10^{-3}$ M

Table 1 The oxidation parameters of the investigated antioxidants in various systems

RUN	ANTIOX.	SOLVENT	pH	[SDS] (M)	βn_β	10^6 D (cm^2s^{-1})
1	AA	aq. buffer	3.9	0	0.52	7.60
2	AA	aq. buffer	3.9	0.01	0.33	3.74
3	AA	aq. buffer	6.9	0	0.53	6.07
4	AA	aq. buffer	6.9	0.01	0.32	5.97
5	AA	aq.+ACN	11.0	0	0.22	3.68
6	AA	aq.+ACN	11.0	0.01	0.19	5.60
7	AA	aq.+EtOH	11.0	0	0.20	2.10
8	AA	aq.+EtOH	11.0	0.01	0.21	1.60
9	AA16	aq. buffer	3.9	0.01	1.50	0.05
10	AA16	aq.+ACN	11.0	0	0.34	2.06
11	AA16	aq.+ACN	11.0	0.01	0.50	1.67
12	PG	aq. buffer	3.9	0	0.37	3.43
13	PG	aq. buffer	3.9	0.01	0.54	4.70
14	LG	aq. buffer	3.9	0.01	1.60	0.30
15	LG	aq.+EtOH	11.0	0	0.28	0.68
16	LG	aq.+EtOH	11.0	0.01	0.31	2.03

shown, all D values for hydrophilic AA and PG are of the same order, indicating that neither [SDS] nor the acidity and polarity of the system change D significantly. Moreover, the calculated D values are orders of magnitude larger than typical chemically controlled reactions (i.e. reactions which are not under diffusion control). Thermal motion of the molecules ensures that the local distributions of components in any microscopic region (but significantly larger than the molecular scale) of the solution are the same as their stoichiometric concentrations in the whole solution and because the concentrations of reactants are usually small compared to the other components, their reaction does not significantly alter the distribution of other components during the time course of the reaction.

Higher ionization of AA molecules due to the increasing pH should increase the diffusion coefficients, because the electrostatic repulsion makes them less prone to associate to the micellar aggregate, hence remaining in the bulk solution, (entries 2, 4). Closer look at the values in Table 1 reveals that SDS does not change much the D values for water soluble antioxidants, nor does the addition of organic solvent (entries 1-2; 3-4; 7-8). This indicates that these antioxidants associate weakly to the micelles.

It seems apparent from the data in Table 1 that the more hydrophobic antioxidant the stronger aggregation with the micelle and hence slower its diffusion as shown in entries 2-9; 6-11 and 13-14. Especially low diffusion coefficient values are observed for AA16 and LG in the micellar SDS solution because in this system these antioxidants are present entirely in the micelles. This is reflected in the mechanism of electrochemical oxidation which is characterized by the value of βn_β. For the hydrophobic antioxidants in the buffered SDS solution the transfer of the first electron determines the rate of oxidation ($\beta n_\beta \sim 1.5$) whereas in all other cases the rate is determined by the second electron transfer ($\beta n_\beta \leq 0.5$). In the mixed aqueous-organic solvents the micellization is hindered and the presence of SDS does not influence much the D values which are characteristic of freely moving molecules.

Conclusions

In conclusion, our studies of the electrochemistry of some relevant antioxidants in different solvents and determination of their diffusion coefficients have shown that the electrochemical behaviour of the antioxidants is determined predominantly by the hydrophilic/hydrophobic interactions of the hydrocarbon side-chain and the electrostatic interactions of the antioxidant with the surfactant. The strong association of the antioxidant molecules with the SDS micelles results in the significant lowering of its diffusion coefficient and may even change the mechanism of oxidation reaction.

References

1. Mackay RA (1994) Colloids Surf A 82:1
2. Kaifer AE, Gómez-Kaifer M (1999) Supramolecular Electrochemistry, Wiley-VCH, NY

3. Russling JF (1994) Electrochemistry in Micelles, Microemulsions and Related Microheterogeneous Fluids, in Electroanalytical Chemistry, V. 18., Marcel Dekker, NY
4. Volke J, Liska F (1994) Electrochemistry in Organic Synthesis, Springer-Verlag, Berlin
5. Pokorny J, Yanishlieva N, Gordon M (2001) Antioxidants in food: practical applications, CRC press, Boca Raton, 2001
6. Gordon M H (2001) Antioxidants and Food Stability, in Antioxidants in Food, Practical Applications; Pokorny J, Yanishlieva N, Gordon M, Eds. CRC Press, NY
7. Frankel EN (2005) Lipid Oxidation, The Oily Press, PJ Barnes & Associates, Bridgwater, England
8. McClements DJ (2005) Food Emulsions, CRC Press, Boca Raton, USA
9. McClemments DJ, Decker EA (2000) J Food Sci 65:1270
10. Gunaseelan K, Romsted LS, Pastoriza-Gallego MJ, González-Romero E, Bravo-Díaz C (2006) Adv Colloid Interf. Sci 123-126:303
11. Gunaseelan K, Romsted LS, González-Romero E, Bravo-Díaz C (2004) Langmuir 20:3047
12. Sánchez-Paz V, Pastoriza-Gallego MJ, Losada-Barreiro S, Bravo-Diaz C, Gunaseelan K, Romsted LS (2008), J Colloid Interface Sci 320:1
13. Ruiz JJ, Aldaz A, Dominguez M (1977) Can J Chem 55:2799
14. Wen XL, Zhang J, Liu ZL, Han ZX, Rieker A (1998) J Chem Soc Perkin Trans 2: 905
15. Kilmartin PA, Vol. 6, p. 941. Mary Ann Liebert, Inc., ISSN 1523-0864, 2001
16. Kilmartin PA, Zou H, Waterhouse AL (2001) J Food Agric Chem 49:1957
17. Szymula M, Szczypa J, Friberg SE (2002) J Dispersion Sci Technol 23:789
18. Szymula M, Narkiewicz-Michałek J (2003) Colloid Polym Sci 281:1142
19. Szymula M, Narkiewicz-Michałek J (2006) J App Electrochem 36:455
20. Costas-Costas U, Bravo-Díaz C, González-Romero E (2003) Langmuir 19:5197
21. Costas-Costas U, Bravo-Díaz C, González-Romero E (2004) Langmuir 20:1631
22. Costas-Costas U, Gonzalez-Romero E, and Bravo-Díaz C (2001) Helv Chim Acta 84:632
23. Costas-Costas U, Bravo-Díaz C, González-Romero E (2005) Langmuir 21**:**10983
24. Kariuki S, Dewald HD (1996) Electroanalysis 8:307
25. Zana R, Mackay RA (1986) Langmuir 2:109
26. Liu T, Xu J, Guo R (2006) Colloid Polymer Sci 284:788
27. Ormonde DE, O'Neill R (1990) J Electroanal Chem 279:109
28. González-Romero E, Fernández-Calvar MB, Bravo-Díaz C (2002) Langmuir 18:10311

Progr Colloid Polym Sci (2011) 138:189–192
DOI: 10.1007/978-3-642-19038-4_34

Human Erythrocyte Hemolysis Induced by Bioinspired Sugar Surfactants

Kazimiera A. Wilk[1], Katarzyna Zielińska[1], Anna Jarzycka[1], and Jadwiga Pietkiewicz[2]

Abstract Hemolytic activity of single-head single-tail nonionic saccharide – derived surfactants (i.e., *N*-alkanoyl-*N*-methyllactitolamines and *N*-alkyl-*N*-methylaldonylamides) as well as dicephalic (i.e., (*N*-dodecyl-*N*,*N*-bis[(3-D-aldonylamido)propyl]amines; aldonyl = gluconyl and lactobionyl) and gemini structures (i.e., *N*,*N*'-bisdodecyl-*N*,*N*'-bis[(3-aldonylamide)propyl]ethylenediamines; aldonyl = gluconyl and lactobionyl) were examined and discussed in relation to both their critical micelle concentration (CMC) values, and structural aspects. The red blood cells lysis is found to depend on the surfactants structure and the hydrophobic tail length, as well as to correlate well with the CMC magnitudes.

Keywords hemolytic activity • sugar surfactants • human erythrocytes

Introduction

Surface and interface properties of bioinspired so-called sugar surfactants enable their application as very versatile excipients in pharmacological and cosmetic applications, and as constituents of many products with important technological significance [1,2]. As a result of increasing environmental awareness in recent years, a variety of such saccharide-derived compounds have emerged, with defined composition and advantages of low toxicity, being readily biodegradable and inactive toward microorganisms compared to classical nonionics [2-5]. Such structures generate a broad spectrum of aggregate morphologies resembling biological systems, e.g., micelles, vesicles, bilayers, lyotropic mesophases or fibers and gels [1,2]. Despite the fact that saccharide-derived surfactants are of interest for pharmaceutical applications, structure–toxicity relationships of hydrocarbon carbohydrate surfactants have been poorly developed, especially in mammalian systems. Only in a few reports the toxicity and hemolytic activities of carbohydrate-derived surfactants were investigated [6-9].

The main purpose of the present contribution is to explore the correlation between the structure, micellization ability and hemolytic activity of three series of single-head single-tail saccharide surfactants [4,10] along with dicephalic (double-headed) [11] and gemini (dimeric) representatives [3,5], whose structure and abbreviations are shown in Scheme 1.

Experimental

Materials. *N*-alkanoyl-*N*-methyllactitolamines (MELA-n), *N*-alkyl-*N*-methylgluconamides (C_n-MGA; *n*-alkyl = *n*-$C_{10}H_{21}$, *n*-$C_{12}H_{25}$, *n*-$C_{14}H_{29}$, *n*-$C_{16}H_{33}$, and *n*-$C_{18}H_{37}$), *N*-alkyl-*N*-methyllactobionamides (C_n-MLA; *n*-alkyl = *n*-$C_{10}H_{21}$, *n*-$C_{12}H_{25}$, *n*-$C_{14}H_{29}$, *n*-$C_{16}H_{33}$, and *n*-$C_{18}H_{37}$) and (*N*-dodecyl-*N*,*N*-bis[(3-D-gluconylamido)propyl]amine (C_{12}-DGA), *N*-dodecyl-*N*,*N*-bis[(3-D-lactobionylamido)propyl]-amine) (C_{12}-DLA) and (*N*,*N*-bisdodecyl-*N*,*N*-bis[(3-gluconylamide) propyl]ethylenediamine, (bis(C_{12}GA)) *N*,*N*-bisdodecyl-*N*,*N*-bis[(3-lactobionylamide)propyl]ethylenediamine) (bis(C_{12}LA)), were synthesized as previously described [3,4,10,11]. *N*-octanoyl-*N*-methylglucamide (MEGA-8), and *N*-decanoyl-*N*-methylglucamide (MEGA-10) were purchased from Fluka Chemie AG, Buchs, Switzerland. The human outdated red blood cells (RBC) concentrate was obtained from the Regional Blood Bank in Wroclaw. The erythrocyte suspension was prepared by washing four times the RBC concentrate with an isotonic PBS and centrifuged. The erythrocytes were then suspended in PBS at cell density $5x10^9$ cells/ml and immediately used for experiments.

K.A. Wilk (✉)
[1]Department of Chemistry, Wrocław University of Technology, Wybrzeże Stanisława Wyspiańskiego 27, 50–370, Wrocław, Poland
e-mail: kazimiera.wilk@pwr.wroc.pl
[2]Department of Medical Biochemistry, Wroclaw Medical University, ul. Chałubińskiego 10, 50–368, Wrocław, Poland

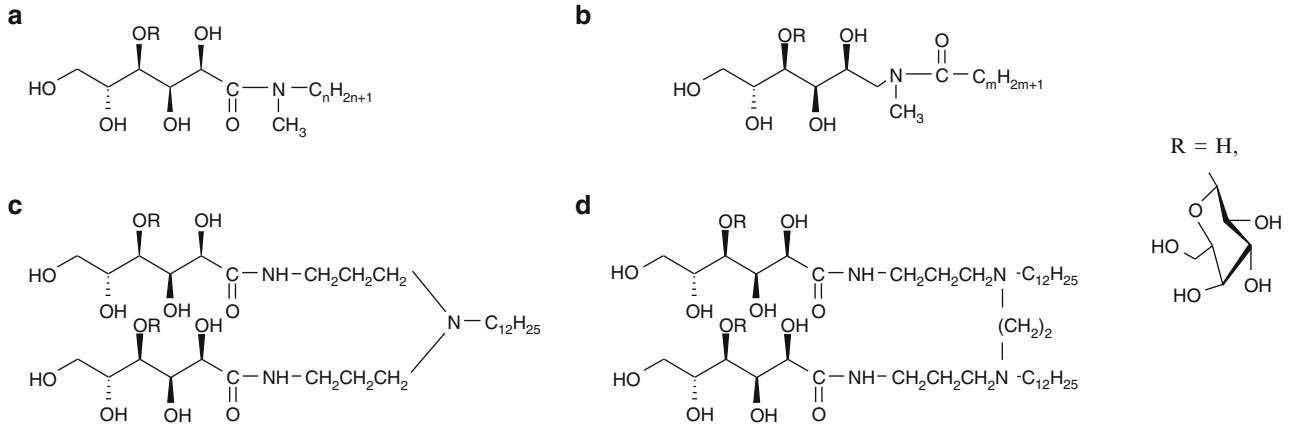

Scheme 1 Structures and abbreviations of the investigated sugar surfactants: a) *N*-alkyl-*N*-methylaldonamides (C_n-MGA, C_n-MLA); b) *N*-alkanoyl-*N*-methylaldonamides (MEGA-n, MELA-n; n = m + 1); c) *N*-dodecyl-*N*,*N*-bis[(3-D-aldonylamido)propyl]amines (C_{12}-DGA, C_{12}-DLA); d) *N*,*N*'-bisdodecyl-*N*,*N*'-bis[(3-aldonylamide)propyl]ethylenediamines (bis(C_{12}-GA), bis(C_{12}-LA))

Erythrocyte hemolysis. The experiments were performed in PBS using a static method according to [12]. The degree of erythrocyte lysis due to sample activity was calculated as the hemolytic index: $\%H = \frac{Hb-Hb_0}{Hb_{tot}} x100\%$, where Hb is the total amount of released hemoglobin in the assayed sample, Hb_0 the amount released due to basal hemolysis (200 µl erythrocytes incubated with 50 µl PBS), and Hb_{tot} the total amount of released hemoglobin in fully disrupted erythrocytes (0.2 ml erythrocytes and 19.8 ml H_2O Milli Q). In each assay, the experimental data are the mean of three independent runs. The data statistical analysis utilized the Student's t-test and statistical significance was accepted at a level of $p<0.05$.

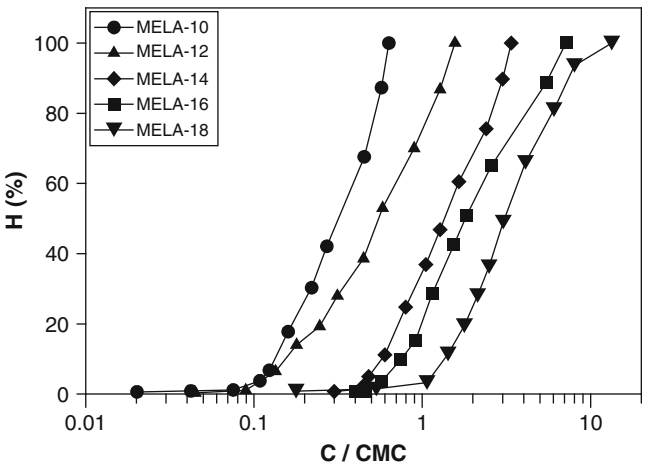

Figure 1 Hemolysis curves of single-head single-tail *N*-alkanoyl-*N*-methyllactitolamines. The surfactant concentrations are related to the respective CMC's

Results and Discussion

The examined saccharide - derived surfactants interact with erythrocyte membranes in a biphasic way by protecting against hypotonic hemolysis at low concentrations and inducing hemolysis at higher concentrations (see Fig.1 for an example). The relative positions of the hemolysis curves are a good reflection of the direct hemolytic activity of surfactants. The position of each curve is characterized by the hemolytic potency HC_{50} index, i.e. surfactant concentration at which the level of hemoglobin released from damaged erythrocytes reached 50 %. Values of HC_{50} along with those of both critical micelle concentration (CMC), and hydrophilic-lipophilic balance (HLB) of the saccharide-derived surfactants are placed in Table 1. The hemolytic activity enhancement was observed with increase of both the carbon amount in the hydrophobic group, and the surfactant concentration in solution. The HC_{50} values plotted against CMC for the examined single-head single-tail surfactants - MELA-n, C_n-MGA and C_n-MLA - as shown at Fig. 2 demonstrate linear relationships between these both parameters (correlation coefficient ca. 0.998). The short-chain surfactants (i.e., MELA-10, MELA-12, C_{10}-MLA, C_{12}-MLA, C_{10}-MGA, C_{12}-MGA) cause substantial RBC damage at concentrations below and close to their CMC's. For the surfactants with C_{14}, C_{16}, and C_{18} the total disruption of erythrocytes was observed for surfactant concentrations much above CMC, making them potential solubilizing agents.

The hemolysis curves of the C_{12} - sugar surfactants comprising the gluconyl, lactobionyl or lactitol-type polar head groups and a varying surfactant structure (single-head single-tail vs. dicephalic vs. gemini) are shown in Fig. 3. Thus, the pyranoside ring presence in the hydrocarbon tail makes the hemolytic activity decrease and for this reason C_{12}-MGA and C_{12}-DGA constitute safer agents for the human RBC than C_{12}-MLA and C_{12}-DLA, respectively. Among the studied

Table 1 Values of hemolytic potency (HC_{50}), critical micelle concentration (CMC) and hydrophilic-lipophilic balance (HLB) of the saccharide-derived surfactants

Surfactant[a]	CMC [b] (mM)	HLB[c]	HC_{50} [d] ± SD (mM)	HC_{50}/CMC [e]
C_{10}-MGA	1.29	7.70	0.64 ± 0.028	0.50
C_{12}-MGA	0.146	6.70	0.15 ± 0.009	1.03
C_{14}- MGA	0.0236	5.80	0.04 ± 0.011	1.70
C_{16}-MGA	0.0077	4.80	0.02 ± 0.003	2.58
C_{18}-MGA	0.0028	3.90	0.01 ± 0.002	3.51
C_{10}-MLA	2.31	11.5	1.32 ± 0.054	0.57
C_{12}-MLA	0.249	10.5	0.21 ± 0.018	0.84
C_{14}-MLA	0.0364	9.60	0.10 ± 0.002	2.72
C_{16}-MLA	0.0093	8.60	0.04 ± 0.004	4.30
C_{18}-MLA	0.0033	7.70	0.02 ± 0.001	6.06
MEGA-8	74.0	8.60	2.00 ± 0.084	0.03
MEGA-10	5.50	8.40	0.70 ± 0.011	7.86
MELA-10	3.32	11.7	1.06 ± 0.016	0.32
MELA-12	0.447	10.9	0.25 ± 0.023	0.56
MELA-14	0.0676	9.81	0.09 ± 0.004	1.33
MELA-16	0.0175	8.86	0.03 ± 0.001	1.71
MELA-18	0.0056	7.91	0.02 ± 0.002	3.56
C_{12}-DGA	0.251	11.8	0.07 ± 0.007	0.28
C_{12}-DLA	0.794	19.0	0.10 ± 0.016	0.13
bis(C_{12}GA)	0.0038	6.30	5.78 ± 0.087	1.52
bis(C_{12}LA)	0.0089	10.9	50.0 ± 2.84	5.62

[a] for the structures see Scheme 1; [b] data from [4] for the C_n-MGA and C_n-MLA series; [14] for MEGA-8; [15] for MEGA-10; [10] for the MELA-n series; [11] for the C_{12}-DGA and C_{12}-DLA; [5] for the bis(C_{12}-GA) and bis(C_{12}-LA); [c] calculated according to McGowan [16]; [d] the surfactant concentration inducing 50% of hemolysis of human erythrocytes ± standard deviation; [e] values of HC_{50}/CMC, where HC_{50} denotes surfactant concentration inducing 50% of hemolysis of human erythrocytes and CMC its critical micelle concentration

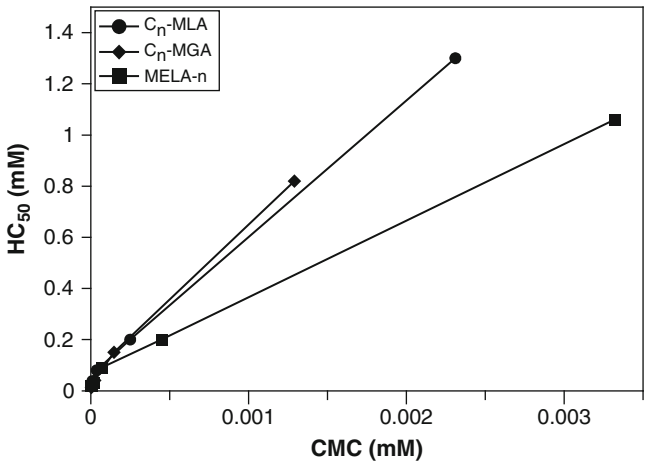

Figure 2 Hemolytic potency, HC_{50}, vs. CMC, for single-head single-tail surfactants

surfactants, the gemini C_{12} derivatives display the lowest hemolytic activity and they cause serious damage of human RBC's only at concentrations highly above CMC; hemolytic potential of bis(C_{12}-LA) is lower than that of bis(C_{12}-GA).

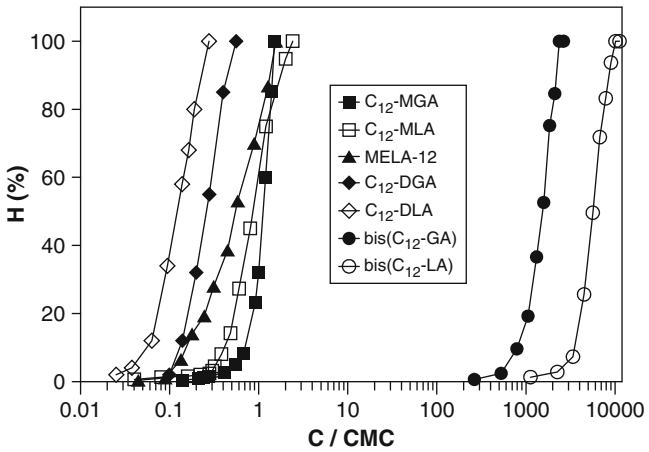

Figure 3 Comparison of the hemolytic activity of C12 saccharide-derived surfactants. The surfactant concentrations are related to the respective CMC's

According to data from Table 1 the damage effect of human erythrocyte membrane in the presence of examined surfactants is dependent also on the surfactant hydrophobicity. Similarly to [13], our results show that inside the MELA-n, C_n-MLA and C_n-MGA series, HLB makes a good parameter to evaluate the ability of a surfactant to bind to the membrane and to be a lytic agent; the lower the HLB the smaller the concentration for membrane solubilization (total lysis). Accordingly, the compounds with higher hydrophobic contents and, therefore, lower HLB reveal a greater tendency to induce the hemolytic action.

Conclusion

The general conclusion evolving from our studies is that the hemolytic activity of structurally related *N*-alkanoyl-*N*-methyllactitolamines and *N*-alkyl-*N*-methylaldonylamides correlate quite linearly with the CMCs of the surfactants. Furthermore, the hemolytic potency of saccharide-derived surfactants is strictly dependent on the surfactant chemical structure and its hydrophilic-lipophilic balance.

Acknowledgement This work was supported by Department of Chemistry, Wroclaw University of Technology, Poland and Wroclaw Research Center EIT+ under the project „Biotechnologies and advanced medical technologies" – BioMed (POIG 01.01.02-02-003/08-00) financed from the European Regional Development Fund (Operational Programme Innovative Economy, 1.1.2)

References

1. Carnero Ruiz C (2008) Sugar-based surfactants. Fundamentals and applications. Taylor & Francis, New York
2. Claesson M, Kjellin URM (2006) Sugar surfactants in: P. Somasundaran, A. Hubbard (Eds), Encyclopedia of Surface and Colloid Science, Taylor & Francis, New York

3. Wilk KA, Syper L, Domagalska BW, Komorek U, Maliszewska I, Gancarz R (2001) J Surfactants Deterg 5:235
4. Burczyk B, Wilk KA, Sokołowski A, Syper L (2001) J Colloid Interface Sci 240:552
5. Komorek U, Wilk KA (2004) J Colloid Interface Sci 271:206
6. Söderlind E, Wollbratt M, von Corswant C (2003) Int J Pharm 252:61
7. Li X, Turánek J, Knötigová P, Kudlačková H, Mašek J, Parkin S, Rankin SE, Knutson BL, Lehmler HJ (2009) Colloids Surf B 73:65
8. Neimert-Andersson K, Sauer S, Panknin O, Borg T, Söderlind E, Somfai P (2006) J Org Chem 70:3623
9. Söderlind E, Karlsson L (2006) Eur J Pharm Biopharm 62:254
10. Wilk KA, Syper L, Burczyk B, Maliszewska I, Jon M, Domagalska BW (2001) J Surfactants Deterg 4:155
11. Wilk KA, Syper L, Burczyk B, Sokołowski A, Domagalska BW (2000) J Surfactants Deterg 3:185
12. Pietkiewicz J, Zielińska K, Saczko J, Kulbacka J, Majkowski M, Wilk KA (2010) Eur J Pharm Sci 39:322
13. Prete PSC, Gomes K, Malheiros SVP, Meirelles NC, de Paula E (2002) Biophys Chem 97:45
14. Harada S, Sahara H (1994) Langmuir 10:4073
15. Kawaizumi F, Kuzuhara T, Nomura H (1998) Langmuir 14: 3749
16. Mc Gowan J (1990) Tenside Surfact Det 27:229

Progr Colloid Polym Sci (2011) 138:193–196
DOI: 10.1007/978-3-642-19038-4_35

Microemulsions Stabilized by Gemini, Dicephalic and Single-Head Single-Tail Sugar Surfactants as Biologically Important Systems: Hemolytic Activity and Cytotoxic Studies

Katarzyna Zielińska[1], Jadwiga Pietkiewicz[2], Jolanta Saczko[2], and Kazimiera A. Wilk[1]

Abstract Influence of oil-in-water microemulsions stabilized by aldonamide – type surfactants on human erythrocytes integrity and human breast cancer MCF-7 cells survival has been investigated. Microemulsion regions were subsequently determined in pseudoternary phase diagrams. The smallest hemolytic and cytotoxic action was exhibited by microemulsions stabilized by gemini surfactants in comparison to their dicephalic and single-head single-tail equivalents.

Key words microemulsion • in vitro toxicology • saccharide - derived surfactants

Introduction

The search for biodegradable and temperature insensitive microemulsions as various solubilizing and reaction media is of increasing importance for emerging applications in several areas, such as: pharmaceutical and medical applications, food products, catalysis, transcriptive syntheses and membrane recognition phenomena, new cosmetic formulations and nanotechnologies. As the medical and pharmaceutical potential of microemulsions needs to be evaluated, the research should be directed not only towards studies of the internal microstructure properties of microemulsions but also at their biological properties such as hemolytic activity and cytotoxicity [1].

As a continuation of our search for new carriers [2], solubilizing media and templates [3,4], we focused on biological characterization of oil-in-water (o/w) microemulsions stabilized by a group of saccharide-derived nonionic surfactants. We have thus applied single-head single-tail *N*-dodecyl-*N*-methylaldonylamides (C_{12}-MGA) and dicephalic structures - *N*-dodecyl-*N*,*N*-bis[(3-D-aldonylamido) propyl]amines (C_{12}-DGA and C_{12}-DLA) as well as gemini ones - *N*,*N*′-bisdodecyl-*N*,*N*′-bis[(3-D-aldonylamido)propyl]ethylenediamines (bis(C_{12}-GA) and bis(C_{12}-LA), gluconyl denoted as GA and lactobionyl as LA). The influence of the designed microemulsions on cells *in vitro* has been assessed in terms of human erythrocytes integrity and human breast cancer MCF-7 cells survival. The o/w microemulsions were selected basing on pseudoternary phase diagrams: surfactant:*iso*-butanol/oil/water (with *iso*-octane and diethylene glycol monoethyl ether as the oils). Conductivity measurements allowed us to distinguish o/w and w/o or bicontinuous microemulsions. Dynamic light scattering (DLS) measurements provided the microemulsion size and polydispersity.

Experimental

Materials. The studied aldonamide surfactants C_{12}-MGA, C_{12}-DGA and C_{12}-DLA, bis(C12-GA) and bis(C_{12}-LA) were obtained from our previous studies [**5–8**]. Diethylene glycol monoethyl ether (EMGD), *iso*-octane and *iso*-butanol were from Sigma. The human outdated red blood cells (RBC) concentrate was obtained from the Regional Blood Bank in Wroclaw.

Microemulsion preparation and characterization. The pseudoternary phase diagram of microemulsion regions was constructed by titration of a given blend of sugar surfactant (bis(C_{12}GA) or bis(C_{12}LA)), *iso*-butanol (surfactant:cosurfactant 1:1) and oil (*iso*-octane or EMGD) with water. Isotropic areas were checked by observation through cross-polarizers (Olympus CX41, Japan). The oil-in-water (o/w), water-in-oil (w/o) and bicontinuous regions

K. Zielińska (✉)
[1]Department of Chemistry, Wrocław University of Technology, Wybrzeże Stanisława Wyspiańskiego 27, 50-370 Wrocław, Poland
e-mail: k.zielinska@pwr.wroc.pl
[2]Department of Medical Biochemistry, Wroclaw Medical University, ul. Chałubińskiego 10, 50-368 Wrocław, Poland

were distinguished by conductance method (EMU, Universal Electrochemical Meter with a platinum electrode). In order to determine the size and polydispersity of the droplets, DLS investigations of the microemulsions were performed with a Zetasizer Nano ZS from Malvern Instruments with the new noninvasive back scatter (NIBS) technology. They were carried out at the scattering angle of 173° with an apparatus equipped with a He–Ne laser (632.8 nm) and an ALV 5000 multibit multitau autocorrelator at 25.0± 0.1 °C.

Erythrocyte hemolysis. Hemolysis experiments were performed in PBS using static method, as previously described [2]. The degree of hemolysis due to sample activity was calculated as the hemolytic index: $\%H = (Hb - Hb_0/Hb_{tot}) 100\%$, where Hb is the total amount of released hemoglobin in the assayed sample, Hb_0 the amount released due to basal hemolysis (200µl erythrocytes incubated with 50µl PBS), and Hb_{tot} the total amount of released hemoglobin in fully disrupted erythrocytes (0.2 ml erythrocytes in 19.8 ml H_2O Milli Q).

Cytotoxicity studies. The MCF-7 breast cancer cells were plated at a density of 2 x 10^5 cells in 0.2 ml of DMEM on 96-well plates and incubated at 37°C in a 5% CO_2 atmosphere. Thereafter, the medium in the wells was replaced with 150 µl of the microemulsion systems and the incubation was continued overnight. The influence of microemulsions on MCF-7 cell survival was assayed after 4-h incubation at 37°C using MTT as it was described in [2]. The MTT was dissolved in PBS (5 mg/ml) and diluted 1:10 in medium without phenol red and serum. A volume of 100 µl of MTT was added to each well after removing the microemulsion from the wells. Then the cells were incubated for 2 h at 37°C to form insoluble formazan crystals and then dissolved in acidic *iso*-propanol. The absorbance of the resulting solutions from three duplicate experiments was read (at 570 nm) in an ELISA microplate reader (Labsystems Multiscan MS, Finland). The calculated data were expressed as the percentage of cell survival.

Results and Discussion

We have recently evaluated and characterized isotropic area magnitudes in the pseudoternary phase diagrams: a single-head single-tail (C_{12}-MGA) or dicephalic (C_{12}-DGA and C_{12}-DLA):*iso*-butanol/oil/water (*iso*-octane or diethylene glycol monoethyl ether as oil phase) [3,4]. In the present contribution we, additionally, describe microemulsion regions for bis(C_{12}-GA) or bis(C_{12}-LA) in the same pseudoternary phase diagrams (Fig. 1). The area in the phase diagrams containing optically isotropic, monophasic systems was designated as the microemulsion region. Systems within this region were identified as water-in-oil (w/o), bicontinuous and oil-in-water (o/w) microemulsions with viscosity, and conductivity measurements (see Fig. 2). Searching for potential nanocarriers of hydrophobic drugs in parenteral delivery system, from the above mentioned pseudoternary phase diagrams ten isotropic monophasic formulations were chosen containing a high proportion of an aqueous component and low amounts of oil and surfactant. All the compositions contained 5% of surfactant, 5% cosurfactant, 5% of oil and 85% of water (Table 1). The diameter of the microemulsion droplets characterized by dynamic light scattering (DLS) ranges from 5.4 to 10.4 nm. The hemolytic activity in human erythrocytes and cytotoxicity for breast cancer MCF-7 cells of microemulsion suspensions were determined after preparing stock solutions with comparable concentrations of investigated samples. Different levels of hemoglobin release after human erythrocyte disruption in the presence of performed microemulsion composed from 10:5:85 weight % ratio of surfactant:cosurfactant/oil/water were observed. Microemulsions stabilized by single-head single-tail and dicephalic surfactants (systems 1–6 from Table 1) demonstrated strong hemolytic activity for human erythrocytes. The non-hemolytic or very weakly hemolytic microemulsions correspond to formulations with *N,N*-bisdodecyl-*N,N*-bis[(3-gluconylamide)propyl]ethylenediamine or *N,N*-bisdodecyl-*N,N*-bis[(3-lactobionylamide)propyl]ethylenediamine as a surfactant. Moreover, systems containing *iso*-octane as the oil were less toxic for erythrocytes and cancer cells than DGME. In the literature there are few reports related to microemulsion hemolysis. Aparicio *et al.* [9] described microemulsions with high hemolytic activity and they concluded that it may be attributed to Labrasol® (caprylocaproyl macrogol-8) glycerides which was used as a surfactant. On the contrary, Nornoo *et al.* [1] reported that formulations examined by them (with glycerides as a surfactants) revealed only insignificant hemolysis.

Cytotoxic effects of the selected microemulsions (Table 1) were measured in MCF-7 cells. The performed cytotoxicity studies demonstrated that only bis(C_{12}-LA) allows for near 75% viability of tumor cells. However, presented data reveal that the lactobionic derivative (systems 9,10) is slightly more safe for MCF-7 cells than the gluconic one (systems 7,8). In the presence of microemulsions stabilized with dicephalic (systems 3–6) and single-head single-tail surfactants (systems 1,2), a significant cytotoxic effect was observed. For these reasons, a utility of those systems for pharmaceutical uses should be limited. From the other hand potential applications of the (C_{12}-DX; X = GA and LA) systems will be studied for preparation of submicron particles type nanocapsules as useful carriers of the safe drug delivery. Moreover, only systems stabilized by the bis(C_{12}-LA) appear to be relatively not toxic for MCF-7 breast cancer cells. Thus microemulsions stabilized by this surfactant may be used in

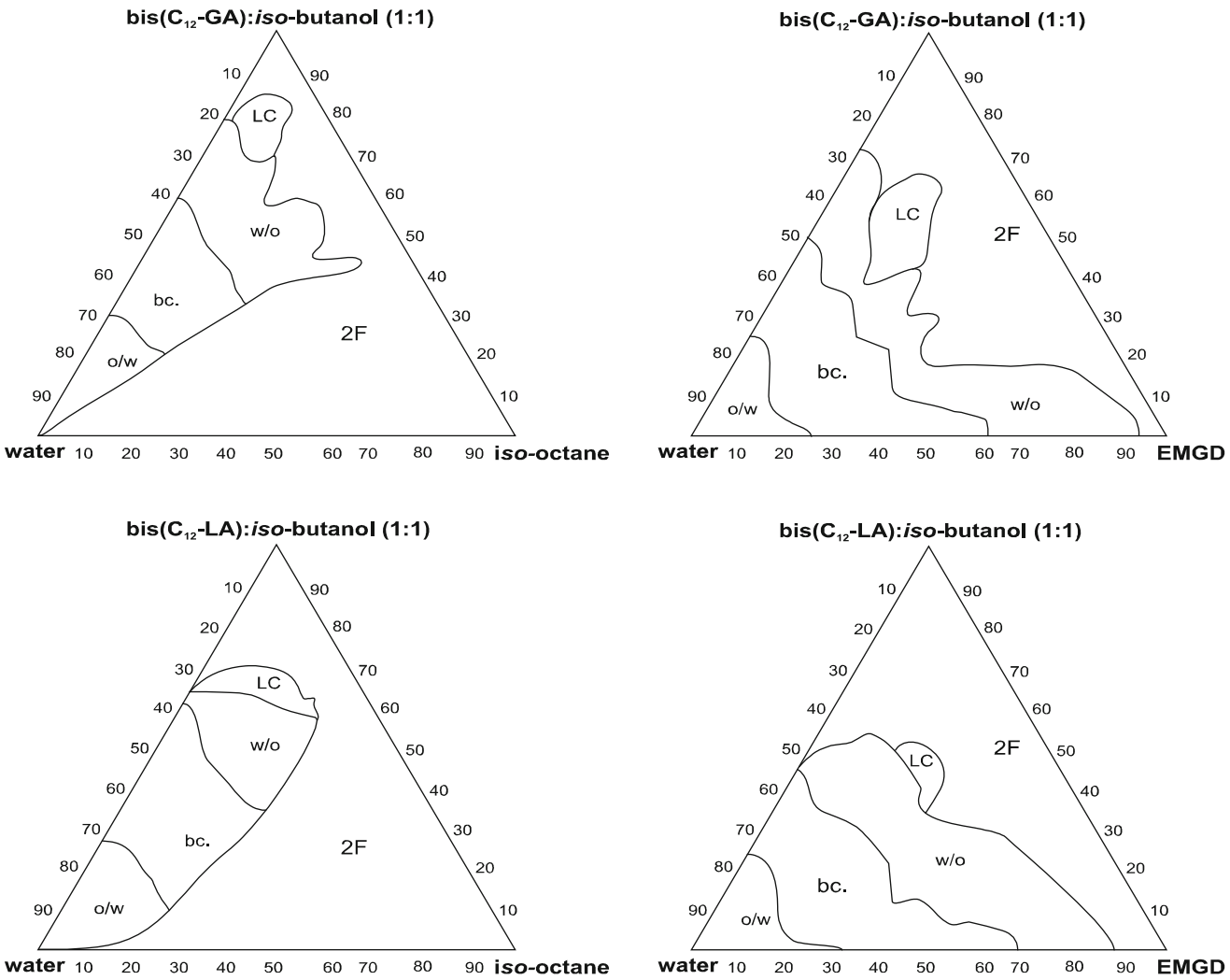

Fig. 1 Phase diagrams of the sugar syrfactant:*iso*-butanol/oil/water systems; EMGD – diethylene glycol monoethyl ether, o/w – oil-in-water microemulsion, w/o – water-in-oil microemulsion, bc. - becontinous microemulsion, LC – liquid crystals, 2F - two phase region

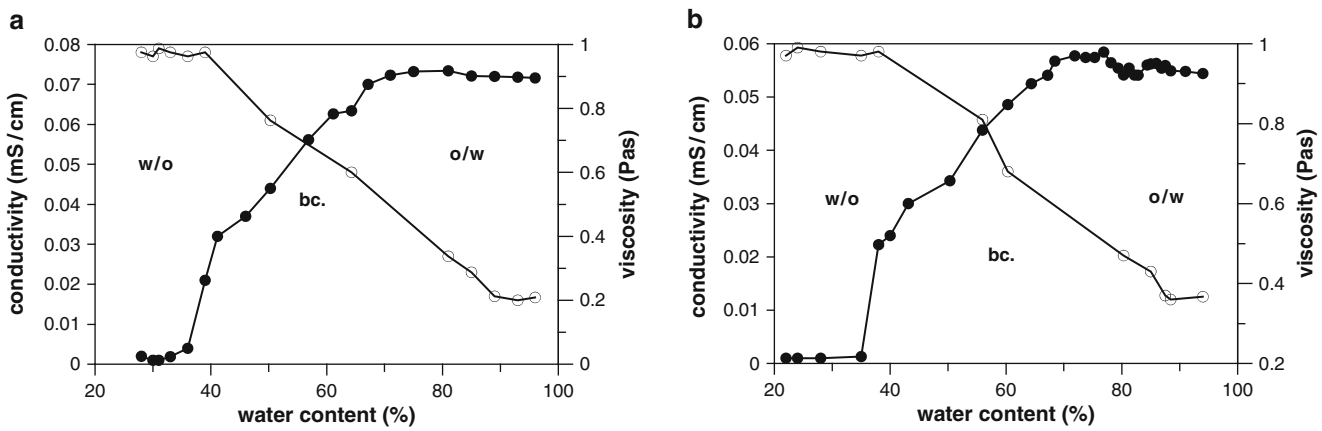

Fig. 2 Electrical conductivity (•) and apparent viscosity (○) of a) bis(C_{12}-GA):*iso*-butanol/*iso*-octane/water and b) bis(C_{12}-LA):*iso*-butanol/*iso*-octane/water microemulsions at constant surfactant-to-oil ratio of 70:30 as a function of water content

Table 1 Hemolysis (H%) and cytotoxicity (expressed as a cell viability, %) induced by the characterized oil-in-water microemulsions

system	o/w microemulsions					H%	cell viability (%)
	sugar surfactant:cosurfactant (weight ratio)	oil (weight ratio)	water (weight ratio)	D_H [c] (nm)	PdI [d]		
1	C_{12}-MGA:*iso*-butanol (10%) [a]	*iso*-octane (5%)	85%	5.4	0.188	48.3	13.0
2		EMGD (5%)	85%	7.6	0.098	54.0	7.5
3	C_{12}-DGA:*iso*-butanol (10%) [b]	*iso*-octane (5%)	85%	5.9	0.113	52.0	20.0
4		EMGD (5%)	85%	7.0	0.091	65.5	27.0
5	C_{12}-DLA:*iso*-butanol (10%) [b]	*iso*-octane (5%)	85%	8.6	0.105	35.7	39.0
6		EMGD (5%)	85%	10.4	0.132	56.0	35.3
7	bis(C_{12}GA):*iso*-butanol (10%)	*iso*-octane (5%)	85%	7.7	0.112	25.8	61.0
8		EMGD (5%)	85%	5.6	0.097	34.4	47.0
9	bis(C_{12}LA):*iso*-butanol (10%)	*iso*-octane (5%)	85%	8.9	0.089	23.0	76.5
10		EMGD (5%)	85%	10.0	0.103	36.6	66.0

[a] phase diagrams from [3]; [b] phase diagrams from [4]; [c] the average diameter of the droplets $D_H = kBT/(3\pi\eta D)$, where D_H, k_B, T, η, and D are the hydrodynamic radius of the droplet, Boltzmann's constant, temperature in Kelvin, viscosity of the microemulsion, and the diffusion constant, respectively; [d] PdI denotes the polydispersity index

pharmaceutical applications as better solubilizing agent than dicephalics or monomeric C_{12} derivatives.

Conclusion

Our performed studies indicate that, among the examined microemulsions stabilized by nonionic aldonamide surfactants only those containing the gemini derivatives are nontoxic for human erythrocytes and for MCF-7 breast cancer cells. The oil-in-water microemulsions stabilized with bis(C_{12}-GA) or bis(C_{12}-GA) appeared to be both good candidates for interface polymerization templates, and they can be used as original hydrophobic drug delivery systems.

Acknowledgement This work was supported by Department of Chemistry, Wroclaw University of Technology, Poland.

References

1. Nornoo AO, Osborne DW, Chow DS-L (2008) Inter J Pharm 349:108
2. Pietkiewicz J, Zielińska K, Saczko J, Kulbacka J, Majkowski M, Wilk KA (2010) Eur J Pharm Sci 39:322
3. Zielińska K, Wilk KA, Jezierski A, Jesionowski T (2008) J Colloid Interface Sci 321:408
4. Wilk KA, Zielińska K, Hamerska-Dudra A, Jezierski A (2009) J Colloid Interface Sci 334:87
5. Wilk KA, Syper L, Domagalska BW, Komorek U, Maliszewska I, Gancarz R (2001) J Surfactants Deterg 5:235
6. Burczyk B, Wilk KA, Sokołowski A, Syper L (2001) J Colloid Interface Sci 240:552
7. Wilk KA, Syper L, Burczyk B, Maliszewska I, Jon M, Domagalska BW (2001) J Surfactants Deterg 4:155
8. Wilk KA, Syper L, Burczyk B, Sokołowski A, Domagalska BW (2000) J Surfactants Deterg 3:185
9. Aparicio RM, Garcia-Celma MJ, Vinardell MP, Mitjans M (2005) J Pharm Biomedical Analysis 39:1063

Index